Monitoring dynamics of grassland with multi-modal and multi-temporal satellite time series analysis

Anatol Garioud

Monitoring grassland dynamics by exploiting multi-modal satellite image time series.

Thèse de doctorat de l'Université Gustave Eiffel

École doctorale n° 532, Mathématiques, Science, et Technologie de l'Information et de la Communication (MSTIC)
Spécialité de doctorat : Sciences et technologie de l'information géographique
Laboratoire des Sciences et Technologies de l'Information Géographique (LASTIG), UGE, IGN, ENSG
Centre d'Etudes Spatiales de la Biosphère (CESBIO), UMR 5126 (CNRS, UPS, IRD, CNES, INRAe)

Thèse présentée et soutenue à l'Université Gustave Eiffel, le 20/05/2022, par

Anatol GARIOUD

Composition du Jury

Clement ATZBERGER Professeur, Univ. für Bodenkultur (BOKU), Autriche	Rapporteur
Dino IENCO Directeur de Recherche, UMR TETIS, INRAe, France	Rapporteur
Marie WEISS Ingénieur de Recherche, UMR EMMAH, INRAe, France	Examinatrice
Thomas CORPETTI Directeur de Recherche, UMR LETG, CNRS, France	Président, Examinateur
Jochem VERRELST Chargé de Recherche, Univ. de València, Espagne	Examinateur
Nicolas DELBART Professeur, Univ. de Paris, UMR LIED, France	Examinateur

Encadrement de la thèse

Clément MALLET Ingénieur, Univ. Gustave Eiffel, IGN, ENSG, LASTIG, France	Directeur de thèse
Silvia VALERO Maître de Conférences, Univ. Paul Sabatier, UMR CESBIO, France	Co-directrice de thèse

Invités

Sébastien GIORDANO Ingénieur de recherche, IGN, France	Invité
Thomas EGLIN Chargé de Mission, ADEME, France	Invité

Acknowledgments

Bird's view is somehow fascinating, rich in contrasts and details, stimulating curiosity. To have been able to work on demonstrating a utility to this atypical point of view, on a current and fascinating subject, and to end up with this PhD is for me an invaluable opportunity. To begin with, I would thus like to thank all those who, from near or far, have made this work progress in any way.

I would like to express my gratitude to my thesis supervisors, Clément Mallet and Silvia Valero, who allowed me to carry out my work in serene and pleasant conditions. On the scientific questions, they were always available and caring, giving me the confidence and tools necessary to succeed. On personal aspects, their listening, support, and sense of compromise were precious. Thank you to Clément who, despite the random posters on the ceiling and the countless football-related tackles, was always one step ahead and encouraging for the following. Thank you to Silvia, for her incredible patience when I was cutting corners...and for the immense amount of time devoted to perfecting the content of this PhD. I would also like to warmly thank Sébastien Giordano, supervisor during the first round. His enthusiasm and transversal vision of the scope of this thesis allowed the work to be on the right track early on. The freedom that the three of you gave me allowed for continuous learning and to make this thesis a pride, so for this, again, merci!

Next, I am thankful to all the members of the jury for accepting to proofread the manuscript, and especially to the rapporteurs Clement Atzberger and Dino Ienco. Thank you to ADEME and CNES who gave me their confidence by financing this thesis, and Météo-France for sharing some valuable data. I would also like to thank Francesco Sarti and Clément Albinet, who during my stay in Rome planted the seed of a pursuit as a PhD candidate.

I had the pleasure of being affiliated with two exceptional laboratories during my thesis years. First and foremost, at the LASTIG of IGN which I thank for the welcome, and where I could appreciate the jovial mood and the characteristic effervescence of research. Thank you to the co-detainee Vivien, to Loic, Yanis, Raphael, Marc, Luc, Emile, Hermann, Arnaud, Mathieu, Ewelina, Paul, Oussama, Stéphane, Pierre-Louis...and all the others. Break a leg to all of you! A big thank you to Jean-Paul Rudant, for the enriching discussions and the opportunities to communicate on my work. I would also like to thank François Lecordix and IGNfab for allowing me to collaborate or exchange with different private actors on various subjects. On the CESBIO lab side, despite my limited stays, a special thank you goes to Jean-François Dejoux who devoted himself to me to dig up validation data… an arduous task! Warm thanks to Jordi Inglada, Mathieu Fauvel, Milena Planells, Eric Ceschia, Rémy Fieuzal...and many others, for the gratifying and fruitful discussions. I hope to have the pleasure of meeting you again.

Then, a sincere thank you to my friends, for helping to take things easy. To my lifelong friends: Benjamin, Nicolas, Julien, Théodore, Hugo…what a journey! To my almost lifelong friends: Ali, Helenka, both Adriens, Julien, Sandrine, Quentin…to many more bro dinners. Cheers to the TGAE team: Zack, Samar, and Ludovic. And also, to Valo's two brothers, stop peeking. Ultimately, to all the ones that are looking for their names...!

Finally, a big thank you to my family, first of all to my parents for their unfailing support and enthusiasm, and to my grandmother, whose pride, despite being over a hundred years old, is nothing but inspiration. Then to the Peyriolans, Wiener, Nargissians, Lyonnais, and Saint-Orennais, who had to sometimes endure my PhD debacles. Although it probably sounded like lucubrations to you, it had to come out! I also have a particular and emotional thought for Manon.

A closing and special mention to you, Amélie, who largely made this thesis possible. Thank you for your awesome support, in every respect, despite the crazy times. Being on the same page while both doing a PhD isn't a walk in the park. But here we are, and it's your time soon.

Abstract

The vast grassland surfaces as well as the growing recognition of the ecosystem services they provide have revealed urgent needs for their conservation and sustainable management. In particular, over-exploitation causes a significant decrease in their capacity to provide multiple ecosystem services. Despite the acknowledged importance of management practices, there are currently no large-scale efforts reporting on their frequency and nature.

Satellite remote sensing appears to be a suitable tool for efficient grassland monitoring. Satellite time series specifically allow synoptic and regular observations. Combined, the characteristics provided by complementary optical and Synthetic Aperture Radar (SAR) images from the Sentinels bring new opportunities to monitor grassland vegetation conditions. The research conducted in this PhD thesis intends to investigate the capabilities and the synergy of Sentinel time series for grassland monitoring. Specifically, it aims to develop methods for detecting grassland management practices. Farmers are managing grasslands with a wide range of practices, having different impacts on biomass and calendars. Therefore, frequent and regular satellite acquisitions are mandatory, especially because grasslands exhibit the particularity of potential rapid regrowth after management.

The joint exploitation of Sentinel-1 and Sentinel-2 and the increase of acquired data raise new challenges. The high dimension and the heterogeneous physical nature of the data, with various spatial, spectral and temporal domains, are among the aspects to be explored. At the same time, recent advances in computing resources and machine learning algorithms are bringing to the forefront deep learning strategies suitable for dealing with the reported requirements, such as large-scale processing and data mining. In this context, the main objective of this PhD is to develop new methodologies allowing the frequent and regular monitoring of grasslands and the detection of their management practices. Under this purpose, this PhD: (i) uses the advances of deep learning architectures to develop a multi-source methodology exploiting the synergy and capabilities of both Sentinel-1 and Sentinel-2 data. The developed recurrent-based methodology targets to regress multivariate SAR time series towards optical NDVI and proposes the incorporation of contextual knowledge to reduce the impact of exogenous factors leading to SAR data variability ; (ii) explores methods aiming to detect heterogeneous changes in vegetation status associated to grassland management practices.

The proposed Sentinels Regression for Vegetation Monitoring (SenRVM) approach provides NDVI time series with no missing data at 6 days. The results, compared to the NDVI obtained by Sentinel-2, show low errors and good stability on contrasted vegetation surfaces and different large-scale geographical contexts. An ablation study of satellite and ancillary features and a comparison to commonly adopted gap-filling methods for retrieving information over short- and long-term data gaps underline the methodological contributions. To accurately detect management practices, a segmentation of grassland parcels at the superpixel-scale, justified by their rotational management, furthermore allows exploiting the dense time series over homogeneous areas. Diverse 1D time series change detection methodologies are compared using two constructed large-scale validation datasets. The results achieve high performances in retrieving the different patterns related to grassland management.

The proposed methodologies integrate freely accessible data, whose continuity is ensured, and exploit deep learning methods favoring large-scale and versatile applications. Therefore, they are foundations for the extraction from multi-modal satellite image time series of relevant information related to the grassland ecosystem whose understanding is essential.

Résumé

Les vastes surfaces de prairies ainsi que la reconnaissance croissante des services écosystémiques qu'elles fournissent ont révélé des besoins urgents pour leur conservation et leur gestion durable. En particulier, leur surexploitation entraîne une diminution de leur capacité à fournir des services écosystémiques. En dépit de la nécessité d'obtenir des données décrivant l'exploitation des prairies, l'observation de la fréquence et de la nature de leur exploitation demeure restreinte.

La télédétection par satellite est un outil approprié pour un suivi efficace des prairies. Les séries temporelles d'images satellites permettent des observations synoptiques et régulières. Combinées, les caractéristiques fournies par les images complémentaires optiques et radars des satellites Sentinel offrent de nouvelles opportunités. Les recherches menées dans le cadre de ce doctorat visent à étudier les capacités et la synergie des séries temporelles Sentinel pour le suivi des prairies. Plus spécifiquement, elles visent le développement de méthodes de détection des pratiques agricoles. La gestion de chaque prairie est faite avec des intensités et des calendriers distincts. Par conséquent, des acquisitions fréquentes et régulières sont d'autant plus indispensables que les prairies peuvent repousser rapidement après leur exploitation.

L'abondance des données de Sentinel-1 et Sentinel-2 et leur exploitation conjointe soulèvent de nouvelles problématiques. La haute dimension et la nature physique hétérogène des données, conjuguant divers domaines spatiaux, spectraux et temporels, font partie des aspects à explorer. Récemment, les progrès en matière de ressources informatiques et d'algorithmes d'apprentissage automatique mettent au premier plan les stratégies d'apprentissage profond, qui permettent de relever les défis exposés, tels que le traitement à grande échelle et l'extraction d'informations complexes. L'objectif principal de la thèse est donc de développer des méthodes permettant le suivi en continu des prairies et la détection de leur exploitation. À cette fin, la thèse : (i) utilise les progrès permis par l'apprentissage profond, pour développer une méthodologie multi-source exploitant la synergie des données Sentinel-1 et Sentinel-2. La méthodologie développée vise spécifiquement à régresser les séries temporelles radars multivariées vers le NDVI optique et propose l'incorporation de connaissances contextuelles pour réduire l'impact de facteurs exogènes ; (ii) explore différentes méthodes permettant de détecter l'exploitation hétérogène des prairies.

L'approche proposée, nommée Sentinels Regression for Vegetation Monitoring (SenRVM), fournit des séries temporelles de NDVI complètes avec une répétitivité de six jours. Les résultats, comparés aux NDVI obtenus par Sentinel-2, indiquent de faibles erreurs et une bonne stabilité sur diverses surfaces de végétation et différents contextes géographiques. Une étude d'ablation des données satellitaires et auxiliaires ainsi qu'une comparaison avec des méthodes communément adoptées pour interpoler les données manquantes soulignent la pertinence des contributions méthodologiques. Pour détecter avec précision les pratiques agricoles, une segmentation des parcelles de prairie à l'échelle du superpixel, justifiée par leur gestion rotative, permet d'exploiter les séries temporelles denses sur des zones homogènes. Différentes méthodologies de détection de changements sont comparées à l'aide de jeux de données de validation construits. Les résultats atteignent des performances élevées dans l'identification des différentes tendances liés à la gestion des prairies.

L'intégration de données accessibles gratuitement, dont la continuité est assurée, et l'exploitation de méthodes d'apprentissage profond favorisant les applications à grande échelle et polyvalentes, ont permis d'introduire des méthodes qui proposent des bases pour la collecte d'informations pertinentes liées à l'écosystème des prairies.

Table of content

List of figures

List of tables

List of Acronyms

ANN	Artificial Neural Network
CAP	Common Agricultural Policy
CNES	Centre National d'Etudes Spatiales
DL	Deep Learning
EM	Electromagnetic
EO	Earth Observation
ESA	European Space Agency
GRD	Ground Range Detected
GRU	Gated Recurrent Unit
IGN	French Mapping Agency
LEO	Low Earth Orbit
LPIS	Land Parcel Identification System
LSTM	Long Short-Term Memory
MAE	Mean Absolute Error
ML	Machine learning
MLP	Multilayer Perceptron
MSE	Mean Square Error
MSS	Multispectral Scanner
NASA	National Aeronautics and Space Administration
NDVI	Normalized Difference Vegetation Index
PELT	Pruned Exact Linear Time
RMSE	Root Mean Square Error
RNN	Recurrent Neural Network
RPG	Registre Parcellaire Graphique
SAR	Synthetic Aperture Radar
SDGs	Sustainable Development Goals
SenRVM	Sentinels Regression for Vegetation Monitoring
SLC	Single Look Complex
SLIC	Simple Linear Iterative Clustering

Part I

INTRODUCTION

Chapter 1

Grasslands and remote sensing: context, diversity and challenges

1.1 Definition, extent and importance of grasslands

1.1.1 A vast and disparate entity

Grasslands have existed for millions of years and constitute biomes (Dinerstein et al., 2017), which are large and homogeneous ecological environments (Figure 1.1). Grasslands biomes are formed under certain climate conditions. The climate must be sufficiently humid for vegetation to grow, otherwise the environment is desert. Conversely, a too humid climate leads to the growth of trees, forming forests (Hibbard et al., 2003; Hou et al., 2019). Grasslands are therefore a transitional biome. Its existence is nevertheless favored by other natural disturbance mechanisms such as defoliation by animals or frequent fires (Begon et al., 2006) that prevent the transition from grassland to forest. Although there are various agronomic, historical, or practical aspects to defining grassland, the consensus is that it is a habitat consisting mostly of grasses the *Poaceae* and other graminoids, with a low abundance of trees or shrubs. The presence in a variable proportion of natural forbs is also a characteristic of grasslands. With more than 12,000 species of solely *Poaceae* recorded (Kellogg, 2015), grasslands induced diversity at the botanical level can already be imagined (Wilsey, 2018). The complexity of grasslands is thus, understandably, reflected in the lack of consensus regarding their precise definition.

Alongside the areas of natural grassland forming biomes, human activities, as for other ecosystems, are a major factor in the maintenance, development or decline of grasslands. Human activities traced back to the domestication of livestock in the Neolithic period and the appearance of grazing and deforestation (Poschlod et al., 2009) have greatly expanded the location and diversity of the natural grasslands (Gibson, 2009). When managed by humans, grasses are commonly associated with leguminous plants, the *Fabaceae*, composed of over 19,000 species (Nadon and Jackson, 2020) increasing again the agronomic variety of grasslands. These newly formed managed grasslands belong to one of the most ancient forms of farming (White et al., 2000). At the same time, human activities through successive evolution, from breeding, mechanization or the fodder revolution, have allowed grasslands to be maintained by eliminating woody resources.

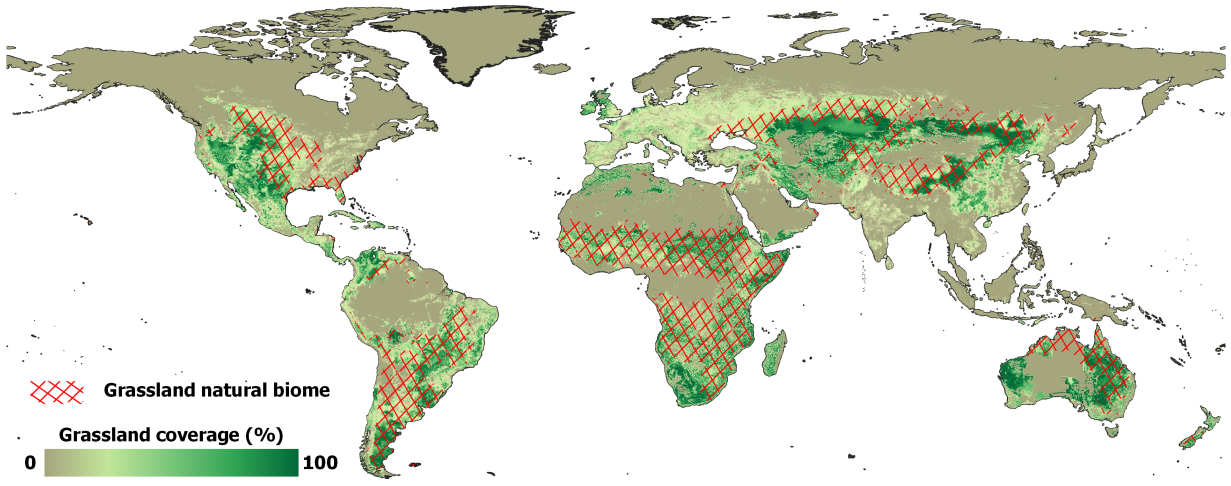

Figure 1.1: Worldwide distribution of pastures retrieved from two satellite (MODIS and SPOT VEGETATION) combined with agricultural inventory data for the year 2000 (*modified from : Ramankutty et al., 2010*). Location of natural grasslands biome are superimposed in red (*modified from : Dinerstein et al., 2017*).

Nowadays, grasslands, *i.e.*, natural and human-induced, cover a significant proportion of about 40% of Earth's surface and near 70% of all agricultural land areas (Suttie et al., 2005). Figure 1.1 includes a map produced from satellite data and agricultural statistics for the year 2000 by Ramankutty et al., 2010. This

map shows the large areas covered by a varying percentage of grasslands and the location of the natural grassland biome. A first remark concerns the unique characteristic of grasslands of being distributed on all continents and especially at every latitude from the Equator to the poles. Grasslands are also encountered at very different altitudes (Allaby, 1998; Pausas and Bond, 2019) showing significant adaptation and resilience to a wide range of climatic conditions. By comparing the location of the natural grassland biome and their current distribution, this map also highlights the historical great expansion of grasslands, primarily due to human intervention. This is particularly noticeable in temperate climates, such as in Europe and South-Western North-America where grasslands are very present, despite a climate rather favorable to the presence of forests. The varied distribution of grasslands leads to varied denominations. The different denominations are mainly based on their location or usage. Steppes and parts of the tundra in Asia, pampas in South America, savanna in Africa and Australia, or Prairies of the Great Plains in North America, and simply grasslands in Europe all refer to grasslands with distinct geographical distributions. Pastures, rangelands, or meadows also refer to grasslands through their main botanic composition and usage.

Through their botanic, agronomic, and geographical diversity, grasslands represent a challenging ecosystem. Being for some part of a natural biome and now covering one of the most extensive ecosystems on our planet, grasslands play an important role in many aspects of climate, economy, society, and health.

1.1.2 Grassland ecosystem services

Some of the major benefits of grasslands are well known: they are habitat for abounding plant and animal species (Watkinson and Ormerod, 2001; Petermann and Buzhdygan, 2021). They feed an important population as the main resource for livestock (O'Mara, 2012; Michalk et al., 2019). Nevertheless, beyond these aspects, the fundamental importance of grasslands lies in their multifunctional capacities, most of which are often neglected or poorly known.

The notion of *ecosystem services* emerged in the 20th century (Ehrlich and Ehrlich, 1981; Mooney and Ehrlich, 1997) and offers a framework at the interface between ecology and economics. Ecosystem services groups together the goods and services that humans can obtain from an ecosystem, directly or indirectly, benefiting their well-being. Ecosystem services are commonly regrouped in four different types (Bishop, 2012): *(i):* provisioning services, define the tangible products that can be exploited like food, raw materials, freshwater or medicinal resources; *(ii):* regulating services, which are intangible, regroup all benefits provided by an ecosystem for maintaining, improving, controlling or preventing environmental effects; *(iii):* socio-cultural services, which are non-material and at the interface between humans and their relationship with nature such as aesthetic, touristic or spiritual benefits; *(iv):* supporting services that include indirect interactions with other elements of the biosphere such as providing living spaces for fauna and flora.

Beyond the two aspects of habitat and resources to livestock, grasslands, due to their variety, are one of the habitats that offer both one of the largest ranges and important number of ecosystem services:

- ***Provisioning services***: these services are the most obvious and include the products of animal husbandry and gathering. The production of fodder and plant protein, the flowers, berries or mushrooms found in the grasslands are at the heart of productivity issues. These grasslands products are directly linked to notions of quality of food value, animal health, and *in-fine* to the quality of the products resulting from breeding and ultimately human health.

- ***Regulating services***: they are perceptible at several scales of analysis, at the grassland parcel level as well as at the level of a farm, a region or finally at the global level. The different scales interact, making grasslands one of the ecosystems providing the most regulating services. Grasslands provide water quality regulation, with the fixation of atmospheric nitrogen by the presence of legumes for

example. They have a filtering effect of collecting and distributing rainfall to surface and ground water. Grasslands also serve to protect against floods and erosion, by retaining water or spreading the flow of floods and fix the soil, especially in areas with a varied topography. Grasslands are also reserves of biodiversity, hosting and feeding an abundant and varied fauna, including grassland dependent species. The flora of grasslands, often accompanied by mellifluous plants, allows the reproduction of pollinating insects. Finally, grasslands fix and store carbon dioxide (CO_2) as well as other atmospheric gases such as nitrous oxide.

- ***Socio-cultural services***: the meadows have a landscape, faunistic, floristic, and therefore educational interest. Their heritage value is part of landscapes such as bocage or estives and alpine pastures, giving them an appreciated scenic value.

- ***Supporting services***: these services result from the previous ones. Combined, they allow the essential cycles of nutrients, water, or the formation of soils which are the supporting services.

1.1.3 Environmental importance and associated threats

In view of contemporary challenges that include climate change, biodiversity loss, and food security, the importance of grasslands is increasing and their essential character emerges (TEEB, 2010; Boval and Dixon, 2012; Yang et al., 2019b). Monitoring the dynamics of grasslands now seems essential, as evidenced by a revival of public policies concerning them (Le Quéré et al., 2013; Luyssaert et al., 2014; UN, 2015; Bengtsson et al., 2019; Powers and Jetz, 2019; Shukla et al., 2019; Bardgett et al., 2021; Chang et al., 2021). This is the case of the global climate policies defined by the United Nations, such as the Decade on Ecosystem Restoration from 2021 to 2030 or the 2030 Agenda for Sustainable Development, which succeeded the Millennium Development Goals in 2012 and defines 17 Sustainable Development Goals (SDGs). Grassland ecosystem services participate in several goals such as achieving zero hunger (SDG 1), ensuring good health and well-being (SDG 3), providing access to clean water and sanitation (SDG 6), leaning towards responsible consumption and production (SDG 12), enforcing climate actions (SDG 13) and protecting life on land (SDG 15). Agreements signed in 2015 notably during the COP21 in Paris (France) or during the Sendai Framework for Disaster Risk Reduction signed in Japan also recognized grasslands as major actors of the future climate. All of these public policies coordinate efforts on a global scale concerning several climate factors, of which one of the most prominent objectives is the reduction of carbon emissions.

As a counterpart to climate change linked to the increase of greenhouse gases in the atmosphere, grasslands are, alongside forests and wetlands, key ecosystems in the fixation and storage of CO_2 (Scurlock and Hall, 1998). In contrast to forests which store carbon mainly in their leaves and woody resources, grasslands sequester carbon underground, in their roots and by transmission to the underlying soil. Deforestation and especially the increasing frequency of fires due to rising temperatures and droughts lead to the release of the stored carbon in trees into the atmosphere. These changes affect the overall carbon budget of forests negatively, while grasslands, with their underground storage, are more adapted to current changes (Hufkens et al., 2016; Dass et al., 2018). While the role of grassland in carbon storage is often omitted, they could currently contain about 30% of the world's soil carbon stock (Bardgett et al., 2021; Chang et al., 2021; Scurlock and Hall, 1998).

Exponential efforts have been made to monitor the current state and trends of our globe's surfaces, among them grasslands (Plummer et al., 2017; Liu et al., 2020a; Winkler et al., 2021). Satellites are one of the tools allowing the monitoring of large areas (Section 1.2) and have therefore been exploited for this purpose. For example, Winkler et al., 2021 have recently proposed to map global changes per 1×1 km grid cell from 1960 to 2019 by combining multiple satellite data (MODIS, Landsat, Sentinel) with historical statistical datasets, such as from the Food and Agriculture Organization of the United Nations. The results were obtained for six

classes, namely urban, cropland, pasture / rangeland, unmanaged grass / shrubland, and sparse/no vegetation classes. Annual dynamics were used to compute a global change rate from the complete period. Four classes of changes which are stability, losses, gains and multiple changes have been defined. Authors have found that 17% of the Earth's land surface has changed at least once between the assessed time intervals. Furthermore, they highlighted that 86% of all multiple changes are related to agriculture such as land transitions related to cropland or pasture/rangeland. Figure 1.2 shows the changes observed for grassland classes (pasture, rangeland and unmanaged grass/shrubland) through the period 1960-2019 found by Winkler et al., 2021. It can be observed that a significant number of grasslands were affected by changes.

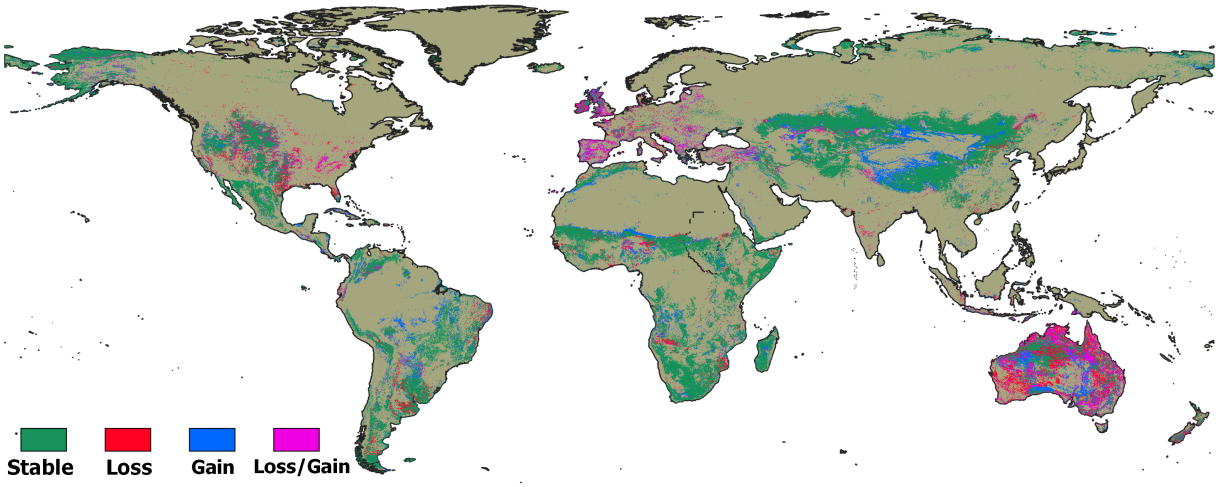

Figure 1.2: Changes in grassland surfaces for the period 1960-2019 detected with satellite and statistical datasets. (*Modified from : Winkler et al., 2021*)

Despite the importance of grasslands and the many explained multi-domain benefits they provide (Section 1.1.2), grassland areas have largely decreased in many parts of the world, mostly in favor of crops (Bardgett et al., 2021; Bongaarts, 2019; Winkler et al., 2021). Furthermore, it is estimated that currently, about 50% of the global grasslands are degraded (Gang et al., 2014; Bardgett et al., 2021). The main factors of degradation are overgrazing, intensive agricultural practices, and climate change. Degradation and losses of grasslands poses important threats for a significant part of the world population relying on them. Food, fuel, and fiber or medicinal products are direct and necessary resources produced by the grasslands.

Because of their geographical distribution and the wide range of ecosystem services they provide it would nevertheless be inappropriate, if not impossible, to consider grasslands as a single environment. A possible and commonly used distinction is based on the origin and history of the grassland. On the one hand, natural grasslands, originating from their biomes, have certain distinct properties with respect to grasslands emerging from human activities. They are are perennial and respond favorably to the full range of grassland-related ecosystem services. In particular, they allow carbon storage over time scales of at least decades or centuries. On the other hand, the majority of agricultural grasslands provide a lower and degraded range of ecosystem services, particularly due to their intensive exploitation. Decline in endemic biodiversity and reduced carbon storage capacity are the main subsequent consequences. Some agricultural grasslands in temperate climates fulfill the same functions as natural grassland but are largely in the minority. These grasslands are generally protected by local policies preventing their conversion to crops or forest. Figures 1.1 and 1.2 highlight that the majority of grasslands that have changed over the last six decades are agricultural grasslands, mainly intensively used for profitable supply services. Consequently, this intensive exploitation through management practices may be a growing problem with respect to the importance of grasslands.

The changes and impacts on grasslands are mainly due, as illustrated, to the effect of humans and their

exploitation. Global scale observations available through remote sensing, including the example of Figure 1.2, provide essential information to understand our environment. They serve as a support for key applications such as long- and short-term climate modeling or for the implementation of public policies to regulate, protect, and change our future. In this sense, grasslands of temperate climate and their management systems are of utmost importance for the overall conservation of grassland ecosystem services.

1.1.4 Temperate managed grasslands and their exploitation

The potential management of a grassland is initially conditioned by abiotic factors such as pedological, climatic, and topographical properties and subsequently its agronomic type. Furthermore, the provisioning services expected from a grassland will constrain its management regime. To obtain the provisioning services, technical acts, decided and conducted by human intervention, are then performed on the grassland throughout the year. Three elements can characterize the technical act: its *intensity*, which roughly defines the impact on the grass resource, its *duration* and *timing* within the agricultural calendar. On grasslands, two main types of technical acts are defined: grazing and mowing. In practice, the management regime of a grassland may be a combination of these two technical acts. Furthermore, grasslands can be ploughed for reseeding or to convert grassland to another type of crop.

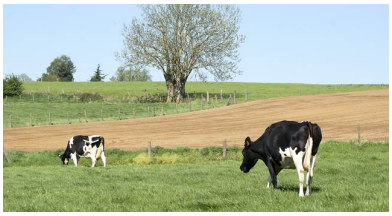

(a) Grazing

(b) Mowing

(c) Ploughing

Figure 1.3: The three types of technical acts performed on grasslands.

Grazing is the traditional type of grassland management. Livestock exploits the grassland resource for the production of animal products such as milk, meat or wool. The grazing of a grassland can be favored by its geographical condition, when mechanical exploitation is made difficult, *e.g.*, for fertilization or mowing. Grazed grasslands will be dominated by fairly low plants with an increased agronomic variety and low spatial homogeneity. Grazed grasslands species are thus adapted to trampling and browsing. Grazing has different regimes, *i.e.*, continuous or rotational grazing (Schmitz and Isselstein, 2020). Continuous grazing provides unrestricted access to a grassland over a long period of time. In this case, the vegetation rarely rest. Continuous grazing offers the advantages of low planning costs and relatively simple livestock management. On the other hand, the timing and intensity of grazing is difficult to control without livestock loading managements. Rotational grazing favors grass regrowth by regulating the pressure of the livestock load successively at distinct areas. This rotation can be done between different grasslands but also within the same grassland. This latter case is more likely in the presence of large parcels and allows among others for a reduction in the travel distance of the livestock. Typically, in this case, the farmer will install a temporary fence delimiting a specific area of the parcel. While the livestock grazes the available resources in this area, the grass in the other areas of the parcel continues to grow. When the resource in the fenced area is exhausted, the farmer moves the livestock to an area that has not yet been grazed. The same principle applies to a rotation between several grasslands parcels. This rotating approach is favorable to the availability of the resource by temporal and spatial management, throughout the season.

Mowing permits over natural grasslands to remove woody vegetation cover. It protects grassland, plant and animal species habitat dependent and reduces risks from natural hazards such as fire. In the agricultural

context, grasslands are mainly mowed to produce resource for livestock feed. The cutting of grass during mowing can also have ecological succession goals to favor certain agronomic species or stimulate grass vigor and regrowth. Grasslands that are mowed can reach significant grass heights of up to one meter. By cutting the grass, the whole aboveground biomass that has been accumulated during a growth cycle is removed at once to a certain cutting height threshold. This threshold generally preserves a biomass of at least 5 to 7 cm in order to leave sufficient plant tissue for photosynthesis and regrowth. In certain cases, the grass can be cut and immediately fed to livestock. In most cases, the forage needs to be conserved. The haymaking may be done by a drying process directly on the parcel or at the barn. Mowing for which the resource will be conserved by drying, is mostly done late in the season regarding the climate. The conservation alternative uses the wet process by reducing oxygen and fermenting the resource. Especially in rainy climates, silage and wrapping permit to preserve the grass quality and can be implemented early in the season.

Grazing and mowing have distinct intensity, duration and timing. Despite the important heterogeneity among grazing and mowing practices due to agronomic, climatic, or management regimes constraints, the following observations can be considered:

Intensity:
- *Grazing*: the grazing effect on vegetation depends on the grazing regime, the grazer's specie, livestock loading, and their time spent grazing. The herbaceous resource can be consumed in a short period of time, leaving the soil almost bare, or can diminish only gradually over time.

- *Mowing*: the cutting height is the factor influencing the intensity. Depending on the expected use of the mowed resource, the grass removal can be minor to almost complete.

Duration:
- *Grazing*: the grazing regime but also the overall exploitation of the grassland make the duration characteristic highly variable. On very small areas, grazing may last only a few days. On vast grasslands, and moreover, in continuous grazing, the duration extends to several months, depending on the climatic conditions, allowing the livestock to be outdoor.

- *Mowing*: mowing is generally accomplished in a very short period of time (*i.e.*, within few hours or at most two days, if the visibility does not allow the technical act to be continued), especially when the technical act is mechanized.

Timing:
- *Grazing*: the timing of grazing is conditioned by the climate. The first grazing can occur as soon as the climatic conditions are favorable, and the grass comes out of its winter dormancy. The exit of the dormancy is allowed when the temperatures reach a certain point, depending on the plant species, globally between 4 and 8°C. For grasslands in temperate climates, and particularly in the case of mixed grazing and mowing management, grazing can be done as early as spring, which will impact the quality, productivity and sustainability of the good species for the coming season. The last pasture should ideally leave around 5cm of grass for dormancy. Its timing will be again dependent on the climate.

- *Mowing*: mowing can occur at almost any time during the growing season. Generally, it is done in good weather, as rainfall can affect the resource. A first mowing can be done early in the growing season to encourage vigorous regrowth. A very late mowing at the end of the growing season can also be carried out to optimize the grass state for its re-entry into dormancy. Indeed, above a certain height of grass (ideally 5 to 6 cm), rotting can affect the grass during the dormancy.

As with any agricultural land, besides grazing and mowing, a grassland can be ploughed. Nevertheless, **ploughing** does not necessarily occurs on every grassland, as they can have constant ground cover and do not inherently require ploughing to subsist. The agronomic type, the parcel history and thus underlying regulation policies or the overall management of a farm can conduct the ploughing of a grasslands. Ploughing is mainly carried for the purpose of reseeding a grassland or changing the crop type. The duration of ploughing is similar to that of mowing, being done at once for a whole parcel (or some part in the case of rotational management). The intensity of ploughing will mainly depend on its timing. A ploughing can immediately follow a mowing and in this case remove only a small amount of biomass. It can also be done according to the crop rotation schemes and agricultural calendars. Ploughing can potentially occur much later than the last technical act and hence remove a larger amount of biomass.

1.2 Earth Observation from space: principles and applications over grasslands

1.2.1 Characteristics and multi-modalities of satellite imagery

Remote sensing is defined by the French Official Journal of 11 December 1980 (JORF, 1980) as "all the knowledge and techniques used to determine the physical and biological characteristics of objects by measurements taken at a distance, without physical contact with them". The underlying principle is the measurement of radiations in different portions of the electromagnetic (EM) spectrum, giving remote sensing multiple potential applications.

Earth observation (EO) by remote sensing began in the 19^{th} century with atmospheric balloons and then spread during the First and Second World Wars as a source of military information. The use of EO satellites, which were first restricted to telecommunications functions, was initially motivated by meteorological concerns. TIROS 1 (Television and InfraRed Observation Satellite) was launched by the National Aeronautics and Space Administration (NASA) in 1960, providing unprecedented global coverage via daily images acquired on board the satellite and transmitted to ground receiving stations located throughout the world (United States, 1956). Landsat-1 launched in 1972 was the first satellite which explicit goal was to monitor Earth's landmasses (Boland, 1976). Ever since, the capacity of EO satellites for synoptic coverage and repeated acquisitions has been increasingly exploited. A multitude of applications on numerous themes have been developed using satellite data: Earth's cover mapping, study of vegetation or snow cover, inventory of crops and forests, land use planning, monitoring of urban growth, mining or oil exploration, monitoring of coastal or marine pollution, hydrology, oceanology or military intelligence among others.

As of end 2021, the United Nation Office for Outer Space Affairs registered more than 7,100 satellites in orbits (United Nations Office for Outer Space Affairs (UNOOSA), 2021). A large majority of them are still dedicated to telecommunications despite an exponential number of EO satellites. Satellites are placed in three main orbits with different characteristics and applications. The Geostationary orbit (GEO) refers to satellites that orbit above the Equator at 35,786 km and follow the Earth rotation. This allows them to be constantly above the same point and therefore are mainly exploited for telecommunication and weather satellites. They further help for data downlink being always in sight of a ground receiving station. Medium Earth Orbit (MEO) is above 1,000 km and below GEO and is almost exclusively used by navigation satellites such as the Global Positioning System or Galileo.

The Low Earth Orbit (LEO) is the closest to the Earth with altitudes ranging from about 150 km to 1,000 km. Apart when global-scale processes are being observed (*e.g.*, atmospheric or weather conditions), the LEO is adopted by EO satellites. For a LEO satellite, it typically takes about 90 minutes to circle the Earth entirely. A conventionally route for LEO called near-polar orbit follows the North-South direction passing approximately

over the Earth's poles. Orbit directions northwards and southwards are, respectively, called ascending and descending orbits. In conjunction with the West-Est Earth's rotation, this permits satellites in LEO to cover the Earth's surface (Figure 1.4). In addition, these satellites are also often sun-synchronous by having a fixed position relative to the sun, allowing them to always observe the same area at the same local time. This ensures consistent illumination conditions over some time intervals (*e.g.*, few days or between years). A main interest which advocates for LEO in the context of EO is their reduced distance to the observed target (*i.e.*, the Earth). This allows to observe phenomena at finer scales, which is for example, necessary for applications related to agriculture. On the other hand, the ground area imaged by the sensors during an overpass (called the swath) may be reduced. Typically, the swath of LEO satellites varies between tens and hundreds of kilometers.

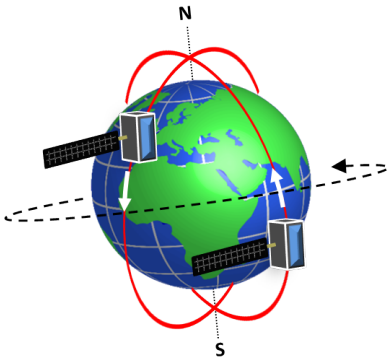

Figure 1.4: Schematic representation of an Earth Observation satellite in near-polar sun-synchronous Low Earth Orbit.

Among the notable characteristics of EO satellites, four specificities, which are based on the satellite's orbit and its payload, *i.e.*, onboard sensor, can be defined:

- The spatial resolution is the ground surface represented by an individual sampling, being the smallest addressable element in an image. This ground surface is therefore the smallest possible feature that can be detected by the sensor. Coarse or low resolution mainly depict large features while fine or high resolution will provide more details. The spatial resolution influences the swath of the satellite depending on the orbit and sensor capabilities. While in 1972 Landsat-1 had a spatial resolution of 80 m, some commercial satellites currently provide sub-metrics spatial resolutions. An example of different optical image spatial resolutions is visible in Figure 1.5.
- The spectral resolution refers to the position, number and width of EM spectrum portions, called bands, being observed by a sensor. A low spectral resolution would, for example be a single panchromatic (black and white) band acquiring at once a wide portion of the EM. High spectral resolutions are for example provided by hyperspectral imaging, with hundreds of EM portions independently observed.
- The radiometric resolution describes the depth of possible values assigned to an energy measurement within a pixel. The larger this number, the higher the radiometric resolution and thus sensitivity and discrimination power.
- The temporal resolution (or revisit time) defines the length of time taken by a satellite to observe again a same point on Earth. The temporal resolution is generally expressed in days. A higher temporal resolution allows to gather dense time series, *i.e.*, successive images of the same location.

Due to physical and engineering constraints and the different resolutions being correlated, a sensor cannot optimize all four resolutions at once (Selva and Krejci, 2012; Shen et al., 2016). Spectral and radiometric

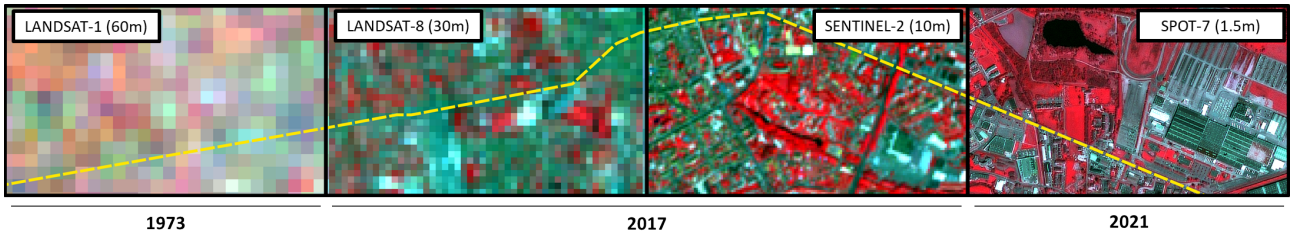

Figure 1.5: Four acquisitions of passive optical satellites with different spatial resolutions over the city of Bourg-en-Bresse in France along a main road (yellow line) are presented. False-color compositions with the Near-infrared, Red and Green bands mapped to the RGB channels are emphasizing the high reflectance of vegetation. The 48 years separating the first and last acquisitions show the improvements in spatial and radiometric resolutions achieved.

resolutions have trade-offs with signal-to-noise ratios. Apart from signal-to-noise ratio, the spatial resolution has a trade-off with spectral resolution and data volume. Eventually, the temporal resolution has a trade-off mainly with spatial resolution. Hence, satellites and their sensor characteristics generally define the resulting potential applications.

Finally, a fundamental distinction of the different EO satellites lies in the source of the energy measured by their sensor. Two types of sensors are thus defined: passive and active sensors.

1.2.1.1 Passive sensors and optical imaging

Passive acquisitions are based on the collection of EM radiation from an off-system source (*i.e.*, not emitted by the satellite), mainly natural sources such as the sun. The visible, infrared and thermal domains are the major domains studied by passive acquisition systems as presented in Figure 1.6. Approaching the human vision perception, one of the main interests of passive sensors are the acquisition of well-known and identifiable phenomena. This allows in many cases a relatively simple exploitation and interpretation of passive-based sensor data.

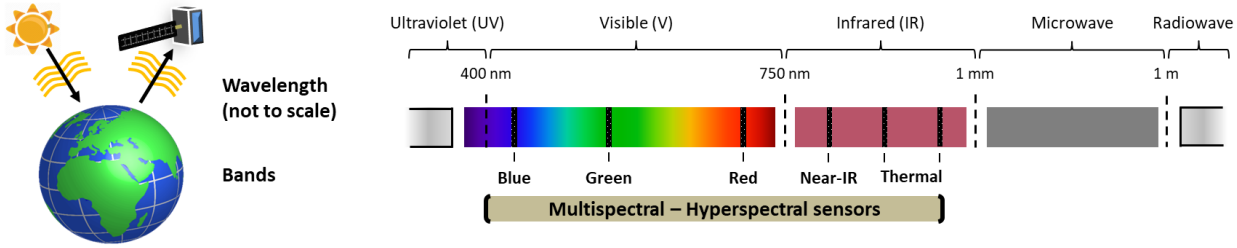

Figure 1.6: Passive sensors principle and commonly acquired bands.

By measuring the energy coming from the target, passive sensors allow to distinguish specific characteristics of each surface. Among passive sensors, optical sensors are the most common. They investigate the interactions between solar radiation and a material, independently for several wavelengths. Except in specific study cases, the bands acquired by passive sensors are selected in atmospheric windows which minimizes atmospheric absorption and scattering. The remainder effects, coming from gases, molecules, and aerosols whose absorption is known, can be modeled. Thus, the measured energy at the sensor provides, after necessary atmospheric and geometric corrections, direct information of the Earth's surface. Solar radiation reaching the surface can be transmitted, absorbed or reflected, which sums to 1 by the law of conservation

of energy. These interactions allow optical imaging, which measures the reflected proportion of the EM, to distinguish a large number of surfaces and phenomena. This proportion depends on the wavelength and acquisition conditions, the object observed and its intrinsic properties.

Passive sensors and optical imaging are therefore primarily sensitive to the chemical properties of the observed surface. Consequently, they are extensively used for monitoring vegetation in which the chemical activities vary with time and condition (Knyazikhin et al., 2013; Kuenzer et al., 2014; De Grave et al., 2020; Zeng et al., 2020). For example when chlorophyll activity is at its peak, vegetation appears to the human vision at a maximum intensity of green wavelengths. Conversely, when chlorophyll activity is lower, the red absorption property of vegetation is lower and its reflection is proportionally higher, making the vegetation appear less green. The interest of optical sensor capabilities to extend their acquisition to the near infrared domain is for vegetation, attested by the strong reflection of these wavelengths by the cell structure of plants. When vegetation grows by photosynthesis, the cell structures are more numerous and the reflection in the near-infrared increases while the reflection in the red decreases. The relationship between solar radiation and chlorophyll thus allows passive optical sensors to determine the spectral signature of the vegetation. The same principle is valid for other types of surfaces such as water or mineral surfaces. Some spectral signatures are presented in Figure 1.7, illustrating how optical sensors allow to separate surface types and provide information on their characteristics depending on different wavelengths.

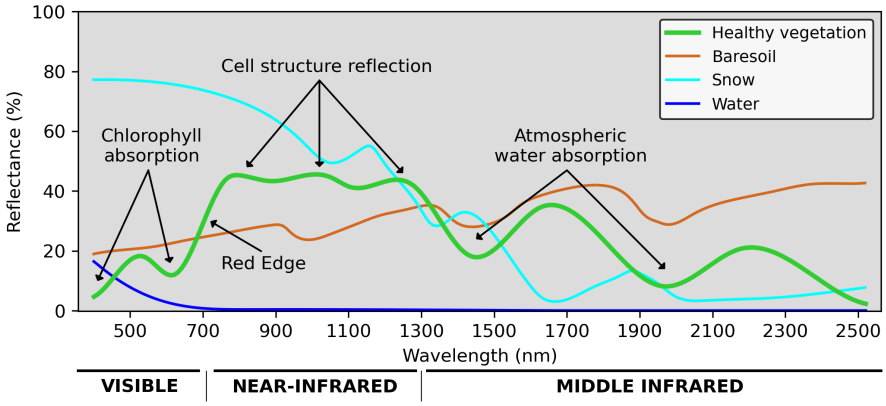

Figure 1.7: Ideal spectral signatures of four types of surfaces in the visible and infrared range. The interactions between radiation and a healthy vegetation surface are illustrated by distinct absorption and reflection mechanisms.

Scanning systems acquiring a variety of different spectral bands, called multispectral scanners (MSS), are therefore a crucial capability of optical sensors to provide information of the Earth's surface. Optical sensors generally acquire a minimum of four spectral bands in the blue, green, red, and near infrared portions of the EM. Despite illustrating the improvements in spatial resolution, the previous Figure 1.5 also illustrates the ability to create color compositions from the different acquired bands by a MSS. Color composition refers to the assignment of specific spectral bands to the Red-Green-Blue (RGB) visible bands. The assignment of data acquired in the near infrared to the red visible portion allows, via the chemical properties of the vegetation previously explained, to highlight the vegetation and its condition in reddish tones.

Depending on satellite sensor characteristics, acquisitions in a larger number of spectral bands (*i.e.*, more than the 4 conventional bands) can be made. Indices, commonly used to enhance the distinct reflectance of distinct materials, are developed from the different acquired bands. A larger number of bands can thus allow the development of a greater number of different indices. A significant number of these indices are designed to study vegetation. Most of these indices, such as the popular Normalized Difference Vegetation Index (NDVI) first proposed in Tucker, 1979, rely on red-edge related bands, which is a thin portion of the EM

spectrum in which chlorophyll-related changes in plant reflectance are highlighted. This phenomena is visible in Figure 1.7 with a steep increase in reflectance of healthy vegetation reflectance. The variety of indices is as numerous as the types of surfaces (Glenn et al., 2008; Xue and Su, 2017). Indices are thus also employed to quantify the soil mineral composition or estimate the severity of fires in forest areas among others. The number of acquired spectral bands can reach several hundred, as it is the case with so-called hyperspectral sensors using narrower bands. Nevertheless, only a few satellite missions have integrated this type of sensor or are planned (*e.g.*, Hyperion, PRISMA, EnMAP). Indeed, the engineering challenges and their high costs are for the moment a brake to their use (Govender et al., 2007; Transon et al., 2018).

Some MSS are also acquiring bands in the thermal infrared domain (Prata et al., 1995; Sobrino et al., 2016). In this case, terrestrial radiation is used directly as the source of energy as opposed to the sun's illumination. Thermal bands are of longer wavelengths and because of the inverse relationship between wavelength and energy, thermal sensors must either sense wider areas to gather enough energy and thus decrease spatial resolution or increase the exposure time through different orbits. Thus, thermal bands are less common than visible or reflected infrared bands and EO satellites providing them are currently more sparse. Passive sensors evolving in the microwave domain, although few in number, are also used (*e.g.*, TRMM, SMOS). These sensors work in a similar way to thermal sensors, collecting the energy emitted by the surface. The capture in the microwave domain mainly enables surface moisture (soil moisture, atmospheric water vapor, cloud liquid water or rainfall rate) related applications (Huffman et al., 2007; Brandt et al., 2018). Their use is therefore mainly made on the oceans or polar ice caps.

Because of their characteristics, optical passive sensors have historically been favored, and still are. Yet, these sensors suffer from important limitations. Their dependence on a energy source first prevents night-time acquisitions. Most importantly, cloud cover is preventing optical sensors from observing the earth's surface. Cloud coverage causes considerable data gaps in both spatial and temporal domains. As a consequence, the temporal sampling of optical time series is irregular due to weather conditions (Sudmanns et al., 2020a; Whitcraft et al., 2015). It is among others, constrained by the geographical location of the area under study (Ju and Roy, 2008; Sudmanns et al., 2020a). In some parts of the world, this constraint makes the use of optical images very complex and almost impossible. In the same way, some applications requiring repeated acquisitions can not depend only on data from optical sensors. Furthermore, optical sensors only observe the top of surfaces. The undergrowth of a forest, for example, cannot be observed. Finally, the similarity of spectral signatures of certain surfaces, as may be the case between tree species or different crop types, may limit the surface distinction possibilities of optical sensors.

1.2.1.2 Active sensors and Synthetic Aperture Radar imaging

In contrast to passive sensors, active remote sensing (Figure 1.8) is based on the emission of a coherent radiation source and the analysis of its return to the sensor. One of the most common active sensor is the Radio Detection And Ranging (radar), which operates in the microwave range. A radar emits a beam from its antenna by focusing short pulses of microwave emitted at regular intervals. The measured strength of the energy backscattered (*i.e.*, returning towards the sensor) from an emitted wavelength refers to the detection part. Ranging is done measuring the time taken between emission and reception of a wavelength, which permits to determine the exact location of the target. Radar data is thus composed of a real (corresponding to the phase) and an imaginary (corresponding to the amplitude) part. Some limitations of passive sensors previously presented are bypassed by the use of the microwave range of the EM. Especially, day and night acquisition are possible and, with wavelengths of several centimeters, the acquisition of data in cloudy conditions is possible.

In the case radar active sensors, the term *band* refers to the wavelength/frequency of the emitted wave. Bands are named with letters, mentioned in Figure 1.8, from very short wavelengths (X-band) to the longest

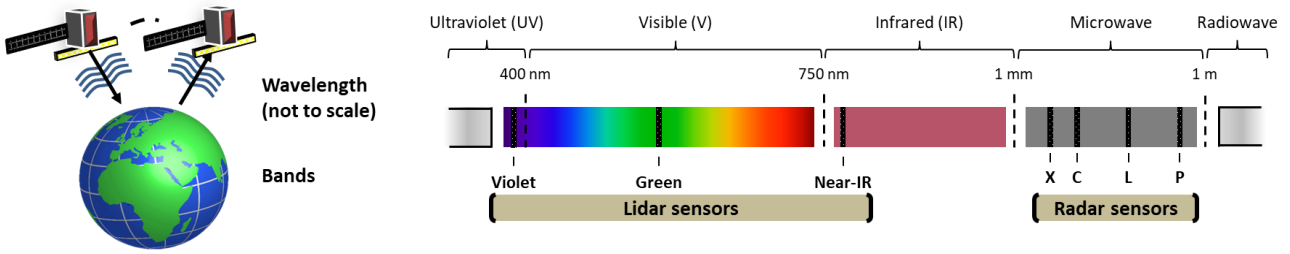

Figure 1.8: Active sensors principle and commonly acquired bands.

radar wavelengths (P-band). The choice of the band will have an impact in particular on the capacity of penetration of the wave in the surface. The longer the higher the penetration capacity, or, longer wavelengths are associated with more coarse spatial resolution (El Hajj et al., 2019; Jiao et al., 2010). The most commonly used bands are X and C bands for their versatility against different surfaces and atmospheric conditions (Van der Sanden et al., 2001).

One further distinction with passive optical imaging lies in the radar sensor acquisition geometry. Unlike optical imaging where sensors are generally pointing at the nadir (*i.e.*, directly bellow its location), a radar satellite illuminates the surface obliquely at a right angle to the motion of the platform. Because SAR distinguished various surfaces based upon the arrival time of the received signal, this side-looking nature is constrained by the fact that two equidistant points left and right from the sensor would be undifferentiated in a nadir-looking SAR. This oblique nature causes significant effects in radar measurements, exacerbated by topographic features on the ground, some of which are presented in Figure 1.9. Radar measurements are made in radar slant range geometry dependent on the viewing incidence angle and observed topography. Acquisition geometry of radar systems can cause phenomena of shortening of surfaces, called foreshortening. Foreshortening occurs when the beam is reaching the bottom of a tall feature such as a mountain tilted towards the radar before it reaches the top. This causes compression phenomena to appear in the resulting images with reduced lengths between the two observed points. Conversely, layover refers to the top of tall objects (*e.g.*, the mountain) being viewed before the bottom. The top will therefore appear nearer than the base in the resulting image causing inversion of the relief (*i.e.* the highest point being considered closer than the base of the terrain). Several types of backscattering products are therefore derived (Rudant and Frison, 2019) for their subsequent use, translating the radar geometry to terrain geometry.

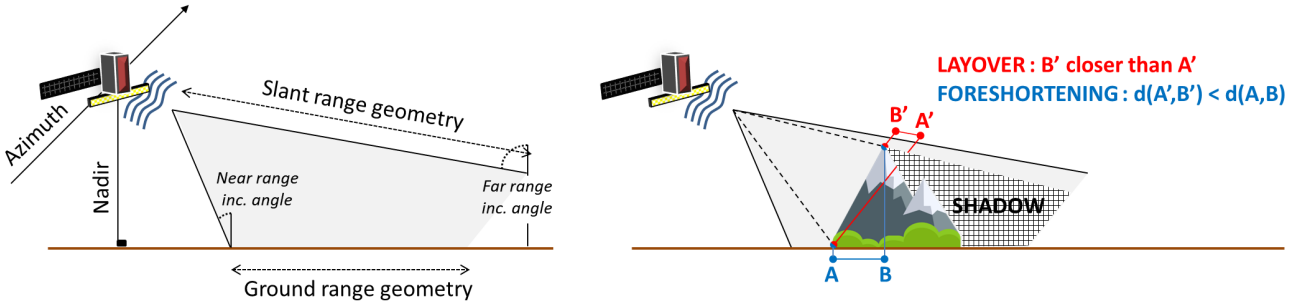

Figure 1.9: Description of geometry elements of a side-looking active satellite acquisition. Main distortions due to topography that are layover, foreshortening and shadow are illustrated.

As a result of slant range geometry acquisition, the spatial resolution of radar sensors has two dimensions, one azimuthal (in the propagation direction of the satellite) and one radial (called range resolution, in the view direction of the sensor). The range resolution will first depend on the distance to the surface and will therefore be variable along the swath (finer for the near-range, lower for the far-range, see Figure 1.9). The frequency of

the emitted beam also influence range resolution but can be improved by pulse modulation techniques called chirp (Prats-Iraola et al., 2014). The azimuthal resolution depends mainly on the size of the antenna and the distance to the surface. On a satellite, this antenna size is necessarily limited by engineering constraints (orbiting and deployment). With the help of chirp and the Doppler effect, the simulation of an antenna much longer than its real physical length is possible (radar echo history). Sensors using this technique, called Synthetic Aperture Radar (SAR), allow a considerable improvement of spatial resolution up to a certain limit defined by the signal to noise ratio.

Radar's ability in surface discrimination is determined, apart from viewing and surface geometry, by very different physical phenomena compared to optical sensors. Radar sensors are sensitive to geometric properties, *e.g.*, surface roughness, and dielectric properties such as surface moisture. The sensitivity is mainly determined by the the wavelength used. The backscattering intensity which is recorded, is partly defined by the Rayleigh criterion characterizing a smooth or rough surface, depending on the wavelength and the incidence angle. This will influence the nature of the backscattering mechanism involved. For example, surface or volumic backscattering are predominant in the case of vegetation, surface specular in the case of very smooth water bodies or double-bounce mechanisms when vertical structures such as buildings are lined up with the beam (McNairn and Brisco, 2004; Picard et al., 2003). The dielectric constant defines the response of a surface to an incident electric field. Since water has a very high dielectric constant, the surface moisture will strongly influence the penetration of the radar wave and increases backscattered intensity (Shao et al., 2003). In addition, while the number of wavelengths used by SAR sensors are relatively limited compared to passive sensors, the direction of the electric field vector of the emitted wave is controlled, defining its polarization. Horizontal (H) and vertical (V) linear polarizations are commonly used by radar sensors. The polarimetric capability of a SAR sensor is thus defined by the transmission and reception polarizations it allow. Single- dual- or quad-polarized (also called full-polarized) measurements are possible depending on the sensor characteristics and allow additional information to discriminate surfaces.

Interferometry is another interest of radar sensors based on the use of two or more images. Since the satellites do not pass perfectly over the same point (typically an offset of several tens of meters), the repeat-pass interferometry technique is based on the phase differences occurring between the acquisitions (Krieger et al., 2005; Perissin and Wang, 2012). By measuring the exact phase difference between both acquisitions, displacements on the size order of the used wavelength (*e.g.*, centimeters) can be calculated. The computation of interferograms enables the production of elevation maps and displacements maps. Nevertheless, such accuracy can only be achieved on relatively stable surfaces and in the presence of low signal decorrelation factors (*e.g.*, spatial or temporal).

Among the limitations of active sensor like SAR, their analysis and interpretation require a good understanding of the above-mentioned characteristics and phenomena. Furthermore, topography, due to the side-looking nature of SAR, is a major limitation in mountainous regions. Finally, inherent to all radar images, the speckle appears as a grainy "salt and pepper" texture in the image. The speckle is due to the coherent sum of random constructive, and destructive interference (random-walk) from the numerous elementary scatterers within a pixel scattering back the signal (Lee et al., 1994; Singh and Shree, 2016). Thus, two adjacent pixels on an apparently homogeneous surface, such as a grass surface, may have very different responses due to the interaction of the signal with individual blades of grass (or any structure of minimal wavelength size). Different techniques have been developed to reduce speckle noise, *e.g.*, multi-looking based on non-coherent averaging, spatial or temporal speckle filtering techniques. They nevertheless have an impact on the radiometric or spatial quality of the original images.

Apart from radar, another type of active sensor operates in the visible and near-infrared EM portion. Light Detection and Ranging (Lidar) emits light from a rapidly firing laser. Likewise radar sensors, the emitted light travels to the ground and reflects on the surface towards the sensor. Time-travel as well as backscattered intensity are recorded forming a point cloud transcribed to elevation (Mallet and Bretar, 2009; Simard et al.,

2011a). The wavelengths used by Lidar potentially allow a spatial resolution clearly superior to that obtained by the radar systems operating in the microwaves. Their penetrating power is reduced is nevertheless reduced, especially regarding the cloud cover. Because of the high energy required for their operation, satellite lidar systems have so far been mainly used for the study of the atmosphere and large polar surfaces mainly (*e.g.*, ICESat-2, CALIPSO, ADM-Aeolus, GEDI), solely with low spatial resolution. They are therefore rarely used for monitoring vegetation surfaces (Simard et al., 2011b; Silva et al., 2018).

1.2.1.3 Copernicus programme and Sentinels

Historically, EO applications were based on a single type of sensor, either passive or active with little crossover in application. The low overlap in spatial and temporal terms between various datasets prevented their combined use. Recently, this paradigm has been challenged by the appearance of satellite constellations (*i.e.*, a more or less large number of identical or complementary satellites), including both passive and active sensors.

A recent and notable programme providing a satellite constellation is the European Union's EO Copernicus programme. Initiated in 1998 and endorsed in 2001 by the European Commission (Lamy and Saint-Martin, 2013), Copernicus aims to develop operational information services on a global scale using both space- and ground-base monitoring systems (Aschbacher and Pérez, 2010). The Copernicus Space Component is a shared responsibility through the European Space Agency (ESA), the European Organization for the Exploitation of Meteorological Satellites (EUMETSAT), and the European Union. The Sentinel satellites, briefly presented in Figure 1.10, the first of which was launched in 2014 (Sentinel-1A or S1A), constitute the satellite constellation of the Copernicus programme.

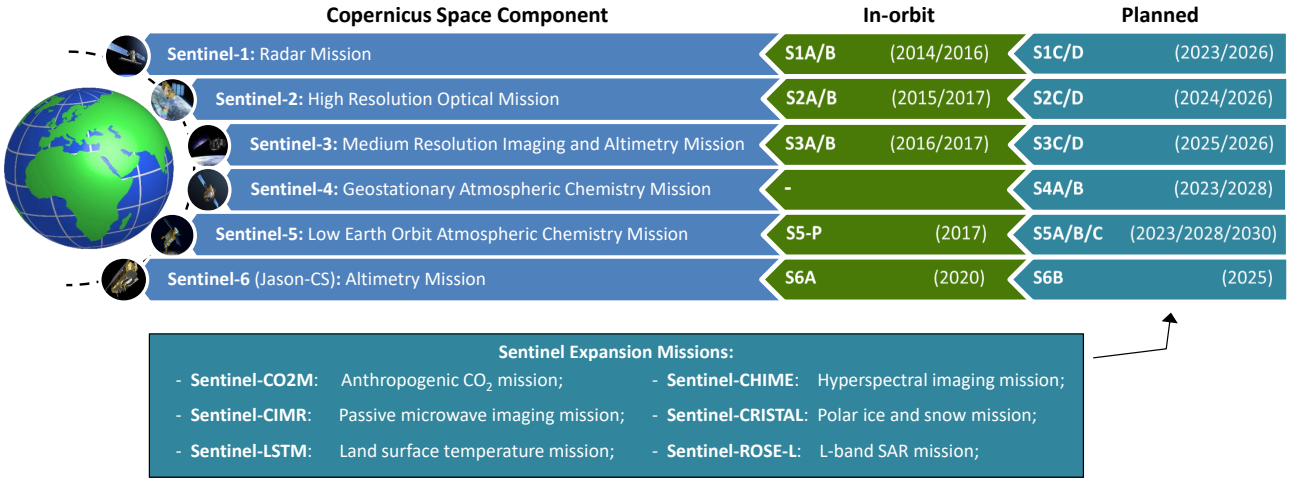

Figure 1.10: Sentinels missions from the European Copernicus programme.

The multi-modality of the sensors on board the Sentinel satellites, together with the temporal revisit allowed by the duplication of the satellites, has allowed an unprecedented gathering of EO images. Specifically, regular optical and SAR time series with similar spatial resolution are available. In addition, a free and open access policy on Sentinel images has allowed the development of numerous methodologies fusing passive and active sensors on a routine basis. These acquisitions have been systematic since 2014 and their sustainability is ensured by the future launch of new satellites.

1.2.2 Satellite remote sensing of grasslands

1.2.2.1 Grasslands extent mapping products

One of the most common application of satellite remote sensing for land surfaces is the production of land cover maps. Land cover refers to the biophysical properties of a land surface aiming at the distinction of its properties (*i.e.*, water, built-up area, vegetation, etc.). Land cover maps are now usually produced on an annual basis and reflect the summarized area status for the year. A number of classes of interests is defined, depending on the used data and the applications. In this context, grasslands are often a distinct class, due to their large and dense coverage. The semantic richness of the classification, *i.e.*, the complexity of the nomenclature to distinguish between different types of grasslands, varies mainly according to the spatial extent of the classification. Taking into account larger areas implies a higher diversity of spectral signatures, under influence of a different climate, for example. In these cases, retrieving surfaces belonging to the same thematic class poses further challenges. As a result, large-scale products tend to have fewer semantic classes.

Land cover maps classifying large areas (region, country, continent, or globe) generally define one or very few grassland classes. These meta-classes contain a large number of grassland areas. Figure 1.11 shows grasslands retrieved by four examples of large-scale land cover products with distinct semantic richness. Three products are continental scale (Europe) while the last one is produced at the country scale (France). Figure 1.11 aggregates all grassland classes among a product for visualization.

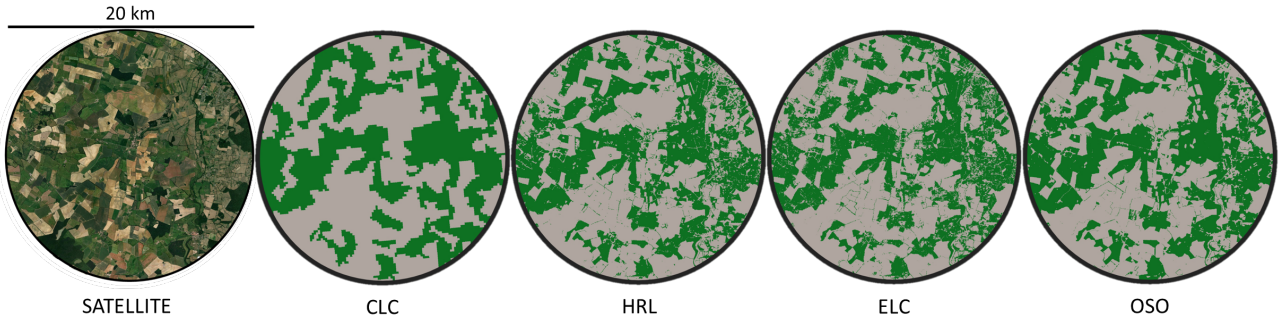

Figure 1.11: Grassland retrieved from large scale satellite-based land cover products available for the year 2018 in France. SATELLITE : Google Maps; CLC : Corine Land Cover, HRL : High Resolution Layer - Grassland, ELC : European Land Cover, OSO : Occupation des SOls.

The Corine Land Cover (CLC) map (Heymann et al., 1994) covers Europe and is currently updated every six years. It is based on visual interpretation of several optical satellite sources and ground-based statistical information and can distinguish up to 44 classes. The grasslands are differentiated solely into two classes, pastures and natural grasslands. The High Resolution grassland Layer (HRL) produced by the European Environment Agency in the framework of the Copernicus Land Monitoring Service proposes a binary map (*grassland / non-grassland*) covering Europe. It is derived from optical Sentinel-2 time series using a Random Forest classifier and learning samples gathered from several agricultural databases (such as the Land Use and Coverage Area frame Survey, LUCAS) and manual sampling (European Union, 2018). The European Land Cover (ECL) map (Venter and Sydenham, 2021) uses the same approach as CLC (*i.e.*, integrating geographical databases and satellite images) but further integrates Sentinel-1 SAR data to distinguish 8 land cover classes, one of which is grassland. While the three previous products were available at the continental scale, most operational approaches in the literature are defined at the country level, due to the computational constraints of larger scale products. For metropolitan France, the Occupation des Sols (OSO) map produced from Sentinel-2 data by the CESBIO (Inglada et al., 2017) proposes the distinction of 23 classes, including agricultural grassland, and natural grasslands regrouped with pasture classes.

A good agreement on the location of grasslands is visible among the different products even if different data sources, techniques, and scales are originally explored. Satellites can therefore effectively differentiate grasslands from other types of surfaces and map their geographical extent over large areas. Especially at large scales when few grassland distinctions are made, most land cover products do not represent a significant added value for grassland monitoring. Indeed, apart from information on their extent, these products only make a very partial difference of grassland types (*i.e.*, as here, mostly a few classes) or do not allow specific intra-annual monitoring.

1.2.2.2 An overview of satellite-based grassland monitoring studies

The interest of satellite data for monitoring grasslands is surely not recent. In this regard, EO data has been exploited since the first images were available. Tucker et al., 1985 were already analyzing NOAA-6 and 7 optical satellite data to compare the total productivity of Senegalese grasslands in the Sahel between 1980 and 1984.

There is a large body of work that includes satellite data and grassland monitoring. Their applications and processed data are diverse, with the aim of obtaining quantitative informations of ecological or economical concerns. A corpus of 286 research papers from 238 different first authors, published in peer-reviewed journals or major satellite remote sensing conferences, is retrieved. Thematic keywords such as *grasslands, pasture, meadow, rangelands, biomass, management, mowing, grazing, ploughing, harvest, productivity, mapping, phenology* were combined with data-related keywords such as *earth observation, remote sensing, satellite, optical, SAR, time series* in various web-based searches. A focus on published works between the years 2000 and 2022 is retained. Some important prior works, *i.e.*, recently repeatedly cited, are also integrated in the corpus.

Clearly, the present corpus is not exhaustive, but it integrates the most recent, most read and cited works concerning satellite remote sensing and grasslands. Moreover, this relatively large corpus already allows us to highlight the distinctions regarding two crucial aspects, namely, the research objective relating to grasslands and the type of used data. Figure 1.12 classifies and quantifies the corpus regarding the two aspects (*i.e.*, research topic and used data). In a sign of the recent revival of interest in the subject of grasslands, several meta-analysis on the subject of satellite remote sensing for grasslands are been recently published (Reinermann et al., 2020; Li et al., 2021; Soubry et al., 2021). The conclusions presented hereafter are in agreement with these reviews.

Seven grassland themes are defined, covering the majority of the applications proposed in the corpus. Some articles deal with several topics at the same time and are counted in each of the topics they deal with. Concerning the types of data, the research concerns satellite data and therefore omits airborne or Unmanned Aerial Vehicles data. While optical and SAR sensors are intensively used, hyperspectral and lidar data are hardly represented. This is due, as previously mentioned, to the low number of satellite sensors offering this type of data. In this corpus, the exploitation of optical or SAR data, or their joint use is retained. The complete corpus organized by research topic and data type used is presented in Tab. 1.7.

Biomass assessment

Similarly to Tucker in 1985, the vast majority of papers (about 208 out of 286, see Figure 1.12) focus primarily on grassland biomass assessment, including information on vegetation quality or quantity, such as biomass, yields or productivity. Aboveground biomass (AGB), Growth Primary Production (GPP), and Net Primary Production (NPP) of grasslands are critical biophysical information serving as input to global circu-

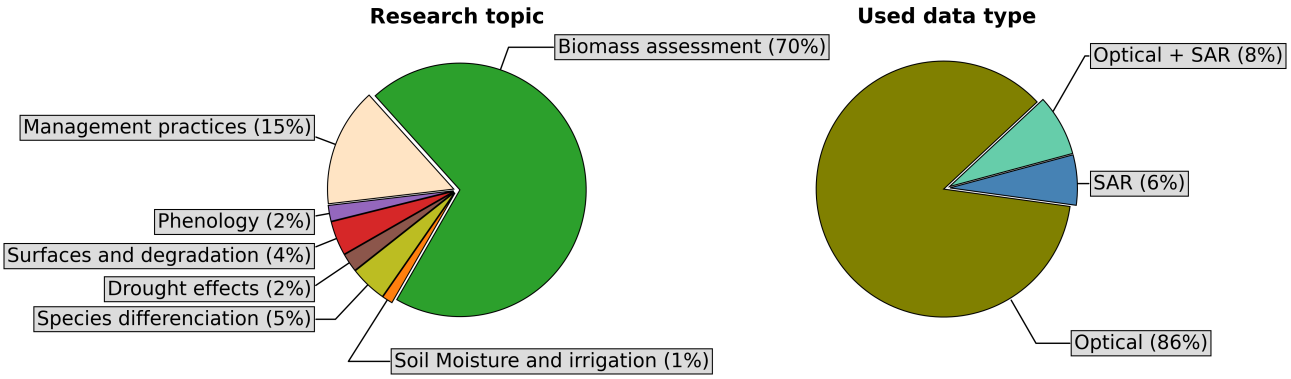

Figure 1.12: Main research topics and data types used in a corpus of 286 papers involving grassland monitoring with satellite remote sensing published in peer-reviewed journals or major conferences (between 2000 and 2022 mainly).

lation models such as carbon and nitrogen cycles and therefore of particular interest. Passive optical satellite data are overwhelmingly preferred (197 articles against solely 4 using SAR images and 7 using both optical and SAR images) following the strong correlation of visible and near-infrared bands with vegetation's photosynthetic activity. To accurately monitor biomass, dense time series of images are necessarily favored, focusing on the vegetation's growth season or spanning one or multiple years. A coarse spatial resolution (*e.g.*, ~100m) in order to obtain more regular images is usually chosen. The Moderate-Resolution Imaging Spectroradiometer (MODIS) (Ali et al., 2017b; Liu et al., 2020b; Roumiguié et al., 2017), onboard Terra and Aqua satellites, is the most used sensor. It is followed by sensors with higher spatial resolution such as Landsat (Clementini et al., 2020; Dara et al., 2020; Röder et al., 2008) and Sentinel-2 (Askari et al., 2019; Buddeberg et al., 2021; Fernández-Habas et al., 2021; Myrgiotis et al., 2021) with nevertheless a reduced temporal resolution that is frequently mentioned as a limitation.

Regarding the used features, vegetation indices (VIs) are commonly derived (partially listed in Cui et al., 2012, and Tong and He, 2017), in particular the NDVI (Chen et al., 2021; Hill et al., 2004; Liu et al., 2020b; Piao et al., 2007; Reeves and Baggett, 2014; Schucknecht et al., 2017; Wang et al., 2020) but also EVI (Ma et al., 2019; Meshesha et al., 2020; Tiscornia et al., 2019), SAVI (Fern et al., 2018; Jiang et al., 2015) or Tasseled Cap (Dara et al., 2020), among others. VIs are calculated from the satellite reflectance values and are used as proxies to grassland biomass. They allow to directly monitor spatio-temporal variations. In support, the joint acquisition of field data allows comparison and correlation with satellite-based data. Field data are obtained from different sources, such as spectral measures from portable spectrometers (Motta et al., 2021; Punalekar et al., 2018), fresh or dried matter (Brinkmann et al., 2011; Chen et al., 2021; Gutiérrez-Guzmán et al., 2017; Qin et al., 2021), eddy covariance flux towers (Gu et al., 2013; He et al., 2014; Maselli et al., 2013; Wylie et al., 2016) or grass canopy height measurements (Ali et al., 2017a; Cimbelli and Vitale, 2017; Nickmilder et al., 2021; Yin et al., 2020).

Subsequently, empirical models are built to correlate satellite data with field data to mainly retrieve biophysical variables which are closely related to biomass. The Leaf Area Index (LAI) (Ding et al., 2017; Dusseux et al., 2015; Yu et al., 2018), the Fraction of Absorbed Photosynthetically Active Radiation (FAPAR) (Diouf et al., 2015; Gaffney et al., 2018; Tiscornia et al., 2019) or the Fraction of green Vegetation Cover (FCOVER) (Dusseux et al., 2015; Roumiguié et al., 2017) are among the most often derived. The used models are mostly linear or multi-linear regression approaches (Baghi and Oldeland, 2019; Clementini et al., 2020; Holtgrave et al., 2020; Wang et al., 2019c) but also rely on machine learning approaches such as Random Forests and Support Vector Machines (Lei et al., 2020; O'Hara et al., 2021; Raab et al., 2020; Schwieder et al., 2020), Gaussian Processes (Yin et al., 2018) or Artificial Neural Networks (Chen et al., 2021; Li et al., 2016; Nickmilder

et al., 2021; Yang et al., 2018). Alternatively, radiative transfer models such as PROSAIL are used to recover these biophysical variables (He et al., 2019; Punalekar et al., 2018; Quan et al., 2017; Schwieder et al., 2020).

Finally, high level information concerning biomass estimation in different forms are retrieved, whether for anomaly detection, yield quantification, correlation between external effects (*e.g.*, climatic or anthropogenic) and biomass, or for assessing the grazing pressure on biomass.

Management practices

The management of grassland parcels is the second most approached topic, accounting for 16% of the corpus. Two main objectives, sometimes approached jointly, follow the management practices purpose. First, satellite data can be used to differentiate between management practices, *i.e.*, mowed or grazed or a mix of both and sometimes ploughing (Chiboub et al., 2019; Dusseux et al., 2014b; Lopes et al., 2017; Myrgiotis et al., 2021; Voormansik et al., 2020), as a classification task. Secondly, the detection and quantification of one or more management practices by detecting for example the frequency of mowing during a season, is explored (De Vroey et al., 2021a; Estel et al., 2018; Griffiths et al., 2019; Kolecka et al., 2018; Lobert et al., 2021). Based on this satellite-derived information, the overall exploitation of a parcel, *e.g.*, extensive or intensive, can be estimated *a posteriori*. This information is possibly obtained by combining information related to biomass.

Regarding the detection of management practice frequency, one key constraint mentioned in all related works is the temporal resolution. Indeed, the effects of management have an important impact on the phenology of the grass, affecting its regime. The duration of the effects on vegetation cover induced by agricultural practices can be very variable but especially very short as explained in Sec. 1.1.4. Thus, a greater temporal resolution will be beneficial to an exhaustive and accurate detection. As a result, the use of optical, which is affected by cloud cover, and radar data, is much more balanced in the works dealing with management practices over grasslands. As previously seen, radar data do not suffer from missing data and allow constant and regular acquisitions, reducing the risk of missing a technical act. Fig. 1.13 illustrates the proportional use of optical, SAR or both optical and SAR images among the different research topics of the corpus. It appears that the research topic of management practices is the one where work most often incorporates SAR data. Out of the 45 articles related to management practices, only 24 are exploiting passive optical images, 11 are using SAR images and 10 are integrating both optical and SAR images. Regarding the use of optical imagery, NDVI (De Vroey et al., 2021b; O'Hara et al., 2021; Reinermann et al., 2021) and LAI (Asam et al., 2015; Dusseux et al., 2014c; Myrgiotis et al., 2021) are the most frequently derived features. Medium spatial resolution from MODIS or SPOT-VEGETATION are used to derive those features (Estel et al., 2018; Halabuk et al., 2015; Zhou et al., 2021). High spatial resolution (*e.g.*, ~10-30m) (Bastin et al., 2012; Kolecka et al., 2018; Zhou et al., 2021) and very high spatial resolution (*e.g.*, ~1-5m) (Franke et al., 2012; Gómez-Giménez et al., 2017; Hadj Said et al., 2011; Sibanda et al., 2017) images are nevertheless largely preferred. This is due to the fact that management practices are generally detected at the agricultural parcel scale. From SAR data, backscattering coefficient information is usually extracted (O'Hara et al., 2021; Schuster et al., 2011; Taravat et al., 2019; Wesemeyer et al., 2021). The temporal information (*i.e.*, related to the task of change detection induced by the management practices) encompassed in the calculation of interferometric coherence is also considered (De Vroey et al., 2021a; Kavats et al., 2019; Tamm et al., 2016; Voormansik et al., 2020). Very high spatial resolution X-band SAR sensors are favored, allowing more spatial texture to be retrieved at the parcel scale. When used in conjunction with optical data, C-band SAR data are more prevalent, increasingly since the availability of freely available Sentinel-1.

Management practices can be numerous during the same agricultural season causing changes in the vegetation. Thus, the totality of work are relying on time series allowing to observe the vegetation at multiple times. These time series are mainly restricted to one year or even to one growing season, *e.g.*, from March to October. Indeed, management practices are mainly expected during this time interval. The areas covered by

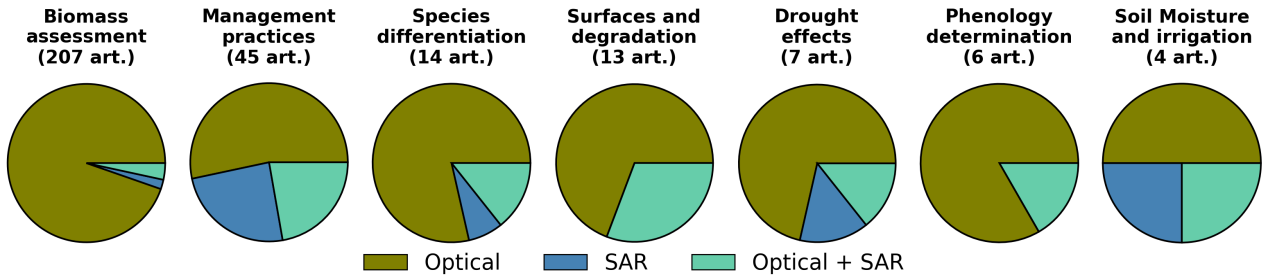

Figure 1.13: Satellite sensor type over grasslands according to the main research topic.

these articles are generally small (of the order of a few parcels to a few hundred). This is due to the complexity of reporting technical acts as well as to a lesser interest, until now than for the measurement of biomass in particular.

Two main methodological approaches are adopted to retrieve the frequency of management practices. A binary temporal classification problem is defined, with classes being the occurrence or not of a technical act. Several machine learning techniques are used such as Decision Trees or Random Forests (Halabuk et al., 2015; O'Hara et al., 2021), k-Nearest Neighbors (Dusseux et al., 2014c), Maximum Likelihood classifier (Kurtz et al., 2010), Extreme Gradient Boosting (O'Hara et al., 2021), Gaussian Kernels (Lopes et al., 2017) or Neural Networks (Lobert et al., 2021; Taravat et al., 2019; Komisarenko et al., 2022). Nevertheless, these approaches are mainly supervised, *i.e.*, dependent on the availability of validation data. As those are scarce, the work relying on supervised machine learning are for the most part exploratory. The second approach, mostly used, is based on the analysis of the time series trend to detect abrupt changes synonymous to technical acts (Stendardi et al., 2019a; Griffiths et al., 2019; Schwieder et al., 2020). These methods generally depend on thresholds, applied either directly to the satellite time series or fitted distributions.

Other research topics

Apart from biomass assessment and management practice evaluation, some other applications of EO on grasslands are investigated but with much lower occurrence.

A certain number of work addresses the topic of species richness of grasslands that can be wide (Sec. 1.1.1). To this concern, the history of grasslands is derived, which is related to the potential of species richness, (Barrett et al., 2014; Hubert-Moy et al., 2019; Lopes et al., 2017). More often, spectral differentiation of species is explored (Adamo et al., 2020; Bekkema and Eleveld, 2018; Fazzini et al., 2021; Radkowski et al., 2021; Tarantino et al., 2021). As field measurements of agronomic variety are complex, unsupervised approaches are often preferred. They rely on raw spectral data or derived feature such as NDVI (Adamo et al., 2020; Hubert-Moy et al., 2019; Xu et al., 2019a), the Sentinel-2 Red-Edge Position (Bekkema and Eleveld, 2018) or Simpson and Shannon indexes (Fauvel et al., 2020). Adopted methodologies are using Random Forests (Barrett et al., 2014; Fauvel et al., 2020), Support Vector Machines (Barrett et al., 2014; Schuster et al., 2015; Xu et al., 2019a), Gaussian Kernels (Lopes et al., 2017) or Convolutional Neural Networks (Fazzini et al., 2021). In order to improve the results, some work also propose the integration of edaphic or climatic auxiliary data that further allow distinction of the species (Adamo et al., 2020; Mansour et al., 2016). As for biomass assessment, optical images are predominantly favored. A wide range of sensors are being exploited. High spatial resolution Sentinel-2, Landsat-8 and SPOT-5, or very high resolution such as RapidEye (Schuster et al., 2015), FORMOSAT-2 (Lopes et al., 2017), PlanetScope (Radkowski et al., 2021) or WorldView-2 (Adamo et al., 2020) images are encountered. SAR images are once again mainly used in support of optical images (*i.e.*, as gap-free data). A single paper uses only SAR images from ENVISAT, ERS and ALOS PALSAR to discriminate

several types of grasslands based on potential species richness (Barrett et al., 2014).

Extent of grassland surfaces and their trend is also assessed by means of satellite time series. The trend of surfaces can be assessed over different grassland classes, such as permanent and temporary grassland or improved, semi-improved, and unimproved (Hubert-Moy et al., 2019; O'Hara et al., 2021; Smit et al., 2008). Another approach consists of differentiation of grassland versus other vegetation types, mainly crops or afforestation (Nicula, 2019; Esch et al., 2014; Kloucek et al., 2018; Parente et al., 2019; Pazúr et al., 2021). Spectral reflectance values or vegetation indices (NDVI, EVI) are mainly used as input for classifiers. Random Forests or Support Vector Machines are employed. RADARSAT-2 (Dusseux et al., 2014a), Sentinel-1 (O'Hara et al., 2021; Samrat et al., 2021; Spagnuolo et al., 2020) and ALOS PALSAR-2 (Spagnuolo et al., 2020) images are also used alongside optical images, in each case improving the classification.

Some articles focus on the effects of drought on grasslands and correlate optical data with climatic data over large areas. These work aim at deriving drought severity information (Abdel-Hamid et al., 2020; Kath et al., 2019; Peratoner et al., 2021). In some cases, prediction on the probability and severity of fire are provided (Cao et al., 2015; Chaivaranont et al., 2018). Large-scale analysis are predominant with the use of MODIS sensor. Other works specifically observe the intra-annual phenology of grasslands. In particular, they attempt to retrieve specific phenological stages such as beginning and end of growing season (Almeida-Ñauñay et al., 2022; Mardian et al., 2021; Stendardi et al., 2019a). MODIS images are again the most widely used, from which NDVI is commonly derived. Seasonality retrieval fitting algorithms like Breaks for Additive Seasonal and Trend (BFAST) (Mardian et al., 2021) or Harmonic ANalysis of Time Series (HANTS) (Li et al., 2020b) are traditionally employed. Finally, a very small number of papers address soil moisture (Asmuß et al., 2019; Baghdadi et al., 2016) and irrigation performances (Abuzar et al., 2017; Reinfelds, 2011) in grasslands. Since SAR data are sensitive to dielectric activity and thus moisture, half of the papers, although their number is limited, exploit the correlation of backscatter and soil moisture, notably through inversion techniques.

Table 1.1: Corpus of scientific publications related to remote sensing and grasslands. Seven main research topics are defined and references are further classified by remote sensing data type. The order of presentation of the topics follows their representation in the corpus.

Biomass assessment	
Optical	Ali et al., 2014, Ali et al., 2017b, An et al., 2013, Anaya et al., 2009, Anderson et al., 1993, Askari et al., 2019, Baeza et al., 2010, Baghi and Oldeland, 2019, Barrachina et al., 2015, Carlos Marcelo et al., 2004, Bellini et al., 2021, Bénié et al., 2005, Blanco et al., 2009, Boschetti et al., 2007, Brinkmann et al., 2011, Buddeberg et al., 2021, Buono et al., 2010, Chen et al., 2011, Chen et al., 2014, Chen et al., 2021, Chi et al., 2018, Cimbelli and Vitale, 2017, Clementini et al., 2020, Courault et al., 2010, Cui et al., 2012, Dara et al., 2020, Ding et al., 2017, Diouf et al., 2015, Donald et al., 2010, Donald et al., 2013, Dube and Pickup, 2001, Dusseux et al., 2015, Edirisinghe et al., 2011, Edirisinghe et al., 2012, Eisfelder et al., 2017, Everitt et al., 1989, Fan et al., 2010, Fassnacht et al., 2018, Feng and Zhao, 2011, Feng et al., 2017, Fern et al., 2018, Fernández-Habas et al., 2021, Friedl et al., 1994, Fu et al., 2014, Gaffney et al., 2018, Gao et al., 2013, Gao et al., 2016, Grant et al., 2013, Gu et al., 2013, Guerini Filho et al., 2019, Guido et al., 2014, Guo et al., 2000a, Guo et al., 2012, Guo et al., 2019, Gutiérrez-Guzmán et al., 2017, Hall et al., 2010, Hardy et al., 2021, He et al., 2014, He et al., 2019, Hill et al., 2004, Ikeda et al., 1999, Irisarri et al., 2012, Jackson and Prince, 2016, Jansen et al., 2018, Jia et al., 2015, Jia et al., 2018, Jiang et al., 2015, Jianlong et al., 1998, Jin et al., 2014, Jin et al., 2019, Jobbágy et al., 2002, John et al., 2018, Justice and Hiernaux, 1986, Kawamura et al., 2005b, Kawamura et al., 2005a, Kogan et al., 2004, Lei et al., 2020, Leimgruber et al., 2001, Li et al., 2013b, Li et al., 2013a, Li et al., 2016, Liang et al., 2016, Liu et al., 2015, Liu et al., 2019, Liu et al., 2020b, Long et al., 2010, Luo et al., 2014, Ma et al., 2019, Magiera et al., 2017, Mao et al., 2014, Marsett et al., 2006, Marwaha et al., 2020, Maselli et al., 2013, Meng et al., 2017, Meshesha et al., 2020, Moreau et al., 2003, Motta et al., 2021, Munyati and Makgale, 2009, Myrgiotis et al., 2021, Na et al., 2018, Numata et al., 2007, Otgonbayar et al., 2019, Palmer et al., 2010, Paruelo et al., 2000, Paudel and Andersen, 2010, Piao et al., 2007, Piñeiro et al., 2005, Porter et al., 2014, Punalekar et al., 2018, Qamer et al., 2016, Qin et al., 2021, Quan et al., 2017, Ramoelo et al., 2015a, Ramoelo et al., 2015b, Reeves et al., 2001, Reeves and Baggett, 2014, Ren and Feng, 2015, Ricotta et al., 2003, Robinson et al., 2019, Röder et al., 2008, Rossini et al., 2012, Roumiguié et al., 2015, Roumiguié et al., 2017, Rufin et al., 2015, Sankey et al., 2009, Schino et al., 2003, Schucknecht et al., 2017, Schwieder et al., 2020, Seaquist et al., 2003, Serrano et al., 2021, Si et al., 2012, Sibanda et al., 2016, Sibanda et al., 2017, Silverman et al., 2019, Smith et al., 2011, Sun et al., 2013, Sun et al., 2017, Sun et al., 2019, Tan et al., 2010, Tang et al., 2014, Tiscornia et al., 2019, Todd et al., 1998, Tong and He, 2017, Tsalyuk et al., 2015, Tucker et al., 1985, Ullah et al., 2012, Vescovo and Gianelle, 2008, Wang et al., 2016, Wang et al., 2017b, Wang et al., 2019e, Wang et al., 2019a, Wang et al., 2020, Wehlage et al., 2016, Wei et al., 2019, Wu et al., 2008, Wu, 2012, Wu et al., 2014, Wylie et al., 1991, Wylie et al., 2002, Wylie et al., 2016, Xia et al., 2014, Xie et al., 2009, Xing et al., 2010, Xiong et al., 2019, Xu et al., 2007, Xu et al., 2013, Xu et al., 2016, Xu et al., 2018, Xu et al., 2019b, Yang et al., 1998, Yang et al., 2009, Yang et al., 2012, Yang et al., 2015, Yang et al., 2017, Yang et al., 2018, Yang et al., 2019a, Yin et al., 2014, Yin et al., 2018, Yin et al., 2020, You et al., 2019, Yu et al., 2018, Yu et al., 2019, Zeng et al., 2019, Zhang et al., 2014a, Zhang et al., 2014b, Zhang et al., 2016, Zhang et al., 2017, Zhang et al., 2018, Zhao et al., 2014, Zhao et al., 2019, Zheng et al., 2020, Zhou et al., 2014a, Zhou et al., 2014b, Zhou et al., 2017a, Zhou et al., 2017b, Zhu et al., 2019
SAR	Ali et al., 2017a, Crabbe et al., 2019, Grant et al., 2015, Yang et al., 2021
Optical+SAR	Ali et al., 2016, Frolking et al., 2005, Holtgrave et al., 2020, Nickmilder et al., 2021, O'Hara et al., 2021, Raab et al., 2020, Wang et al., 2019c

Management practices	
Optical	Asam et al., 2015, Bastin et al., 2012, Dusseux et al., 2014b, Dusseux et al., 2014c, Estel et al., 2018, Franke et al., 2012, Gómez-Giménez et al., 2017, Griffiths et al., 2019, Guo et al., 2000a, Guo et al., 2003, Guo et al., 2004, Hadj Said et al., 2011, Halabuk et al., 2015, Kolecka et al., 2018, Kurtz et al., 2010, Lopes et al., 2017, Myrgiotis et al., 2021, Reinermann et al., 2021, Rossi et al., 2018, Rossi et al., 2019, Sibanda et al., 2016, Sibanda et al., 2017, Stumpf et al., 2020, Schwieder et al., 2021
SAR	Chiboub et al., 2019, De Vroey et al., 2021a, Kavats et al., 2019, Schuster et al., 2011, Siegmund et al., 2016, Tamm et al., 2016, Taravat et al., 2019, Voormansik et al., 2013, Voormansik et al., 2016, Zalite et al., 2014, Zalite et al., 2016
Optical+SAR	D'Andrimont et al., 2018, Dabrowska-Zielinska et al., 2017, De Vroey et al., 2021b, Lobert et al., 2021, O'Hara et al., 2021, Stendardi et al., 2019a, Voormansik et al., 2020, Wesemeyer et al., 2021, Zhou et al., 2021, Komisarenko et al., 2022

Species differentiation	
Optical	Adamo et al., 2020, Bekkema and Eleveld, 2018, Fazzini et al., 2021, Hubert-Moy et al., 2019, Lopes et al., 2017, Mansour et al., 2016, Radkowski et al., 2021, Tarantino et al., 2021, Toivonen et al., 2003, Xu et al., 2019a, Zongyao and Yongfei, 2013
SAR	Barrett et al., 2014
Optical+SAR	Fauvel et al., 2020, Schuster et al., 2015

Surfaces and degradation	
Optical	Nicula, 2019, Esch et al., 2014, Hubert-Moy et al., 2019, Kloucek et al., 2018, Kurtz et al., 2010, Munyati and Makgale, 2009, Parente et al., 2019, Pazúr et al., 2021, Smit et al., 2008
SAR	-
Optical+SAR	Dusseux et al., 2014a, O'Hara et al., 2021, Samrat et al., 2021, Spagnuolo et al., 2020

Drought effects	
Optical	Cao et al., 2015, Kath et al., 2019, Li et al., 2017, Peratoner et al., 2021, Wang et al., 2019d
SAR	Abdel-Hamid et al., 2020
Optical+SAR	Chaivaranont et al., 2018

Phenology characterization	
Optical	Almeida-Ñauñay et al., 2022, Lara and Gandini, 2016, Fontana et al., 2008, Li et al., 2020b, Mardian et al., 2021
SAR	-
Optical+SAR	Stendardi et al., 2019a

Soil moisture and irrigation	
Optical	Abuzar et al., 2017, Reinfelds, 2011
SAR	Asmuß et al., 2019
Optical+SAR	Baghdadi et al., 2016

1.3 Problem statement and objectives

The vast grassland surfaces as well as the growing recognition of the ecosystem services they provide have revealed urgent needs for their conservation and sustainable management. Grasslands serve major functions in climate change mitigation, particularly through global carbon storage and sequestration. The extent of the grassland biome has evolved greatly through history with abiotic factors such as climate, mostly at the interface between desert and forest areas. Beyond climate change, grasslands have decreased considerably as a result of human activities, such as conversion to impervious surfaces or agricultural activities. This decline has been reported by many works which have observed increasing surface losses. The conversion of grasslands to croplands compromises ecosystem services with harmful effects on soil, water, and air quality. Besides the impact of grassland conversion, the overexploitation of grassland through overgrazing, frequent mowing, and depletion of seeded species lead to a significant decrease in their capacity to provide multiple ecosystem services: lower captured CO_2 through a decrease in biomass, alteration of biodiversity through a decrease in floral diversity, soil impoverishment, and threats to wildlife corridors, among others. Accordingly, although monitoring crop management has until recently received more attention, new governmental efforts are foreseen for the conservation of grasslands through promoting land preservation, grassland friendly policies on land use, and sustainable management efforts.

For instance, in Europe, the first pillar of the Common Agricultural Policy (CAP) and especially its *Greening* component are aiming to maintain highly valued ecological surfaces such as grasslands. The component *Greening* is intended, among others, to protect permanent grassland areas and prevent their conversion to other surfaces such as crops, by means of financial support. Permanent grasslands refer to land used continuously to grow herbaceous fodder, forage, or energy purpose crops. They are not part of crop rotation on the holding and occupy the land for five years or longer. Therefore, permanent grasslands are often linked to grasslands that provide higher ecosystemic services with a positive impact on carbon sequestration and biodiversity.

Monitoring management practices is essential to ensure grassland conservation and promote sustainable management. The regulation of grassland exploitation intensity and management calendars have proven to be effective measures to preserve or restore the environmental quality of grasslands. Despite growing interest, monitoring the management of grasslands poses many challenges due to their great agronomic diversity and the multitude of management practices to which they are subject. Numerous technical acts are performed on grasslands such as grazing, mowing, and ploughing. They have a direct but varying impact on above-ground or root biomass and are the underlying factor in grassland degradation. Detecting a high mowing frequency can, for instance, hint at frequent fertilizer inputs synonymous with a negative impact on various ecosystem services. Similarly, the precocity of technical acts during the growing season, while often beneficial for grass production throughout the year, affects ecosystem services. Thus, information that describes the nature and quantity of technical acts performed can provide useful information to predict the quality of rendered ecosystem services. Despite the acknowledged importance of management practices, large-scale information is currently not available reporting on the frequency and nature of technical acts.

Satellite remote sensing appears to be a suitable tool for efficient grassland monitoring. In particular, satellite image time series allow synoptic and regular analysis. As demonstrated by the numerous works existing in the literature, research on grassland monitoring by using satellite images is rich and growing. Recent data acquired from the Sentinel satellites in the framework of the Copernicus programme further highlight the interest of satellite images for grassland monitoring. Sentinels offer high spatial and temporal resolutions, complementary optical and Synthetic Aperture Radar (SAR) images, and free and large-scale data. Combined, these characteristics bring new opportunities for monitoring grassland vegetation conditions. Consequently, the research conducted in this thesis aims at **investigating the capabilities and the synergy of recent Sentinel time series for continuous grassland monitoring**. Specifically, the thesis focuses on **develop-**

ing methods for detecting grassland management practices from complementary optical and SAR multivariate image time series.

The retrieval of relevant signal patterns associated with grassland management practices from multivariate time series is challenging. As previously mentioned, grasslands exhibit highly variable phenologies, unlike crops or forests, for example, due to the multitude of agronomic species. Hence, farmers manage each grassland with different calendars and frequency through nutrient management, water management, or different types of practice. Besides the challenge of the diversity of management practices, their spatio-temporal detections imply important temporal constraints. The accurate management practices detection requires frequent and regular satellite acquisitions. Consequently, the exploitation of low temporal resolution time series can lead to substantial errors. This is particularly caused by rapid changes in the state of the grassland vegetation. For instance, under favorable climatic conditions or with the help of nitrogenous fertilizers, the vegetation can rapidly recover after mowing or grazing.

To illustrate the rapid regrowth of grass cover, Figure 1.14 shows five consecutive cloudless Sentinel-2 images acquired over a ryegrass parcel. A complete regrowth of the grass cover is visible on June 9th within seven days after the first mowing occurring on June 2nd. As observed, the grass cover on June 9th is similar to May 27th, prior to mowing. As a consequence, if the image of June 2nd had been missing, the mowing could not have been detected. Furthermore, after the complete regrowth on June 9th, a second mowing takes place ten days later on June 19th. As in the previous example, if the image of June 9th had been missing, the second mowing would have been missed considering the already low grass cover on June 2nd. These examples emphasize the rapid regrowth of grasslands and the short temporal window during which they can be observed. Therefore, dense temporal sampling is mandatory to monitor changes in grassland vegetation status associated with management practices.

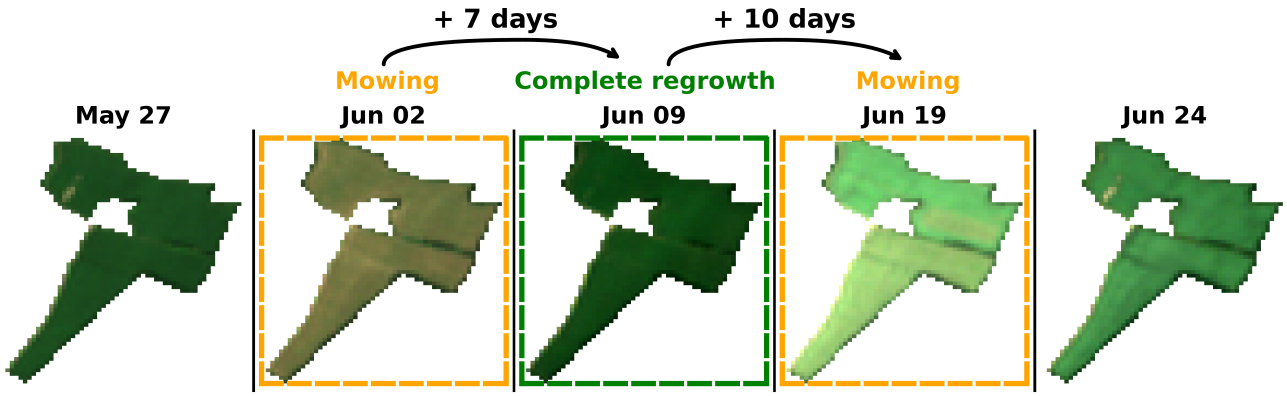

Figure 1.14: Consecutive Sentinel-2 images illustrating the rapid regrowth of grassland surfaces.

In terms of temporal resolution, Sentinel satellites offer unprecedented opportunities. Especially, weather-independent SAR sensors enable regular acquisitions in compliance with grassland rapid regrowth. Despite its high temporal revisit, the exploitation of SAR time series is not straightforward. SAR images suffer from inherent speckle noise and important signal fluctuations, mainly due to the climate conditions during acquisition. These fluctuations can be confused with changes in the state of vegetation. For this reason, the use of SAR time series in the context of grassland monitoring is less often observed, as previously reported in favor of optical data. As it is well-known, optical time series provide relevant information that describes the evolution of vegetation cover (as seen in Figure 1.14). Simple yet effective vegetation indexes, such as the Normalized Difference Vegetation Index (NDVI), are widely exploited and have shown some interest in detecting management practices. However, the observed temporal resolution of optical data due to frequent and persistent cloud cover still remains an important limitation. NDVI time series consequently suffer from missing data, which, as previously seen, will prevent monitoring of management practices. Large temporal

data gaps can last from weeks to months and may occur at key moments involving important vegetation changes (*e.g.*, during growth or senescence, or even at harvest time). The reconstruction of optical indices can be seen as a mandatory step to allow for continuous monitoring of grassland surfaces. Accordingly, the first goal of this thesis is the **reconstruction of dense NDVI time series by exploiting the synergy of both optical and SAR Sentinels.**

Besides the requirement of dense temporal time series, the analysis scale at which the detection of practices is possible also needs to be addressed. The finer pixel-scale analysis involves high computational costs and is more prone to noise. As management practices are assumed to be performed at the parcel scale, the suggestion is made to work at the parcel scale. In addition, large-scale information on the location of grasslands is available in a growing number of countries through various agricultural policies, as it is the case in France. However, it was observed that grassland can be managed at a finer scale, lying between the pixel- and parcel-scale. With additionally various lengths and intensities impacts of management practices on the vegetation, this intermediate scale seems to be necessary to allow to reduce the uncertainties involved in their detection. The second goal of this thesis is therefore to **propose a methodology to detect grassland management practices.**

The joint exploitation of Sentinel-1 and Sentinel-2 data for grassland monitoring, which both permit a adequate spatial resolution, thus appears promising. Nevertheless, the data proliferation raises new challenges. The high dimension and the heterogeneous physical nature of the data, with various spatial, spectral and temporal domains are among the aspects to be explored. Especially, among the few works exploiting Sentinel-1 and Sentinel-2 for grassland monitoring, the information from both satellites is generally individually processed. The methodologies exploited are, as a result, specific to some grassland types, areas, or evolving administrative constraints. At the same time, recent advances in computing resources and machine learning algorithms have brought deep learning strategies to the forefront as suitable for dealing with the reported challenges. Among others, the interests of deep learning methods for key considerations such as data mining, large-scale processing, and reproducibility have been highlighted.

In this context, the main goal of the thesis is to develop methods that allow the continuous monitoring of grasslands and the detection of their management practices from complementary Sentinel satellite data. For this purpose, the thesis will: **(i) employ advances in deep learning to develop a multi-source methodology exploiting the synergy and capabilities of both Sentinel-1 and Sentinel-2 data sources**. Deep-based methods allow for early fusion of multi-modal data streams which is advantageous in view of the heterogeneous dimensions of the data exploited herein. The developed methodology targets to regress multivariate SAR time series towards optical NDVI and proposes the incorporation of contextual knowledge to reduce the impact of exogenous factors leading to SAR data variability. NDVI was chosen as an easily interpretable and widely used variable. This choice also supports the potential use of the results in post-processing that does not require expert knowledge of remote sensing; **(ii) explore methods aiming at detecting vegetation status changes related to management practices on grasslands.** The proposed methods, necessarily unsupervised as reference data about management practices do not exist, will exploit the previously obtained gap-free NDVI time series. Different strategies are compared, taking into account the heterogeneous nature of grassland management practices.

1.4 Outline of the manuscript

The introduction proposed in this chapter focused on grasslands, their systemic diversity and associated threats, and the different management practices they are subject to. Satellite remote sensing and relevant works from the scientific literature have been presented.

Chapter 2 is devoted to the description of the reference and ancillary data used to define an experimental

setup to meet the objectives of this manuscript. Sentinel-1 and 2 missions are briefly presented, and the interest of exploiting both data types for grassland monitoring is illustrated. The pre-processing steps of the different pertinent datasets are detailed. A first qualitative and quantitative evaluation of the different satellite features is performed on several grassland datasets as well as on other vegetation types introduced for comparison.

After having determined the strengths and weaknesses of optical and SAR features, **Chapter 3** defines the deep learning methodology, namely, Sentinels Regression for Vegetation Monitoring (SenRVM), allowing to encompass the advantages of both active and passive sensors for grassland monitoring. The existing approaches used in the literature to obtain dense time series are reviewed. Classical deep-based architectures and their relevance for the defined task are outlined. Subsequently, the new deep-based regression methodology is detailed, which exploits Sentinel-1 and Sentinel-2 time series in order to recover NDVI from SAR-based features.

Chapter 4 includes a in-depth analysis of the results obtained with the SenRVM approach. The analysis will address common challenging aspects of both machine learning and Earth Observation data exploitation (*e.g.*, datasets, features, generalization capabilities). The benefits of the SenRVM approach to increase temporally available observations are illustrated and compared on several types of vegetation. The impact of spatio-temporal variations in the datasets is explored both in the learning process of SenRVM and on the results. Relevance and importance of the selected satellite and ancillary features are assessed. Next, a comparison of the SenRVM approach with related and widely used methods is proposed for a gap-filling task on short- and long-term data gaps. Lastly, further post-processing steps with the objective of introducing possible improvements to the results are discussed.

The challenge of detecting management practices in grasslands is presented in **Chapter 5**. A review of the pertinent literature is first proposed. This allows to highlight the drawbacks of the existing approaches and suggest improvements. In particular, a superpixel-scale approach is defined as an alternative to the pixel- and parcel-based approaches. Comprehensive validation datasets are subsequently constructed. Different time series change detection methods are defined to retrieve technical acts performed on grasslands. Methods are compared and their sensitivity to different parameters is assessed. Finally, examples of applications to obtain information describing the exploitation of grasslands are introduced.

Finally, conclusions and perspectives are presented in **Chapter 6**.

Chapter 2

Study areas and datasets

2.1 Study areas

The study areas are located in France, which had, in 2020, the largest extent of grasslands in Europe (Eurostat, 2021). The coverage of agricultural land amounted to 52% of the French metropolitan territory. Grasslands in the broad sense (grass, fodder crops, and fallow land) covered 12.8 million hectares, *i.e.*, approximately 45% of agricultural land. In other words, in 2020, nearly a quarter of the French metropolitan territory was grasslands, greatly contributing in the production of agricultural goods (Agreste, 2021). Their monitoring thus appears necessary, relating these important surfaces to ecosystemic and economic challenges.

Different study areas with distinct geographical contexts are selected. Several criteria are taken into account for their selection such as the abundance of grasslands, data availability, or the topography as it impacts both satellite acquisition and phenologies. The exact extent of the different areas is induced by the division in tiles of satellite products, done for their latter distribution. This division is based on a commonly used tiling system which is the Military Grid Reference System (MGRS).

The resulting study areas are divided in two groups. The first group corresponds to Mâcon and Toulouse areas, described in Section 2.1.1, which are the primary study areas used in this work. Both areas are selected for the further design and implementation of the experiments and the extensive analysis of the results. The second group, described in Section 2.1.2, are additional sites covering large geographical surfaces, only dedicated for further assessment in a few experiments.

2.1.1 Mâcon and Toulouse sites

These two areas are defined as the main study areas.

***Mâcon* area - T31TFM**
This area is located in the East of France (purple area in Figure 2.1). The area is first defined by the extent of the MGRS tile T31TFM. Agricultural season from October 2016 to October 2017 is studied, being the one for which reference data describing the grasslands was available at the start of this work. Consequently, only one of the two satellites composing the Sentinel-2 optical constellation is considered until June 2017. The full capacity of the constellation is exploited once the Sentinel-2B satellite becomes operational. The study site is therefore selected over a smaller area where overlapping swaths of two adjacent orbits are available. The selected area allows an increased temporal resolution despite the momentary availability of only one satellite. While Bourg-en-Bresse becomes the major city of the study area, the name of Mâcon is retained as the main city of the original tile extent. The final area of $5,328$ km^2 is depicted by a varied topography. The area is characterized by a river valley on the Western side, hills and plateaus of the Jura mountains on the Eastern side (Figure 2.1).

***Toulouse* area - T31TCJ/CH**
This area, denoted as Toulouse, is located in the South-West of France (blue area in Figure 2.1) and straddles two MGRS tiles, T31TCJ and T31TCH. The area covers $15,120$ km^2. It is characterized by different landscapes with an important topographic gradient. Lowlands with little topography are located in the Northern part, whereas the Pyrenees mountains cover a vast Southern part of the area (Figure 2.1). For this area, the time interval under consideration is from February 2017 to April 2018. Same exact time interval as for Mâcon could not be considered, due to the temporary unavailability of Sentinel-1A data because of a change in the acquisition plan of the relative orbits between October 2016 and February 2017. As for the Mâcon area, the full capacity of the Sentinel-2 constellation is only available from the end of June 2017.

2.1.2 Additional sites

Five Sentinel-2 tiles covering the French territory are further considered as additional areas. These areas are proposed to assess the results obtained over the previous Mâcon and Toulouse sites. The additional sites aim to validate the results on large scale areas with higher diversity. They will also allow us to assess the generalization capacity of the proposed methods. The five tiles are regrouped in two distinct large areas, namely the Western- and Northern-area. The first Western-area (cyan color in Figure 2.1) is located in the West of France, mainly in the Pays de la Loire region. This area of $26,713$ km^2 contains parts of three contiguous MRGS tile, namely T30TXS, T30TXT, T30TWT, covering respectively $7,914$ km^2, $11,746$ km^2 and $9,098$ km^2. The second Northern-area covers the city of Paris on the South-West and extends Northward (khaki area in Figure 2.1). The area is $20,107$ km^2. It regroups parts of the two T31UDQ and T31UEQ MGRS tiles, respectively $12,065$ km^2 and $9,117$ km^2. The two additional areas are characterized by low topography but distinct climates and therefore phenologies. In addition, the types of agricultural systems and grassland cultivated are also different. The agricultural season ranging from October 2018 to October 2019 is considered for both additional areas, thus granting the full temporal resolution of the Sentinel-1 and 2 constellations.

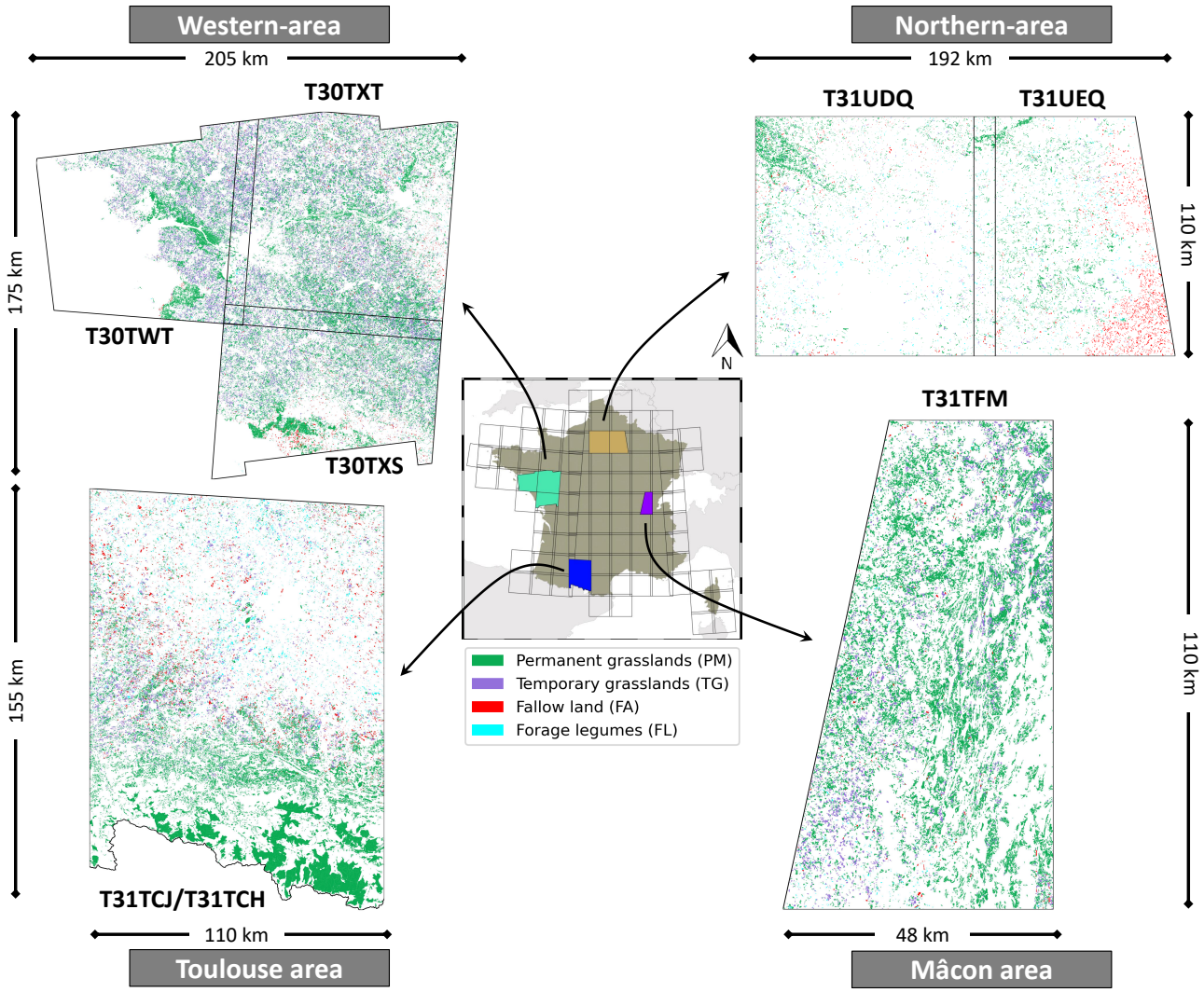

Figure 2.1: Location of the study areas Mâcon (purple) and Toulouse (blue), and the additional study sites (Northern-area in brown and Western-area in cyan). Grasslands located in the study sites are colored according to the four meta-classes described in Section 2.3.1.1

2.2 Satellite data

2.2.1 Sentinel-2 optical imagery

The twin satellites Sentinel-2A and Sentinel-2B, launched in 2015 and 2017 respectively, are carrying multispectral optical sensors (Drusch et al., 2012). Acquisitions have a swath of 290 km but are divided and distributed according to the MRGS tiling system (Section 2.1.1) in 110 km tiles. Thirteen spectral bands are available with different spatial resolutions. Bands at 10 m and 20 m spatial resolutions are mainly used for terrestrial applications and the three bands acquired at 60 m spatial resolution are mostly used for atmospheric corrections or related applications (Table 2.1). Both satellites have the same orbit but are phased at 180°, permitting a temporal resolution of 5 days at the equator and lower at higher latitudes. Nevertheless, temporal revisit is only theoretical. The cloud cover more or less important according to the geographical areas, strongly degrades the data availability (Sudmanns et al., 2020a). Since the beginning of operations and until end of 2020, the Sentinel-2 constellation has made available about 14×10^6 gigabyte (GB) of data covering the globe and freely accessible (ESA, 2021a).

Table 2.1: Spectral band ranges and spatial resolutions of the Sentinel-2 constellation Multispectral Instrument (MSI) sensors. Bold spectral bands (B2, B3, B4 and B8) are the ones used in this work.

Band Number	Band Description	Wavelength range (nm)	Spatial Resolution (m)
B1	Coastal aerosol	443 - 453	60
B2	**Blue**	**458 - 523**	**10**
B3	**Green**	**543 - 578**	**10**
B4	**Red**	**650 - 680**	**10**
B5	Vegetation Red Edge	698 - 713	20
B6	Vegetation Red Edge	733 - 748	20
B7	Vegetation Red Edge	773 - 793	20
B8	**NIR**	**785 - 900**	**10**
B8a	Vegetation Red Edge	855 - 875	20
B9	Water vapor	935 - 955	60
B10	SWIR - Cirrus	1360 - 1390	60
B11	SWIR	1565 - 1655	20
B12	SWIR	2100 - 2280	20

Sentinel-2 images are mainly distributed according to two levels of pre-processing. The first level of processing provides geometric correction (Level-1), allowing to take into account several possible distortions related to the acquisition angle, the orbit, the motion of the satellite or Earth's rotation and terrain topography. Images are further geo-referenced providing accurate location to each pixel. However, pixel values of Level-1 do not take into account the atmosphere's properties at the time of acquisition or the nature of the observed target. The atmospheric properties are not constant in time, and corrections may be necessary.

For some applications that do not require an evolving process to be monitored continuously, such as land cover classification, these further corrections may be optional. For the temporal analysis of physical phenomena such as grassland cover dynamic, they are of utmost importance. It will allow a comparison of the surface, independently from exogenous factors such as atmospheric absorption or scattering. The correction step permits to convert Sentinel-2 Top Of Atmosphere (TOA) reflectance including the atmospheric effect provided by Level-1 into Bottom Of Atmosphere (BOA), describing the corrected reflectance of the observed surface (Level-2). Several operational processing chains enable to retrieve Level-2 images such as Sen2Cor (Main-Knorn et al., 2017), FMask (Zhu et al., 2015) or the MACCS-ATCOR joint algorithm (MAJA, Hagolle et al., 2015). The latter was developed as a joint effort of the Centre National des Études Spatiales (CNES) and

the Deutsches Zentrum für Luft- und Raumfahrt (DLR). Being distributed by several French data providers and having reported higher accuracies compared to the other approaches (Baetens et al., 2019; Doxani et al., 2018), the Sentinel-2 Level-2 products produced by MAJA have been adopted.

Table 2.2 provides the number of Level-2 Sentinel-2 images considered over the different study areas, ranging from 53 to 80. In Mâcon (T31TFM) and Toulouse (T31TCJ/CH), the initial availability of only one of the two satellites reduces the number of exploited images.

Table 2.2: Description of Sentinel-2 images, first and last acquisitions dates for the study areas.

Area name	Tile	Images	First date	Last Date
Mâcon	T31TFM	53	22-Oct-2016	12-Oct-2017
Toulouse	T31TCJ/CH	73	15-Feb-2017	16-Apr-2018
Western-area	T30TXS	80	1-Oct-2018	31-Oct-2019
	T30TXT	80	1-Oct-2018	31-Oct-2019
	T30TWT	79	4-Oct-2018	29-Oct-2019
Northern-area	T31UDQ	79	3-Oct-2018	28-Oct-2019
	T31UEQ	79	3-Oct-2018	28-Oct-2019

2.2.2 Masks: clouds & shadow, snow

The MAJA chain producing Level-2 Sentinel-2 images includes a first step that identifies and locates clouds and their shadows. This detection is done by both a mono- and multi-temporal analysis of blue and atmospheric reflectance bands (Hagolle et al., 2015). In addition, a geophysical mask is also provided that contains information on snow-covered areas (Gascoin et al., 2019). Cloud & shadows and snow masks are available at the same spatial resolution as the reflectance images (10 m).

Cloud & shadow masks are available for each image of the time series. The temporal distribution of the cloud cover can thus be extracted. Considering all pixels belonging to grasslands (retrieved from the RPG, see Section 2.3.1.1), a cloud-cover percentage is calculated. This percentage is reported for each study area in Table 2.3. This cloud-cover percentage allows us to observe that for all tiles over roughly one-year time intervals, more than half of the acquisitions made by Sentinel-2 could be considered as cloudy. For the two main study areas, only about 26 and 24 images, for Mâcon and Toulouse respectively, were cloud-free over a grassland pixel. The percentage of cloud cover even reaches 72% over the T31UDQ tile near Paris, where only 22 images were available on average over a complete year. These cloud cover percentages illustrate that the nominal 5-day temporal resolution of the Sentinel-2 constellation is only theoretical, largely degraded over the study areas.

Table 2.3: Cloud cover percentages of optical imagery acquired over the different study areas. The percentage is computed by considering all pixels over grasslands (Table 2.6) during the studied time intervals.

	Mâcon	Toulouse	Western-area			Northern-area	
	T31TFM	T31TCJ/CH	T30TXS	T30TXT	T30TWT	T31UDQ	T31UEQ
Total cloud-cover percentage of grassland pixels (%)	51	66	58	60	63	72	67

Furthermore, the cloud cover is indeed not uniformly distributed during the season. Figure 2.2 illustrates this cloud cover percentage per date, for both Mâcon and Toulouse areas. As expected, cloud-cover is higher in winter months. Several months over the Toulouse area are depicted by very few valid Sentinel-2 observations. The 66% of cloud-cover percentage observed for the Sentinel-2 time series over Toulouse does not

inform on lasting cloud cover that can further prevent acquisition over longer time intervals. It can also be observed that cloud cover occurs during the active vegetation period of grasslands, in spring or summer. Especially, successive cloudy dates are numerous as it is the case end of July for both Mâcon and Toulouse areas. Therefore, the characterization of the phenological evolution of the vegetation surfaces from the resulting times series can be obstructed, even at key time intervals such as July.

The efficiency of the masks may prove to be essential to discard acquisitions that do not provide relevant information and may pollute the time series. Indeed, over- or under-detection of invalid pixels can convey wrong information to be used in subsequent time series exploitation. A valid observation can be discarded, while an invalid observation can be included in the analysis. While the task of constructing these masks is complex and not addressed in this work, the potential impact of mask errors will be briefly discussed in Chapter 4 and 5.

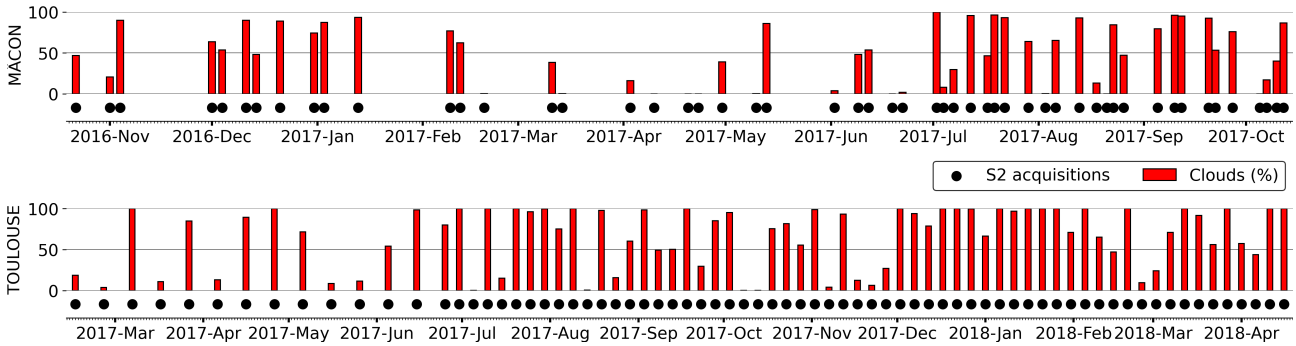

Figure 2.2: Percentage of pixels from the grassland datasets (Table 2.6) detected as invalid by the cloud & shadow masks. Each acquisition date of Mâcon and Toulouse areas are considered.

2.2.3 Sentinel-1 SAR imagery

Sentinel-1A & 1B are C-band (wavelength of 5.6 cm) SAR satellites launched in 2014 and 2016 and orbiting on the same plane (Potin et al., 2019). The Sentinel-1 constellation offers a 6 days temporal resolution at the equator, in one orbit direction (ascending or descending). Since the orbit track spacing varies with latitude, the revisit rate is greater at higher latitudes than at the equator. Available acquisitions also vary with the acquisition plan of the satellites. As previously stated in Section 1.2.1.2, active sensors such as the one carried by Sentinel-1 can acquire images regardless of illumination conditions. Images are thus available from both ascending and descending orbits. Four imaging modes are available: Interferometric Wide Swath (IW), Extra Wide Swath (EW), Strip Map (SM) and Wave (WV). Over land surfaces, the IW is the nominal imaging mode of Sentinel-1. The IW mode uses the Terrain Observation with Progressive Scan (TOPS) technique helping to achieve a homogeneous image quality throughout the 250 km swath. The swath is subdivided in three subswaths (IW1, IW2, IW3) each composed of about ten bursts. The sensors have a dual-polarization capability with vertical transmitted and receive (VV) or vertical transmitted and horizontal received (VH) polarizations bands.

For SAR active sensors, the spatial resolution is two-fold. *Resolution* as referred in Table 2.4 defines the minimum distance at which the sensor can discriminate between two closely spaced scatterers that have approximately responses of equal strength. *Pixel spacing* on the other hand denotes the size of the pixels that have been sampled (*i.e.*, aggregating the individuals scatterers) throughout the scene and corresponds to the pixel size distributed by the SAR products.

Single Look Complex (SLC) and Ground Range Detected (GRD) are the two main types of products available for Sentinel-1 data, for which the important characteristics are reported in Table 2.4.

Table 2.4: Sentinel-1 Interferometric Wide (IW) swath mode SLC and GRD product characteristics. *rg* stands for range and *az* for azimuth. ENL stands for Equivalent Number of Looks.

Product	Wavelenght	Frequency	Swath	Incidence angle	Polarizations	Resolution (rg×az)	Pixel spacing (rg×az)	ENL
IW-SLC	5.6 cm	5.405 GHz	250 km	29.1° - 46.0°	VV, VH	3.1 × 22 m	2.3 × 14.1 m	1
IW-GRD						20 × 22 m	10 × 10 m	4.4

SLC product consists of focused (*i.e.*, processing of azimuth and range signals to form an image) SAR data, geo-referenced using orbit and attitude data from the satellite. SLC products are in slant-range geometry, defined as the line-of-sight from the sensor to each reflecting object. The full spatial resolution is provided (single look) and complex signals (real and imaginary parts) preserving the phase information are available.

GRD product also consists of focused SAR data but only provides backscatter magnitude and the phase information is lost. GRD products are projected to ground range, *i.e.*, onto the ellipsoid of the Earth and multi-looked (averaging in the spatial domain). Consequently, GRD products of Sentinel-1 have approximately square pixel spacing (10 m). While the speckle effect is reduced by multi-looking from which the Equivalent Number of Looks (ENL) is calculated, *resolution* and *pixel spacing* are lower than for SLC products.

Since amplitude and phase are distinct information, both SLC and GRD products of Sentinel-1 are exploited. Table 2.5 shows the number of images for ascending and descending orbits, gathered for the different study areas. The agricultural seasons considered with Sentinel-1 imagery are the same as for optical imagery (Table2.2).

Table 2.5: Description of Sentinel-1 acquisitions used over the study areas. For each area, both GRD and SLC products are exploited.

Area name	Tile	Asc. orbits images	Des. orbits images	Total images	SLC / GRD
Mâcon	T31TFM	60	60	120	✓/ ✓
Toulouse	T31TCJ/CH	71	71	142	✓/ ✓
Western-area	T30TXS	69	69	138	✓/ ✓
	T30TXT	69	69	138	✓/ ✓
	T30TWT	69	69	138	✓/ ✓
Northern-area	T31UDQ	64	64	128	✓/ ✓
	T31UEQ	64	64	128	✓/ ✓

2.3 Reference and ancillary datasets

2.3.1 Land Parcel Identification System

Within the framework of the Common Agricultural Policy (CAP), the Land Parcel Identification System (LPIS) is a core component of the Integrated Administration and Control System used for the payment of subsidies. The LPIS spatially registers agricultural parcels with several attributes such as its size, precise location, and a unique identifier. In particular, farmers are asked each year to provide the main crop grown on their parcel, which is associated to a certain code. The Registre Parcellaire Graphique (RPG), the French LPIS, is produced annually and made available after anonymization by the Institut National de l'Information Géographique et Forestière (IGN) on the basis of data produced by the Agence des Services et des Paiements (ASP).

2.3.1.1 Grasslands

The RPG defines several codes for grassland or fodder crops associated to grassland, *i.e.*, that have a similar cover and provisioning service. The differences between grassland types are made mainly according to two criteria, the agronomic criterion and the temporal criterion, which is defined by the time since the grassland has not been converted to another crop. Four grassland meta-classes can be defined from administrative declarations, each meta-class regrouping several declarative codes (see Appendix 6.2 for details):

- **Permanent grassland or pasture (PM)** refers to parcels with predominantly herbaceous cover in place for five or more years. Three cover types are further differentiated: (i) permanent grasslands, that are grasslands with little or no woody forage resource; (ii) grasslands which occur in long rotation schemes but are in place since at least five years; (iii) that are herbaceous pastoral areas (such as moors or summer and alpine pastures) where grass is the main cover.
  RPG codes: PPH, PRL, SPH.
- **Temporary grassy areas (TG)** are grasslands seeded since less than five years, composed mainly of grass cover such as ryegrass, orchardgrass, borage, bromegrass, or fescue in pure composition or in mixtures.
  RPG codes: BRH, BRO, CRA, DTY, FET, FLO, PAT, PCL, RGA, XFE, GFP, MLG, PTR.
- **Fallow land (FA)** are land left without sowing and where the grassy resource is present. A distinction of several fallow land types is made trough the duration of its presence.
  RPG codes: J5M, J6P, J6S.
- **Forage legumes (FL)** are assimilated to highly productive grasslands with similar management practices, including agronomic varieties such as alfalfa, clover, or sainfoin.
  RPG codes: FFO, JOS, LFH, LFP, LUZ, MEL, PFH, PFP, SAI, SER, TRE, VES.

While the fallow land (FA) and forage legumes (FL) meta-classes have clear agronomic distinctions, the two meta-classes of permanent (PM) and temporary (TG) grasslands may share some similarities. In theory, TG can be associated with more productive varieties and consequently increased exploitation in contrast to PM that are more related to extensive farming. Thus different phenologies should be observed on both meta-classes. Nevertheless, RPG codes related to one or the other meta-classes are solely distinguished based on the length of time the grassland has been established (*i.e.*, more or less than five years). While older grasslands (PM) are eligible to certain subsidies, this implies certain constraints. For example, it has been noticed that the ratio of permanent grassland must be maintained within the framework of the CAP. As a result, some temporary grasslands older than five years are not declared as permanent to alleviate the constraints on their exploitation. The RPG codes associated with permanent and temporary grasslands, both of which are the predominantly reported grassland areas, therefore do not allow a strict distinction of agronomic type or associated management practices.

The four grassland meta-classes constitute the further exploited grassland dataset. Grassland locations for the selected RPG codes are subsequently retrieved from the RPG. Figure 2.1 shows the description of grassland parcels extracted from the RPG for Mâcon and Toulouse areas as well as for the two Western- and Norther-areas. Table 2.6 reports the different grassland datasets obtained from the RPG for the seven areas. A total of 284,881 parcels are extracted covering 12,056 km^2 of grasslands. The sizes of the parcels are relatively similar among the areas, except for Toulouse, where very large pasture parcels are found in the Pyrenees. Permanent grasslands and pastures constitute approximately 75% of the grasslands in the Mâcon area. The remaining grasslands are mostly temporary grasslands with a very low number of fallow lands and forage legumes. These are more prevalent in the Toulouse area, accounting for about 25% of the surface area, with a consequently reduced number of permanent grasslands and pastures.

Table 2.6: Description of grassland datasets for the different study areas retrieved from the RPG. Information about grassland surfaces and their corresponding parcel sizes is provided. The proportion of different grassland types per area is visually given according to four main grasslands meta-classes defined from the RPG. PM= permanent grassland or pasture; TG= temporary grassy area; FA= fallow land; FL= forage legumes.

Tile	Grasslands parcels	Total grasslands surface (km²)	Parcels size (ha)				Meta-classes
			Min	Max	Mean	Median	PM TG FA FL
- Main areas							
T31TFM	27,832	1,275	0.89	87.32	4.58	3.22	
T31TCJ/CH	50,103	2,758	0.88	1,733	5.5	2.66	
- Add. areas							
T30TXS	52,352	1,985	0.88	240.8	3.79	2.8	
T30TXT	84,757	3,254	0.87	124.55	3.84	2.92	
T30TWT	43,559	1,647	0.88	159.26	3.78	2.78	
T31UDQ	14,279	583	0.3	92.14	4.08	2.71	
T31UEQ	11,999	554	0.91	70.4	4.62	3.04	

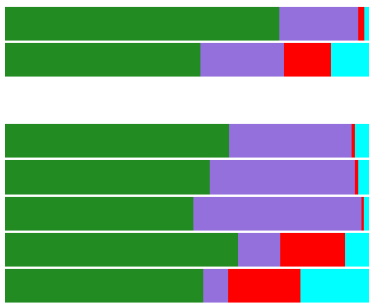

2.3.1.2 Further vegetation surfaces

Monitoring the status and evolution of vegetation surfaces are not solely required for grassland areas. Accordingly, the methodologies proposed in this work aiming the reconstruction of dense time series are studied on other vegetation data sets. In addition to the grassland datasets, two other common vegetation classes are studied for both Mâcon and Toulouse areas. Two additional datasets, as for grasslands, are subsequently constructed (see Appendix 6.2 for details):

- The crops dataset, which is composed of the three major cereals cultivated throughout Mâcon and Toulouse areas: maize, winter wheat and winter barley.
- The forests dataset, that includes different species of closed-canopy deciduous and coniferous forests. The resulting datasets contain 11 forest subclasses for both studied areas.

Crops have more pronounced phenologies than grasslands, generally modeled by a logistic function during growth, a plateau, and a single decrease at harvest (Zhang et al., 2003; Beck et al., 2006; Salinero-Delgado et al., 2022). Forests, apart in silviculture schemes, and abrupt changes such as fires, are not influenced by human activities. Therefore, they have relatively stable phenologies throughout the season, depending on the deciduous or evergreen coniferous species for example. Depicted by different phenologies, the study of crops and forests alongside grasslands will be proposed in experiments of Chapter 4.

Polygons describing crop parcel boundaries are, likewise grasslands retrieved from the RPG. Concerning forests, the French database BD FORET (IGN, 2021) is used. It delineates forest areas and provides semantic information on the dominant species. For this database, only polygons having sizes ranging from 4 to 50 hectares are considered. This consideration permits to balance the size of the forest polygons with respect to the grassland and crop ones. Information about crop and forest datasets with a recall about grassland for comparison, are given for Mâcon and Toulouse in Table 2.7.

Besides taking into account the three vegetation classes datasets separately, a supplementary multi-class dataset is constructed merging the three (grassland, crops and forest) vegetation datasets. The total number of parcels of the two multi-class datasets constructed for Mâcon and Toulouse areas is given in Table 2.7 (*Total polygons*). The multi-class datasets will help to assess the generalization performances of the proposed

methodology. It will also support to investigate possible improvements regarding the use of larger datasets as reference data.

Table 2.7: Spatial statistics for grassland, crops, and forest polygons, which are obtained for Mâcon and Toulouse areas. The subsequent additional merging into multi-class datasets results in a total number of polygons of 46, 001 and 98, 203 for Mâcon and Toulouse, respectively.

Area	**Class**	**Polygons**	**Total surface**	**Parcels size (ha)**				**Total**
			(km^2)	Min	Max	Mean	Median	**polygons**
Mâcon	Grasslands	27,832	1,274.9	0.89	87.32	4.58	3.22	46,001
	Crops	12,557	594.9	0.88	52.02	4.74	3.53	
	Forests	5,612	579.2	3.01	49.89	10.33	6.84	
Toulouse	Grasslands	50,103	2,758	0.88	1,733	5.5	2.66	98,203
	Crops	34,504	1,870.4	0.89	82.06	5.42	3.82	
	Forests	13,596	1,177.4	3.01	39.79	8.66	6.03	

2.3.2 Ancillary data

Non-Agricultural Surfaces (SNA)

Grasslands often contain non-agricultural elements within the boundaries extracted from the RPG. In fact, grasslands are often located in areas less suitable for crops, such as mountainous areas, parcels with limited access or complex shapes. These non-agricultural elements are not associated with the grassland phenology and can lead to mixed pixels. Mixed pixels are characterized by distinct surfaces and mixed spectral signatures. Non-agricultural elements regroup several surfaces that can be artificial (roads, paths, buildings,...), natural vegetation (trees, forests, brushes,...), or natural non-vegetation (ponds, rock formations,...).

Some of these elements are informed by the farmers during the CAP declaration and are later post-processed and complemented by IGN. The dataset *Non Agricultural Areas* (Surfaces Non-Agricoles, referred to in the following as SNA) is gathered for each study area and used to locate the non-agricultural surfaces within the RPG parcels. These elements are subsequently excluded from the grassland parcel boundaries. This greatly reduces the potential mixed pixels.

Figure 2.3 illustrates an area of the RPG that provides color-coded information on the cultivated species of each parcel (Figure 2.3a). The SNA of the corresponding area is shown in Figure 2.3b. Grassland parcels are extracted and the SNA is superimposed (Figure 2.3c), allowing to discard the non-agricultural areas from their boundaries.

Digital Terrain Model

Topographic data are retrieved with 5×5 m spatial resolution Digital Terrain Models (DTMs) from the very high resolution height layer provided in the RGE ALTI acquired by IGN. This DTM is multi-source (lidar, radar and aerial photography dense matching) and its altimetric accuracy therefore varies from 0.2 m to 7 m depending on the data source. The use of a DTM must be considered hereafter on the one hand to differentiate grasslands according to their topographic characteristics (Nasrallah et al., 2019) but also for geometric corrections related to the adoption of SAR images (Section 1.2.1.2). The DTMs of the main study areas are visible in Figure 2.4, superimposed by the major water network for visualization. The Mâcon area has elevations ranging from 173 m in the Western part along the water network to 1,295 m in the Southeastern part. For the Toulouse area, the altitudes range from 68 m in the Northern plains to 3,127 m (Pique d'Estats) in the summit of the French Pyrénées.

Figure 2.3: (a): Agricultural parcels describing cropland and grassland surfaces retrieved from the RPG; (b) Non-agricultural surfaces (SNA); (c) Final grasslands extent, after SNA subtraction.

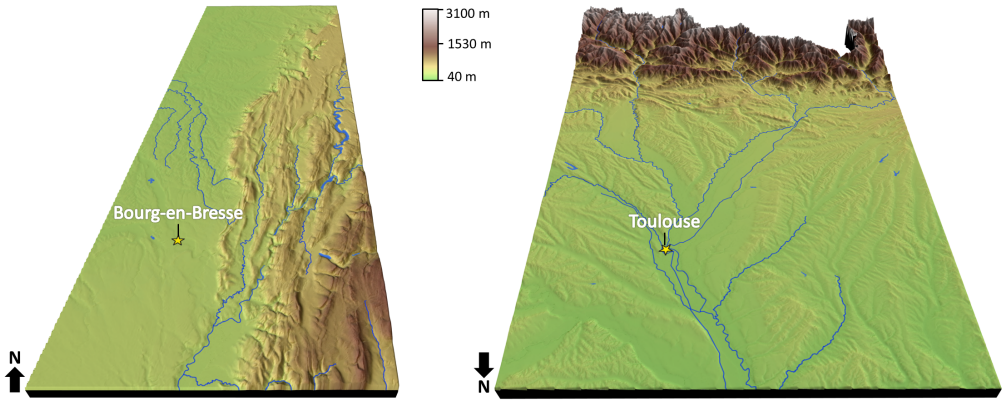

Figure 2.4: Digital Terrain Models (DEMs) with 5 m spatial high resolution of the two main study areas (Mâcon and Toulouse areas respectively, left and right). The altitudes range from 40 m to 3127 m.

Weather data

Climate data are extracted from the Météo France SAFRAN-ISBA dataset (Quintana-Seguí et al., 2008; Vidal et al., 2010). This dataset gathers measurements from several hundreds of climate stations of the French national meteorological service. The dataset provides daily aggregated measurements of 25 climatic variables. The available variables are (for some acquired on the ground and others at 1 m altitude): liquid precipitation, solid precipitation, total precipitation, effective rainfall, daily mean temperature, minimum/maximum of 24 hourly temperatures, daily mean wind speed, atmospheric radiation, visible radiation, actual evaporation, potential evapotranspiration, specific humidity, relative humidity, soil moisture index, drainage, runoff, liquid water content in root layer, solid water content in root layer, snow-pack water equivalent, snow-pack thickness, fraction of mesh covered by snow and snow-pack base runoff.

The gathered dataset uses a point grid evenly spaced 8 km apart as spatial sampling. Each point gathers data which is spatially interpolated from the nearest meteorological station. The large number of climate stations allows to ensure data variability despite the low spatial resolution of the grid. An example of the climate variables, daily temperature and precipitation, is given via climographs for the two main study areas in Figure 2.5. The climate datasets obtained over the studied areas have potentially two applications, similar to the use of topographic data. Depending on the agronomic variety, a grassland's phenology will, at least partially, vary according to the climate. The use of climate variables may in this case, help to differentiate

between agronomic types and geographical areas. The use of a DTM aims at describing and processing the geometry of SAR images. In the case of climate data, their use must allow to constrain or explain the differences observed in SAR radiometry (Vreugdenhil et al., 2018). In particular, humidity-related variables should help to explain SAR fluctuations that are sensitive to surface properties (Section 1.2.1.2).

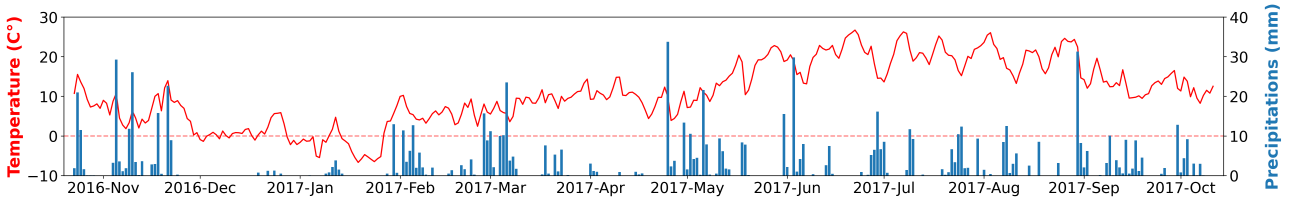

(a) Mâcon

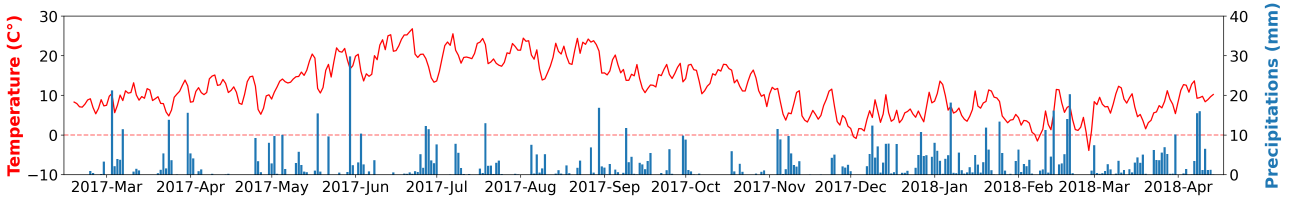

(b) Toulouse

Figure 2.5: Average climographs (temperature and precipitations) obtained for the two main study areas during the studied periods.

2.4 Features derived from Sentinel images for grassland monitoring

High-level description of the satellite images can be extracted by the calculation of features. In this work, handcrafted features are computed to provide useful information for grassland monitoring by exploiting the content of the original Sentinel-2 and Sentinel-1 images. From optical imagery, the well-known Normalized Difference Vegetation Index (NDVI) is retained. In the case of Sentinel-1 images, two features are considered for grassland monitoring. The first is the backscatter coefficient computed from GRD products and the second is the coherence computed from SLC products. The different features exploited in the experiments of this manuscript are detailed hereafter.

2.4.1 Normalized Difference Vegetation Index

The red edge portion of the electromagnetic spectrum was shown to have a significant correlation with chlorophyll content and leaf structures (Section 1.2.1.1). Vegetation indexes exploiting red edge portions are therefore preferred for temporal monitoring of grasslands and detection of management practices. The NDVI (Rouse et al., 1974; Tucker, 1979) has been previously mentioned, being one of the first indexes developed from satellite remote sensing data. More importantly, it is by far the most widely used vegetation index (Xue and Su, 2017; Ali et al., 2014; Gao et al., 2016; Fern et al., 2018; Griffiths et al., 2019; Clementini et al., 2020; Reinermann et al., 2021). Besides, the interest of NDVI as a reliable indicator for monitoring vegetation and grasslands has been demonstrated. NDVI is calculated as follows:

$$\mathrm{NDVI} = \frac{\rho_{\mathrm{NIR}} - \rho_{\mathrm{Red}}}{\rho_{\mathrm{NIR}} + \rho_{\mathrm{Red}}} \quad , \qquad -1 \leqslant \mathrm{NDVI} \leqslant 1 \tag{2.1}$$

with ρ_{NIR} the reflectance in the near infrared and ρ_{Red} the red reflectance, respectively, B8 and B4 bands

of Sentinel-2 satellites. NDVI normalizes the leaf structure, chlorophyll scattering and absorption effects taking place in the red and near-infrared wavelengths. Negative NDVI values typically approaching -1 correspond to water surfaces. Barren areas of rock, sand or snow show very low NDVI values, generally ranging in $[-0.1, 0.1]$. NDVI over vegetation has values above 0.2, increasing with the vegetation's activity. Peak growth of vegetation potentially reaches values close to 1.

Figure 2.6 shows the yearly NDVI evolution of a permanent grassland of the Mâcon area. The displayed NDVI is the average of all pixels within the parcels boundaries. This parcel appears to be very lightly exploited with a high and stable NDVI level throughout the year. NDVI analysis allows the deduction that this parcel has probably not been mowed or ploughed during this agricultural season, but was rather extensively grazed or not exploited at all.

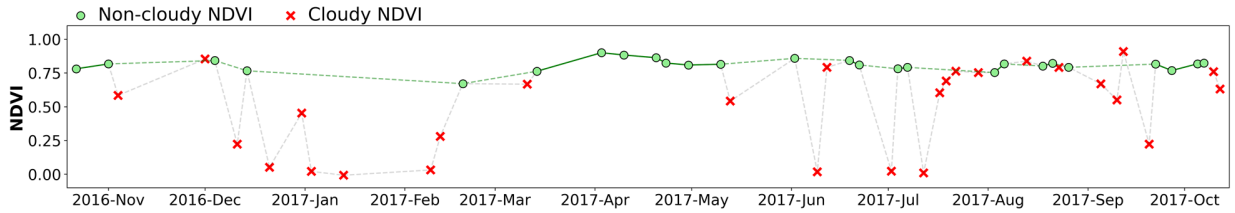

Figure 2.6: NDVI temporal evolution over a permanent grassland of the Mâcon area. The stability of NDVI throughout the agricultural season indicates a parcel that is not or very extensively farmed. Green dots indicate a valid non-cloudy acquisitions whereas red crosses indicate an acquisition flagged as cloudy by the masks.

The temporal variation of NDVI on a alfalfa parcel shown in Figure 2.7 illustrates the ability of NDVI to capture fluctuations in vegetation evolution. Sentinel-2 images over this parcel are provided at some key stages of the vegetation's phenology. This parcel contains several phenological cycles within the same agricultural season. These cycles are close together over a short period of time where the parcel successively exhibits high and low NDVI values. Despite the numerous missing data due to clouds denoted by the red crosses, valid acquisitions allow to observe sudden drops exceeding 0.3 of NDVI. These rapid and abrupt decreases clearly indicate a change in vegetation status that can be easily related to human intervention. Mowing events are thus detected, evidenced by the Sentinel-2 optical imagery corresponding to the dates of change.

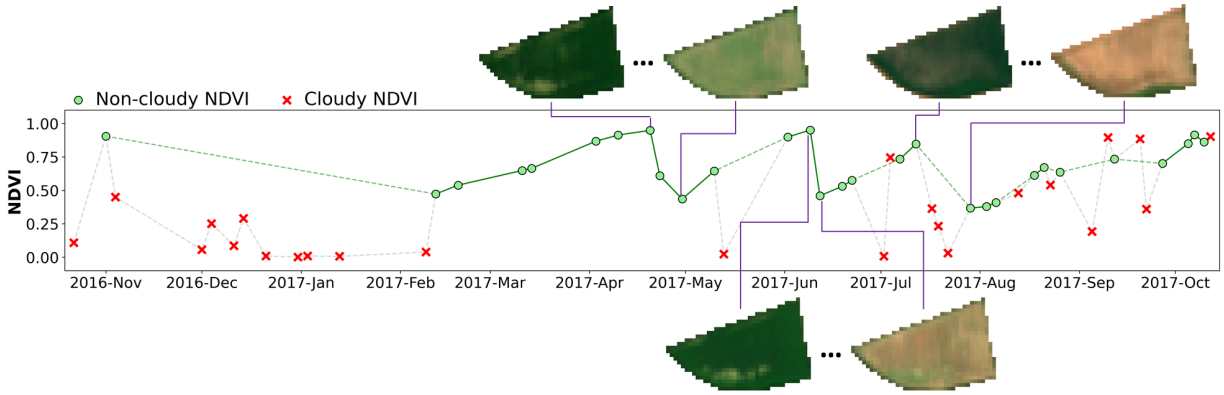

Figure 2.7: NDVI temporal evolution over an intensively exploited alfalfa parcel of the Mâcon area. Sudden NDVI drops correspond to management practices which is attested by the visualization of Sentinel-2 images over the parcel.

A possible shortcoming of NDVI is its tendency to saturate (*i.e.*, no longer reflects variation) once the cover

is spatially very dense. For a minority of grasslands whose agronomic type implies a very dense cover and which are generally highly productive and intensively exploited, NDVI can become saturated. Nevertheless, several factors advocate for the use of NDVI in this work:

(i) its availability for almost all optical sensors, as its calculation relies on two widely used spectral bands;

(ii) its prominence in the literature, helping to provide extensive examples of NDVI behavior related to vegetation;

(iii) its simplicity, on the contrary of other optical derived features whose computation incorporate interpolations or constants related to the observed surface, such as the LAI. This simplicity minimizes the potential sources of errors and uncertainties in the measurements. For operational studies, simplicity also means explainability;

(iv) finally, the illustrated examples allowed us to demonstrate the satisfactory capacity of the NDVI to characterize the phenology of grasslands.

2.4.2 Backscattering coefficient

A SAR sensor records the echo received from the emitted pulse through a digital number (DN). The value of the DN is proportional to the emitted energy and system properties, to the radar cross-section (RCS) of the target and thus to the incoming energy. The RCS is defined as the scaled ratio of the scattered power to the incident power per unit area, as if the radiation were isotropic. The RCS therefore broadly refers to the target reflectivity. As the RCS will depend, among others, on the form and the composition of the target, its variations will allow to discriminate surfaces. To compare DN from several sensors or between acquisitions, radiometric calibrations are commonly performed. The Beta naught calibration scales the DN with system characteristics and is called radar brightness (Raney et al., 1994; Rudant and Frison, 2019; Schmidt et al., 2020):

$$\beta^0 = \frac{DN^2}{k_s}\,, \tag{2.2}$$

with k_s a sensor-specific calibration constant provided through look-up-tables alongside acquisitions. The area normalization of β^0 is aligned with the sensor's acquisition geometry (*i.e.*, slant range). In order to deal with consistent spatially areas, the normalization can be aligned with the ground range plane (Atwood et al., 2012). The radar cross-section or backscattering coefficient, Sigma naught (Sigma^0 or σ^0), is extensively adopted to normalize DN into an area of one square meter on the ground:

$$\sigma^0 = \beta^0 \cdot \sin(\theta_{iloc})\,, \tag{2.3}$$

with θ_{iloc} the incidence angle of the incoming beam with respect to the ground as modeled by an ellipsoidal Earth model. Sigma^0 is usually expressed in decibels (dB), which modifies the initial distribution to stretch out the low values variations that are usually associated with natural landscapes:

$$\sigma^0 dB = 10 \cdot \log_{10}(\sigma^0)\,, \tag{2.4}$$

Backscattering coefficient over a vegetation surface first varies according to SAR system characteristics, which are previously known (Table 2.4). The different polarizations and beam incidence angles, for example, will allow distinct geometric interactions with the observed vegetation. Most importantly, the frequency

band used by the sensor will imply a varying contribution of vegetation biomass, structure and ground conditions to the backscattering coefficient. C-band wavelengths such as the ones used by Sentinel-1 penetrates the vegetation's canopy of most agricultural surfaces, making ground's contribution significant. Vegetation contribution due to volume scattering will increase with vegetation's leaf orientations, sizes, density, and, correlatively, water content. Potentially, the backscattering coefficient will thus vary with the species and its phenology. The increase of vegetation will gradually attenuate the contribution of the ground. Nonetheless, grasslands often feature low cover heights, *i.e.*, compared to most crops for example, and do not have a strong vertical structure. This will allow ground contribution to the backscatter coefficient to remain important. The ground contribution to the backscatter coefficient also fluctuates over time, as a function of soil moisture, surface roughness or local terrain topography (McNairn and Brisco, 2004; Veloso et al., 2017).

Figure 2.8 illustrates both σ^0_{VV} and σ^0_{VH} polarization time series of the previously observed permanent grassland of Figure 2.6. Using NDVI time series, it was observed that the vegetation remained stable during the entire agricultural season and that no management practice was made. The temporal dynamic of backscattering coefficient (σ^0) is substantially different. Strong temporal instability affects the time series and a magnitude of about 4 dB for both polarizations is observed.

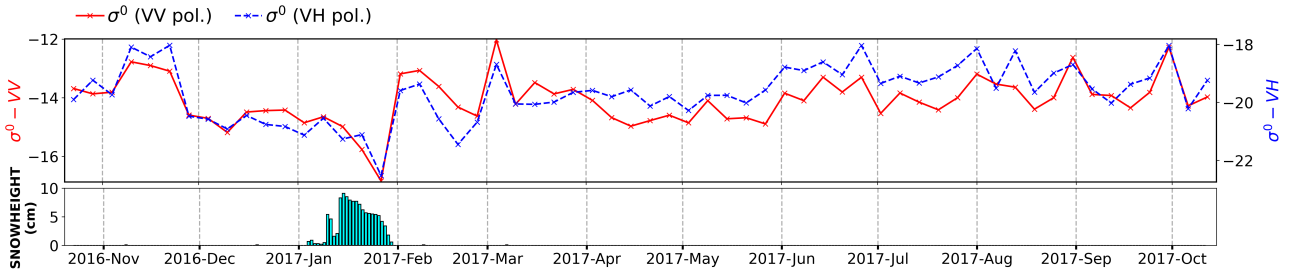

Figure 2.8: Average σ^0_{VV} and σ^0_{VH} time series over the Mâcon permanent grassland already observed in Figure 2.6. The temporal variations of both σ^0 polarizations are greatly fluctuating over short time intervals and do not allows us to characterize the phenological curve pattern. The fluctuations of σ^0 due to the snow cover are visible during the month of January.

The discordance between a stable NDVI time series and a highly fluctuating backscatter coefficient can be explained by relevant climate variables (Section 2.3.2). Snow cover over the parcel is shown by blue bars in the lower part of Figure 2.8. It is observed that the strong drops in both polarizations visible in January are correlated to the snow cover. During the time snow covers the parcel, the backscattering coefficient reaches a minimum at -16.7 dB and -22.2 dB for VV and VH polarizations, respectively. The drastic drops in the backscattering coefficient time series, which should remain stable as observed with NDVI, are explained by the appearance and subsequent melting of up to 10 cm of snow cover. Backscattering coefficient of snow decreases with increasing liquid water content due to the high dielectric loss of water which affects the penetration depth capacity of the wave. This is why, during the snowfall itself in mid-January, the signal remained relatively unaffected. It is dominated by volume scattering as the wavelengths used allow the signal to pass through the snow cover (Nagler et al., 2016; Tsai et al., 2019). The melting occurring in the second half of January increased water content leading to the observed decrease of backscattering coefficients. While the effects induced by snow cover as illustrated in Figure 2.8 are particularly significant, the same artifacts can be consecutive to frost, or much more frequently, to rain (El Hajj et al., 2019). Wet soils for example, may affect the backscatter signal up to several days after precipitations, increasing significantly the backscattering coefficients. On the contrary, intense rains leading to stagnant water may decrease considerably the backscattering coefficients. Climatic data are therefore useful to help explaining the temporal fluctuations observed in the time series.

The study of the backscattering coefficients is also proposed for the same alfalfa parcel shown in Figure 2.7. Previously, three consecutive mowings have been identified by observing NDVI time series. The

backscattering coefficient time series are shown in Figure 2.9.

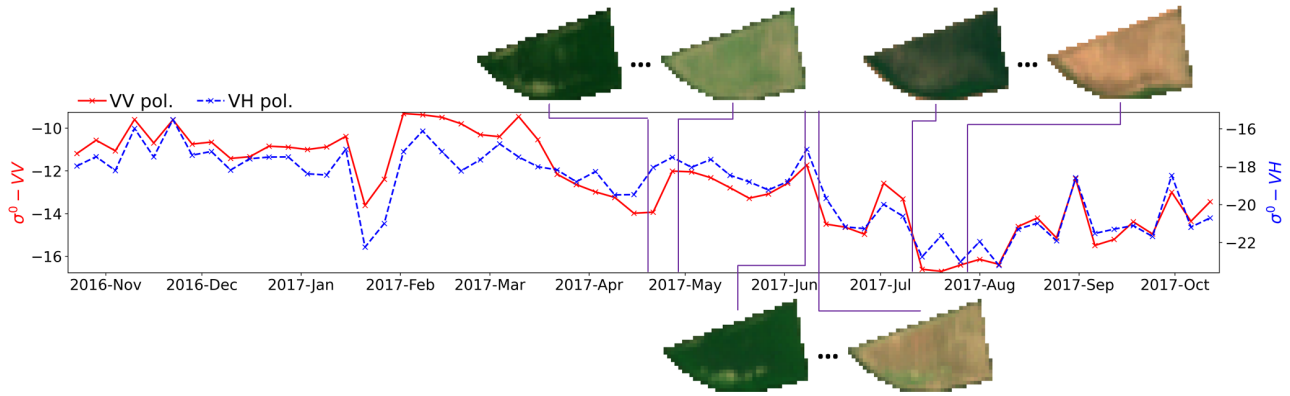

Figure 2.9: Average σ^0_{VV} and σ^0_{VH} time series over an alfalfa grassland from the Mâcon area, already observed in Figure 2.7. The σ^0 temporal variation does not allow us the characterization of the grassland phenology evolution nor the detection of management practices.

Figure 2.9 allows us to observe that both polarizations provide hardly interpretable time series with respect to phenology or mowing related vegetation changes. The slope change with the highest magnitude coincides with the snow event previously observed in January in Figure 2.8.

For the three mowings, different behaviors are observed for both polarizations. The backscatter coefficients increases during the first mowing but decreases during the two following ones. Several works have reported notable changes in the backscatter coefficient time series during crop harvesting or parcel plowing (Meroni et al., 2021; Van Tricht et al., 2018; Veloso et al., 2017; Vreugdenhil et al., 2018). Depending on the considered species and used polarization, increases, decreases or both successively have been observed. Nevertheless, the variety of grassland management practices and their influence on the canopy results in a significant diversity of backscatter coefficient responses. For example, the first mowing observed on the alfalfa parcel at the end of April increases the backscattering coefficient as a response to higher soil surface roughness. The two following mowings are short, and a slight tillage of the soil could be done. In these cases, the slight tillage implies a reduced surface roughness which results in a decrease of the backscatter coefficient. These differences in behavior, coupled with the significant impact of weather conditions, make the overall interpretation of the backscattering coefficient challenging.

2.4.3 Interferometric coherence

The interferometric coherence module, called coherence or γ, estimates the complex correlation in amplitude and phase on a local neighborhood of N×N pixels between two different SAR acquisitions. Coherence evaluates the temporal stability of the surface and provides a ratio between coherent and incoherent summations (Touzi et al., 1999; Tamm et al., 2016; Mestre-Quereda et al., 2020):

$$\gamma = \frac{|\langle T_i T_j^* \rangle|}{\sqrt{\langle T_i T_i^* \rangle \langle T_j T_j^* \rangle}} \quad , \qquad 0 \leqslant \gamma \leqslant 1 \tag{2.5}$$

where T_i and T_j are two complex SAR images, $|\cdot|$ denotes the absolute value, $\langle \cdot \rangle$ denotes the averaging operation done over range and azimuth pixels and the superscript * denotes the complex conjugate product.

Coherence is a product of several decorrelation sources that can occur between the two T_i and T_j acquisitions or from computation parameters:

$$\gamma_{overall} = \gamma_{temporal} \cdot \gamma_{SNR} \cdot \gamma_{param} \cdot \gamma_{others}\,, \tag{2.6}$$

where $\gamma_{temporal}$ corresponds to the temporal decorrelation. System-related noises are depicted by γ_{SNR}, γ_{param} relates spatial averaging operations that depends on the local neighborhood window size selected and the resulting ENL, and γ_{others} to potential orbital or data processing errors. In this work, the temporal decorrelation factor is the most important as it provides information about the vegetation's evolution. The window size selected for the coherence calculation will also influence its capability to discriminate values in low coherence areas, with increased smoothing through bigger window sizes. Apart from temporal decorrelation and window size, the additional decorrelation sources, although potentially having an impact, will not be considered or discussed in the following.

Coherence value varies between 0 and 1. Coherence theoretically reaches 1 if the position and physical properties of all elementary scatterers within the $\langle\cdot\rangle$ window are strictly identical between the two acquisitions T_1 and T_2. Man-made structures, for example, typically exhibit high coherence values as remaining stable over time. Changes in position and physical properties of the elementary scatterers between the two images will decrease the coherence towards 0, roughly proportionally to the importance of the change.

Over grasslands, likewise for the backscatter coefficient, coherence values will depend on the condition of the canopy and ground. The growth of vegetation, because the pattern and condition of the canopy differ from date to date, will cause temporal decorrelation and lower values. As the centimeter wavelength as the one used by Sentinel-1 allows the interaction with elements having larger or similar size, the pattern generated by individual grass blades can be a source of temporal decorrelation. Furthermore, rain, air temperature or wind, influencing both vegetation and ground surfaces will also affect the coherence values. Thus, coherence values over vegetation can be very sensitive to a wide range of factors which are hardly predictable.

The NDVI (Figure 2.6) and the backscattering coefficient (Figure 2.8) have already been studied over a permanent grassland parcel. Figure 2.10 illustrates coherence time series of both polarizations over the same parcel, computed with a window size of 9×3 for range and azimuth, respectively. Relatively low coherence values are observed, but the time series appear relatively stable. This stability is similar as the one observed with NDVI. As observed with backscattering coefficient, the relatively large drop in coherence in January is due to snowfall. Nevertheless, comparing with backscattering coefficient, coherence time series are more stable. This is notably due to the spatial averaging and temporal smoothing by encompassing two dates in its calculation.

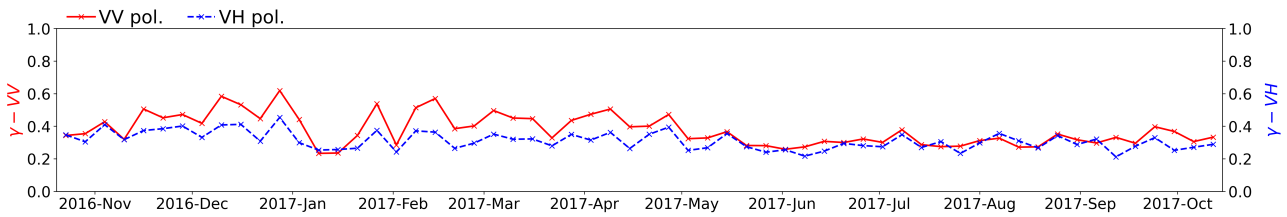

Figure 2.10: Average γ_{VV} and γ_{VH} time series over the permanent grassland already observed in Figure 2.6. The little temporal variations are responsive to the dense but stable herbaceous cover observed on this parcel.

To assess the sensitivity of coherence to vegetation changes, the alfalfa parcel of Figure 2.7 and Figure 2.9 is also studied. Figure 2.11 illustrates the coherence time series of both polarizations over this parcel, which has been managed three times. Several works have already investigated the exploitation of coherence information

for studying management practices (Chiboub et al., 2019; De Vroey et al., 2021b; Schuster et al., 2011; Tamm et al., 2016; Voormansik et al., 2016).

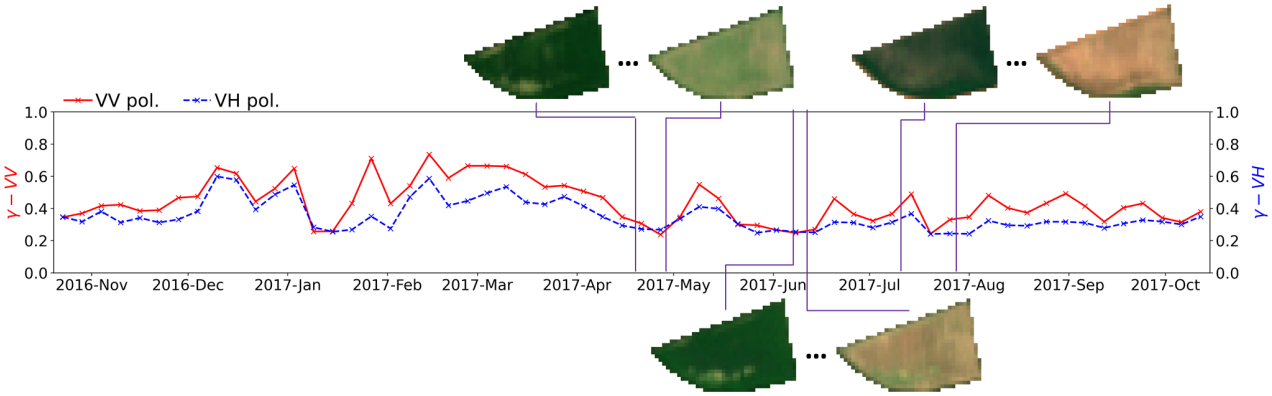

Figure 2.11: Average γ_{VV} and γ_{VH} time series over the Mâcon alfalfa grassland previously studied. Increased coherence values are observed after the three management practices. This is due to a high temporal stability of ground cover compared to vegetation.

The coherence values are computed by taking into account a time interval defined by two dates (T_i and T_j of Eq. 2.5). The management practices can occur in the middle of the used time interval (i) or before the first image T_i (ii). Considering these two situations, two different coherence responses can be expected:

(i) In this first case, the grassland is covered by an important vegetation in the T_i image. In contrast, the vegetation has been removed due to a management practice before the T_j image. Hence, a coherence decrease is expected due to temporal decorrelation, as T_i and T_j images depict different surfaces with a higher ground contribution from the T_j image.

(ii) In the second case, the T_i image already depicts a strong ground contribution due to the prior management practice. The T_j image also depicts a strong ground contribution. Provided that the grass does not regrow in-between, an increase of coherence is expected, considering the temporal stability of both T_i and T_j ground responses.

Both cases are induced by the management practices performed on the alfalfa parcel shown in Figure 2.11. The three management practices detected over this parcel lead to a first decrease of coherence (case (i)) due to the two different vegetation states of T_i and T_j, with high and low vegetation cover, respectively. This decrease is directly followed by an increase in coherence, expected as both T_i and T_j images observe a strong ground contribution (case (ii)). As with the backscattering coefficient, climatic conditions can also affect the coherence. Therefore, the fluctuations of coherence time series can not only be the consequence of management practices. Notably, the snow cover in January leads to the coherence increase. Without knowledge of this climatic event, the high frequencies of the signal could be interpreted as management practices.

As a result, coherence time series appear less fluctuating than backscattering coefficient time series and allow us to better characterize the vegetation phenology. Besides, it can help in the identification of management practices. However, it is shown that their interpretation requires to take into account multiple factors such as the temporal interval considered for coherence computation and the climate context.

2.5 Description of the feature engineering steps

The last section has shown how different features extracted from satellite and ancillary datasets can help to monitor the phenology of vegetation surfaces. This section presents the feature engineering steps performed on the data described in Section 2.2 and Section 2.3. The different steps aim to extract multiple sets of features for each polygon of the grasslands, crops and forests datasets (Table 2.7). Distinct types of features are proposed, considering the spatial and temporal characteristics of the datasets and the main goal of vegetation monitoring. Figure 2.12 illustrates some satellite features further used to describe the vegetation polygons.

► *Step 1: Exploiting reference polygon boundaries to define an object-level scale*

The RPG, BD FORET, and SNA are vector data providing information about the location of the different polygons (*i.e.*, grasslands, crops and forests) and the non-agricultural surfaces. In order to limit the integration of mixed pixels, two tasks are routinely performed on the different datasets. First, the RPG and BD FORET polygons are eroded by an internal buffer of 10 m, corresponding to the spatial resolution of Sentinel pixels. Secondly, the SNA has been used to remove non-agricultural objects within the RPG grassland polygons. A buffer of 5 m is applied on the polygonal and linear elements of the SNA, while a 10 m buffer is used for point elements (*e.g.*, trees). The resulting SNA layer is then subtracted from the RPG grassland polygons.

Eroded and filtered polygons of grasslands, crops and forests are subsequently exploited to define an object-level scale, *i.e.*, all spatial information gathered over a polygon is reduced as one single value describing the object. The object-oriented strategy is chosen for three reasons:

(i) the reference data permit the delineation of relatively homogeneous clusters (parcels). This reduces possible inconsistencies in spatial measurements (Atzberger, 2004) that may occur among the different reference and satellite datasets;

(ii) pixel-wise analysis would require further SAR processing to reduce speckle noise (Section 1.2.1.2), and would lead to adding additional parameters (*e.g.*, the window size and the used algorithm). The object-level approach allows its reduction through adopting spatial averaging;

(iii) the computational and storage challenges associated to the high data volume (Atzberger, 2013; Inglada et al., 2017; Mallet and Le Bris, 2020) can be reduced.

► *Step 2: Extracting optical features from Sentinel-2*

From the Sentinel-2 Level-2 images, the NDVI is calculated. Object-level statistics are next derived using the datasets obtained from the first step. The average NDVI for all the pixels of each polygon is calculated using the Orfeo Toolbox (OTB) library (Grizonnet et al., 2017) and the *Object Radiometric Statistics* remote module and bash scripting.

The Sentinel-2 images obtained in the study areas were associated with the two cloud & shadow and snow masks. Although the cloud & shadow masks can differentiate certain types of clouds depending on the detection methods (mono- and multi-temporal), the use of masks is done in the strictest possible way. The information contained on the two masks are merged, leading to define a validity mask. This merged information is referred to as *masks* in the followings. Object-level statistics are derived from the masks which are then converted to binary masks: "0" indicating no invalidity report from the two masks, while "1" indicates at least one pixel of the grassland is flagged as invalid by at least one of the two masks.

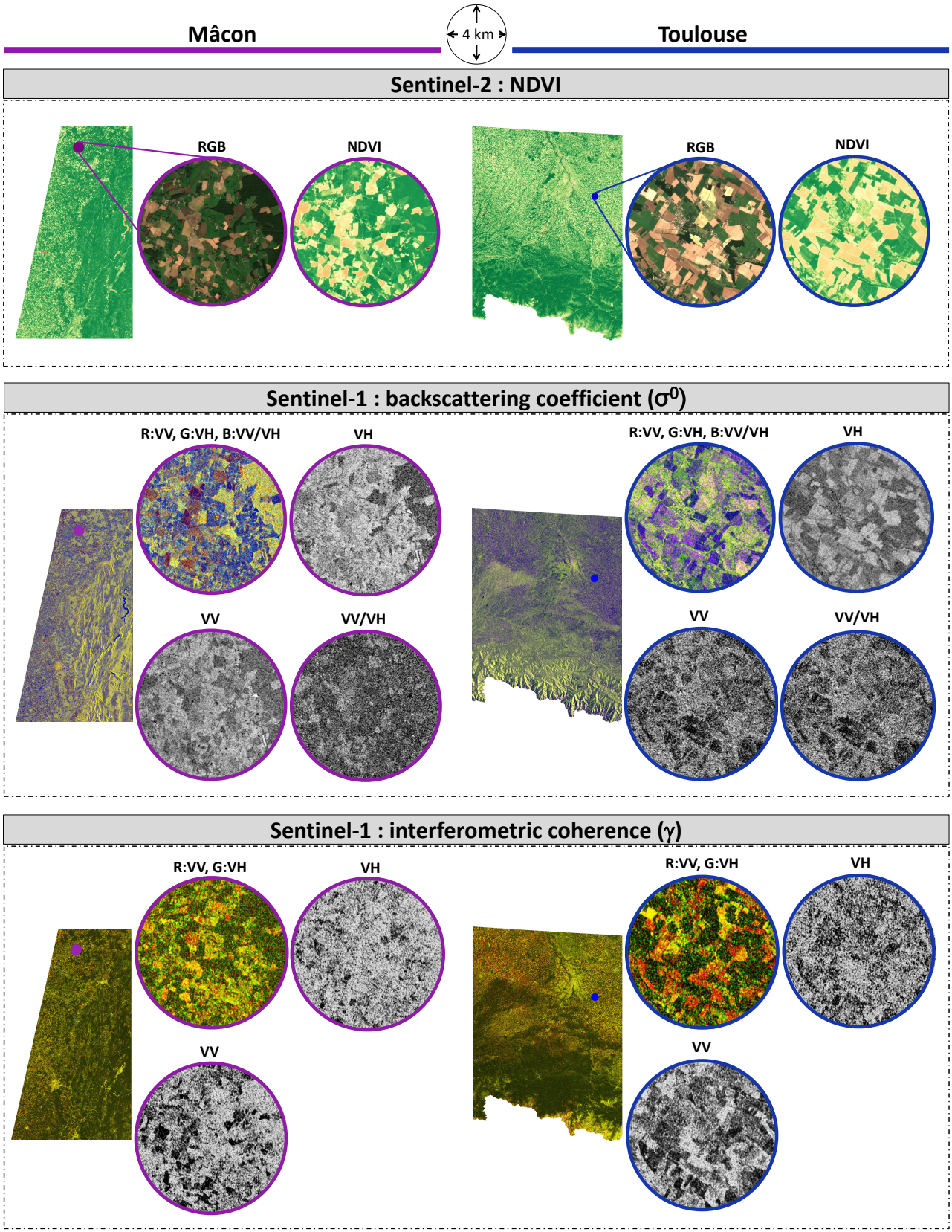

Figure 2.12: NDVI, backscattering coefficient (σ^0) and coherence (γ) images and 4 km diameter close-up containing grassland surfaces of Mâcon and Toulouse areas. RGB compositions are provided for visualization purposes.

Table 2.8: Summary of features computed at the polygon level from Sentinel-2 data.

Sentinel-2 features		
(1)	NDVI	mean values of the pixels belonging to each polygon.
(2)	Masks	boolean value indicating the presence or absence of clouds, shadows or snow.

► *Step 3: Extracting SAR features from Sentinel-1*

Sentinel-1 GRD and SLC images are processed using the freely accessible Sentinel Application Platform (SNAP) software and its command line Graph Processing Tool (GPT) option (ESA, 2021b). Ascending and Descending orbits are considered separately given the very different incidence angles of the two orbits. From GRD images, calibration to backscattering coefficient (σ^0) is performed followed by a sensor thermal noise removal, and a de-burst operation to produce an overlap between the different bursts acquired. Finally, a conversion from linear scale to dB is performed. Both σ^0_{VV} and σ^0_{VH} polarizations are selected. A cross-ratio band between σ^0_{VV} and σ^0_{VH} polarizations (VV/VH) is additionally calculated for each date. The interest of this cross-ratio band is its high correlation with vegetation biophysical parameters and its capability to somewhat mitigate topographic and climatic effects on the backscatter coefficient (Veloso et al., 2017; Vreugdenhil et al., 2020).

SLC images are processed in pairs. The two images of each pair are first back-geocoded together, *i.e.* spatial matching with sub-pixel accuracy. A bi-cubic interpolation and the Shuttle Radar Topographic Mission (SRTM) 1 DTM are used during the back-geocoding. The SRTM DTM is preferred to the higher resolution IGN DTM for two reasons. First, SRTM is acquired from a C-band similarly to Sentinel-1 images and thus features the approximately same surface penetration depth. Secondly, the spatial resolution of the IGN DTM is finer than that of Sentinel-1. An oversampling step to match the spatial resolutions would have been necessary. Following the back-geocoding step, coherence (γ) bands are calculated for both polarizations with a window size of 9×3 (range and azimuth, respectively) and deburst is performed. All images are then orthorectified using the Range Doppler Terrain Correction algorithm (Small and Schubert, 2019) and the SRTM 1 Arc-Second corresponding elevation data. Resulting images have an output spatial resolution of 10×10 m, matching the optical ones.

Object-level statistics are subsequently extracted for each date from the 3 backscattering coefficient σ^0 and 2 coherence γ bands. Two categories of features are further computed for each parcel. The first category describes the statistics computed on the different polarization bands and is denoted as (3) and (4) in Table 2.9. The statistics correspond to the mean, median, and standard deviation values calculated on the processed GRD and SLC images. These statistical descriptors are chosen to integrate measures of central tendency which are expected to provide distinct information on small populations such as the number of pixels in a parcel, as well as measure of dispersion. For each date, the resulting datasets contain 9 features describing the statistics of σ^0 bands and 6 features from the coherence bands.

The second category of Sentinel-1 features corresponds to the datasets (5) and (6) of the Table 2.9. These features provide information about the first-order derivatives computed on the time series considered in (3) and (4). The features in (5) describe the statistics previously computed with (3) and (4) for the first-order derivative between date t and date t_{-1}. In order to incorporate information about the polygon neighborhood, the set of features in (6) is also proposed. The feature set (6) contains then the average of features computed on (5) on a specific neighborhood. The polygon neighborhood is defined by all the polygons belonging to the same vegetation class inside a given empirically pre-defined radius of 2 km. The goal of features in (6) is to highlight if a specific polygon has a diverging behavior (due to management practices, climatic conditions or sensor noise) compared to its neighborhood (Ding et al., 2017).

Table 2.9: Summary of features computed at the polygon level from Sentinel-1 data.

Sentinel-1 features computed for ascending and descending orbits		
(3)	Sigma^0 dB	mean, median and standard deviation for VV, VH and VV/VH bands
(4)	Coherence	mean, median and standard deviation for VV and VH bands
(5)	Derivatives	first order derivative computed for the previous (3) and (4) mean features
(6)	Neighborhood	features in (5) are averaged on the polygon neighborhood within a specific radius

► *Step 4: Extracting features from ancillary data*

Alongside the altitude provided by the RGE Alti, two additional information are calculated: slopes and exposure. Mean and standard deviation values are computed from the height, slope, and exposure bands for each polygon. Furthermore, polygon shape features are also considered: area in hectares, perimeter and the number of Sentinel pixels. This provides information on the spatial context of the parcel, which may be different for small, productive parcels, or large, extensively farmed ones, for example.

For each Sentinel-1 acquisition date and the previous day, 25 climatic variables are collected. Information about the previous day of the acquisition is incorporated to take into account the morning schedule of some SAR acquisitions as well as rain accumulation. Additionally, two types of metadata information are stored. The first one concerns the temporal information of Sentinel's acquisitions converted to day of the year. Finally, the agronomic class from the RPG is attached to each polygon.

Table 2.10: Summary of features computed at the polygon level from ancillary data.

Ancillary and metadata features		
(7)	Topography	mean and standard deviation for height, slope, exposure; area, perimeter and parcel size
(8)	Climate	day of SAR acquisition and day before with 25 variables
(9)	Metadata	temporal distribution of satellite acquisition and RPG subclass

► *Step 5: Building a common temporal grid*

As Sentinel-1 and Sentinel-2 time series have different temporal grids, the definition of a common temporal grid is proposed. This new temporal grid must permit to statistically correlate the extracted Sentinel features to analyze their joint temporal evolution. Furthermore, irregular time series or with different sequence length (*i.e.*, with missing data) lead to additional challenges in automated processing.

Alternating ascending and descending orbits, SAR features from Sentinel-1 are obtained every 3 days. Sentinel-2 NDVI features, on the other hand, have a more irregular temporal sampling due to cloud coverage. Furthermore, the availability of only one satellite until June 2017 for the two main study areas, and, for Mâcon, a orbit overlap area, increases this irregularity. The definition of the common temporal grid is made by the utility of coupling an NDVI value with ascending and descending orbit SAR features. In this work, we propose the definition of a temporal grid keeping a 6 day interval. Based on the 3-day revisit of both Sentinel-1 orbits, the dates retained for the common temporal grid are in between the two temporal grids of the ascending and descending orbits. The resampling of features to the new common temporal grid follows the nearest neighbor approach. This method is generally considered simplistic and is discarded in favor of methods that take into account the trend of the signal. Methods such as polynomial methods, based on the Fourier Transform or auto-regressive methods (Lepot et al., 2017) are commonly adopted. Nevertheless, resampling is here only used for matching several temporal grids. As most of the methods extrapolate from the data and produce new values, the nearest neighbor approach was adopted as a method that preserves

the original dynamics of acquired values. For example, as significant changes can occur in the time series, particularly as a result of management practices, trend-based interpolation would alter the original magnitude of the variations observed. The nearest neighbor approach introduces a time lag in the resampling task but preserves the original values.

The resampling task is illustrated for Mâcon and Toulouse areas in Figure 2.13. As SAR features have a fixed and gap-free temporal grid, their association with the new dates of the common temporal grid is straightforward. To each date of the new temporal grid, descending and ascending orbit features of Sentinel-1 which are 1 day apart from the new dates, are gathered (blue lines of Figure 2.13). Regarding the resampling of Sentinel-2 features, the temporal nearest acquisition to the new date is selected (green lines in Figure 2.13). Because of the irregular temporal sampling of the Sentinel-2 original grid, some acquisitions are nevertheless resampled to several new dates of the common temporal grid. In some cases, especially when the full capacity of the Sentinel-2 constellation is obtained, the temporal sampling of Sentinel-2 is lower than the one of the common temporal grid. Hence, several Sentinel-2 acquisitions are associated with the same date of the common temporal grid (red lines of Figure 2.13). In this case, if one of the two observations is flagged as invalid, the other one is kept. If both are flagged as invalid, the one with the shortest temporal gap to the new date is kept. If both have the same temporal distance to the new date, the one with the lowest first order derivative to the previous valid NDVI observation is kept.

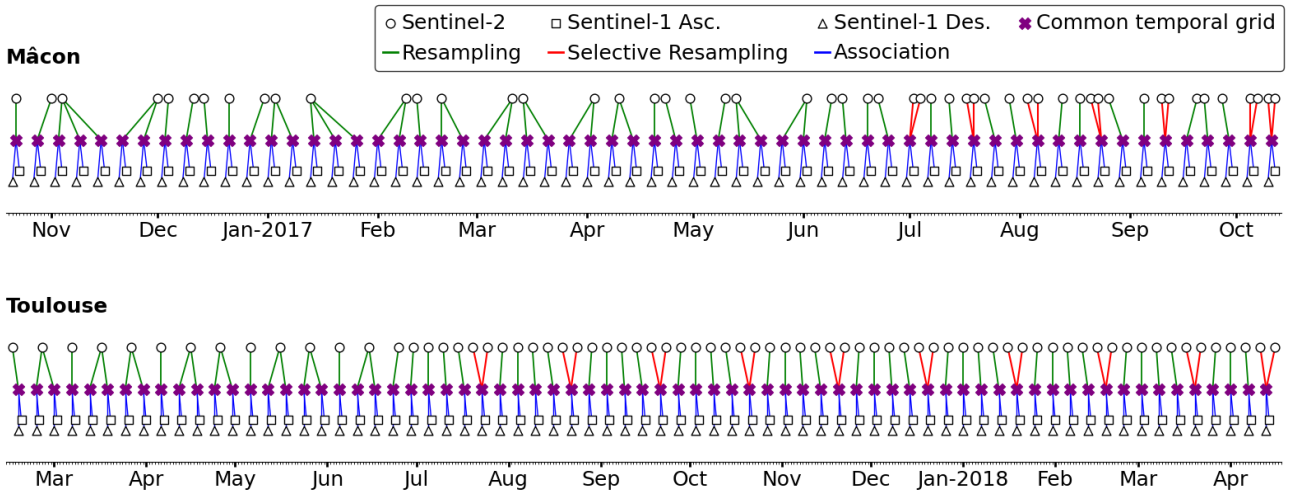

Figure 2.13: Description of the construction of a new common temporal grid allowing Sentinel-1 and Sentinel-2 features to be jointly observed. Having a more irregular temporal sampling, Sentinel-2 features are resampled by the nearest neighbor approach. When two Sentinel-2 acquisitions are close to the new resampled date (red lines), only one of both is kept. Sentinel-1 coming from ascending and descending orbits are associated to each date of the common temporal grid.

2.6 Exploring the relationships between derived satellite features

The previous subsections have shown that information coming from multiple sources could provide complementary knowledge. Nevertheless, several strengths and flaws have been identified for each of the extracted features (Section 2.4). In this manuscript, multi-modal satellite features will be considered to monitor grasslands as well as crops and forest vegetation. Thereby, it is proposed to assess the temporal correlation through statistical analysis between the extracted features.

The relation between optical (NDVI) and SAR features (backscattering coefficient and coherence) is assessed for both Mâcon and Toulouse areas. The mean values at object-level are taken into account for NDVI. Similarly, the mean values of σ^0 in VV, VH and VV/VH and γ in VV and VH polarizations features are considered from both ascending and descending orbits. The common temporal grid described in step 5 of Section 2.5 is used. In order to cope with missing data, a linear interpolation is performed on NDVI features rather than the nearest neighbor approach. Linear interpolation provides a relatively smoother temporal trend and is therefore closer to the natural evolution of the vegetation. The common temporal grid contains 60 and 71 dates for the Mâcon and Toulouse areas, respectively.

To evaluate the statistical relationship between NDVI and the selected SAR features, the Pearson correlation coefficient (r_p) and the Spearman correlation coefficient (r_s) are calculated. Pearson correlation estimates the linear relationship between the two populations. Spearman correlation is based on monotonic rank-order correlation, providing further information on non-linear relationships. Both correlation coefficients range from -1 to 1, with 0 implying no correlation. Correlations of -1 or +1 imply an exact relationship between the two variables. Positive correlations imply that as one variable increases, so does the other. Negative correlations imply that as one increases, the other decreases (De Winter et al., 2016).

2.6.1 Feature correlation for grassland, crop and forest surfaces

Grasslands, crops and forest datasets described in Table 2.7 are here considered. The objective is to analyze if the correlations between NDVI and different SAR features strongly vary according to the type of vegetation. Considering all dates and valid pixels of the different datasets, large populations (N) are obtained. For Mâcon and Toulouse, respectively, the number of considered pixels for the different vegetation types is: 1,669,920 and 3,557,313 for grasslands, 753,420 and 2,449,784 for crops and 336,720 and 965,316 for forest. Table 2.11 reports both r_p and r_s correlation coefficients for Mâcon and Toulouse areas over grasslands, crops and forests.

Between the three vegetation types, the correlation found between NDVI and SAR features are clearly higher over crops. Significant negative correlations are found with VV polarization features for both σ^0 and γ ($\approx$ -0.400 to -0.500). As crops have marked phenologies, backscattering attenuations with vegetation growth are strongly marked in VV polarizations. $\sigma^0_{VV/VH}$ feature appears as the most correlated SAR feature with NDVI over both areas and for both correlation coefficients. r_p of -0.667 and -0.735 are obtained, respectively, for Mâcon and Toulouse in ascending orbits. Ascending orbit for Mâcon and descending orbit for Toulouse obtain r_s for -0.663 and -0.727, respectively. A strong correlation with NDVI is thus suggested by both r_p and r_s for $\sigma^0_{VV/VH}$ features, indicating a good complementarity for crop vegetation monitoring.

Over forests, the computed correlations are lower than for crops. The highest correlation is obtained, similarly as for crops, with $\sigma^0_{VV/VH}$ feature from Mâcon descending orbit (r_s=+0.477) and Toulouse descending orbit (r_s=+0.509). Differences are nevertheless notable for correlations assessed over crops. σ^0_{VH} polarization features are more correlated with NDVI that VV polarization, due to the strong volume scattering of the forest canopy. Furthermore, the resulting correlations for VH polarization are positive, meaning that when the NDVI over forests growth or decreases, the $\sigma^0_{VV/VH}$ features will follow its direction. γ features show a relatively weak correlation for both polarizations and both orbits. As the temporal fluctuation of forests is rather low, so does the NDVI. Stability of coherence features could thus be expected. The low correlation found may indicate decorrelation of another type, such as due to weather conditions.

Obtained correlations between SAR features and NDVI over grasslands are the lowest among the three vegetation types. The highest is r_p=-0.405 for γ_{VV} in descending orbit on the Toulouse area. VV polarization features are systematically more correlated than VH features. The low vegetation cover of grasslands and subsequent volume scattering from ground contribution can explain theses findings. While for the Mâcon area, $\sigma^0_{VV/VH}$ features (as for crops and forests) obtain the highest correlations, γ features are overall weakly

Table 2.11: Pearson (r_p) and Spearman (r_s) correlation coefficients between NDVI and derived SAR features (mean values of (3) and (4) of Table 2.9). Grasslands, crops and forest datasets are considered for the Mâcon and Toulouse areas. Green color indicates the highest obtained correlations, while the red color denotes the lowest ones.

			Asc. orbit			Desc. orbit			Asc. orbit		Desc. orbit	
			σ^0_{VV}	σ^0_{VH}	$\sigma^0_{VV/VH}$	σ^0_{VV}	σ^0_{VH}	$\sigma^0_{VV/VH}$	γ_{VV}	γ_{VH}	γ_{VV}	γ_{VH}
Grasslands (N= Mâcon: 1,669,920 ; Toulouse: 3,557,313)												
Mâcon	r_p	NDVI	-0.141	+0.052	-0.265	-0.123	+0.044	-0.221	-0.231	-0.129	-0.164	-0.079
	r_s		-0.125	+0.033	-0.233	-0.101	+0.021	-0.188	-0.223	-0.120	-0.132	-0.041
Toulouse	r_p		-0.142	+0.096	-0.378	-0.116	+0.068	-0.311	-0.367	-0.235	-0.405	-0.300
	r_s		-0.120	+0.103	-0.315	-0.061	+0.078	-0.223	-0.353	-0.227	-0.389	-0.289
Crops (N= Mâcon: 753,420 ; Toulouse: 2,449,784)												
Mâcon	r_p	NDVI	-0.400	+0.121	-0.667	-0.405	+0.042	-0.588	-0.443	-0.242	-0.433	-0.287
	r_s		-0.323	+0.137	-0.663	-0.335	+0.047	-0.591	-0.406	-0.180	-0.393	-0.220
Toulouse	r_p		-0.508	+0.039	-0.735	-0.485	-0.045	-0.700	-0.521	-0.306	-0.575	-0.440
	r_s		-0.446	+0.076	-0.726	-0.438	-0.011	-0.727	-0.501	-0.263	-0.559	-0.421
Forests (N= Mâcon: 336,720 ; Toulouse: 965,316)												
Mâcon	r_p	NDVI	-0.054	-0.260	+0.424	+0.043	-0.133	+0.357	-0.251	-0.247	-0.148	-0.122
	r_s		-0.074	-0.316	+0.477	+0.017	-0.199	+0.407	-0.225	-0.217	-0.167	-0.143
Toulouse	r_p		-0.086	-0.244	+0.408	-0.077	-0.264	+0.473	-0.277	-0.246	-0.202	-0.172
	r_s		-0.122	-0.317	+0.450	-0.106	-0.332	+0.509	-0.291	-0.256	-0.209	-0.174

correlated. In contrast, γ features on the Toulouse area are found more correlated than σ^0 features. A uneven distribution of grassland species between the two areas, and consequently heterogeneous phenologies can be the reason for these differences.

2.6.2 Feature correlation for various grassland surfaces

The same correlation study is carried out but considering the four different meta-classes (PM, TG, FA, FL) of grasslands described in Section 2.3.1.1. As grassland types have a strong influence on vegetation's phenology (*i.e.*, from extensively exploited to highly exploited), correlation analysis could illustrate these differences. Table 2.12 reports both r_p and r_s correlation coefficients for the four grasslands meta-classes obtained in Mâcon and Toulouse areas.

In all cases, a negative correlation with NDVI is found, except for some σ^0_{VH} features in both orbits. It can be noted that both Pearson and Spearman correlation coefficients provide broadly similar values and that they are similar for both Mâcon and Toulouse areas. For Pearson's r_p, the lowest and highest obtained correlations among the four grassland meta-classes and two areas are respectively +0.046 and -0.539. Spearman's

Table 2.12: Pearson (r_p) and Spearman (r_s) correlation coefficients between NDVI and derived SAR features (mean values of (3) and (4) described in Table 2.9). Results are provided according to the four grassland meta-classes defined in Section 2.3.1.1. Green color indicates the highest correlation found with NDVI, while the red color denotes the lowest ones.

			Asc. orbit			Desc. orbit			Asc. orbit		Desc. orbit	
			σ^0_{VV}	σ^0_{VH}	$\sigma^0_{VV/VH}$	σ^0_{VV}	σ^0_{VH}	$\sigma^0_{VV/VH}$	γ_{VV}	γ_{VH}	γ_{VV}	γ_{VH}
Permanent grasslands (PM) (N= Mâcon: 1,259,640 ; Toulouse: 1,921,189)												
Mâcon	r_p	NDVI	-0.101	+0.057	-0.224	-0.084	+0.055	-0.190	-0.183	-0.095	-0.101	-0.026
Mâcon	r_s	NDVI	-0.111	+0.036	-0.226	-0.091	+0.027	-0.189	-0.188	-0.091	-0.095	-0.009
Toulouse	r_p	NDVI	-0.113	-0.001	-0.228	-0.046	+0.026	-0.148	-0.251	-0.176	-0.290	-0.216
Toulouse	r_s	NDVI	-0.113	+0.024	-0.220	-0.014	+0.060	-0.126	-0.281	-0.196	-0.325	-0.239
Temporary grasslands (TG) (N= Mâcon: 361,020 ; Toulouse: 819,766)												
Mâcon	r_p	NDVI	-0.206	+0.074	-0.340	-0.191	+0.046	-0.285	-0.327	-0.198	-0.279	-0.167
Mâcon	r_s	NDVI	-0.143	+0.050	-0.252	-0.117	+0.023	-0.198	-0.313	-0.194	-0.221	-0.114
Toulouse	r_p	NDVI	-0.254	-0.116	-0.475	-0.268	+0.032	-0.414	-0.390	-0.212	-0.435	-0.302
Toulouse	r_s	NDVI	-0.180	+0.124	-0.405	-0.164	+0.038	-0.312	-0.370	-0.195	-0.408	-0.284
Fallow land (FA) (N= Mâcon: 27,720 ; Toulouse: 456,743)												
Mâcon	r_p	NDVI	-0.194	+0.096	-0.371	-0.139	+0.086	-0.289	-0.292	-0.138	-0.261	-0.137
Mâcon	r_s	NDVI	-0.211	+0.049	-0.337	-0.138	+0.049	-0.246	-0.275	-0.122	-0.229	-0.100
Toulouse	r_p	NDVI	-0.284	-0.040	-0.428	-0.259	-0.014	-0.353	-0.335	-0.198	-0.364	-0.237
Toulouse	r_s	NDVI	-0.216	+0.052	-0.360	-0.164	+0.009	-0.267	-0.300	-0.168	-0.313	-0.194
Forage legumes (FL) (N= Mâcon: 19,500 ; Toulouse: 356,278)												
Mâcon	r_p	NDVI	-0.229	+0.165	-0.477	-0.279	+0.078	-0.417	-0.459	-0.251	-0.441	-0.265
Mâcon	r_s	NDVI	-0.167	+0.153	-0.392	-0.197	+0.067	-0.331	-0.447	-0.257	-0.378	-0.210
Toulouse	r_p	NDVI	-0.241	+0.174	-0.539	-0.247	+0.112	-0.510	-0.450	-0.214	-0.484	-0.325
Toulouse	r_s	NDVI	-0.186	+0.192	-0.509	-0.172	+0.122	-0.457	-0.441	-0.193	-0.469	-0.315

r_s provides broadly similar values with the lowest and the highest correlations being +0.009 and -0.509.

As above explained in Section 2.6.1, over grasslands, VV polarization features appear more correlated than VH polarization for both σ^0 and γ. By analyzing the most correlated features (highlighted in green in the Table 2.12), in almost all cases, the $\sigma^0_{VV/VH}$ features in the ascending orbit are the most correlated ones with NDVI. This can first be related to the topography present in both study areas. Furthermore, differences in local acquisition time (early morning and late afternoon for descending and ascending orbits, respectively) can change the observed surface with for example, potential dew in the morning.

The analysis of correlations between the different meta-classes permits to complete the results obtained

in the previous section, where all grasslands were considered regardless of their meta-class. For the Toulouse area, considering all grasslands, γ features obtained the highest correlations. It is here still the case for permanent grasslands for both correlation coefficients and for r_s of temporal grasslands, but not for fallow land and forage legumes. While γ features are the most correlated ones, the $\sigma^0_{VV/VH}$ features follow closely, further indicating that this feature generally seems to be the most correlated with NDVI.

Another important distinction concerns the strength of correlation obtained for the different grassland meta-classes. By taking into account the most correlated feature ($\sigma^0_{VV/VH}$ in ascending orbit), it can be remarked that the lowest correlations are obtained by permanent grassland. They increase for temporal grasslands, again for fallow land features and achieve the highest correlations for forage legumes.

The results could be explained by the different intensity of exploitation related to each meta-class. Permanent grasslands are globally less exploited compared to forage legumes, whose agronomic species implies an intensive production with marked phenological cycles constrained by human activities. Forage legumes are thus phenologically close to crops, for which a strong correlation has been previously obtained. In addition, a relationship between slope and grassland meta-class can also be made. Indeed, the steeper the slope, the less easy the exploitation of the parcel is. The permanent grasslands, requiring less human intervention, are thus in majority in presence of slope. It was seen previously that the slope could influence the SAR features (even completely obstructing the observation of the parcel). On the contrary, the nadir acquired NDVI is relatively insensitive to slope. This can further explain the poor correlation obtained over permanent grasslands.

2.7 Concluding remarks

This chapter first introduced, discussed, and illustrated the two aspects of reference data and satellite time series. Comprehensive datasets on several vegetation types, geographical areas, and agricultural seasons were presented.

Several features derived from Sentinel-1 and Sentinel-2 time series have been proposed for monitoring vegetation, with a focus on grasslands. In particular, the simple NDVI vegetation index, derived from Sentinel-2, has shown its interest to characterize both the temporal evolution of vegetation and the important variations induced by management practices on grassland parcels. Nevertheless, an important limitation to the use of optical data due to the frequent cloud cover was demonstrated. The need for regular and frequent data to capture rapid variations in grassland vegetation led to the conclusion that the sole use of NDVI to monitor grasslands was insufficient.

SAR data has been presented as a workaround to the concern of missing data. Sentinel-1 time series ensure a regular temporal observation in compliance with the task of grassland monitoring. The potential complementarity of optical and SAR features for vegetation and grassland monitoring has been presented with the help of relevant reference data including topographic and meteorological. As a drawback, in contrast to NDVI, SAR time series require a complex and thorough interpretation for their exploitation.

The construction of a methodology allowing a joint exploitation, taking advantage of both the efficiency of NDVI and the repetitivity of SAR features, is the main need identified in this chapter by the study of the exploited satellite data.

Part II

HIGH-TEMPORAL SAMPLED TIME-SERIES

Chapter 3

Sentinels Regression for Vegetation Monitoring

3.1 Monitoring vegetation through optical-SAR synergy

When dealing with vegetation monitoring, previous chapters have highlighted the essential need for temporal highly sampled time series. This appeared especially important for grassland surfaces as a consequence of quickly evolving phenologies, a large variety of agronomic species as well as management practices. The analysis of the derived satellite features used to characterize grasslands (Section 2.4) has clearly illustrated the good ability of optical time series to capture both the seasonal phenology of grasslands as well as abrupt changes related to management practices. Consequently, a large number of approaches are understandably relying on the use of optical time series mainly through vegetation indices such as the NDVI (see Section 1.2.2.2).

Although affected by missing data, the Sentinel-2 constellation allows the acquisition of a significant number of non-cloudy NDVI values. The nominal temporal resolution of 5 days allows, at least in Europe, to ensure, *a minima*, several valid observations for each season, allowing an essential temporal variety of observations. Furthermore, the 110×110 km tiles of Sentinel-2 encompass broadly 10,980 pixels (10×10 m). Referring to the average available non-cloudy images per study area in Chapter 2 and Table 2.3, several million examples of non-cloudy NDVI values are thus available for each of the study areas. While this stands at large scales, at the local scale, the cloud cover and subsequent missing data are a major limitation for grassland monitoring. Missing data can prevent exhaustive and fine-scale monitoring especially on intensively managed grasslands with rapid vegetation regrowth.

A large number of methods has been devoted to the crucial task of recovering missing optical data. Section 3.2 will propose to review the most prominent existing methods. Two different categories are considered. The first cone addresses interpolation methods (Section 3.2.1) which exploit optical data only. They mostly rely on time series temporal trend to recover information. The second category explores methods using Machine Learning (ML) algorithms (Section 3.2.2). These methods rely on the use of complementary SAR data alongside optical data to describe a supervised regression task. In the last decade, deep neural networks have particularly attracted a lot of attention of the scientific community for solving regression problems (LeCun et al., 2015; Goodfellow et al., 2016; Zhu et al., 2017; Lathuilière et al., 2019; Reichstein et al., 2019). The increasing computer capabilities and the availability of large datasets for supervision have greatly supported their expansion. Modern neural network architectures have proven to be efficient for time series data mining where there is limited knowledge about the underlying physical processes. The use of large training datasets describing high variability further improves their generalization ability on unseen data. This capability is essential to developing robust methodologies on large geographical areas.

A newly constructed deep-based regression architecture is proposed to exploit the complementarity of optical and SAR time series. To overcome the complexity of analyzing SAR data and taking into account the observed efficiency of NDVI time series for vegetation monitoring, the deep-based architecture targets the regression of SAR features towards NDVI. Since the availability of training labels (*i.e.*, valid NDVI values) is important, a fully supervised regression approach permitting extensive learning and accuracy assessment is possible. Furthermore, based on the feature analysis carried in Section 2.4, it is proposed to integrate ancillary data handling SAR limitations into the network.

Considering the supervised regime allowed by the availability of massive data, the high dimensionality of the features, their complex relationships and the yearly time series exploited, deep-based methods provide adequate and proven tools for the targeted regression task. Section 3.3.1 will propose the introduction of two extensively used deep learning architectures, serving as a basis for the proposed architecture for SAR to NDVI feature regression. Section 3.3.2 will present compulsory pre-processing steps for the use of the derived features presented in Section 2.5. Finally, Section 3.3.3 explains the proposed regression framework and will present the deep-based architecture, namely, the Sentinels Regression for Vegetation Monitoring (**SenRVM**) approach.

3.2 Retrieving missing data in optical time series

A large range of research efforts has been devoted to develop non-parametric methodologies (*i.e.*, that don't require any distributional assumptions about data) for recovering time series of optical-derived vegetation indices with high temporal sampling (Verrelst et al., 2015; Cai et al., 2017; Belda et al., 2020a). Two main categories of methods are found in the literature that target to recover the temporal resolution of the time series: standard interpolation methods and machine learning (ML) regression algorithms. A review of used methods according to the two categories is proposed in the following.

3.2.1 Standard interpolation methods

Standard interpolation methods can be considered as gap filling reconstruction strategies recovering missing information. These methodologies can be divided into different categories (Shen et al., 2015; Desai and Ganatra, 2012; Yin et al., 2017; Lepot et al., 2017; Gerber et al., 2018; Moreno-Martínez et al., 2020). Traditionally, these mono-sensor approaches exploit past and future observations acquired by the same sensor to estimate missing data. Despite numerous relevant spatial and spatio-temporal approaches (Kang et al., 2005; Zhang et al., 2007; Das and Ghosh, 2016; Ding et al., 2017; Vuolo et al., 2017; Moreno-Martínez et al., 2020), local and global temporal interpolation approaches remain the most prevalent methods when dealing with evolving processes such as vegetation.

Local temporal methods exploit the temporal evolution of the time series by using a sliding temporal window. Among these approaches, the classical linear interpolation method is the most well-known, straightforward, and used (Inglada et al., 2017; Defourny et al., 2019; Hubert-Moy et al., 2019; Bolton et al., 2020; Kamir et al., 2020). Polynomial-based strategies have been extensively proposed as alternatives. While linear interpolation methods are computationally effective and minimize the extrapolation of data, polynomial approaches are naturally more suited for approximating non-linear relationships such as it can be the case in vegetation changes. Polynomial regressions are nevertheless sensitive to outliers as prone to overfitting, which can be a disadvantage in the presence of errors in the masks for instance Some examples are spline interpolation methods (Xu et al., 2017; Meng and Li, 2019), Savitzky-Golay filter-based methodologies (Chen et al., 2004; Jönsson and Eklundh, 2004; Kandasamy et al., 2013; Julien and Sobrino, 2019) or locally weighted scatterplot smoothing (Moreno et al., 2014) methods. The gap-filling accuracies of these methods are directly influenced by the sliding window size, which is a predefined parameter related to the gap length. As non-uniform gaps are usually encountered in the time series, the requirement for an adequate window size is an important limitation.

Instead of working at the local scale, global temporal methods propose to recover missing information by fitting the data to predefined parametric functions. For instance, the widely used Whittaker smoother fits the time series by minimizing penalized weighted spline regression squared errors (Atkinson et al., 2012; Kandasamy et al., 2013). Further global approaches include asymmetric Gaussian function fitting (Jonsson and Eklundh, 2002; Beck et al., 2006) or Fourier-based harmonic analysis (de Wit and Su, 2005; Zhou et al., 2015; Julien and Sobrino, 2019; Solano-Correa et al., 2020). One of the main limitations of global strategies is that they generally assume that the data follows some *a priori* distribution shape. They are therefore class-specific, resulting in a lack of flexibility in the presence of non-stationary data (Chen et al., 2004; Moreno-Martínez et al., 2020).

One of the main weaknesses of the standard interpolation methods is their poor effectiveness when large data gaps are occurring. In these situations, these methods fail in reconstructing temporal trajectories describing high frequency variations. It can result in missing crucial information about vegetation changes described by such variations. The effectiveness of standard interpolation approaches directly depends on the

valid number of observations acquired by the used sensor. Consequently, these methods have been mostly applied to dense optical time series with a temporal resolution of a few days but with with coarse spatial resolutions (*e.g.*, MODIS or SPOT-VEGETATION) or for tasks requiring limited temporal information, *e.g.*, yearly land-cover classification (Cai et al., 2017; Sun et al., 2021a).

The temporal resolution of time series acquired at high spatial resolution (*e.g.*, Landsat or Sentinel) is usually less dense. In this case, missing data periods can range from weeks to months (Roy et al., 2008). To address such limitations, some interpolation methods consider the fusion of complementary optical data such as Sentinel-2 and Landsat-8 (Gao et al., 2017; Claverie et al., 2018; Dwyer et al., 2018; Dong et al., 2020; Griffiths et al., 2019; Moreno-Martínez et al., 2020). Unfortunately, these multi-sensor methods require important corrections to homogenize the different spatial (Zhu et al., 2016) and spectral (Barsi et al., 2018; Bolton et al., 2020) resolutions. Additionally, complementary optical data is also affected by cloud coverage and cannot guarantee to provide a high number of supplementary valid observations.

3.2.2 Supervised machine learning regression methods

The exploitation of multi-sensor observations for recovering time series of optical-derived vegetation indices are emphasized by ML regression methodologies (Kamilaris and Prenafeta-Boldú, 2018; Reichstein et al., 2019). An increasing number of works is proposing the use of optical and weather-independent SAR time series (Schmitt and Zhu, 2016). The availability of complementary optical and SAR satellite missions (*e.g.*, Sentinels) has supported their joint exploitation. Three categories of ML regression algorithms approaches can be found in the literature, exploiting multi-sensor images: classical ML approaches, Gaussian processes, and deep learning methods.

Classical ML approaches such as Support Vector Machines (SVM) or Random Forests (RF) are commonly adopted. For instance, the work in (Wang et al., 2019b) proposes to apply SVM and RF algorithms on Sentinel-1, Sentinel-2 and Landsat 8 data to predict frequent Leaf Area Index (LAI) estimations. RF and Support Vector Regression are used in (Mohite et al., 2020) to generate a dense NDVI time series. A six-month time interval is investigated over five different crop types. Despite the good results obtained by SVM and RF approaches, it must be noticed that they are mostly validated on small agricultural datasets of a few dozen or hundreds and furthermore composed almost only of crops samples. It is therefore difficult to assess whether these techniques could be efficiently applied over large areas with different vegetation covers. In addition, these techniques require a handcrafted feature extraction step and do not exploit the temporal trajectory of the input time series.

Gaussian process (GP) is another supervised regression method which is increasingly exploited in several works. Pipia et al., 2019, is proposing a multi-output GP methodology to fill gaps in LAI time series derived from the joint exploitation of Sentinel-2 and Sentinel-1 observations. Besides time series reconstruction, the GP performances is also corroborated by other regression tasks involving vegetation monitoring. An example is found in (Mercier et al., 2020) where biophysical parameters are extracted from wheat and rapeseed parcels by exploiting Sentinel-1&2 time series. Although neglecting Sentinel images, the use of GP for crop yield estimation is also studied in (Martínez-Ferrer et al., 2020), combining MODIS and SMAP datasets. Despite previous works are showing a satisfactory capability of GP for regression tasks, the scalability of these methods can be challenging. Long training times and significant computational resources are required. The tuning of GP is also complex and very sensitive to the choice of the kernel. Such a choice questions its generalization capacity in the presence of very heterogeneous covers. Finally, likewise classical ML approaches, GP does not exploit the temporal order of the input data used for regression.

Leveraging the significant advances in machine learning and computer vision, deep-learning approaches are increasingly adopted in satellite Earth Observation related tasks. Deep-learning approaches are taking

advantage of the exponential availability of satellite time series, which furthermore offer multi-modality and rich spectral and spatio-temporal structures. The flexibility in design of deep-based methods combined with the increasing computational resources and data availability allows their exploitation in various tasks, including regression.

Deep-based SAR-to-optical regression architectures proposed for Sentinel data have first been devoted to exploit the spatial dimension of images acquired at a single date (He and Yokoya, 2018; Cresson et al., 2019; Gao et al., 2020; Meraner et al., 2020). Convolutional Neural Networks (CNNs) or Generative Adversarial Networks architectures (GANs) are proposed as a single-date regression solution without exploiting the temporal information of times series. The main objective of this work is the regression of SAR data to optical raw spectral bands to fill the missing data. Only a few deep-based architectures are proposed to exploit the temporal information of high resolution remote sensing time series and almost exclusively for classification tasks (land-cover mapping). Scarpa et al., 2018, is proposing the use of CNNs to estimate NDVI from Sentinel data for dates between May and November. Several scenarios are investigated to exploit optical and SAR data either separately or jointly. The images preceding or following the date to be estimated are used to integrate temporal information. While the scenario involving both optical and SAR data as input to their architecture allows a satisfying estimation of NDVI, in the case of SAR data only, the results are found less accurate. The need for non-cloudy optical data can nevertheless be a problem depending on the persistence of the cloud cover. The satisfactory results also highlight the interest of deep learning approaches compared to standard interpolation methods. High regression scores are obtained, albeit the very limited time series used.

To the best of our knowledge, at the time of writing the manuscript, a single example (Zhao et al., 2020) of a deep-based regression framework based on yearly SAR time series to retrieve optical-derived vegetation indices has been found. The authors combine CNNs and RNNs in a reconstruction framework aiming at predicting gap-free optical NDVI time series. 1D-CNNs are used to extract information from SAR time series separately for VV and VH polarizations. RNNs are then exploited to integrate the temporal evolution of the time series. Promising results are presented by this latter approach. Nevertheless, its generalization capability over heterogeneous vegetation types and large areas can be questioned. Indeed, the work proposed in Zhao et al., 2020, is primarily focusing on crops and a limited spatial extent. Crops are known to have a clearly defined phenological cycle. This is especially true in restricted areas, where agricultural practices take place at the same time and phenological cycles are similar. Consequently, the limited geographical area and the lack of class variability do not allow to conclude on the potential accuracy in the context of larger areas and more complex vegetation types. Furthermore, high calculation costs and long training times, which may be challenging in an operational context are reported due to the pixel-wise approach. Finally, the input data in Zhao et al., 2020, seems restricted: only descending orbit Sentinel-1 acquisitions are used, discarding the ascending orbit, which could provide additional information to the regression process. Concerning Sentinel-2, cloud & shadow masks are used to select only non- or partially-cloudy images for both training and validation. The predictions are thus made on dates that are extensively seen during training. This strategy does not allow to assess the approach neither on dates strongly affected by clouds nor on unseen dates. As for the feature used, only SAR backscatter coefficient information is selected. Additional features such as coherence information, which embeds temporal information and has demonstrated its usefulness for the study of vegetation could have been considered. Furthermore, Zhao et al., 2020, reports inferior results when important changes in scattering mechanism (*e.g.*, from diffuse soil scattering to vegetation volume scattering) are occurring. The introduction of ancillary information to support the contextualization of SAR measurements could improve the results. Moreover, this inclusion could allow to improve the generalization of the regression over larger geographical areas and heterogeneous vegetation covers.

3.3 SenRVM: A deep learning-based regression framework

The following sections are dedicated to the description of the deep-based methodology proposed for monitoring vegetation. The outputs of the SenRVM approach are gap-free NDVI time series, retrieved from the SAR-based inputs. Figure 3.1 provides a schematic view of the overall SenRVM regression methodology. Object-level, *i.e.*, LPIS parcel, statistics are first computed from the features derived from the raw satellite images and databases. SAR and ancillary features are fed as input to the SenRVM network and incomplete NDVI time series (*i.e.*, with missing data due to cloud cover) are fed as labels.

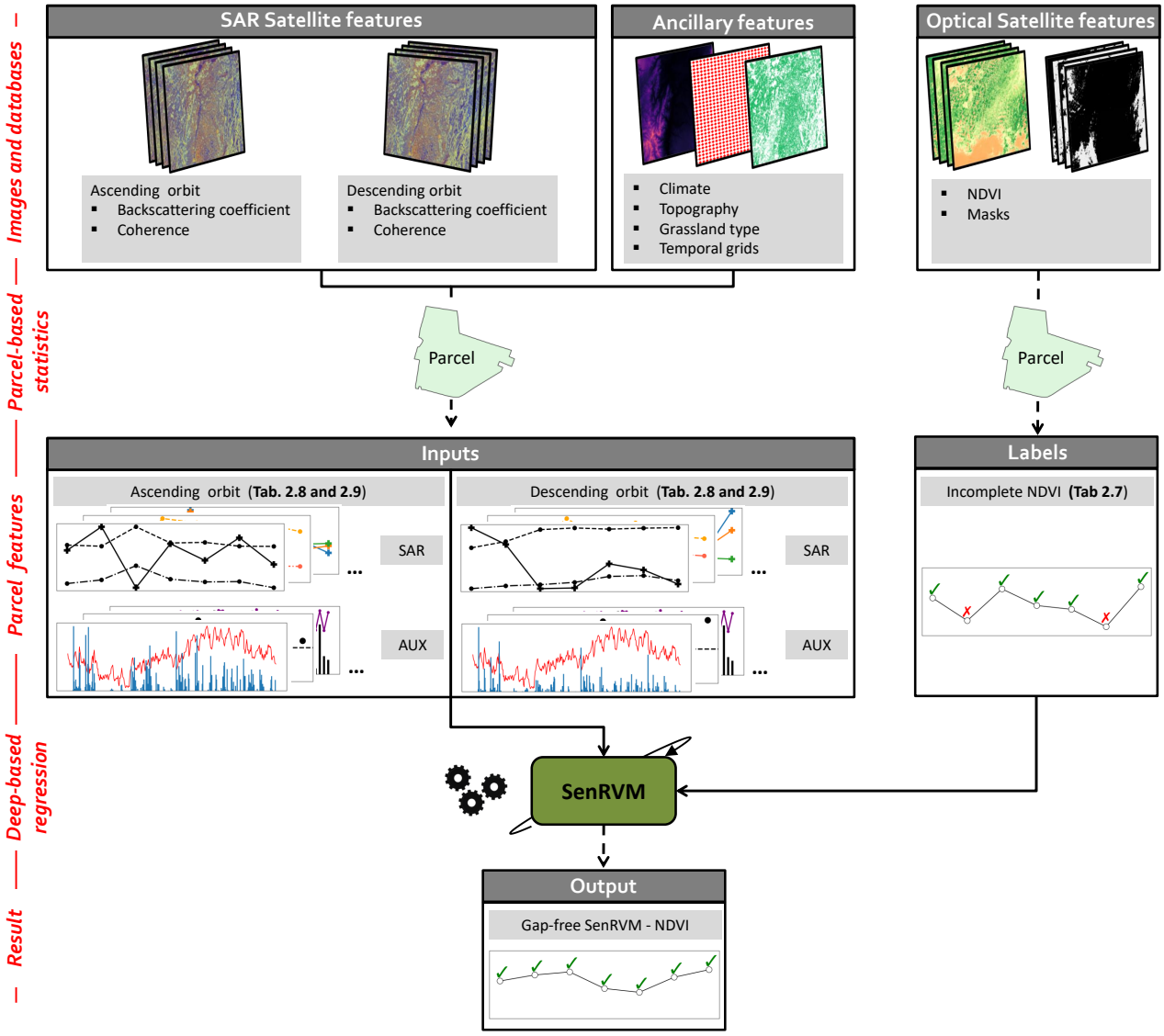

Figure 3.1: Overview of the SenRVM regression framework.

Providing state-of-the-art results in multiple domains, Neural Networks (NN) have proven to be effective for regression problems (Alom et al., 2019; Lathuilière et al., 2019). The proposed deep-based SenRVM methodology relies on two extensively used NN architectures, namely the Multi-layer Perceptron (MLP) and a Recurrent Neural Network (RNN). MLPs allow to obtain a high-dimensional representation of multivariate data by leveraging possible interactions. Section 3.3.1.1 will introduce the concepts that allowed MLPs to be extensively used in data mining. RNNs are designed to foster information extraction from the temporal

domain. Section 3.3.1.2 introduces the concepts underlying RNNs and architectures which will be exploited to characterize the evolution of vegetation.

Derived features identified as relevant for the monitoring of vegetation and presented in Section 2.5 are exploited. The SenRVM methodology is based on the joint exploitation of optical (*i.e.*, NDVI and masks) and SAR (*i.e.*, backscattering coefficient and coherence) time series as well as ancillary data (*i.e.*, topography, climate, and several metadata). Besides, the proposed methodology requires some further pre-processing steps described in Section 3.3.2. The resampling task to compute a common temporal grid (Step 5 of Section 2.5), the rescaling of SenRVM inputs and the encoding of categorical features are specifically discussed. Finally, the formulation of the SAR to NDVI regression problem and its loss function are defined in Section 3.3.3.1 and the SenRVM architecture is detailed in Section 3.3.3.2.

3.3.1 Basic deep learning architectures

3.3.1.1 From Artificial Neuron to Multi-layer Perceptrons

Multilayer perceptron (MLP) is the simplest form of deep neural network. It consists of inter-connected neurons transmitting information to each other. A MLP is composed of a input layer containing the inputs, one or more hidden layers and an output layer. A layer consists of several units (*i.e.*, the inputs for the input layer) or neurons (*i.e.*, performing calculations) for the hidden and output layers. Hidden and output layers of a MLP are connected in a feedforward manner: a neuron of a layer is connected to each neuron of the previous layer. Traditionally, MLPs are used to map inputs into an output representation describing the complex and non-linear relation among the data, which is known as the *encoding* task. Similarly, they are used for *decoding* tasks, which intend to output the closest match from the given input to the intended output. To understand how MLP performs encoding or decoding tasks and which computations are involved, we can trace back the premises of neural networks.

McCulloch and Pitts, 1943, published *a logical calculus of the ideas immanent in nervous activity* introducing a mathematical formalization of the concept of biological neuron, the Artificial Neuron (AN). In this framework, the purpose of the AN, illustrated in Figure 3.2a, was to recognize linearly separable patterns of its inputs. At that time, inputs and outputs were boolean, *i.e.*, forming a two-class classification problem. To perform the classification, the AN relied on several calculations. The key concept of AN was that to each input, a weight was attached. The first computation (the so-called net input function, z) of a AN is a weighted sum of the inputs, furthermore adding a bias term b. The output of the net input function is next passed through a logic thresholding step function (s), such as the Heaviside or sign step functions, yielding the result ($\hat{y}$).

$$z = \sum_{i=1}^{n} w_i \cdot x_i \, , \tag{3.1}$$

$$\hat{y} = s(z), \in \{0, 1\}, \tag{3.2}$$

The weights w, bias term b, and the threshold of the s function were the tunable parameters. Limitations from the AN were that their tuning was analytically and manually determined after each AN computation and therefore fixed.

Following Hebb, 1949, who put emphasis on the evolving nature of neural interconnections, Rosenblatt, 1958, extended the AN to the so-called Perceptron, concept, which is used today as the foundation of most types of Artificial Neural Networks (ANNs, Atkinson and Tatnall, 1997). Conversely to the AN whose tunable parameters were determined with respect to the network results, the Perceptron introduced a network capable

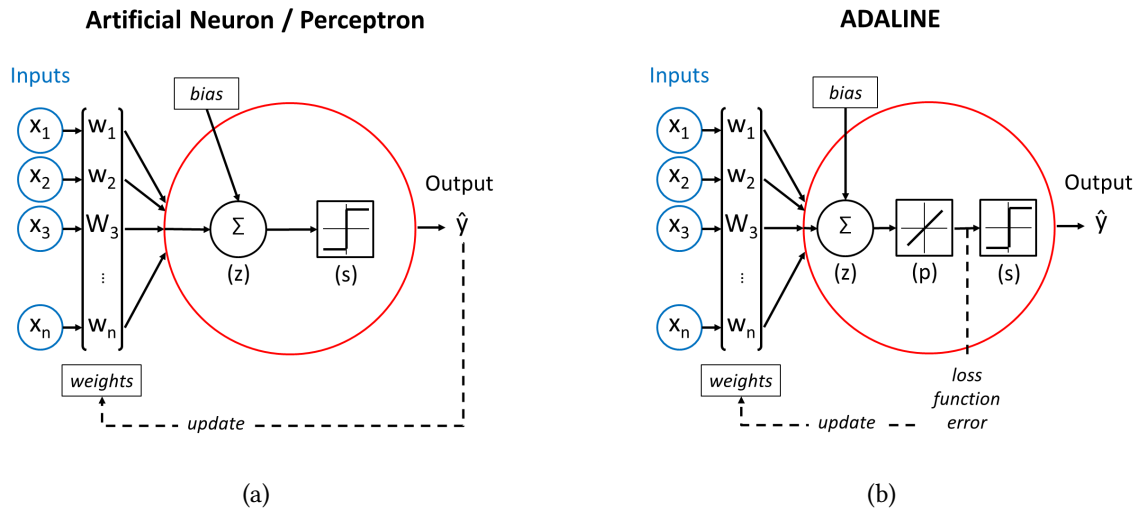

(a) (b)

Figure 3.2: Structural graph of (a) a Artificial Neuron / Perceptron and (b) a ADALINE learning neuron. Both are using inputs which are associated to weights and perform weighted summation with a dedicated function (z). A activation function (s) is used to yield the outputs. ADALINE introduces a linear activation function (p) helping the network to learn during training.

of learning by itself. The perceptron used real-values inputs (*i.e.*, non-boolean), and its weights and biases were iteratively and automatically adjusted. The output of a Perceptron is achieved through the same computing steps as for the AN, with a random initialization of the weights. The result $\hat{y}$ was compared to the expected categorical output. The computed error was then propagated backward to adjust the weights and bias (*i.e.*, kept, decreased or increased). These steps are repeated, thus allowing the network to learn until an exact output prediction is produced.

A further step in the learning process has been achieved in Widrow and Hoff, 1960, with the Adaptative Linear Element (ADALINE) approach (Figure 3.2b). Compared to the Perceptron who learned by comparing errors made from the boolean outputs, the ADALINE proposed to add a linear activation function (p) preceding the binarization of the outputs step (s). This approach allowed a major improvement as it permitted the ADALINE neuron to continuously learn by using the continuous values yielded by the linear activation function p for error backpropagation. Using such continuous values instead of boolean values permitted to define a convex minimization problem. The minimization problem relies on the so-called cost function or loss (*i.e.*, typically Manhattan distances between expectations and predictions, L_1 norm, or Euclidean distances, L_2 norm) to asses the network error. Gradient descent techniques were used to efficiently solve the minimization problem. The gradient descent technique searches for a global minimum of the cost function by evaluating the partial derivatives, or gradients, with respect to each individual weight and bias parameter. Gradient descent, whose concept is still in use in modern NN, relies on a hyperparameter, the learning rate, which is a fixed user-defined value. The learning rate controls how much (*i.e.*, the magnitude) weights and bias are updated taking into account the corresponding gradient.

The shift from fixed weights and bias in the first AN to learnable Boolean values in the Perceptron and finally continuous values with the ADALINE approach lead to a significant speed-up of convergence and abstraction capabilities of these early neural networks. Eventually, more output neurons were stacked to form an output layer. This allowed to evolve from the binary classification problem to more complex problems. Multi-layered - deep - networks were then proposed using the outputs as input to a second layer with an arbitrary number of neurons. Figure 3.3 illustrates a single-layer Perceptron and a MLP. The single layer Perceptron is composed of a input layer (blue layer) and an output layer (red layer). In contrast, the MLP of Figure 3.3b

is constructed with the same input and output layers but additionally has three hidden layers (green layers). These hidden layers have distinct number of neurons and interconnected in a feedforward manner the same way the Single layer Perceptron was. The MLP shows how additional neurons stacked in layers were added to build deep networks capable or numerous computations and learning. The theoretical depth of deep multi-layer neural networks is unlimited. However, until now, the backward propagation method used for learning was not able to differentiate errors between different layers. Parameters were updated uniformly, thus making more deep networks inefficient. The introduction of the backpropagation algorithm (Werbos and John, 1974; Linnainmaa, 1976; Rumelhart and McClelland, 1987) helped to overcome this limitation and extended the use of the gradient descent technique to networks with any number of hidden layer, further increasing their learning capacity.

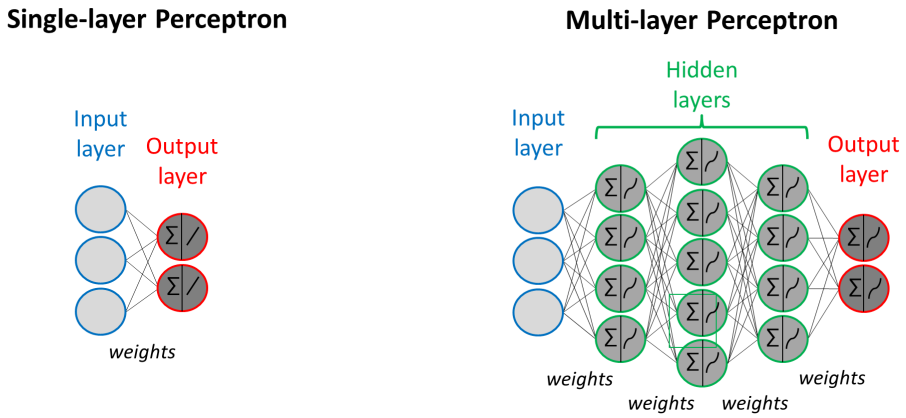

(a) (b)

Figure 3.3: Single-layer Perceptron with multiple outputs (a) and a Multi-layer Perceptron with hidden layers and multiple outputs (b).

Modern MLPs rely on the consecutive improvements of the AN. With increasing computational resources and interest towards deep learning, the depth (*i.e.*, the number of layers) and number of neurons of each layer tremendously increased. To help training and thus learning MLPs, several further improvements have been proposed and are now routinely used. The logic thresholding or linear activation function have been replaced by non-linear but differentiable activation functions, allowing to solve complex non-linear problems. Commonly used activation functions are the Sigmoid function (scaling the output between 0 and 1), Hyperbolic Tangent function (tanh, scaling between -1 and 1) or Rectified Linear Unit function (ReLU, output 0 if negative, otherwise x). To speed-up training, gradient descent in the backpropagation algorithm is applied on batches, *i.e.*, a subset of the training dataset. Furthermore, training is now commonly performed using an optimizer, such as Adam, AdaGrad or RMSprop. The Adam optimizer for example permits to modify the learning rate during training for each networks parameter. Stochastic gradient descent in contrast was maintaining a single learning rate, set as a upper limit, for all weight updates during the complete learning process. Finally, to improve the generalization of training and prevent overfitting (*i.e.*, fitting too closely to the data used for training), regularization techniques such as dropout or normalization layers are routinely used. Dropout limits the interdependence between neurons in a layer by randomly ignoring neurons during training. Normalization of the layers outputs helps to stabilize the training accuracy when data have different ranges. Different normalization techniques exist, such as using mean and variance of the outputs within a batch, along certain dimensions, or within groups of features.

3.3.1.2 Neural Networks and temporal sequence

MLPs previously presented are feedforward networks, meaning that each layer output is fed into the next layer in a unidirectional fashion. The imposed feedforward rule limits the exploitation of inter-dependencies that can occur when dealing with time- or sequence-dependent problems. A dedicated type of Neural Networks, called Recurrent neural networks (RNNs), are capable of learning features and time dependencies among ordered data (Campos-Taberner et al., 2020).

The first successful example of a recurrent network trained with backpropagation was published in Elman, 1990, who introduced recurrent connections and memory cells. The term "recurrent" indicates that the network performs the same task over each instance of sequential data. At each time step, a hidden state is learned and stored into a memory cell. Recurrent connections between memory cells and hidden states imply that the output at a certain time step depends on the previous computations and results. As for previous feedforward networks, weights are associated to each connection allowing adjustments and learning. These recurrent connections are used for dynamic information processing and are naturally suited to satellite time series. RNNs leverages Backpropagation Through Time (BPTT) to determine the gradients used to update the weights and biases of the network, which is a slightly modified backpropagation algorithm taking into account the sequential nature of the processing.

To illustrate the recurrent process in a RNN layer, Figure 3.4 exemplifies the two ways RNNs can be represented. On the left, a compact visualization referred to as *folded*, indicates the recurrent cyclic process of the RNN layer (green outlined circle with curved arrow). On the right, the *unfolded* version illustrates in a feedforward manner the notion of time step calculation with as much 'copies' of the recurrent cells as time steps in the input sequential data, sharing the same weights. BPTT is relying on this *unfolded* dimension to calculate the error and perform update.

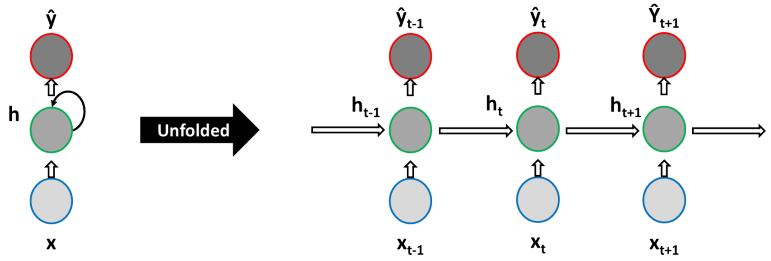

Figure 3.4: Schematic representation of a folded RNN on the left, and unfolded on the right. x are the inputs, h are the hidden states, $\hat{y}$ are the outputs and t the time steps.

However, RNNs stressed a problem that was already affecting the feedforward multi-layer networks: gradient vanishing and explosion (Bengio et al., 1994). As multiplication is involved in the backpropagation process, when starting with small or large values in the last layers, the gradients can exponentially grow or decrease towards zero while being propagated to the first layers. As unfolded RNNs can be seen as having as much layers as time steps, this caused RNNs to be poorly effective in dealing with long sequences, learning long-term dependencies and prone to errors on top of long computation times.

The introduction of Long Short-Term Memory (LSTM, Hochreiter and Schmidhuber, 1997) and Gated Recurrent Units (GRU, Cho et al., 2014) cells addressed the major issues of the former RNNs. As the name suggests, it is achieved through the addition of units combining both short-memory and long-memory capabilities and controlling the passed hidden states. Figure 3.5 illustrates the functioning of both LSTM and GRU cells.

RNNs were called *forgetful* as we saw that they retained mostly memory only from the previous time step.

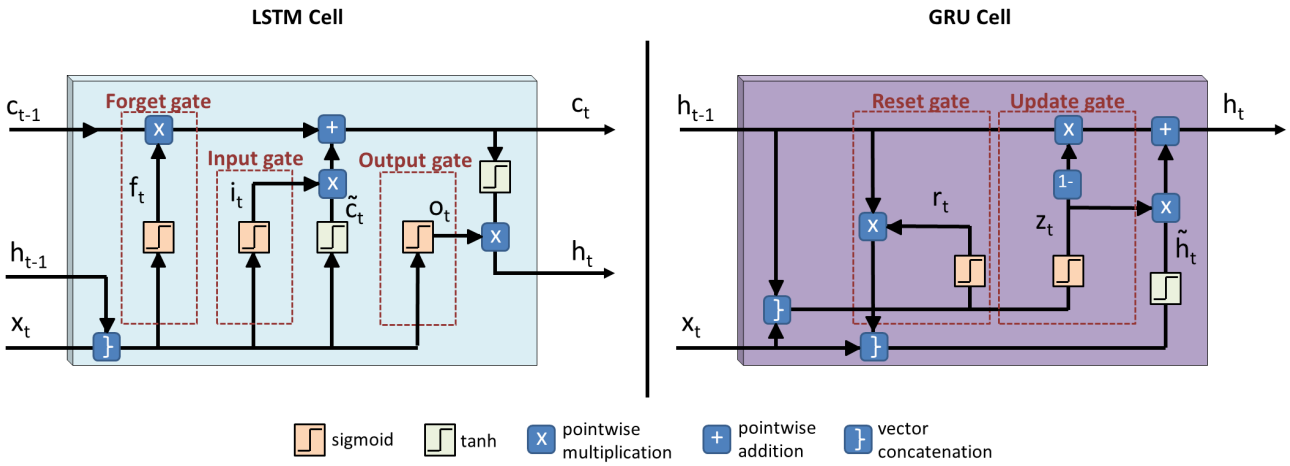

Figure 3.5: Long Short-Term Memory (LSTM) cell left and Gated Recurrent Unit (GRU) cell right. x are the inputs, h are the hidden states, c is the cell state and t is the current time step.

LSTM cell (left in Figure 3.5) by contrast, introduces loops that can generate long-term gradients and such memory. The final output of a LSTM cell ties together three information: the current input data (x_t), the short-term memory from the previous time step (h_{t-1}) and a long-term memory from more remote time steps (c_{t-1}). A gating system inside the LSTM cell regulates the flow of information by carrying out specific calculations. A *forget gate* first decides based on previous hidden state and current time step input what information should be kept or deleted from the long-term memory. The *input gate* aims to add new information to the long-term memory from the current time step. The *output gate* controls what information should be passed to the next time step cell. Obviously, weights are added to each calculation step, allowing LSTM cells to learn which information are effective to reduce the prediction error (*i.e.*, by 'opening' and 'closing' gates).

Gated Recurrent Units (GRU) were introduced as a variant of LSTM. Unlike LSTM, GRU uses only two gates to control the memory. A *reset gate* at time step t (r_t) allows information from the previous hidden state to be discarded while the *update gate* (z_t) controls how much information is to be passed along the next hidden state. Furthermore, compared to LSTM which has two distinct memory states passed between the time steps (*i.e.*, h_t and c_t), GRU operates inner-cell computation between previous hidden state and a current candidate hidden state $\tilde{h}_t$. Thus, a single hidden state h_t is passed along the time steps. With respect to the notation of Figure 3.5, the computations of a GRU cell are as follows:

$$r_t = \sigma\left(W_{ir}x_t + b_{ir} + W_{hr}h_{t-1} + b_{hr}\right), \tag{3.3}$$

$$z_t = \sigma\left(W_{iz}x_t + b_{iz} + W_{hz}h_{t-1} + b_{hz}\right), \tag{3.4}$$

$$\tilde{h}_t = \tanh\left(W_{ih}x_t + b_{ih} + r_t \odot \left(W_{hh}h_{t-1} + b_{hh}\right)\right), \tag{3.5}$$

$$h_t = (1 - z_t) \odot \tilde{h}_t + z_t \odot h_{t-1}, \tag{3.6}$$

where
x_t = input at time step t
h_{t-1} = hidden state from previous time step t_{-1}
W_{ir},W_{iz},W_{ih} = learnable weights related to the inputs
W_{hr},W_{hz},W_{hh} = learnable weights related to the previous hidden state
b_{ir},b_{iz},b_{ih} = learnable biases related to the inputs
b_{hr},b_{hz},b_{hh} = learnable biases related to the previous hidden state
$\odot$ = Hadamard product
σ = sigmoid function

$\tanh$ = hyperbolic tangent function.

Due to a greater simplicity, GRU allow for significant decrease in network parameters and computing time compared to LSTM (Shewalkar et al., 2019; Mateus et al., 2021). For example, Yang et al., 2020 reported GRU as 29.29% faster than LSTM for processing the same dataset. GRU has also been found to provide similar results to LSTM (Ndikumana et al., 2018; Yang et al., 2020; Mateus et al., 2021), thus often preferred.

A further advantage of RNNs, and therefore LSTM and GRU, is their flexibility regarding input-output configurations. Sequential data takes many different forms (*e.g.*, a sequence within a single image, or along a time series). The hidden states computed for each time step can either be used as a resulting prediction or probability, or be passed to the next time step. Thus, multiple sequence-related tasks can be performed. The five main configurations are illustrated in Figure 3.6: *one-to-one*, which basically yields the same as a feed-forward MLP and is not a RNN, *one-to-many* (*e.g.*, captioning an image where elements are inter-connected), *many-to-one* (*e.g.*, classification task such as determining a crop type at the end of the season), *many-to-many* where the number of inputs and outputs don't necessarily match (*e.g.*, characterizing an involving process such as vegetation growth). Obviously, in the case of predicting continuous NDVI over grasslands, the *many-to-many* case will be accurate.

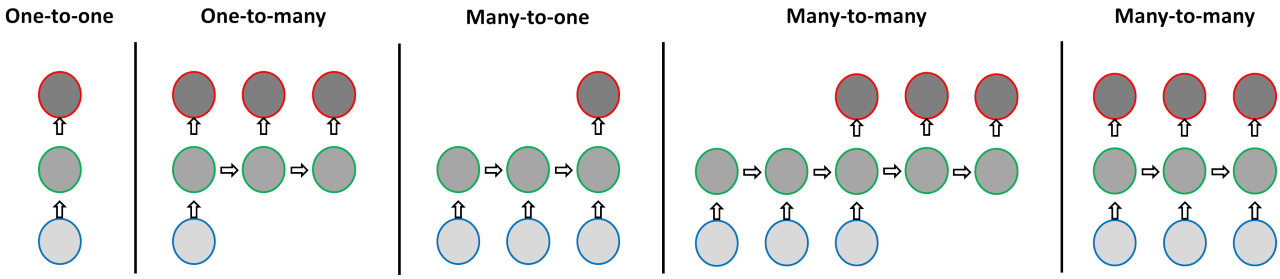

Figure 3.6: Variation of Recurrent Neural Network (unfolded) regarding input and output sequences.

Finally, as for feedforward networks, RNN layers can be stacked together where the outputs of the first RNN layer are used as inputs to a second RNN layer. RNNs can also be bi-directional (BRNN) by processing the sequence in both directions (Schuster and Paliwal, 1997). Typically, two separate RNNs are used: one for the forward direction and one for the reverse direction. This offers the advantage of learning temporal patterns independently from the beginning of the sequence (the first input) in addition to observing the sequence in a reverse order.

Recently, Vaswani et al., 2017 have introduced Transformers which, like RNNs, are designed to process sequential input data. Transformers adopt Multihead-Self-Attention mechanisms, efficiently relating different positions of a given input sequence. Self-attention is computed by weighting the significance of each part with respect to the other parts of the sequence, to gather information and learn dynamic temporal contextual information. Transformers have been massively adopted in many sequence-related tasks, providing state-of-the-art results and notably greatly reducing training times and parameter number. While RNNs have to process the sequence successively, Transformers overcome this bottleneck and allow long-term memory to be efficiently retained. Transformers have been successfully adapted and applied to satellite image time series only very recently (Sainte Fare Garnot et al., 2020; Rußwurm and Körner, 2020).

Despite very promising, Transformers have for now, in the context of satellite image time series, only been explored in *many-to-one* contexts. The specific regression task intended in this work, which is *many-to-many* (far right in Figure 3.6), may convey questions on the interest of the use of Transformers. Indeed, the parallel processing of Transformers is initially done in an order-invariant way, meaning the actual order of the sequence is not kept. Techniques such as positional embedding and attention masking have addressed

this concern and are now routinely employed (Shaw et al., 2018; Wang et al., 2021). Nevertheless, they increase the complexity and number of parameters of the network and the temporal order is still only implicitly added. Eventually, for some regression problems such as in this work, the sequential processing of RNNs may be enough. The prediction task of the state of the vegetation at a certain time step must predominantly depend on the vegetation state at close temporal observations. Indeed, it was observed that grasslands are very responsive to climate factors and numerous management practices imply variable and unpredictable phenologies. Carrying temporal information build principally on a few preceding time steps such as with RNNs may be adequate and appropriate. The main advantage of Transformers for long-term memory processing might therefore prove to be unnecessary. Lastly, Transformers have shown to outperform RNNs regarding satellite image time series classification tasks (*i.e.*, predicting a crop type) mainly in end-to-end learning schemes were unprocessed raw data are fed as inputs. When pre-processing of features is been considered, such as it is the case in this work, performances of Transformers and RNNs were relatively similar (Rußwurm and Körner, 2020).

3.3.2 SenRVM input pre-processings

We adopt a MLP-RNN based framework for regressing Sentinel-2 variables from Sentinel-1 and ancillary inputs. We put the focus on NDVI retrieval, since it was seen that the latter responded favorably to the initial issue of grassland monitoring. Given the asynchronous and multivariate nature of the data and the prerequisite of deep-based methods, some pre-processing task are first performed on the input datasets described in Section 2.5. Three pre-processing tasks are considered: a resampling step already mentioned in Section 2.5, a scaling transformation of the inputs features and an encoding task of categorical variables.

Resampling of satellite inputs: As optical, SAR and ancillary data do not share the same temporal sampling, the common temporal grid defined in Step 5 of Section 2.5 is used in the regression framework. Thus, the optical, SAR and ancillary data share the same time step spacing, permitting to associate each input with a label to be compared with the network output. As a recall, the shift in days caused by the common temporal grid with respect to the original one is kept as ancillary data and will be used to provide temporal context information to the regression framework.

Scaling transformation: Any optimization problems require data to be scaled for efficient and tractable learning. It is the case of most ML and deep learning methods using gradient descend optimization techniques. As the input data values are used in several calculations, they will affect the weights of a deep-based network. Having different feature ranges can lead the network to prioritize higher values and slow or harm convergence. Thus, a common scale is preferred, ensuring an update of parameters at the same rate, regardless of the original data range.

Several scaling techniques are commonly used, among them mainly normalization and standardization. Normalization re-scales the data between 0 and 1 using *argmin* and *argmax* of the distribution. Standardization on the other hand uses the mean and standard deviation of a distribution to perform scaling:

$$x' = x - \mu/\sigma \tag{3.7}$$

where x is the input value, μ is the mean and σ is the standard deviation of the concerned distribution of x. Thus, a centered and reduced variable has a mean equal to 0 and a standard deviation equal to 1. Standardization does not have a bounded range, but will change according to the distribution. As the input data used is assumed to have what can be referred to as wide ranges (*i.e.*, very different values between active vegetation and bare soil after management practice), standardization is preferred to normalization. The bounded nature of normalization $\in [0, 1]$ would lead to a compression of the distribution dynamics.

Standardization is performed independently for each SAR and ancillary inputs and for each data type (*i.e.*, VV polarization, VH polarization, altitude, precipitation...). For the following, inputs mentioned in the regression framework refer to those standardized (x'). NDVI values, as further used in the regression framework solely as target values are kept unchanged.

Encoding categorical variables: Among the used ancillary data, the specie type is provided in codes (*e.g.*, PPH, PTR, PRL...) that are categorical variables (Section 2.3.1). Numerical variables are nevertheless expected in ML. Several techniques are proposed to encode categorical data which are ordinal (Hancock and Khoshgoftaar, 2020), such as the simplest label encoding technique which assigns an integer to each class. The case of specie codes is nevertheless nominal conversely to ordinal, as each code has the same importance as another.

The One-Hot-Encoding (OHE) technique is commonly used to encode categorical to numerical data when they do not have a notion of order. OHE will represent each categorical variable by a vector having the length of the possible categories containing only 0 and 1. This ensures an equal numerical value to each class. The position of the 1 will then depend on the category such that each category has a unique vector. As an example, considering three possible codes, the OHE will process as follows:

$$\begin{array}{lccc} \text{Categorical variable} = & \text{PPH} & \text{PTR} & \text{PRL} \\ \text{One-hot-encoding} = & [\,1,0,0\,] & [\,0,1,0\,] & [\,0,0,1\,] \end{array} \tag{3.8}$$

Drawbacks of OHE is the heavy amount of dimensionality to the data that can be added (*i.e.*, when there is a high number of classes). Furthermore, the number of categories can change on a new dataset for example. Nevertheless, few other options are available for nominal encoding (Hancock and Khoshgoftaar, 2020) and as only about 20 grassland and forest and 3 crop codes are retrieved, OHE remains a convenient and efficient encoding strategy.

3.3.3 SenRVM methodology

3.3.3.1 Regression task and loss function

Let us denote as $X = (x_1, x_2, ..., x_T)$ the multivariate time series of length T containing all features derived from Sentinel-1 (Table 2.9). For each $t \in \{1, 2, ..., T\}$, SAR features derived from an image acquired at instant t are represented by x_t. In parallel, $Z = (z_1, z_2, ..., z_T)$ is the multivariate time series where each z_t contains the features computed from ancillary data (Table 2.10), tailored to provide information about SAR measurements (see Section 2.4). Considering these definitions, $\{X, Z\}^{asc}$ and $\{X, Z\}^{desc}$ correspond to the couples of features from ascending and descending orbits. SAR orbits are individually processed to avoid mixing information acquired from different viewing angles. The proposed SenRVM regression method then uses both couples to predict the time series $\hat{Y} = (\hat{y}_1, \hat{y}_2, ..., \hat{y}_T)$ where $\hat{y}_t$ denotes the predicted NDVI measure at the instant t.

To supervise SenRVM, NDVI time series $Y = (y_1, y_2, ..., y_T)$ of length T derived from Sentinel-2 acquisitions are used (Table 2.8). The training process estimates the network parameters by minimizing a loss function $\mathcal{J}$. This function quantifies the error $\mathcal{L}$ between predicted and expected NDVI values. Given n training samples, $\mathcal{J}$ is defined as the average Mean Squared Error (MSE) $\mathcal{L}$ and is committed during the forward training propagation step as:

$$\mathcal{J} = \frac{1}{n} \sum_{i=1}^{n} \mathcal{L}(\hat{Y}_i, Y_i)\,, \tag{3.9}$$

where $\mathcal{L}$ evaluates the average error between prediction $\hat{y}_t$ and expected y_t values at instant t. The MSE

is preferred to other classical regression loss functions (Lathuilière et al., 2019) given its ability to converge towards the optimal solution. Note that the Mean Absolute Error outputs continuously large gradients even in the case of small errors, which can lead to convergence problems. The alternative Huber loss requires the setting of a hyper-parameter δ. The setting of this value can be data dependent and can be an iterative problem.

To take into account the sensitivity of MSE to outliers, cloudy NDVI acquisitions are removed from the MSE computation. The information contained in the cloud & shadow masking vector $M = (m_1, m_2, ..., m_T)$ is incorporated in Eq. 3.9 with the validity flag $m_t \in \{0, 1\}$ associated with each y_t :

$$\mathcal{L} = \frac{1}{T} \sum_{t=1}^{T} m_t (\hat{y}_t - y_t)^2 . \tag{3.10}$$

It must be noticed that the presence of outliers in the training data cannot be entirely discarded since cloud & shadow masks can contain errors. The performance impact of such errors is discussed in Section 4.5.1 where a re-training/refinement strategy is presented to slightly improve the SenRVM performances.

3.3.3.2 SenRVM architecture

The SenRVM architecture, which is based on the previously presented deep-based MLP and RNN architecture, is decomposed into three blocks as depicted in Figure 3.7. Firstly, the *encoder block* combines SAR and ancillary data to extract a joint complex representation. Secondly, the *recurrent block* captures the temporal dependencies among the previous representations. Finally, the *decoder block* translates the network representations into the target variable, namely, NDVI.

The encoding block individually processes ascending and descending orbit datasets by two parallel branches, which are fed by $\{X, Z\}^{asc}$ or $\{X, Z\}^{desc}$ couples. As previously stated, ascending and descending orbits propose drastically different angles of acquisition and therefore bring a disjointed information. Each branch is composed of two MLPs, which separately maps each $\{x_t, z_t\}$ couple to an output representation of 256 features. The four MLPs composing the encoder block contain 4 fully connected (FC) layers whose output sizes are equal to $128, 128, 200$ and 256. FC layers, except for the last one, are followed by batch normalization, dropout, and non-linear activation layers. As described in Section 3.3.1.1, these layers are used to improve the accuracy and generalization of the learning. A fixed probability p for the dropout layers is set to 0.2 and a rectified linear unit (ReLU) is used as non-linear activation function. The use of MLPs allows us to obtain a feature representation with the same output size (256) from both X and Z. This intermediate representation encodes complex relationships for each data modality and allows their fusion without prior correlation knowledge. An element-wise multiplication (Hadamard product) is then proposed to combine the encoded SAR and ancillary feature representations computed for each acquisition date. Alternatives such as concatenation, summation, or subtraction are discarded because lower performances were obtained for these strategies in preliminary experiments. Finally, the encoding block concatenates the two ascending and descending branches in a single vector of 512 features for each date t. The concatenation is chosen here to keep the raw information from both orbits.

The second block is a single layer Bi-directional RNN (BRNN), scanning the input in both directions. The choice of a BRNN is made to obtain robust predictions using past and future observations enclosing each time step. A single BRNN layer is proposed as it achieves similar performances than more complex multi-layers stacked BRNNs while reducing the number of network parameters. This block takes as input the outputs of the encoder block (*i.e.*, the joint SAR and ancillary representation). The RNN is composed of GRU cells which have a memory size h_t equal to 256. Working with short-length satellite time series (*i.e.*, less than 80 time

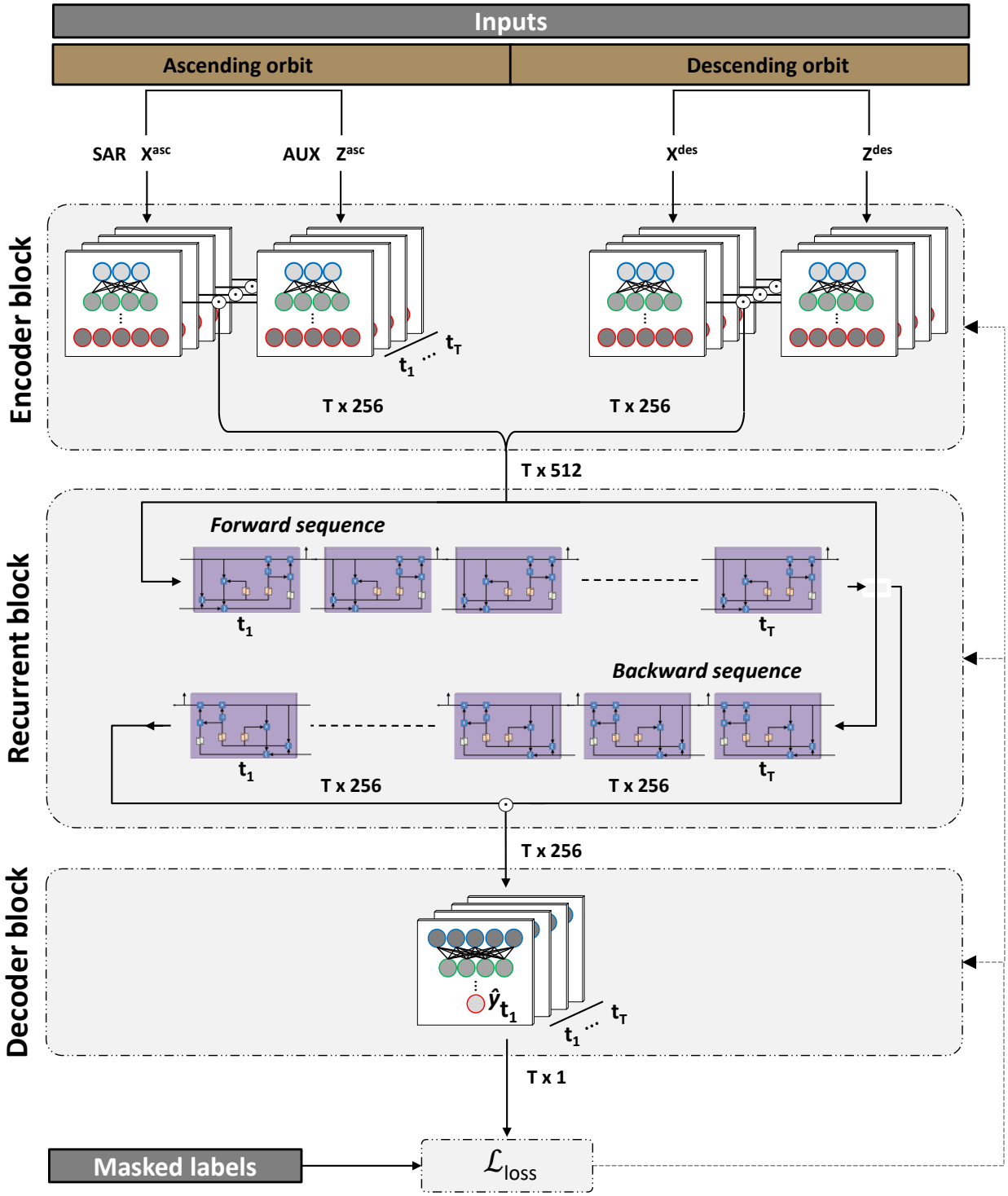

Figure 3.7: SenRVM architecture taking as input object-based statistics of SAR and ancillary features and yielding NDVI predictions. MLPs compose the encoder and decoder blocks and GRU cells the recurrent block.

steps), and because of the limitations exposed previously (Section 3.3.1.2), GRU has been preferred to LSTM and Transformers. The purpose of this block is to extract the underlying temporal information contained in the time series described for each t by 512 features previously learned. The bi-directional RNN outputs two vectors corresponding to forward and backward sequence scanning. These two vectors are element-wise

multiplied to obtain a single vector of 256 values per date which is passed to the next block. Thus, the recurrent block outputs a time series of size $T \times 256$.

For each date t, the last SenRVM block processes its corresponding 256 features to predict $\hat{y}$. This last block is composed of a funnel-shaped MLP which is a succession of six FC layers whose input sizes are equal to $256, 64, 32, 16, 8$, and 4. As previously proposed, FC layers are followed by batch normalization, dropout, and ReLU activation layers. Dropout probability is here initially set to 0.4 and decreases by 0.1 for the successive following layers. Finally, the last FC layer applies the sigmoid function as the final activation function, considering the dynamic range of NDVI values. The decoding block regresses the 256 features to a single NDVI value $\hat{y}$ for all dates $t \in T$.

SenRVM network weights and biases are learned through the training phase by minimizing the loss function of Eq. 3.10. Iterative backpropagation with Adaptive Moment Estimation (Adam) algorithm is used to find the optimal network weights (Kingma and Ba, 2017). After each iteration, Adam algorithm updates the weights towards the global minimum of the loss function.

3.4 Concluding remarks

Obtaining dense time series was previously identified as critical for grassland monitoring. Prominent techniques to recover missing data in optical satellite time series were presented. Mono-modal approaches were nevertheless found inappropriate as not capable at accurately depicting sudden changes in the time series. In contrast, machine learning approaches proposing a joint optical-SAR data exploitation were found to be more promising.

In particular, deep learning methods can address some of the issues raised by the grassland monitoring task. As massive, multi-modal and noisy data must be exploited, deep learning allows the learning of complex correlations and dependencies. In order to capitalize on the proven efficiency of NDVI time series for grassland monitoring, a supervised regression task from SAR and ancillary features towards NDVI was proposed.

The Sentinels Regression for Vegetation Monitoring (SenRVM) regression framework presented aims at obtaining gap-free NDVI time series at a 6-day temporal resolution. The basic building blocks of deep learning have been introduced with emphasis on the networks that address the proposed regression problem. A new architecture based on multi-layer perceptron and recurrent neural networks was presented.

Chapter 4

Outcomes of the SenRVM approach

4.1 Experimental design for training and evaluating SenRVM models

Multiple experiments are carried out to evaluate the performances of the SenRVM methodology. The accuracy of the predicted NDVI time series at high temporal sampling is assessed.

Results are first investigated over a multi-class dataset including three vegetation types (Section 4.2.1). This targets to confront the SenRVM approach to different phenologies and assess its capabilities to generalize over heterogeneous vegetation covers. In a second step, single-class model results are presented (Section 4.2.2).

Next, different spatial and temporal criteria are considered to analyze the per-class results (Section 4.3) .The importance of the different input SenRVM features is then evaluated by an ablation study. To further assess the SenRVM performances, the proposed methodology is compared with several standard interpolation and machine learning regression methodologies. The SenRVM prediction accuracy is evaluated on small and significant data gaps to explore its predictive ability under different simulated clouding conditions. A related investigation of SenRVM capability in retrieving time series breaks is proposed.

Focusing on SenRVM models obtained over grasslands, generalization capabilities are assessed in Section 4.4, with models trained on an area and inferred on another area, or learned on one year and inferred on a different year. Finally, post-processing steps are explored in Section 4.5, fostering the potential improvements of SenRVM results.

4.1.1 Experimental setup

For the experiments, the reference data is randomly splitted into disjoint train, validation and test data subsets. The training dataset contains $3/5^{th}$ of the polygons describing the complete reference dataset. The remaining polygons are divided equally for the validation and test datasets. A 5-fold cross-validation is performed during training by repeating the splitting procedure five times and re-run. This minimizes the possible randomness effects with respect to the initialization of the network layers as well as the effects due to the sampling strategy (such as imbalanced sampling or spatial auto-correlation of training samples). Hereinafter, the presented results, except when stipulated otherwise, are obtained by averaging the 5-fold results.

The SenRVM input features are described in Section 2.4 and are pre-processed as mentioned in Section 2.5. For the experiments, a notable difference concerning the used dataset for training and evaluation is made. Single-class and multi-class (see Section 2.3.1) models are considered. Single-class models refer to the training and evaluation using one single dataset among the grassland, crops and forest datasets. Multi-class models are trained and evaluated over larger datasets regrouping the three types of vegetation surfaces.

For the different experiments, the batch size (Bs) and learning rate (Lr) are empirically set. The batch size refers to how many input-output pairs are used in a single back-propagation pass (*i.e.*, update of the network weights, see Section 3.3.1). The hyperparameters ultimately used for single-class and multi-class models obtained over the Mâcon and Toulouse areas are reported in Table 4.1. Except when explicitly given, these hyperparameters are valid for all SenRVM models assessed in the following.

During the training process, the number of epochs is set to 150. The validation dataset is used during training to asses the model's accuracy and update its parameters. The epoch obtaining the highest accuracy on the validation dataset is considered as the best model. For each parcel, only the observations flagged as non-cloudy by the masks are taken into account. Since the cloud cover does not impact the parcels equally, the length of the time series T_v, which depicts the number of non-cloudy observation in the time series T, will therefore vary from one parcel to another.

Table 4.1: Main SenRVM hyperparameters, learning rate (Lr) and batch size (Bs), as well as training time (T).

Area	Class	Lr	Bs	T (min)
Mâcon	Grasslands	5×10^{-4}	256	57
	Crops	5×10^{-4}	256	32
	Forests	1×10^{-3}	128	24
	Multi-class	5×10^{-4}	512	71
Toulouse	Grasslands	1×10^{-4}	256	96
	Crops	5×10^{-4}	512	61
	Forests	1×10^{-3}	256	36
	Multi-class	5×10^{4}	512	145

4.1.2 Evaluation metrics

Four classical regression metrics are selected to assess the SenRVM performances. Prediction errors are first evaluated by three metrics which are the Mean Absolute Error (MAE), Mean Squared Error (MSE), and the Root Mean Squared Error (RMSE):

$$MAE = \frac{1}{T}\sum_{t=1}^{T} |y_t - \hat{y}_t| \,, \tag{4.1}$$

$$MSE = \frac{1}{T}\sum_{t=1}^{T} (y_t - \hat{y}_t)^2 \,, \tag{4.2}$$

$$RMSE = \sqrt{MSE} = \sqrt{\frac{1}{T}\sum_{t=1}^{T} (y_t - \hat{y}_t)^2} \,, \tag{4.3}$$

with T_ν the number of non-cloudy observations, y_t the observed NDVI value at the t^{th} time series date, and $\hat{y}_t$ the predicted NDVI value at the corresponding t^{th} time series date. Both MAE and MSE are complementary metrics. MAE has the advantage of being simply interpretable and expressed in the same units as the variable being evaluated as it directly reports the absolute potential error. The MSE, already presented in the context of the loss of the model, allows through squaring, to penalize large errors. Its interpretation is nevertheless more complex. RMSE allows to relate the value of the MSE to the units of the evaluated variable, while penalizing large errors. For the three previous metrics, the lower the values obtained, the higher the accuracy.

The fourth metric is the coefficient of determination R^2 which is used to estimate how strong the linear relationship is between the expected and predicted NDVI measures:

$$R^2 = 1 - \frac{\frac{1}{T}\sum_{t=1}^{T}(y_t - \hat{y}_t)^2}{\frac{1}{T}\sum_{t=1}^{T}(y_t - \bar{y})^2} \,, \tag{4.4}$$

with T_ν the number of observations, y_t the observed NDVI value at the t^{th} time series date, $\hat{y}_t$ the predicted NDVI value at the corresponding date t, and $\bar{y}$ the average of $y \in T$. The three previous metrics have arbitrary ranges depending on the evaluated variable units. In the case of a simple linear regression, R^2 varies between 0 and 1. This allow using R^2 for model comparison. Contrary to MAE, MSE, and RMSE, the higher the R^2, *i.e.*, the closer to 1, the better the fit and the higher the prediction accuracy.

4.2 Assessment of SenRVM predictions

4.2.1 Evaluation of the multi-class SenRVM model

For Mâcon, 27, 599 polygons from a total of 46, 001 elements from the corresponding multi-class (*i.e.* grassland, crops and forest) dataset are used for training the models while 58, 921 out of 98, 203 polygons are used for the Toulouse area (Table 2.7). As previously mentioned, the three vegetation classes, grasslands, crops and forests, respectively, have distinct phenologies, which leads to a high data variability.

Results obtained for the multi-class SenRVM model are shown in Table 4.2. Results are averaged over all polygons belonging to the test dataset and for all dates of the time series. Highly accurate results are obtained, with R^2 above 0.86 and MAE errors below 0.042. Low standard deviations are also found across the four metrics for both areas. The R^2 found values of 0.86 and 0.89 for Mâcon and Toulouse, respectively, indicate a strong correlation between the Sentinel-2 acquired and the SenRVM predicted time series. Considering that NDVI $\in [-1, 1]$, the MAE represent a $\approx 2\%$ error rate. This shows the ability of the SenRVM network to provide good predictions despite the different phenologies of the vegetation types.

Table 4.2: Average results and $\pm$ standard deviation obtained by multi-class SenRVM models.

		Mâcon	Toulouse
Multi-class	R^2	0.8650 ± 0.0039	0.8947 ± 0.0016
	MAE	0.0419 ± 0.0016	0.0404 ± 0.0016
	MSE	0.0039 ± 0.0002	0.0030 ± 0.0002
	RMSE	0.0628 ± 0.0021	0.0547 ± 0.0017

The best performances are reached in Toulouse. Nonetheless, the differences found between both areas are relatively small accounting the important number of samples. The differences can be justified by several reasons. The Mâcon area has a more spatially distributed topography. Because of the side-looking nature of SAR data, this can lead to data being masked by topography (see Section 1.2.1.2). On the other hand, large parts of plains marked by a subtle topography characterize the Toulouse area. The temporal distribution of satellite acquisitions, with more dates for the Toulouse area can also favor the learning process of the model. Lastly, the uneven number of training samples allows the models of Toulouse to integrate twice the number of polygons used for Mâcon for learning each vegetation class (see Table 2.7).

4.2.2 Evaluation of single-class SenRVM models

This study aims to investigate if multi-class model results could be improved by training SenRVM on single-class datasets. Hence, three SenRVM models are individually trained on grassland, crop and forest datasets. Hyperparameters are empirically tuned according to each vegetation class (Table 4.1). Results obtained over Mâcon and Toulouse are shown in Table 4.3. The minimum R^2 and the maximum MAE are here respectively equal to 0.8384 and 0.0443. Results of single-class and multi-class models are of the same order of magnitude. The differences found with the multi-class model are highlighted in green (improvement) or red (decrease).

The highest accuracies are reached by the crops class for both study areas, exhibiting similar results. Conversely, grasslands obtain the worst results and the highest standard deviations. This can be explained by its high intra-class variability and the important number of abrupt events impacting them. Although some R^2 differences are observed between crops and grasslands, similar results are obtained for the rest of the precision metrics. Forest class results obtain the lowest precision errors which are related to the class signal stability. Human intervention in forests remains rare and their phenology response curve only variates with

some specific factors such as climate. Some differences are observed by comparing the forest results obtained in the two study areas. The best performances are reached in Toulouse which can be justified by a higher number of training samples, that is, as previously stated, approximately double that of the Mâcon area.

Sub-class results (*i.e.*, according to the grassland or crop declarative code and the forest species) are subsequently computed from the single-class. Sub-class related results can be found in Appendix. 6.2. Satisfactory stability of the results are observed among the sub-classes despite a considerable variation in the number of samples. The results for three sub-classes, namely, maize, winter wheat and alfalfa, can be compared to those obtained in a similar study (Zhao et al., 2020). For maize and winter wheat, Zhao et al., 2020, obtained R^2=0.9409 and R^2=0.9157, respectively. SenRVM results, averaged on both Mâcon and Toulouse areas, are broadly similar although higher, especially for maize, with R^2=0.9465 and R^2=0.9635 for winter wheat and maize, respectively. It should be noted that the SenRVM results were obtained over much larger study areas than those evaluated in Zhao et al., 2020. For the alfalfa class, the only one related to grasslands in Zhao et al., 2020, the results obtained by SenRVM largely outperform the ones presented in Zhao et al., 2020. In the latter study, authors stipulate *the very complex alfalfa NDVI trends compared to other major crops* to justify the decrease in accuracy found. For the alfalfa class, authors achieved a R^2 of 0.7018. SenRVM obtains significantly higher correlation, with R^2=0.8425 over alfalfa classes (*i.e.*, several declarative codes are related to alfalfa, which are averaged). This difference can be explained by several factors, such as the integration of the two Sentinel-1 orbits, larger study areas allowing for more robust model learning, or the integration of ancillary data allowing for contextualization of the SAR measurements. Section 4.3.4 will further compare SenRVM results with other commonly employed methods in two contexts of missing data.

Table 4.3: Class-specific average results ± standard deviations, over all the predicted instant of times and for all testing polygons. Differences with results obtained with the multi-class model are marked in green (improvement) or red (decrease).

		Mâcon	Toulouse
Grasslands	R^2	0.8384 (+0.0038) ± 0.0152	**0.8464** (+0.0089) ± 0.0115
	MAE	**0.0418** (+0.0011) ± 0.0058	0.0443 (-0.0002) ± 0.0029
	MSE	0.0040 (+0.0003) ± 0.0009	**0.0037** (-0.0002) ± 0.0006
	RMSE	0.0629 (+0.0018) ± 0.0069	**0.0606** (-0.0011) ± 0.0049
Crops	R^2	0.9433 (+0.0033) ± 0.0017	**0.9676** (+0.0001) ± 0.0037
	MAE	0.0420 (-0.0061) ± 0.0014	**0.0353** (-0.0019) ± 0.0038
	MSE	0.0040 (+0.0008) ± 0.0001	**0.0026** (+0.0001) ± 0.0005
	RMSE	0.0630 (+0.0065) ± 0.0010	**0.0503** (-0.0001) ± 0.0044
Forests	R^2	0.8486 (+0.0006) ± 0.0268	**0.9235** (+0.0030) ± 0.0106
	MAE	0.0343 (-0.0001) ± 0.0066	**0.0318** (-0.0017) ± 0.0051
	MSE	0.0032 (+0.0002) ± 0.0007	**0.0020** (-0.0001) ± 0.0005
	RMSE	0.0562 (+0.0013) ± 0.0057	**0.0450** (-0.0013) ± 0.0049

The little variations in results evidenced in Table 4.3 between single-class and multi-class models corroborate the accurate predictions of SenRVM, even in the case of a multi-class dataset with high data heterogeneity. Compared to single-class models, training a multi-class SenRVM model can offer some advantages as, for instance, the reduction of the number of parameters to be learned. Furthermore, the use of a large training dataset permits to increase the batch size, which reduces the computational times. The multi-class dataset learning phase took in average 71 mn while 113 mn were necessary to obtain the three single-class models. Similarly for Toulouse, 145 mn and 196 mn for multi-class and single-class models, respectively, were needed. Besides simplifying the parameter tuning, the reference data scarcity problem which may exist for minority classes can be reduced by training a multi-class model. In addition, the variability of multi-class training data

is usually increased. Therefore, multi-class SenRVM models can improve their generalization performances and potentially reduce overfitting, while preserving accurate results.

Figure 4.1 provides visual examples of SenRVM predicted time series for the three vegetation classes and for both main study areas (Mâcon on the top and Toulouse at the bottom).

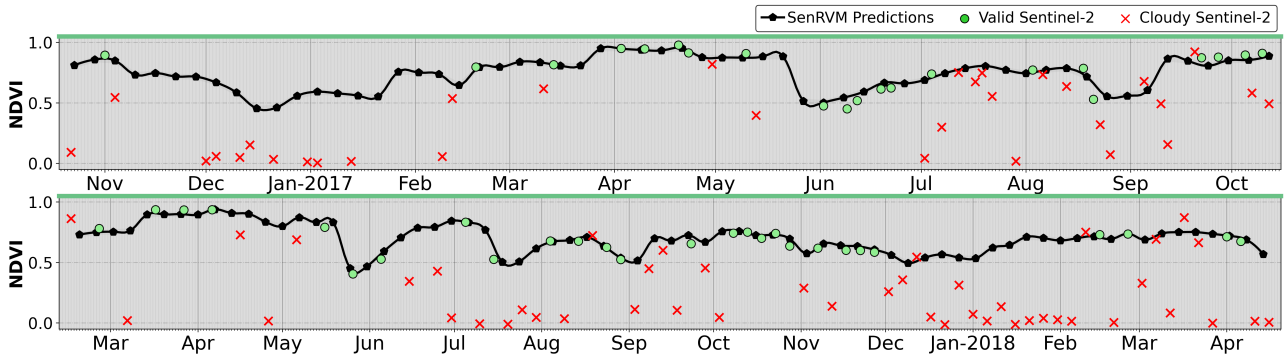

(a) SenRVM grassland time series: *top :* permanent grassland in Mâcon; *bottom :* rye-grass in Toulouse.

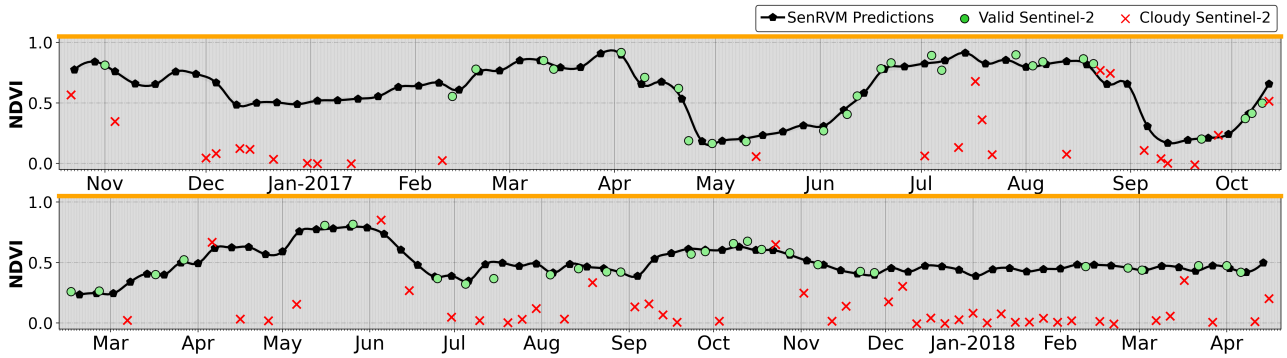

(b) SenRVM crop time series: *top :* maize in Mâcon; *bottom :* winter barley in Toulouse.

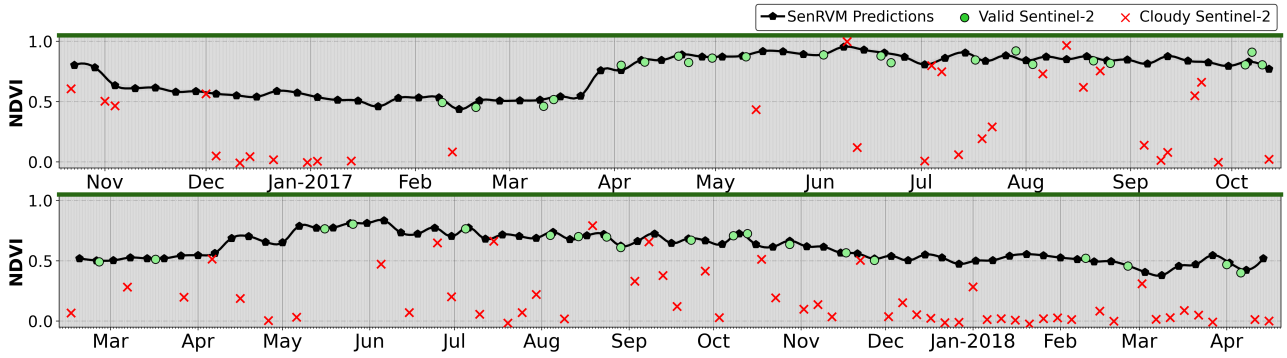

(c) SenRVM forest time series: *top :* scots pine in Mâcon; *bottom :* deciduous oak in Toulouse.

Figure 4.1: NDVI time-series predicted from SenRVM for the Mâcon and Toulouse areas over three common vegetation classes: *top:* grasslands, *middle:* crops, *bottom:* forests. Sentinel-2 acquired NDVI is depicted with green dots while red crosses indicates cloudy observations. Illustrated parcels are from the test datasets meaning that they were not used during training.

The six illustrated polygons belong to the test dataset and have not been used during training. It is visually possible to see that the predictions are very close to the NDVI values observed by Sentinel-2. Moreover, the

different phenologies apparent between vegetation types are accurately reproduced by SenRVM predictions. Several technical acts are observable for the two grassland time series and for the Macon corn parcel with a catch crop harvested late April. The stability of forests is evidenced by time series with low temporal variance.

4.3 Empirical analysis of the SenRVM results

Both fine quantitative and qualitative analysis are carried out for the Mâcon and Toulouse areas. First, spatial assessment evaluates the effect of size and location of polygons on the reconstruction accuracy. In a second step, the time-dependent accuracy of SenRVM is evaluated on different dates and seasons of the year. The temporal assessment also evaluates how the number of valid Sentinel-2 acquisitions can influence the SenRVM performances. The importance of the different input SenRVM features is then evaluated by an ablation study. To further assess the SenRVM performances, the proposed methodology is compared with standard interpolation and ML regression methodologies. The SenRVM prediction accuracy is evaluated on small and significant temporal data gaps.

4.3.1 Spatial and qualitative analysis

Ten size categories are defined to assess if the results fluctuate according to the size of the parcels. Each category contains the same number of polygons. In general, the number of polygons for each category is similar for both study areas (Figure 4.2). Only small differences are found for grasslands since large summer pastures covering several hundred hectares are present in the Toulouse area.

The SenRVM single-class results obtained in Section 4.2.2 are studied according to the ten size categories. Figure 4.2 shows the obtained results where, for each vegetation class, the Pearson correlation coefficient r_p between the polygon size and the R^2 score is also displayed. The results show that a strong correlation exists between both the polygon size and the prediction performances, with the highest accuracy obtained by the largest polygons.

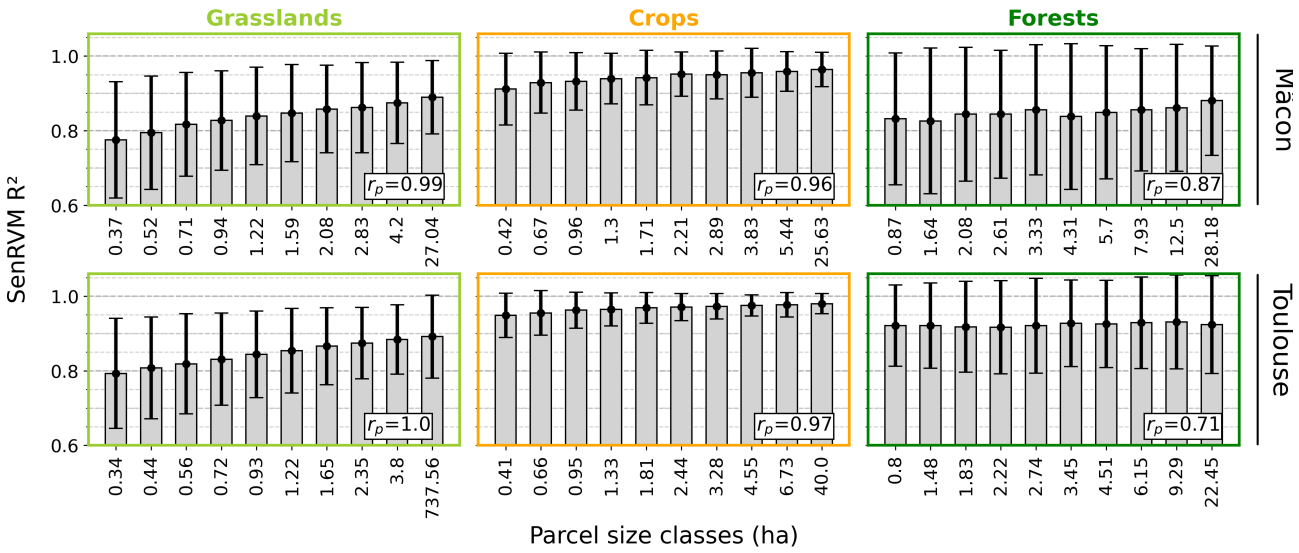

Figure 4.2: SenRVM accuracy evaluated according to the polygon size. Ten polygon size classes of equal population are defined for each vegetation class (columns) and both areas (rows). Average R^2 of SenRVM per-class predictions and their standard deviation are displayed. Pearson correlation coefficient r_p between SenRVM predictions and polygon sizes are displayed on the bottom right corner of each plot.

Grasslands reach the highest correlation coefficients, higher than 0.99 for both study areas. In contrast, the lowest correlation coefficients are obtained on forests. The strong correlation obtained on grasslands and crops can be mainly explained by three reasons. First, large polygons contain more pixels and the resulting statistics (*i.e.*, mean, median, and standard deviation used as features) are more meaningful and less sensitive to outliers. Second, the mechanization of farming practices on large agricultural parcels leads to the presence of more homogeneous and human-controlled vegetation covers. Time series describing homogeneous vegetation polygons lead to more predictable and reliable results. Lastly, large polygons are less affected by the SAR speckle noise given the proposed object-oriented approach. Although similar satisfactory results are obtained for the three classes, the effects of polygon size on prediction accuracies are different. The R^2 difference between small and large polygons is minimal for crops and forests. In contrast, for grasslands, the impact of polygon size appears greater with R^2 gains of about 0.1 for larger polygons.

Following the same idea, the effects of the altitude, slope, and exposure of polygons on SenRVM results are also studied. The altitude of the parcels does not seem to influence the SenRVM performances with correlation coefficients close to 0. Slope and exposure exhibit a significant negative correlation ($-0.75 < r < -0.6$), except for forests. In the case of grasslands and crops, the increase of slope and exposure decreases the prediction quality. A possible explanation for these correlations is related to grassland management. Parcel with a significant slope are less suitable for intensive exploitation and are generally larger (*e.g.*, mountain pastures). Larger plots are likely to incorporate greater intra-plot variability and extensively farmed plots have less predictable phenologies, which may explain lower SenRVM performance. Nevertheless, the correlations obtained for these three topographic features are not as significant as the ones presented in Figure 4.2. Consequently, these results are not further explored in the following.

Figure 4.3 shows the spatial distribution of the R^2 results obtained by SenRVM for both study areas. A four-color map is used to evaluate the defined the R^2 scale ranges. Ranges are chosen accordingly to the results, with four classes that can correspond to *poor*, *average*, *good* and *very good* results. Results show that high relief areas obtain the poorest SenRVM performances. This can be observed by looking at the Eastern part of Mâcon and the Southern part of Toulouse. The zoom box of each area is superimposed with a DTM. Light colors describe high altitude areas, where an accuracy decrease is observed in mountainous areas. Polygons located on mountain regions can suffer from non-exploitable Sentinel-1 data (*i.e.*, due to geometric effects such as layover or foreshortening). Furthermore, as these high relief parts also have strong slopes and exposures, this visual assessment confirms the quantitative correlation results.

Another interesting remark is that SenRVM errors seem not to be concentrated in specific areas but rather isolated. It is worth reminding that the R^2 measures the co-variation between the labels and the predictions. Low R^2 values therefore do not necessarily indicate erroneous predictions. Conversely, high R^2 can be obtained from far predictions with a constant shift. For example, if predictions are constantly shifted to 0.1 from the labels, the R^2 would be of 1. As such, a combined analysis of R^2 and MAE is needed to detect parcels with potential learning errors. Only 0.15% of the parcels for Mâcon (43 out of 27,932) and Toulouse (out of 50,103) have R^2<0.5 and MAE>0.1.

Qualitative analysis of the results obtained over these parcels has highlighted three potential error sources which will affect the accuracy metrics: (i) cloud & shadow mask errors; (ii) parcels remaining as bare soil thorough the entire agricultural season; (iii) reference data errors.

Figure 4.4 illustrates examples of the three error sources over the Mâcon area. For the three SenRVM predicted time series, accuracy metrics are poor (R^2<0.5 and MAE>0.1).

Figure 4.4a shows a cloud mask error occurring on January 13: a cloudy acquisition is marked as valid. The corresponding Sentinel-2 RGB image easily confirms the error. SenRVM prediction for this date is far from the erroneously valid label. On the one hand, it can be considered satisfactory that the prediction does not replicate the mask error. Nevertheless, this label is taken into account in the calculation of metrics, which

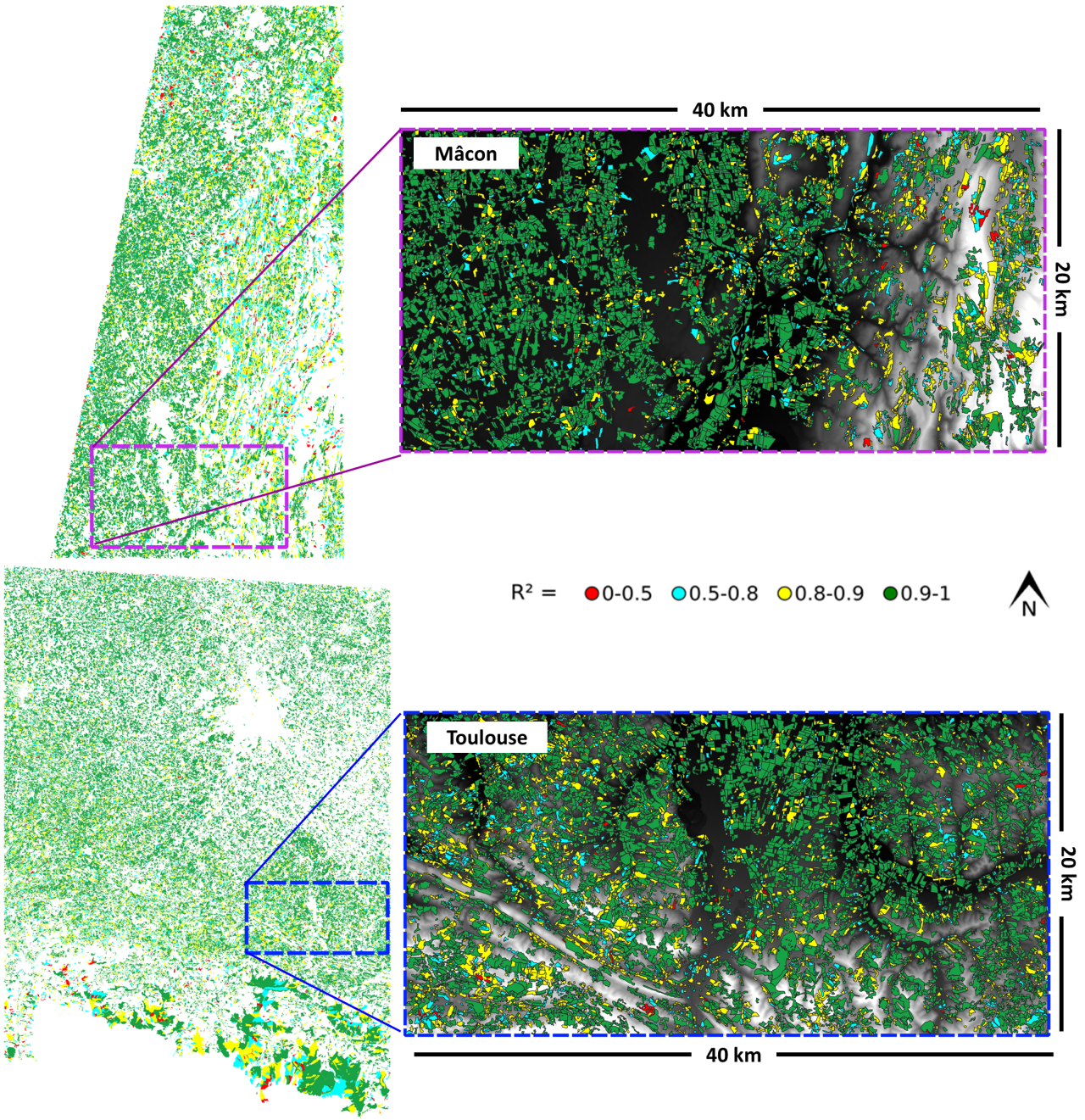

Figure 4.3: Spatial visualization of the SenRVM performance obtained on all vegetation polygons. DTM is displayed as base-map in the zoom boxes. Four scale R2 ranges are used to evaluate SenRVM predictions which exhibit less accurate prediction in mountainous areas (East part of Mâcon and South part of Toulouse).

will be low. The impact of these mask errors will be discussed later in Section 4.5.1.

A parcel declared as permanent grassland in the RPG is depicted in Figure 4.4b. Nonetheless, from the NDVI time series as well as the Sentinel-2 RGB images, it is observed that this parcel remains in bare ground thorough the entire agricultural season. The sufficient number of valid dates, especially during the growing season, suggests no doubt about this outcome. Although the corresponding SenRVM time series appropriately has little temporal variation, it is observed a relatively constant overestimation for most of the predictions.

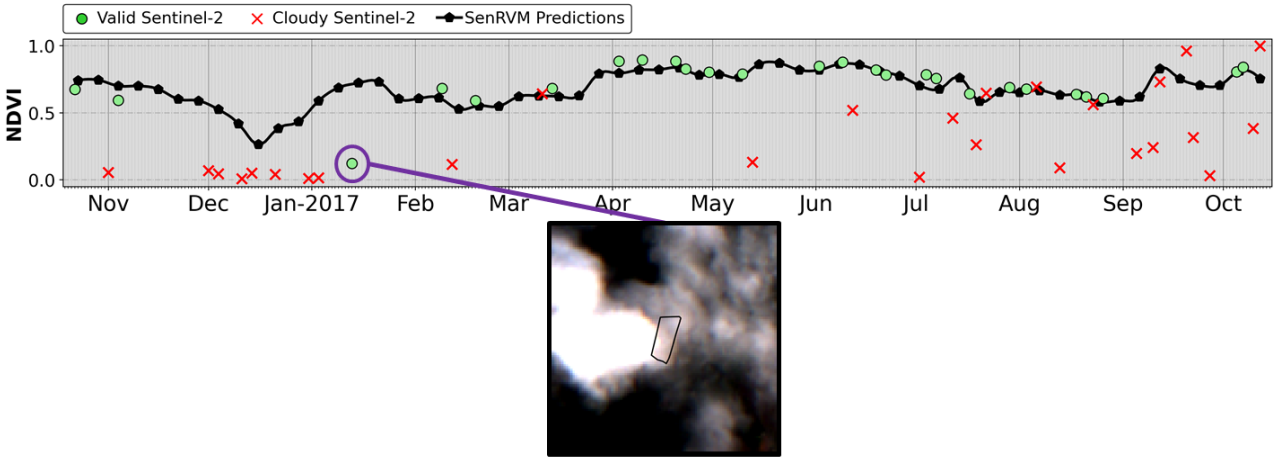

(a) Cloud mask error flagging a cloudy acquisition as valid.

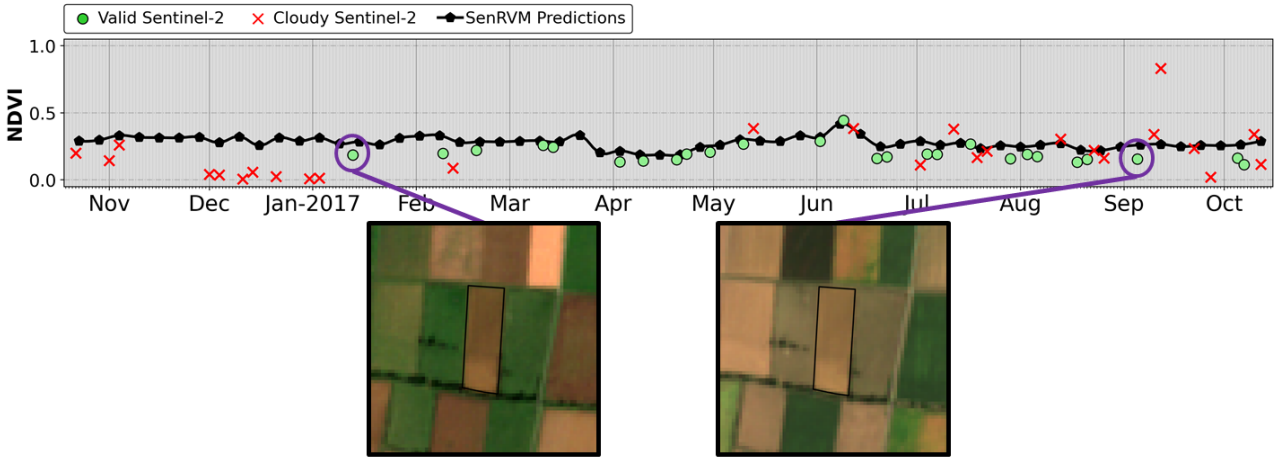

(b) Bare soil characterizing a permanent grassland thorough the entire agricultural season.

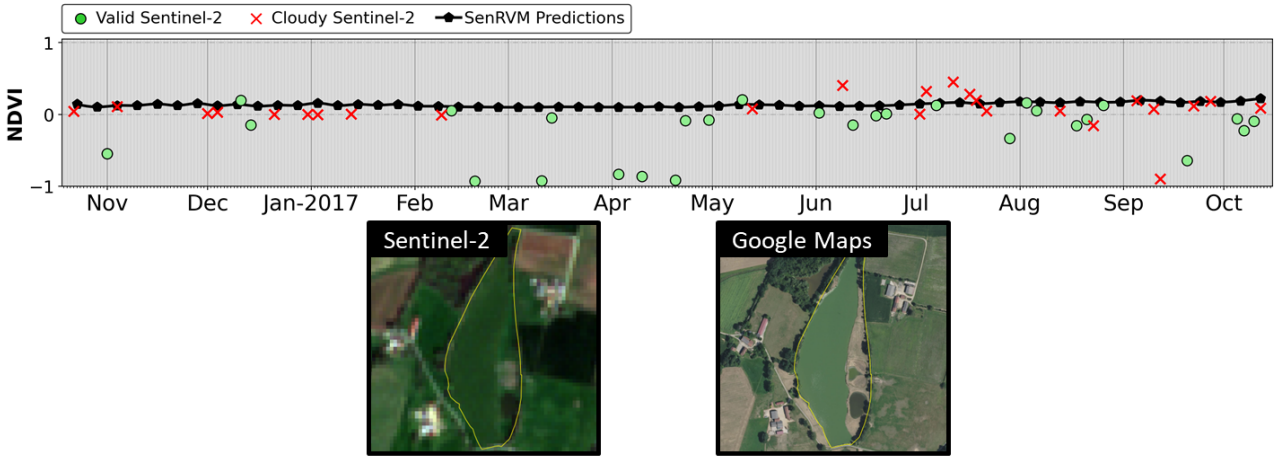

(c) RPG declared permanent grassland being a pond.

Figure 4.4: Most prominent types of errors leading to poor SenRVM regression accuracy metrics.

It is first possible to explain this overestimation by the very small number of parcels with such low NDVI values. Furthermore, the use of a sigmoid activation as an output of the network is not suitable for estimating NDVI of a surface other than vegetation.

Finally, Figure 4.4c illustrates a type of error that is fortunately relatively uncommon but can be encountered. A RPG declared parcel as permanent grassland is characterized by very low NDVI values, mostly bellow zero. The Sentinel-2 spatial resolution does not directly explain these low values. Using a higher spatial resolution image (from the same year on Google Maps), we can nevertheless see that this parcel declared as grassland is in fact a pond. This is confirmed by the sun glitter observed on the pond. Water surfaces appear specular to SAR, which is very sensitive to humidity (Section 2.4.2). Thus, the resulting time series of SenRVM appear flat. Although these cases necessarily affect the metrics obtained by SenRVM, they are inherent to the reference data. In the framework of large-scale studies proposed here, the fine quantification of errors, their impact, and the correction of reference data is practically unfeasible. An uncertainty on the exact quality of the results can therefore be included, but can only with difficulty be quantified and rectified. Within the framework of this work, a qualification step of the reference data is therefore not included.

4.3.2 Temporal analysis

The second evaluation carried out here assesses the intra-annual consistency of the SenRVM results. For each single date, the SenRVM performances are evaluated by computing the MAE. Only valid NDVI measurements not affected by clouds are considered. The MAEs and their respective standard deviations obtained are shown in Figure 4.5. To simplify the result interpretation (and considering the similar results obtained for the three classes), the results are averaged across the three vegetation classes.

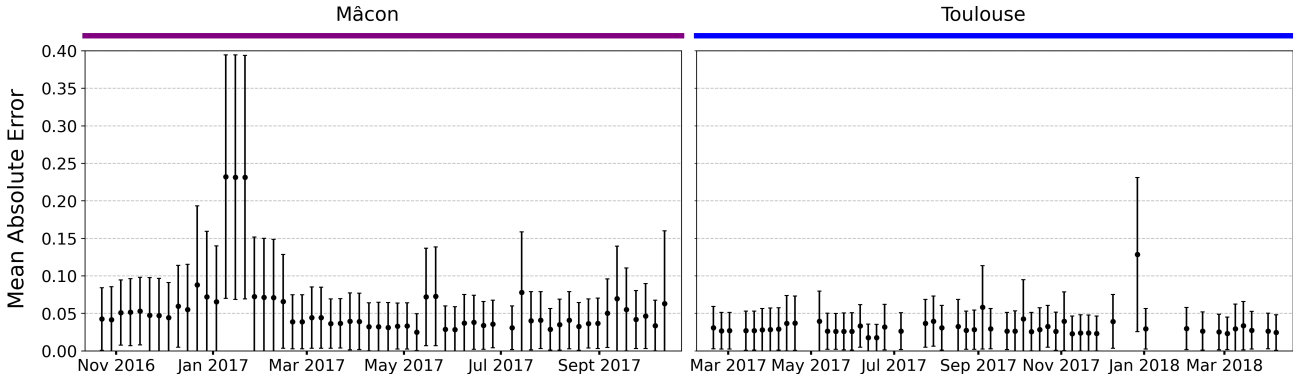

Figure 4.5: MAE obtained for each date comparing the non cloudy NDVI observations with their corresponding SenRVM predictions. Results are averaged for the three classes and reported for the Mâcon (left) and Toulouse (right) areas. Large MAE are explained by the presence of cloud & shadow mask errors.

As observed, most of the dates obtain MAE lower than 0.05, which confirms the high SenRVM performances. The two study areas show similar and satisfactory results despite the timelines of image acquisitions are different. Some abnormal MAE higher than 0.2 are visible in January (Mâcon area) and December (Toulouse area). These high values are explained by the presence of cloud & shadow mask errors which were visually confirmed. At these dates, the corresponding validity flags denote as valid numerous cloudy Sentinel-2 observations. In this situation, the NDVI values predicted by SenRVM are compared with invalid NDVI measures (see Section 4.5.1). As a result, MAE calculated for those dates is high, however, without indicating a limitation in the learning process.

Further analysis is carried out to evaluate if MAEs are influenced by the yearly season. Previous per-date results are averaged over the four seasons of the year as illustrated in Figure 4.6. At the bottom of the figure,

the percentages of cloudless NDVI measurements per season are also reported. Despite the seasons having a similar number of valid optical observations (except for spring in Mâcon), the winter period obtains the highest MAEs. These high values can be explained by the persistent winter cloud coverage producing large gaps without Sentinel-2 images (see Figure 2.2.2).

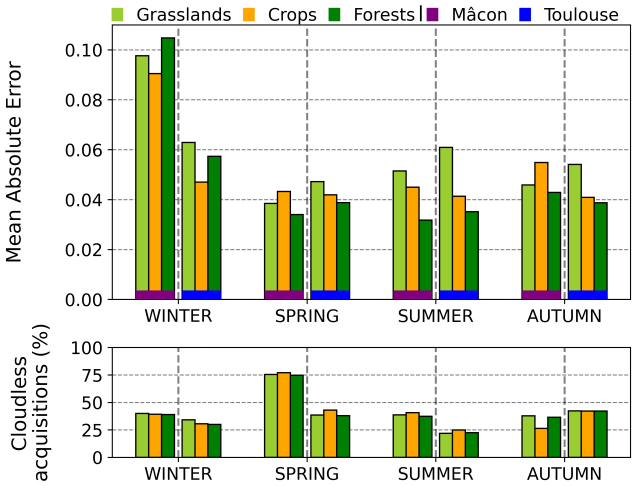

Figure 4.6: On top, MAE computed for the four seasons of the year are shown for both study areas. The bottom chart indicates the percentage of cloudless observations available per season.

Although Figure 4.5 shows similar MAEs for both study areas, they are differently impacted by cloud coverage as shown in Figure 2.2. Considering the R^2 between predicted and expected NDVI time series of each polygon, correlation between R^2 and the number of cloudless NDVI observations used is also investigated. Although 60 dates are available for the Mâcon area, cloudless measurements are ranging from 18 to 43 among all polygons. Concerning Mâcon, the valid number of observations ranges from 7 to 35 out of the 71 dates. Significant correlation, above 0.7, is only found for grasslands and crops from the Mâcon area. In these cases, the performances are improved with an increased number of cloudless NDVI observations available for training. These results must be nevertheless tempered since the temporal distribution of missing data nor their duration are taken into account in this study. Moreover, the number of polygons greatly varies between classes. The results are therefore indicative and are not illustrative.

4.3.3 Ablation study of SenRVM inputs

The proposed ablation study describes the relevance assessment of the various features. The potential simplification or complexity in the design of the deep-based architecture is not evaluated. An ablation study is presented here by analyzing the SenRVM performances obtained with 6 input feature set scenarios. The study aims to evaluate the impact of the input features on the SenRVM predictions. The first scenario is the baseline (denoted as ALL), in which the input SenRVM data corresponds to all features described in Section 2.5. The other 5 scenarios are constructed by removing some specific features from the baseline one.

Referring to Table 2.8, 2.9 and 2.10, the σ^0 (3) and γ (4) features are removed, respectively, for the SIG and COH scenarios. In the SAR scenario, all features derived from Sentinel-1 and denoted as (3), (4), (5), and (6) are not considered. This should help to observe the importance of the SAR-based features for the regression task. The AUX scenario studies the removal of (7), (8), and (9) ancillary features from ALL. Finally, the MASK scenario investigates how SenRVM performance differ when the validity flags provided by the cloud & shadow masks are not incorporated in the loss function. The different scenarios consider the same SenRVM parameter configurations and the same train/validation/test datasets. Table 4.4 provides information

on the different families of features removed for each scenario, while Table 4.5 shows the size of the inputs for each parcel at each date and for one branch of the SenRVM encoder w.r.t. each scenario.

Table 4.4: SenRVM ablation study with 6 scenarios. For detailed features description, see Table 2.8, 2.9 and 2.10 of Chapter. 2.

		SenRVM INPUTS					
		σ^0	γ	climate	topography	metadata	masks
SCENARIOS	ALL	✓	✓	✓	✓	✓	✓
	SIG	✗	✓	✓	✓	✓	✓
	COH	✓	✗	✓	✓	✓	✓
	SAR	✗	✗	✓	✓	✓	✓
	AUX	✓	✓	✗	✗	✗	✓
	MASK	✓	✓	✓	✓	✓	✗

Table 4.5: Inputs size of the SenRVM methodology varying with the different ablation study scenarios. The input sizes correspond to the SAR and AUX features (Section 3.3.3.1) of one branch of the architecture used in the SenRVM methodology (Section 3.3.3.2).

		SenRVM INPUT SIZES (SAR / AUX)							
		Mâcon				Toulouse			
		Multi-class	Grasslands	Crops	Forests	Multi-class	Graslands	Crops	Forests
SCENARIOS	ALL	25 / 104	25 / 83	25 / 63	25 / 79	25 / 103	25 / 81	25 / 63	25 / 79
	SIG	10 / 104	10 / 83	10 / 63	10 / 79	10 / 103	10 / 81	10 / 63	10 / 79
	COH	15 / 104	15 / 83	15 / 63	15 / 79	15 / 103	15 / 81	15 / 63	15 / 79
	SAR	0 / 104	0 / 83	0 / 63	0 / 79	0 / 103	0 / 81	0 / 63	0 / 79
	AUX	25 / 0	25 / 0	25 / 0	25 / 0	25 / 0	25 / 0	25 / 0	25 / 0
	MASK	25 / 104	25 / 83	25 / 63	25 / 79	25 / 103	25 / 81	25 / 63	25 / 79

A visual interpretation of the ablation study results is illustrated in Figure 4.7, where the summarized results of each specific scenario are compared with the ALL scenario. For this visual evaluation, a global score is computed by averaging the four metrics obtained by both study areas. To take into account that the metrics have different ranges, they are normalized between 0 and 1 by considering the results of the different scenarios. The best result, obtained here in each case by ALL, is 1. Conversely, 0 indicates the worst result among the assessed scenarios. The global score is used to represent the accuracy decrease in Figure 4.7. The arrow direction represents the accuracy decrease between the best (top) and worst (bottom) scenarios.

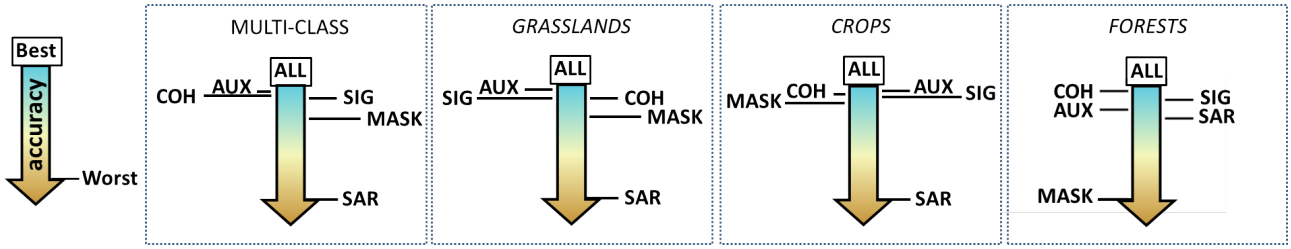

Figure 4.7: Ablation study results obtained by the multi-class and single-class SenRVM models. The accuracies of the five scenarios are compared to the baseline (ALL) by using a global score summarizing the four metrics results obtained for both study areas. The arrow direction represents the accuracy decrease between the best and worst scenarios.

The results of the ablation study are detailed in Table 4.6, where the different scenarios are both evaluated

with multi-class and single-class models. The four metrics (MAE, MSE, RMSE and R^2) are computed to assess the results over Mâcon and Toulouse. Both study areas obtain similar results and attest that as expected, the highest accuracies are obtained by the ALL scenario. This result corroborates that none of the set of features removed from the different input data scenarios decrease the optimal ALL SenRVM accuracy. Only forest class models obtain different feature removal impact, indicating a contrasting feature importance in the regression task over forests.

SAR results : the worst prediction accuracies are obtained by the SAR scenario where all features derived from Sentinel-1 are removed. Looking at the R^2 values obtained by single-class grassland model, it can be observed that SAR scenario obtains low values (around 0.55) compared to the baseline ALL scenario ($\approx$ 0.84) for both study areas. Similar results are obtained by the multi-class model, which is expected given that multi-class data is mostly populated by grasslands. The R^2 performance decrease is also observed on single-class crop results, however lesser with a decrease of 0.2. As discussed in Section 2.6.1 a high intra-class variability exists in grasslands and crops classes. Furthermore, the time series describing these classes have many abrupt breaks (*i.e.*, due to agricultural practices). Ancillary data are in these cases not sufficient to model the NDVI yearly behavior. The importance of Sentinel-1 data is here highlighted by its capacity in delivering precise and temporally close information describing vegetation polygons. The SAR scenario thus leads to a significant performance decrease. Concerning single-class forest models, the removal of SAR features seems less important (decrease of about 0.02) for both study areas. This result is explained by the importance of ancillary data over forests, explained below.

AUX results : the lowest accuracy decrease ($\approx$ 0.02 of R^2) is obtained by single-class models trained on grasslands and crops and, consequently to their important number of samples, by the multi-class model. In contrast, the removal of AUX features seems to have a strong impact on the single-class forests model. Results obtained by the AUX scenario are, for forests, almost equivalent to the SAR scenario. This surprising results are explained by the low temporal variability of forest NDVI curves, which only exhibit small fluctuations due to seasonal climate evolution. Information provided by the ancillary data is less prone to noise compared to satellite remote sensing features. For forests, ancillary data are thus valuable for obtaining satisfactory reconstruction results.

SIG and COH results : the results obtained by all SenRVM models for both study areas corroborate that the importance of σ^0 and γ features are relatively similar. The decrease of R^2 observed for the two scenarios ranges from 0.01 to 0.06. Despite the similar results, some differences can be discussed between both scenarios. For instance, the high standard deviations obtained by SIG scenario indicate a slightly superior importance of σ^0 features. In this case, the results may be more stable as the number of inputs differs between both scenarios (*i.e.*, σ^0 additional VV/VH polarization ratio band). Furthermore, while temporal information is directly integrated in γ features, the use of RNNs to extract temporal dependencies akin to γ information may explain this result. Opposite results can be observed between Mâcon and Toulouse areas concerning the impact of the SIG and COH scenarios. The contradictory results may be due to temporal and spatial differences existing in both areas. Concerning single-class forest results, it can be observed that the removal of one of these two families of features does not greatly impact the performances.

MASK results : in general, the MASK scenario results obtained by the different SenRVM models indicate that the incorporation of the validity flags in the loss function is beneficial. This scenario obtains, excluding the single-class forest results, the second most significant performance reduction. The performance decrease is more visible on single-class grassland results with R^2 of 0.78 and 0.73 for Mâcon and Toulouse, respectively. For forests, the MASK scenario leads to the worst overall results. As in this case cloud & shadow mask information is not incorporated in the loss function, important label noise is affecting the training process. This noise prevents an accurate learning of the small variations observed in the forest time series (see Figure 4.1).

Table 4.6: Average results and ± standard deviation for the ablation study. Five input data scenarios are compared to the baseline scenario (ALL) for which the complete dataset described in Table 2.8, 2.9 and 2.10 is used. Four metrics are provided for the grasslands, crops, forests and multi-class datasets. Grey indicates the baseline, green color indicates the input removal having the lowest impact on performances, while the red color denotes the highest.

Multi-class (Grasslands, Crops, Forests)

		R^2	MAE	MSE	RMSE
Mâcon	**ALL**	**0.8650 ± 0.0121**	**0.0419 ± 0.0065**	**0.0039 ± 0.0010**	**0.0624 ± 0.0069**
	- COH	0.8293 ± 0.0097	0.0459 ± 0.0030	0.0046 ± 0.0004	0.0681 ± 0.0028
	- SIG	0.8346 ± 0.0100	0.0469 ± 0.0029	0.0048 ± 0.0004	0.0689 ± 0.0029
	- AUX	0.8458 ± 0.0145	0.0443 ± 0.0060	0.0043 ± 0.0008	0.0654 ± 0.0058
	- SAR	0.6314± 0.0084	0.0848 ± 0.0019	0.0148 ± 0.0004	0.1217 ± 0.0015
	- MASK	0.7854 ± 0.0152	0.0532 ± 0.0041	0.0058 ± 0.0007	0.0761 ± 0.0041
Toulouse	**ALL**	**0.8947 ± 0.0056**	**0.0404 ± 0.0039**	**0.0030 ± 0.0005**	**0.0545 ± 0.0038**
	- COH	0.8669 ± 0.0071	0.0452 ± 0.0024	0.0038 ± 0.0003	0.0616 ± 0.0022
	- SIG	0.8562 ± 0.0111	0.0498 ± 0.0050	0.0045 ± 0.0007	0.0671 ± 0.0049
	- AUX	0.8778 ± 0.0135	0.0435 ± 0.0055	0.0035 ± 0.0008	0.0587 ± 0.0057
	- SAR	0.5758 ± 0.0067	0.1194 ± 0.0021	0.0267 ± 0.0004	0.1634 ± 0.0012
	- MASK	0.8179 ± 0.0152	0.0531 ± 0.0044	0.0054 ± 0.0007	0.0732 ± 0.0046

Grasslands

		R^2	MAE	MSE	RMSE
Mâcon	**ALL**	**0.8384 ± 0.0152**	**0.0418 ± 0.0058**	**0.0040 ± 0.0009**	**0.0629 ± 0.0069**
	- COH	0.7891 ± 0.0081	0.0470 ± 0.0021	0.0048 ± 0.0004	0.0691 ± 0.0027
	- SIG	0.8011 ± 0.0115	0.0470 ± 0.0038	0.0048 ± 0.0006	0.0690 ± 0.0041
	- AUX	0.8159 ± 0.0147	0.0439 ± 0.0043	0.0043 ± 0.0007	0.0657 ± 0.0048
	- SAR	0.5557 ± 0.0061	0.0791 ± 0.0019	0.0122 ± 0.0005	0.1106 ± 0.0023
	- MASK	0.7893 ± 0.0819	0.0528 ± 0.0063	0.0060 ± 0.0011	0.0772 ± 0.0063
Toulouse	**ALL**	**0.8464 ± 0.0115**	**0.0443 ± 0.0029**	**0.0037 ± 0.0006**	**0.0606 ± 0.0049**
	- COH	0.8076 ± 0.0106	0.0506 ± 0.0032	0.0046 ± 0.0005	0.0677 ± 0.0037
	- SIG	0.7976 ± 0.0173	0.0526 ± 0.0040	0.0050 ± 0.0007	0.0706 ± 0.0047
	- AUX	0.8256 ± 0.0114	0.0470 ± 0.0025	0.0040 ± 0.0005	0.0635 ± 0.0037
	- SAR	0.5535 ± 0.0093	0.0914 ± 0.0016	0.0151 ± 0.0004	0.1231 ± 0.0016
	- MASK	0.7332 ± 0.0173	0.0579 ± 0.0034	0.0063 ± 0.0006	0.0791 ± 0.0034

Crops

		R^2	MAE	MSE	RMSE
Mâcon	**ALL**	**0.9433 ± 0.0017**	**0.0420 ± 0.0014**	**0.0040 ± 0.0001**	**0.0630 ± 0.0010**
	- COH	0.9270 ± 0.0070	0.0490 ± 0.0042	0.0052 ± 0.0007	0.0718 ± 0.0043
	- SIG	0.9220 ± 0.0080	0.0516 ± 0.0058	0.0057 ± 0.0010	0.0753 ± 0.0059
	- AUX	0.9358 ± 0.0081	0.0466 ± 0.0075	0.0047 ± 0.0010	0.0684 ± 0.0076
	- SAR	0.7212 ± 0.0080	0.1181 ± 0.0051	0.0257 ± 0.0011	0.1603 ± 0.0034
	- MASK	0.9176 ± 0.0100	0.0536 ± 0.0077	0.0061 ± 0.0015	0.0776 ± 0.0085
Toulouse	**ALL**	**0.9676 ± 0.0037**	**0.0353 ± 0.0038**	**0.0026 ± 0.0005**	**0.0503 ± 0.0044**
	- COH	0.9584 ± 0.0048	0.0389 ± 0.0040	0.0031 ± 0.0005	0.0551 ± 0.0042
	- SIG	0.9526 ± 0.0039	0.0422 ± 0.0048	0.0037 ± 0.0006	0.0608 ± 0.0045
	- AUX	0.9652 ± 0.0026	0.0363 ± 0.0031	0.0027 ± 0.0004	0.0517 ± 0.0035
	- SAR	0.7151 ± 0.0076	0.1293 ± 0.0039	0.0296 ± 0.0007	0.1720 ± 0.0021
	- MASK	0.9501 ± 0.0062	0.0440 ± 0.0063	0.0041 ± 0.0011	0.0634 ± 0.0076

Forests

		R^2	MAE	MSE	RMSE
Mâcon	**ALL**	**0.8486 ± 0.0268**	**0.0343 ± 0.0066**	**0.0032 ± 0.0007**	**0.0562 ± 0.0057**
	- COH	0.8443 ± 0.0182	0.0352 ± 0.0042	0.0034 ± 0.0005	0.0582 ± 0.0043
	- SIG	0.8349 ± 0.0234	0.0365 ± 0.0050	0.0035 ± 0.0006	0.0587 ± 0.0044
	- AUX	0.8189 ± 0.0243	0.0373 ± 0.0050	0.0037 ± 0.0005	0.0604 ± 0.0041
	- SAR	0.8207 ± 0.0056	0.0403 ± 0.0009	0.0043 ± 0.0003	0.0653 ± 0.0021
	- MASK	0.7119 ± 0.0266	0.0514 ± 0.0073	0.0064 ± 0.0010	0.0795 ± 0.0059
Toulouse	**ALL**	**0.9235 ± 0.0106**	**0.0318 ± 0.0051**	**0.0020 ± 0.0005**	**0.0450 ± 0.0049**
	- COH	0.9232 ± 0.0041	0.0317 ± 0.0015	0.0021 ± 0.0001	0.0454 ± 0.0015
	- SIG	0.9152 ± 0.0076	0.0340 ± 0.0034	0.0024 ± 0.0004	0.0484 ± 0.0033
	- AUX	0.9086 ± 0.0047	0.0343 ± 0.0026	0.0024 ± 0.0002	0.0487 ± 0.0024
	- SAR	0.9058 ± 0.0050	0.0395 ± 0.0012	0.0033 ± 0.0002	0.0577 ± 0.0018
	- MASK	0.8454 ± 0.0204	0.0483 ± 0.0081	0.0049 ± 0.0011	0.0698 ± 0.0070

4.3.4 Assessment against existing methodologies

Single-class SenRVM models are here evaluated against standard interpolation and machine learning (ML) regression methodologies. The robustness and efficiency of the methods are evaluated through their ability to reconstruct short- and long-term missing data gaps. The MAEs obtained for these two different scenarios are discussed in Sec 4.3.4.1 and Sec 4.3.4.2.

In these experiments, a new learning constraint is incorporated in the SenRVM training stage. The learning constraint ensures that satellite observations acquired on the dates that want to be predicted are not used to train the SenRVM models. It must be remarked that the same temporal grid is shared for the disjoint training and testing datasets used in the previous experiments. Therefore, a few non-cloudy observations acquired on the specific predicted date are most of the time considered in the training step. This is prevented here by completely masking the date during the training step.

The three ML regression algorithms described in the following are studied. For the three methods, the same SAR and ancillary input data as SenRVM is considered.

- a Random Forest Regression (RF) algorithm. This ensemble learning method is based on the construction of multiple decision tree classifiers (Belgiu and Drăguţ, 2016; Li et al., 2020c). The individual trees are built by applying a bagging strategy which randomly selects a subset of training samples and features. Following (Pelletier et al., 2016) conclusions, the number of trees is set to 100. The maximum number of features taken into account for tree splitting is set to the square root of the number of input features and the maximum depth of a tree to 25.
- a Gaussian Processes Regression function (GPR) with a squared exponential kernel (RBF) and length scale parameter of 10 with initialized bounds (*i.e.*, that are optimized during training) of [1e-3, 1e3]. The L-BFGS-B optimization algorithm commonly used with Gaussian Processes is retained (Liu and Nocedal, 1989). GPR is a non-parametric kernel-based probabilistic regression algorithm based on a Bayesian framework. GPR is selected given the convincing results obtained in similar regression tasks (Belda et al., 2020b; Mercier et al., 2020).
- a deep-based method using MLPs architecture (MLP). This simplified version of the SenRVM is obtained by removing the recurrent block (*i.e.*, GRU cells) from the architecture (Figure 3.7). The training is thus performed for each date individually without handling the inherent temporal information of the time series. The MLP method integrates 4 MLPs for encoding and 1 MLP for decoding.

A fair comparison of the three previous regression algorithms with SenRVM requires the use of the same training samples. Nevertheless, substantial computational problems can occur if all polygons and their entire corresponding NDVI time series are used for training RF and GPR methods. Therefore, a temporal sampling strategy is proposed for RF and GPR methods. The solution here proposed is to discard some dates that are temporally far from the prediction date. For half of the training polygons of SenRVM, the selected training dates correspond to the nearest past cloud-free date of each polygon. For the other half, the following cloud-free date is used. It must be remarked that besides the sampling selection strategy, the space-time evolution of the cloud coverage makes it possible to include numerous dates and cover up to several months. The same training sample size as for SenRVM and MLP is thus kept for the RF method while temporal information is fed to the model. Concerning the GPR method, the number of training polygons is nevertheless limited to 10, 000 polygons, due to long calculation times and memory constraints. It must be remarked that despite reducing the number of training samples, the resulting training dataset of GPR having 10,000 polygons remains significant. This only impacts grasslands in both areas and crops in the Toulouse area.

Besides the previous ML algorithms, two mono-sensor standard interpolation methods are also considered in this study:

- a Whittaker smoother (`WHIT`), which is based on a penalized least-square regression algorithm combining fidelity to the data and smoothness of the filtered sequence (Vuolo et al., 2017; d'Andrimont et al., 2020). The smoothing criterion (λ value) is set to 1. This low value preserves the temporal variability of the original signal, describing important changes in vegetation cover. The *d* parameter used in the penalty calculation is set to 2.
- a weighted linear interpolation method (`linear`), which assigns weights to neighboring observations (two before and after), based on the distance to the interpolated value.

Compared to the previous methods, the main difference is that `WHIT` and `linear` interpolation approaches only consider valid Sentinel-2 observations. These mono-sensor methods focus on exploiting the temporal trajectory of neighboring NDVI observations.The Decomposition and Analysis of Time Series Software (DATimeS, Belda et al., 2020a) is selected for the `WHIT` method. For the `linear` interpolation, the Orfeo ToolBox implementation (Grizonnet et al., 2017) is used.

4.3.4.1 Short-term data gaps

The short-term study consists in removing 6 individual non-consecutive acquisitions from the training datasets. The number of dates has been chosen to keep a sufficient learning set and to have a substantial amount of validation data available. The deletion of 6 dates corresponds to 10% and 8.45% of the time series of Mâcon and Toulouse, respectively, not taking into account the cloudy dates which increase these numbers considerably. The chosen dates are distributed along the complete year and have a low cloud cover rate. This therefore implies that a high number of measurements can be used to validate this experiment. Prediction results obtained on the six reconstructed dates are evaluated for the three vegetation classes and over the two study areas.

In the case of SenRVM and MLP method, a unique model is trained and used for the prediction of the six dates. In contrast, as a temporal sampling strategy is defined for the RF and GPR methods, six models are independently trained for the six masked dates.

Figure 4.8 shows that similar satisfactory results are obtained by the different methods which most of the time achieve MAE lower than 0.15. Grassland and forest results obtained on Mâcon show that high errors are obtained on the second reconstructed date (*i.e.*, February 14th). These high values are justified by the high number of cloud & shadow mask errors existing at this date.

Results show how SenRVM achieves accurate and comparable performances w.r.t. to standard interpolation methods. Furthermore, SenRVM obtains in most cases the lowest standard deviations. The interest of SenRVM is especially remarkable at the dates of June 8th over Mâcon and June 6th over Toulouse. At these dates, numerous anthropic activities exist given the agricultural calendar of grasslands and crops. These activities lead to phenology breaks in the time series (see Figure 2.7) occurring during the masked dates. For the ML regression methods, based on SAR data, an accurate reconstruction of these breaks is possible, whereas standard interpolation methods fail. A complementary discussion about break reconstruction can be found in Section 4.3.4.3. Concerning forests, the stability of the NDVI temporal trajectory of this class leads to obtain similar results for all methods. For this class, SenRVM obtains the best accuracies for three dates.

The RF, GPR and MLP methods generally obtain comparable results. The highest MAEs are obtained by these methods, especially remarkable on grasslands and crops. The RF method obtains slightly better results than GPR for several dates, and notably lower standard deviations. Over 18 assessed dates for each area, RF achieves greater accuracy than SenRVM for 4 dates over Mâcon and 3 dates over Toulouse. GPR reaches lower MAE than SenRVM for 2 dates over Mâcon and only one date over Toulouse. The upper accuracy found with SenRVM can be explained by several factors. In comparison to RF and GPR methods, entire time series are fed to SenRVM. The bi-directional RNN used in SenRVM can therefore extract long-term phenological stages

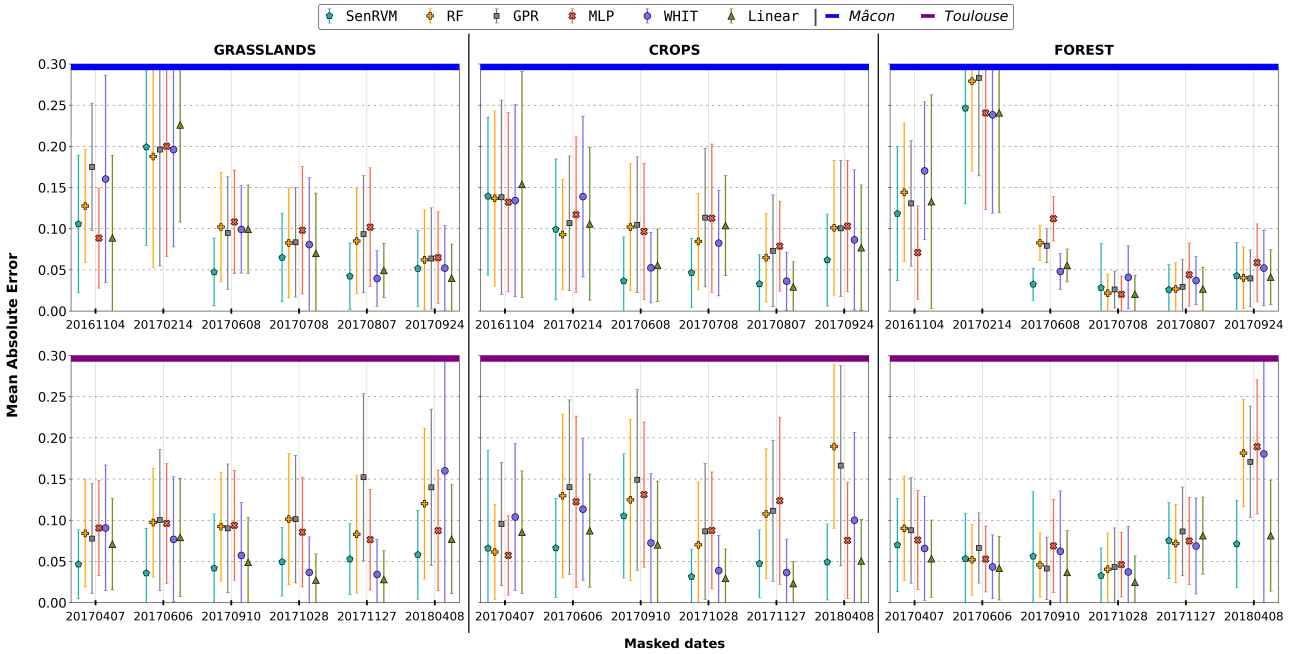

Figure 4.8: Comparison of gap filling performances over six non-consecutive dates, corresponding to short-term data gaps. Mean Absolute Error are assessed over Mâcon and Toulouse areas for the three vegetation classes.

helping accurate predictions. This long-term evolution may be neglected by the temporal sampling strategy of the RF and GPR methods. Another explanatory factor is the adoption of several encoding branches in the SenRVM and MLP methods, allowing more complex and descriptive features to be considered.

Regarding the results obtained by the MLP method, it only achieves the best results over the first date on crops for both areas and the first date over forests of the Mâcon area. The main explanatory factor is that MLP processed each date individually without exploiting temporal information. Comparing MLP with SenRVM results, the improvements achieved by recurrent networks are highlighted. For example, crop results obtained by MLP show a high MAE in Toulouse at the date of November 27th. At this date, bare soil covers most of the crops parcels which leads to the presence of large fluctuations in SAR time series. Processing individual dates with the MLP method produces low prediction results while recurrent cells permit accurate predictions, taking advantage of the full temporal trajectory.

This experiment also corroborates the good results of the commonly used `linear` interpolation method. Over the 12 reconstructed dates, the `linear` interpolation reaches the highest accuracies for 5 dates on grasslands and forests and 3 dates on crops. The satisfactory results can be explained by the availability of cloudless neighboring Sentinel-2 acquisitions, close to the reconstructed dates (see Figure 2.2). Therefore, information describing the temporal trajectory of NDVI allows the `linear` method to obtain low MAE. As expected, the WHIT approach obtains results similar to the `linear` method. This method exhibits the highest variability in the results that can be explained by the use of a smoothing function. This function is mostly well adapted for filtering purposes over long time series.

4.3.4.2 Long-term datagaps

Consecutive missing values are likely to occur in optical time series (up to one or several months). Consequently, the performances of gap filling methods can strongly decrease when the temporal frequency of

exploitable observations is reduced. As previously discussed with Figure2.2, the presence of long-term gaps during winter can lead to a decrease of SenRVM performances. The robustness of the different methods in the presence of a significant data gap is here assessed.

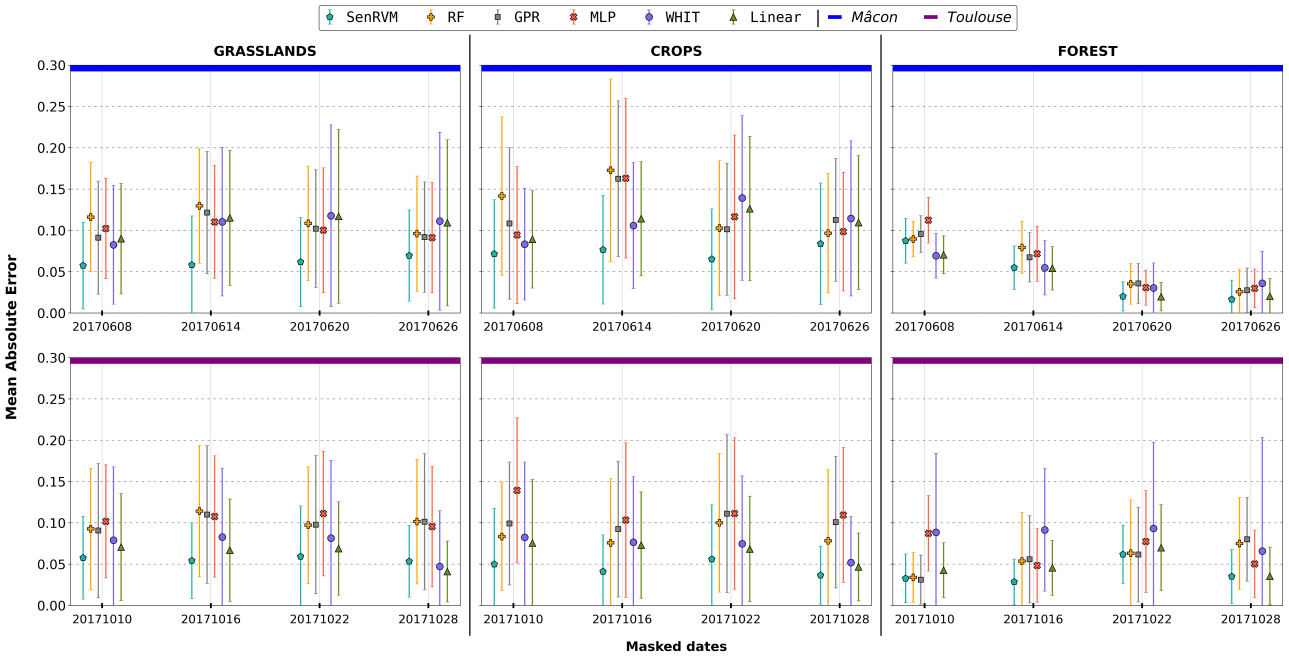

Figure 4.9: Comparison of gap filling performances over four continuous dates, corresponding to long-term data gaps. Mean Absolute Error are assessed over Mâcon and Toulouse areas for the three vegetation classes.

To perform this study, long-term data gaps are artificially created by removing 4 consecutive dates from the valid NDVI time series. The 4 consecutive dates induce an entire month without acquisitions, which implies a sufficiently long period of time for significant changes in vegetation surfaces to occur. In addition, the number of consecutive acquisitions contaminated by clouds can potentially affect the study areas (Figure 2.2.

The four consecutive dates are removed over different time periods for the two study areas. The number of valid observations as well as the agricultural practices calendars are considered as selection criteria. A long gap is then considered in June for the Mâcon area. Concerning Toulouse, October is chosen. For this experiment, as the four masked dates are consecutive, a unique model is trained for all ML regression methods.

The results obtained by the different methods can be visually compared in Figure 4.9. The reconstruction performances consolidate the previous results and further demonstrate the interest of the SenRVM approach. Grassland and crop results show how SenRVM obtains almost in all cases the lowest MAE and standard deviations. The performance improvement is more remarkable over Mâcon. This is explained by the frequent presence of anthropic interventions taking place during the reconstructed time period. Solely the first date over forest for the Mâcon area and the last date over grasslands for the Toulouse area is better predicted by the two optical-based methods than by SenRVM. Nevertheless, the difference in MAE difference between SenRVM and the two methods is very low for this specific date. Concerning forests, similar results are obtained by all the methods. The low temporal variation of NDVI curves of forests again explains these similarities.

Close MAEs are obtained for both areas by RF, GPR, and MLP methods for the three vegetation classes. GPR and MLP methods provide superior results than RF for the Mâcon area while it is the opposite for the Mâcon area. The exploitation of the temporal SAR trajectory and the use of multiple encoding branches explain the good SenRVM results.

`Linear` and `WHIT` methods exhibit substantially lower results than SenRVM, except for two dates presumably with less vegetation changes. The differences are more noticeable for the Mâcon area. This is related to the presence of numerous agricultural practices, which are not detected by the mono-sensor interpolation methods. Consequently, differences are less marked for the Toulouse area, where few agricultural practices are performed.

4.3.4.3 Reconstruction of time series breaks

We explore the ability to reconstruct time series breaks, which are usually associated with vegetation changes over agricultural areas (*i.e.*, grasslands and crops). SenRVM is especially relevant, w.r.t. the other methods, for dates containing numerous breaks (June 8th and June 6th for Mâcon and Toulouse respectively, in Figure 4.8). The long-term experiment (Section 4.3.4.2) shows such conclusions, SenRVM reaching the highest accuracies on agricultural classes, but without significant differences in terms of MAE. A qualitative evaluation of the results obtained in Section 4.3.4.2 is proposed. As a recall, four consecutive dates are masked from learning and used to assess the predictions of the different methods. This evaluation permits to highlight the interest of the SenRVM method to recover vegetation changes. The reconstructions of two types of breaks are considered:

(i) a drastic decrease in NDVI due to mowing or ploughing;

(ii) an increase due to vegetation growth.

Figure 4.10 shows four examples over two grassland and two crop polygons. It corroborates the interest of ML regression methods: the results show that the reconstruction performances of mono-sensor methods (`linear`, `WHIT`) are strongly affected by the distance between the reconstructed date and the valid NDVI measurements used in the reconstruction. Because of the simulated data gap of about one month, the standard interpolation methods are relying on temporally distant dates for interpolation. On intensively exploited and quickly evolving agricultural parcels, this interpolation significantly or even entirely obscures part of their phenological cycles. SAR-based multi-sensor solutions can integrate temporally close knowledge, and efficiently recover these cycles. Comparing RF, GPR, MLP and SenRVM, the latter exhibiting the highest accuracies obtained and more stable results.

Figure 4.10a shows the results for a permanent grassland parcel (a mowing followed by a vegetation regrowth). Standard interpolation approaches use the dates of June 2nd and July 26th for reconstructing the missing period. Despite the mowing occurring in-between, the vegetation has grown back on July 26th, reaching high NDVI values. The resulting reconstructed time series follow a gradual but not significant decrease in NDVI, preventing abrupt change detection.

Figure 4.10b, illustrates the capability of the methods for recovering vegetation changes on a maize parcel. As observed, the four masked dates result in a gap of two months without cloudless measurements. The vegetation growth is well captured by all methods. However, the standard interpolation methods show gradual and weak growth, whereas ML regression methods suggest that such a growth occurs mainly in June. The image acquired on June 20th confirms the accurate reconstruction of the four multi-sensor methods.

A complete phenological cycle showing the growth and harvest periods is shown in Figure 4.10c. The two dates related to both growth and mowing stages are unfortunately acquired during the data gap. As a result, the two successive dates available for the standard interpolation methods both correspond to a bare ground cover with close NDVI values. The reconstructed time series are therefore flat and do not reflect vegetation changes. In contrast, ML regression approaches accurately fit the phenology cycle of the parcel.

The harvest period of a winter wheat parcel is shown in Figure 4.10d. In this example, a single cloudless NDVI observation is masked. It results in a two-month data gap between September 10th and November

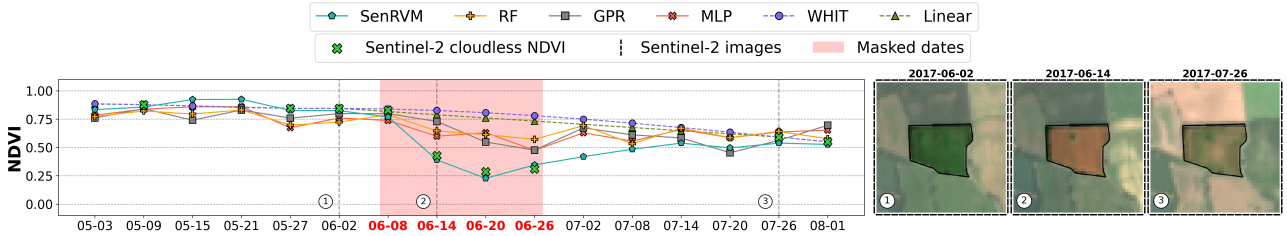

(a) Mowing of a permanent grassland over the *Mâcon* area.

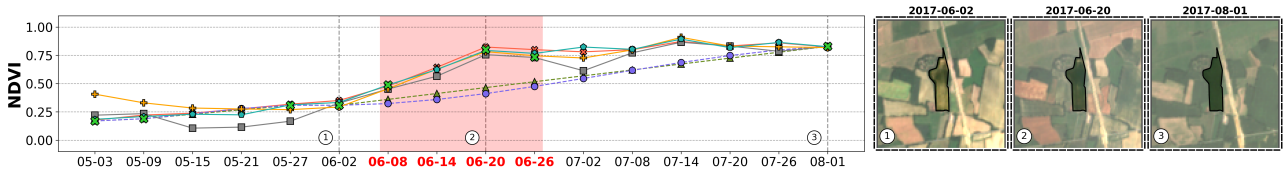

(b) Greening of a maize parcel over the *Mâcon* area.

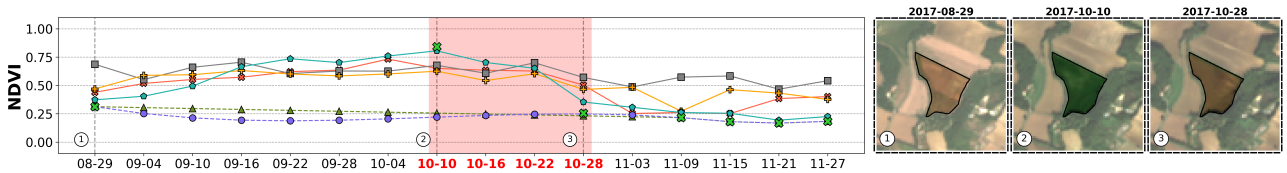

(c) Growth and mowing of an alfalfa parcel over the *Toulouse* area.

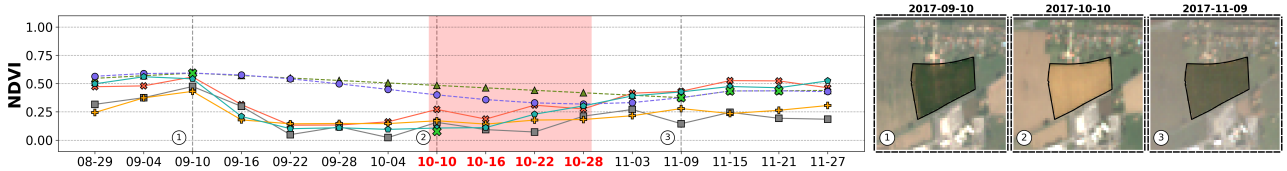

(d) Harvest of a winter wheat parcel over the *Toulouse* area.

Figure 4.10: Performance assessment comparing six different methods aiming at recovering vegetation changes occurring during a long-term data gap (red square). NDVI values evaluating the reconstruction results are depicted by the green crosses. Black-dashed lines and circle numbers correspond to the specific dates which are analyzed by the Sentinel-2 images shown on the right part of the figures.

9th. The standard interpolation methods fail to reconstruct the vegetation decrease, while ML regression approaches accurately mark a clear decrease in NDVI values, suggesting that the mowing occurred between September 10th and September 16th. Even without masking the date of October 10th to the standard interpolation methods, it would have been impossible to determine the date of mowing with such precision.

These last results further corroborate that regular vegetation monitoring needs the exploitation of multi-sensor information such as it has been proposed by the SenRVM approach.

4.4 Generalization capabilities of single-class grassland SenRVM models

Only the grassland datasets are considered here, as being the main thematic vegetation class. SenRVM models are first assessed on larger geographical areas (Section 4.4.1), to consolidate the results obtained on the two main study areas. Subsequently, spatial (Section 4.4.2 and Section 4.4.3) and temporal (Sec 4.4.4) generalization capabilities of SenRVM models are explored. The generalization experiments must first assess if a model trained in one geographical area can yield accurate predictions in another geographical area. This implies

different phenologies, acquisition dates and climate contexts. Temporal generalization focuses on the same geographical area but assesses the prediction accuracy of a model learned on one specific year and inferred on another year.

4.4.1 Evaluation over larger geographical areas

Single-class models are also trained over the 5 supplementary areas presented in Section 2.1.2. Results obtained are presented in Table 4.7. Satisfactory results are observed with similar regression scores as in the case of Mâcon and Toulouse areas. However, comparing the results of the five tiles belonging to the Western-area (T30TXS, T30TXT and T30TWT) and to the Northern-area (T31UDQ and T31UEQ), some differences can be noticed.

Table 4.7: Average results and ± standard deviations obtained by single-class SenRVM models over grasslands of supplementary areas.

		Western-area			Northern-area	
		T30TXS	T30TXT	T30TWT	T31UDQ	T31UEQ
Grasslands	R^2	0.8658 ± 0.0104	0.8851 ± 0.0069	0.8710 ± 0.0097	0.8034 ± 0.0168	0.8113 ± 0.0104
	MAE	0.0511 ± 0.0408	0.0484 ± 0.0398	0.0529 ± 0.0430	0.0541 ± 0.0580	0.0524 ± 0.0522
	MSE	0.0051 ± 0.0009	0.0046 ± 0.0008	0.0050 ± 0.0009	0.0054 ± 0.0009	0.0053 ± 0.0008
	RMSE	0.0714 ± 0.0073	0.0678 ± 0.0069	0.0707 ± 0.0070	0.0735 ± 0.0075	0.0732 ± 0.0070

The three T30TXS, T30TXT and T30TWT tiles in the Western-area have significantly higher R^2 scores. The reasons identified for these differences are threefold. Firstly, these three tiles have a much larger number of grasslands, on the order of 4 to 8 times more than for the tiles in the Northern-area. Secondly, the cloud cover over the Western-area is lower. This implies a better temporal distribution and a higher number of training labels. Finally, the proportion of fallow land and forage legumes is lower in the Western-area. These grassland types are associated with higher productive agronomic species and more intensive exploitation and therefore are potentially more challenging to predict (see for example Section 2.4.1).

4.4.2 Spatial generalization of SenRVM

Dealing with geo-spatial data necessarily implies geographical differences. For example, differences can be climatic, topological, pedological, species-related or management related. This subsection proposes to analyze the ability of a SenRVM model learned on a study area to predict the NDVI of another study area, which refers to evaluating the generalization capabilities.

Sharing the same agricultural season and number of features, this analysis is done on Western- and Northern-areas grasslands. To speed up the processing (*i.e.*, 5 models with 5 folds for the 5 tiles are newly considered) and to minimize the possible differences between the areas especially in the number of samples, partial SenRVM models learned only on a subset of the features are considered. For each tile, the backscatter coefficient features are retained, as well as the climate, topographical and temporal context metadata features. The γ features, being the most complicated to gather and coming roughly from the same Sentinel-1 data source as σ^0 are discarded. The grassland RPG class information is also discarded, being considered of less primary importance for the regression task. Moreover, a different number of species is present in the different areas, which would require a new one-hot-encoding procedure. SenRVM models are trained for each area, with a batch size of 512 and a learning rate of $5 \cdot 10^{-4}$.

To evaluate the generalization, the fold among all models (for each area independently) having the highest R^2 and the lowest MAE is selected. This model is subsequently inferred one-by-one on the datasets of the other study areas, without re-training. Table 4.8 provides the R^2 and MAE results of the SenRVM models trained and inferred on one study area (self-training, grey cells) and learned on one study area and inferred on another.

Table 4.8: Spatial generalization of SenRVM models learned on one study area and inferred on a different study area. Scores of models learned and inferred on the same area are highlighted with grey cells. Green results correspond to the area on which inference obtains the highest accuracy while red ones correspond to the lowest results.

INFERENCE: \ LEARNING:	T30TXS	T30TXT	T30TWT	T31UDQ	T31UEQ
T30TXS	R^2=0.857±0.112 MAE=0.053±0.015	R^2=0.805±0.152 MAE=0.066±0.022	R^2=0.667±0.195 MAE=0.098±0.022	R^2=0.288±0.198 MAE=0.137±0.026	R^2=0.461±0.207 MAE=0.111±0.024
T30TXT	R^2=0.808±0.244 MAE=0.067±0.031	R^2=0.864±0.109 MAE=0.049±0.017	R^2=0.673±0.209 MAE=0.096±0.023	R^2=0.251±0.192 MAE=0.146±0.028	R^2=0.479±0.214 MAE=0.113±0.024
T30TWT	R^2=0.688±0.244 MAE=0.108±0.031	R^2=0.637±0.233 MAE=0.099±0.022	R^2=0.813±0.161 MAE=0.052±0.018	R^2=0.319±0.231 MAE=0.117±0.025	R^2=0.421±0.242 MAE=0.104±0.026
T31UDQ	R^2=0.443±0.244 MAE=0.113±0.031	R^2=0.465±0.24 MAE=0.099±0.027	R^2=0.342±0.237 MAE=0.11±0.029	R^2=0.748±0.184 MAE=0.064±0.026	R^2=0.627±0.217 MAE=0.076±0.026
T31UEQ	R^2=0.414±0.244 MAE=0.115±0.031	R^2=0.425±0.235 MAE=0.105±0.031	R^2=0.285±0.232 MAE=0.122±0.036	R^2=0.662±0.211 MAE=0.077±0.032	R^2=0.769±0.181 MAE=0.059±0.022

By comparing the obtained self-training results with Table 4.7, it can be observed that discarding gamma and RPG class features lead to a decrease in model accuracy. On average, for the five tiles, a decrease of 4.4% of R^2 and an increase of 7.4% of MAE are observed. This decrease in accuracy, especially visible for the T30TWT, T31UDQ and T31UEQ study areas, hints at a dependence of regression accuracy on the deleted features for this experiment. A more in-depth study on the importance of input features is proposed later in this chapter, in Section 4.3.3.

Table 4.8 also indicates that the inference on distinct study areas significantly degrades the prediction results for all assessed cases. A clear distinction can be noted between inference on a study area within the same larger geographical area (Western-area or Northern-area), and inference from an area of a larger area to another. Using a model learned on the T30TXS area, for example, still achieves relatively good regression scores for the T30TXT and T30TWT areas (respectively, 0.808 and 0.688 of R^2) but fails on the two areas T31UDQ and T31UEQ that are geographically distant (respectively 0.443 and 0.414 of R^2). Conversely, a model learned on the T31UDQ tile will perform better on the T31UEQ area than for the three tiles in the Western-area. Inference on a tile from the Northern-area with models learned on the Western-area will in average lead to a decrease of 50.97% of R^2 and an increase of 108.96% of MAE. Similarly, learning on the Northern-area and inference on the Western-area shows a decrease of 57.62% of R^2 and increase of 139% of MAE. The geographical proximity, particularly hinting less climatic differences and thus phenologies, appears as an important factor with regard to generalization. This may indicate that despite the relevance of climate variables (Section 2.4.2) for regression, different climate contexts may hinder learning and require distinct models to be trained.

4.4.3 Multi-tile model and spatial generalization of SenRVM

Each geographical area has its own characteristics and the re-use of a model from one geographical study area to another has proven rather inefficient in the previous subsection. It is therefore proposed here to analyze the ability to predict NDVI on the different tiles with a single model encompassing for learning samples from all areas.

From the five tiles, 10,000 samples per tile are randomly gathered and merged to form a multi-tile grassland dataset. New SenRVM models are trained and accuracy metrics are computed. As previously done, the model with the highest R^2 and lowest MAE is selected and inferred on the five tiles.

Results obtained from the inference of the multi-tile model are presented in Table 4.9. By comparing the results presented in grey cells of Table 4.8 which correspond to training and learning on the same study area, a decrease in accuracy is observed for the results of the five tiles. Marginal decrease in $R^2 < 0.03$ and an increase in MAE < 0.01, except for T31UDQ, are nevertheless found. These similar regression accuracies indicate that a model encompassing different geographical areas does not appear to be penalizing. Above all, these results were obtained with a smaller number of samples (10,000 from a tile) and could be improved by increasing the number of training samples.

Table 4.9: Spatial generalization accuracies of a SenRVM model trained with 50,000 samples gathered from five study areas.

	MULTI-TILE LEARNED MODEL	
	R^2	MAE
Multi-tiles	0.787 ± 0.176	0.059 ± 0.022
T30TXS	0.853 ± 0.119	0.057 ± 0.016
T30TXT	0.863 ± 0.120	0.056 ± 0.017
T30TWT	0.799 ± 0.174	0.057 ± 0.018
T31UDQ	0.695 ± 0.209	0.071 ± 0.025
T31UEQ	0.737 ± 0.166	0.058 ± 0.020

4.4.4 Temporal generalization of SenRVM

Rather than assessing spatial generalization, it is proposed here to explore if temporal generalization with suitable accuracy can be reached between two different years. Having two years permits to learn a model on one year and infer on the other year. For the current experiment, the considered features are σ^0, climate, topography and metadata. These features are computed over the Mâcon area for the agricultural season of 2019. Solely one area is assessed, because of the heavy imagery processing needed to obtain new datasets.

Although the same area is considered for both 2017 and 2019, changes in agricultural parcels are common. It is first observed that 1,200 parcels were not included in the 2017 LPIS, probably either for administrative reasons or technical omissions. Furthermore, a large number of crops, primarily triticale, rye, and maize, became grasslands in 2019. Finally, some LPIS-based rules have evolved between 2017 and 2019 and some declarative codes (*i.e.*, mixture of predominantly forage legumes, and forbs or grasses) were suppressed, leading to an increasing number of temporary grasslands to be declared. Thus, the grassland dataset of 2019 contains 36,754 parcels compared to 27,832 in 2017.

SenRVM models for the year 2019 are trained by using the same hyperparameters as for 2017. The best resulting model is selected for inference on the 2017 dataset. Conversely, the best model previously selected for 2017 is inferred on the new 2019 dataset. Results for training and inference on the same year and on the other year are presented in Table 4.10.

Table 4.10: Temporal generalization of a SenRVM models trained on the same study area but on different years. Grey cells correspond to the results obtained with the same years is used to train and to evaluate the SenRVM model.

		Learning	
		Mâcon 2017	**Mâcon 2019**
Inference	**Mâcon 2017**	R^2=0.827±0.144 MAE=0.040±0.017	R^2=0.193±0.179 MAE=0.151±0.059
	Mâcon 2019	R^2=0.262±0.216 MAE=0.141±0.042	R^2=0.818±0.150 MAE=0.039±0.016

Poor regression accuracy is found in both inferences from 2017 to 2019 and from 2019 to 2017 cases. The potential changes in grassland parcels between the two years outlined above may initially explain the inability of the network to predict in a different year. More importantly, apart from different years, the intra-annual acquisition dates are also not identical. The number of calendar days not necessarily being a multiple of the temporal resolution of a satellite (*e.g.*, the 12 days of a Sentinel-1 satellite), the acquisition dates of the following year are thus shifted. The acquisition plans of each satellite are also evolving which can accentuate these differences. In our case, moreover, an orbit overlap area was used in 2017 (see Section 2.1.1) changing the nominal temporal resolution, which is in this case only available for the year 2019. This mismatch in acquisition time grids between the years 2017 and 2019 is the primary hypothesis for the observed inefficiency of using a model from year to year. Although a temporal context around the acquisition dates is provided as information to the network, it does not appear to be sufficiently effective for the task being explored. A potential solution would be to assign more weight to this information.

4.5 Further post-processing of SenRVM results

4.5.1 Cloud & shadow mask refinement

Accurate cloud and shadow detection remains a well-known challenge in optical remote sensing, despite a plethora of approaches (Baetens et al., 2019; Chen et al., 2019; López-Puigdollers et al., 2021; Zekoll et al., 2021; He et al., 2022). Errors can be divided into two categories. Undetected observations flagged as valid measurements are known as *omission* errors, while *commission* errors correspond to the non-cloudy observations detected as invalid measurements. The presence of errors can occur, negatively impacting a large number of reference polygons, and subsequently the SenRVM performances.

In Figure 4.11, a Sentinel-2 image is overlaid by its associated validity mask, where the detected cloudy areas are highlighted by red stripes. Omission errors are observed in the center part of the image, with a large clouded area appearing outside the red mask boundaries. The same figure also shows the commission errors, which are visible in the right part. In this case, some valid observations can be observed inside the validity mask boundaries, detected as shadow areas probably because of the evergreen forests that appear very dark on this area. Unfortunately, the presence of errors, either omissions or commissions, can be found on large geographical areas impacting tens, even hundreds or thousands of grassland polygons.

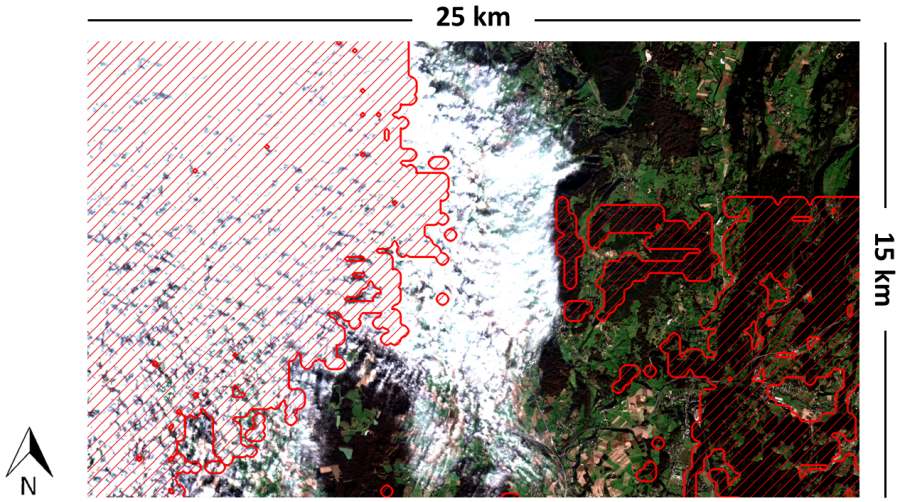

Figure 4.11: Example of a cloudy Sentinel-2 true-color composition acquired December 14th 2016 over the T31TFM tile. Cloudy areas detected by the cloud & shadow mask are represented by the red stripes. Omission and commission errors are visible in the center and right part of the image.

Commission errors basically only result in a reduced number of valid dates being considered. Omission errors, on the other hand, can lead to much greater complications. These errors involve the inclusion of outliers in the temporal analysis. These outliers often induce strong and sudden variations, which can be falsely interpreted as a significant change in vegetation, especially on grasslands as a result of management practices. Cloud masks are therefore essential to eliminate the invalid pixels that would appear as outliers in time series. Fortunately, errors at the scales shown in Figure 4.11 that affects large areas are relatively rare. Most of the errors are more confined to the parcels covered by cloud or shadow edges.

Figure 4.12 depicts how significant SenRVM errors could be associated to cloud *omission* and *commission* (Figure 4.12a and 4.12b, respectively). SenRVM is particularly insensitive to such errors and could be used as a solution to improve the mask quality. An experimental set-up is proposed here.

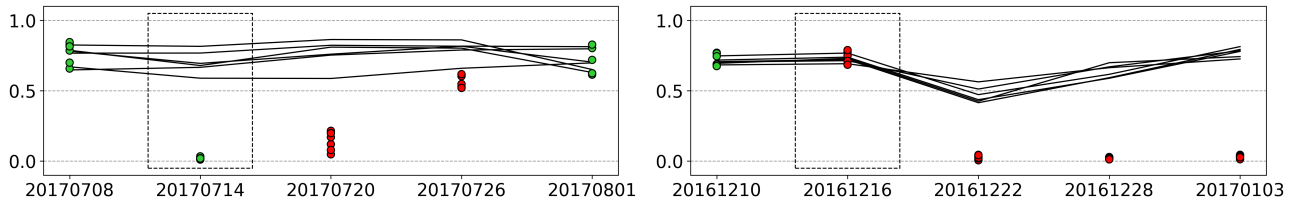

(a) *Omission of the cloud & shadow mask.*

(b) *Commission of the cloud & shadow mask.*

Figure 4.12: Two examples on how cloud/shadow mask errors could lead to an erroneous performance assessment. *Omission* (a) and *commission* (b) errors are shown in the black dashed boxes. As seen, accurate SenRVM results over neighboring polygons (black lines) are obtained on dates affected by cloud/shadow mask errors. Red dots are masked dates.

To filter the errors, the MAE of SenRVM predictions are considered. This refinement is performed by applying at each date simple thresholds:

$$\tilde{m} = \begin{cases} 0, & \text{if } m_t = 1 \text{ and } |y_t - \hat{y}_t| > \alpha_{om} \\ 1, & \text{if } m_t = 0 \text{ and } |y_t - \hat{y}_t| < \alpha_{com} \\ m_t, & \text{otherwise.} \end{cases} \tag{4.5}$$

m_t is the original mask validity flag for the instant t. The expected NDVI and SenRVM predicted NDVI values are y_t and $\hat{y}_t$, respectively. The performance of the refinement process depends on the *commission* and *omission* thresholds, which are sensitively set: $\alpha_{om} = 0.3$ and $\alpha_{com} = 0.02$. Eq. 4.5 is applied on the original masks of both study areas by considering the prediction results obtained by the single-class SenRVM models presented in Table 4.3. It results in removing or adding a few validation measurements: for each polygon, 1.26 and 1.82 dates were found as *omission* and *commission*, respectively. To investigate the impact of outliers on performances, the resulting $\tilde{m}$ masks are inserted in the SenRVM, which is retrained for the three vegetation classes (the same datasets and hyperparameters as those in Table 4.3). Results obtained by using the refined mask are reported in Table 4.11.

Table 4.11: SenRVM performances obtained after mask refinement.

		Mâcon	Toulouse
Grasslands	R^2	0.8718 ± 0.0043	0.8692 ± 0.0023
	MAE	0.3981 ± 0.0014	0.0409 ± 0.0007
	MSE	0.0038 ± 0.0002	0.0029 ± 0.0001
	RMSE	0.0546 ± 0.0023	0.0542 ± 0.0011
Crops	R^2	0.9532 ± 0.0024	0.9705 ± 0.0010
	MAE	0.0395 ± 0.0013	0.0327 ± 0.0008
	MSE	0.0031 ± 0.0001	0.0021 ± 0.0001
	RMSE	0.0560 ± 0.0013	0.0454 ± 0.0015
Forests	R^2	0.8786 ± 0.0035	0.9327 ± 0.0044
	MAE	0.0310 ± 0.0004	0.0314 ± 0.0037
	MSE	0.0024 ± 0.0001	0.0020 ± 0.0004
	RMSE	0.0493 ± 0.0016	0.0447 ± 0.0038

The gain in accuracy, observed by comparing the results obtained in Table 4.3 (Sec. 4.2.2), corroborates that the removal of numerous cloud & shadow mask errors could improve the SenRVM performances. The benefit is observed for both areas and the three vegetation classes and across the four metrics. The minimum R^2 of 0.83 is improved to 0.86 by using the $\tilde{m}$ masks.

Percentage of variation (Δ%) achieved by the use of refined $\tilde{m}$ masks are calculated and presented for R^2 and MAE metrics in Table 4.12. Accounting for both areas, the R^2 is increased in average by 2.08% (2.85% and 1.32% for Mâcon and Toulouse, respectively) and the MAE decreased by 6.74% (8.04% and 5.43% for Mâcon and Toulouse, respectively). Improvements are especially significant in the Mâcon area, given its important number of mask errors, and over grasslands and forest. Concerning crops, the improvement is less noticeable given that very good scores are already obtained by using the original masks. For both grassland and crop classes, MAE errors are largely improved. MAE below 0.04 is achieved for both classes over the Mâcon area. The interest of the refinement strategy is finally reflected in the standard deviation values of Table 4.11, which are much lower than those described in Table 4.3.

Table 4.12: Percentage of variations (Δ%) in R^2 and MAE observed by using the refined $\tilde{m}$ masks compared to the results presented in Table 4.3 (Sec. 4.2.2) using the original masks.

		Mâcon	Toulouse
Grasslands	$\Delta\%_{R^2}$	+3.98	+2.69
	$\Delta\%_{MAE}$	-8.85	-7.67
Crops	$\Delta\%_{R^2}$	+1.05	+0.29
	$\Delta\%_{MAE}$	-5.95	-7.37
Forests	$\Delta\%_{R^2}$	+3.53	+0.99
	$\Delta\%_{MAE}$	-9.33	-1.26

4.5.2 Blending SenRVM predictions with Sentinel-2 observations

Although the SenRVM approach remains a reliable method to recover NDVI measurements, the resulting time series could be improved in terms of temporal sampling and quality by incorporating the available valid NDVI observations acquired from Sentinel-2. This post-processing step allows to preserve the original NDVI variations and marginally reduce the SenRVM errors. Two straightforward blending strategies are considered without taking into account more advanced techniques requiring the tuning of additional parameters (Wang and Cheng, 2007; Lim et al., 2021):

- The first blending strategy (**OR-S2**) consists in replacing SenRVM predictions by the available Sentinel-2 non-cloudy NDVI values. A pre-processing step of the SenRVM approach has already resampled the Sentinel-2 NDVI values to a common temporal grid. The OR-S2 strategy takes advantage of this common temporal grid. The refined masks (Sec. 4.5.1) are used to select the valid Sentinel-2 NDVI values that are replacing the predictions. This strategy allows to preserve the output SenRVM temporal grid (6-days) albeit still considering the time-lag of Sentinel-2 acquisitions induced by the resampling step.

- The second strategy (**AND-S2**) consists in taking advantage of the distinct temporal grids of non-resampled Sentinel-2 and SenRVM. True valid NDVI acquisitions are thus inserted in the SenRVM time series. If Sentinel-2 NDVI was acquired at the same date as a SenRVM prediction, the Sentinel-2 NDVI value is kept. Since cloud cover affects each parcel differently, the resulting time series have different lengths. In average, 86 and 113 NDVI values are, respectively, obtained for Mâcon and Toulouse. Despite accurate SenRVM results, the AND-S2 strategy can induce some jumps in the resulting time series. This can especially be the case when original S2 acquisition dates are very close to SenRVM dates. Theses jumps may be reduced either by adding rules to the selection of Sentinel-2 and SenRVM values during the blending process (*e.g.*, thresholding on the absolute difference) or by an additional temporal smoothing strategy. This additional post-processing is not considered here.

The interest of both blending strategies is especially visible when vegetation changes are occurring. Both strategies allow us to recover the original magnitudes of change observed by Sentinel-2. The AND-S2 strategy further increases the temporal resolution and incorporates the original dates when the changes were observed by Sentinel-2.

Figure 4.13 shows some examples obtained by the two proposed blending strategies. The results are illustrated over two grassland parcels of the Mâcon area. On the left part, the original Sentinel-2 acquisitions and the predicted SenRVM NDVI time series are displayed. On the right, the results of the two blending strategies OR- and AND-S2 are compared with the SenRVM results in the presence of management practices

in mid-August (Figure 4.13a) and end of April (Figure 4.13b). For both parcels, the use of the OR-S2 strategy (purple line) permits to retrieve the original drop of NDVI induced by the management practice, which were in these cases minored in the SenRVM predictions. While the management practices are satisfactorily depicted in the OR-S2 time series, the AND-S2 strategy (yellow line) allows us to further recover with more precision the temporal schedules of the management practices. In both cases, the changes can be observed by the AND-S2 strategy within a 3-day time interval, while a 6-day time interval is allowed by the OR-S2 strategy.

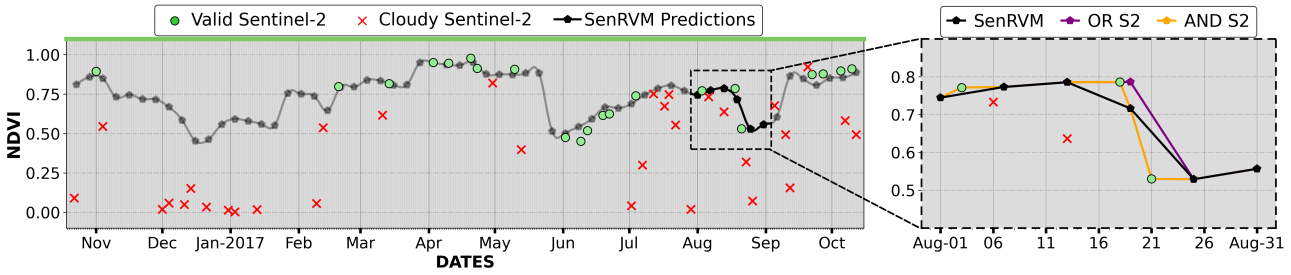

(a)

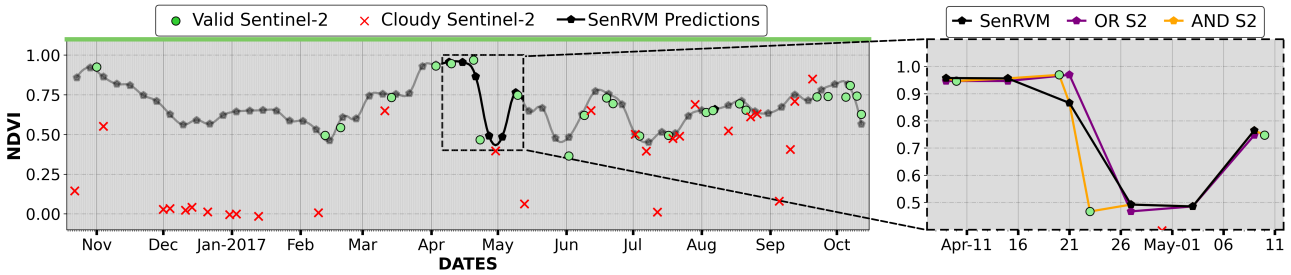

(b)

Figure 4.13: Two examples of post-processed SenRVM time series obtained by the two proposed blending strategies (OR-S2, AND-S2). Both strategies incorporate valid NDVI observations acquired by Sentinel-2 in SenRVM output result.

4.5.3 Deriving uncertainty for SenRVM predictions ?

Uncertainty refers to the quantitative measurement of potential randomness in the outcomes of an experiment. Measures of uncertainty are essential in decision-based processes and in particular when deriving operational pipelines from research outcomes. In the SenRVM framework, uncertainty should inform on the confidence in a predicted value and the importance it should be given in a decision process.

Prediction using supervised machine learning regression methodologies rarely comes with uncertainty measures, especially when single values are expected as output. Gaussian Processes are ideal to estimate uncertainty based on their probabilistic outputs. Neural networks, on the contrary, do not inherently allow the retrieval of uncertainty measures (Antoran et al., 2020; Abdar et al., 2021).

Uncertainty is commonly classified into two types (Kendall and Gal, 2017): *epistemic uncertainty*, is understood as the the uncertainty of the model itself, or its parameters, and *aleatoric uncertainty*, which arises with the natural stochasticity of the data, such as clouds in optical data. Epistemic uncertainty of Neural Networks has been partially addressed in the literature with advanced techniques such as deep ensembles (Lakshminarayanan et al., 2017), Monte Carlo dropout (Gal and Ghahramani, 2016) or stochastic batch normalization (Atanov et al., 2018). In the case of SenRVM, the use of dropout, data folding strategies allowed

by an important number of training samples and results computed from the averages of several model runs have permitted to already quantify some epistemic uncertainty of the results. Aleatoric uncertainty, on the other hand, is rarely handled.

An attempt is here proposed to obtain uncertainty measures associated to the SenRVM predictions. Five criteria (Cr.), based on both epistemic and aleatoric uncertainty, are considered. They are derived from information mainly based on SenRVM results and temporal distribution of the input data:

- (**Cr.1**) *Label spatial availability*: this criterion is based on the total number of valid (*i.e.*, non-cloudy) labels, available for each date throughout the dataset and used for training the models. This information is easily retrieved from the associated masks. The relationship between the number of observations and the quality of the regression may not be linear due to the possible introduction of noise and false examples. Nevertheless, it can be considered that a logarithmic relationship exists between the number of examples and the accuracy of predictions. A higher number of samples allows the network to encompass an increased variability in the data used and gain generalization.
- (**Cr.2**) *Model Error*: this corresponds to the average accuracy of the model for each date. The MAE between each valid label and the corresponding prediction is computed and averaged for each date. Some dates do not have any valid label as they are entirely covered by clouds. In this case, this criterion cannot be calculated and is not taken into account for these dates.
- *Label shifts and temporal availability*: three criteria are proposed, which are illustrated in Figure 4.14. For each SenRVM prediction (purple point), the temporal distribution of the nearest label features (green dots and red cross) are taken into account. Based on the common temporal grid of the labels, the three following criteria are derived:
  - (**Cr.3**) considering the resampling step of Sentinel-2 acquisition to the common temporal grid (Section 2.4), the shift with respect to the real date of acquisition is considered. The shift is expressed as the absolute distance in days. The suggestion is that the smaller the shift, the lowest the uncertainty in the prediction should be (*i.e.*, lower changes in vegetation cover).
  - (**Cr.4**) as cloudy acquisitions occur, the distance in days to the nearest valid label is computed for each date. For non-cloudy dates, this criterion is thus set to 0. It indicates whether the condition of the vegetation was known at a near or distant time.
  - (**Cr.5**) the total distance in days between the nearest preceding and following valid labels is computed. For the first and last dates, only the following or preceding, respectively, is used. On the contrary to the previous criterion, this allows to know if the temporal evolution of the vegetation could be observed at short or long intervals.

Considering the five above criteria, different uncertainty measures can be associated with each NDVI value predicted by SenRVM at each specific date. To facilitate the display and handling of uncertainty measures, it is proposed to calculate a global uncertainty score (U_{global}) integrating all these criteria and allowing a simplification of interpretation. To account for different ranges, a normalization between 0 and 100 is also performed for each date:

$$Cr'.i_t = \left(\frac{Cr.i_t - min(Cr.i)}{max(Cr.i) - min(Cr.i)} \right) \times 100 \quad \Big| \; i \in [1,5] \;\&\; t \in T\,, \tag{4.6}$$

with $Cr'.i_t$ being the normalized criterion i among the five criteria for each date t of the time series T. It can be noted that a data dependent normalization is proposed here (*i.e.*, taking into account the minimum

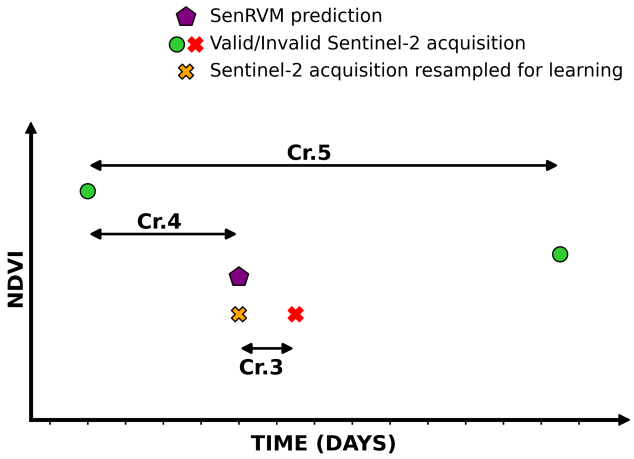

Figure 4.14: Illustration of three uncertainty criteria calculated for a SenRVM prediction related to the temporal distribution.

and maximum distance in days with a valid label for example). It would be possible to fix these values as absolute, *e.g.*, 1 for the MAE as the NDVI is assessed, or 365 days for the temporal distance. Nevertheless, to enhance differences in uncertainty regarding model predictions, this possibility is here discarded. The global uncertainty score for each date t is then the average of the five normalized criteria:

$$U_{global_t} = \frac{1}{n}\sum_{i=1}^{n} Cr'.i_t \quad \Big| \; n = 5 \;\&\; t \in T\,, \tag{4.7}$$

The resulting uncertainty is expressed in percentage, with 0 indicating low uncertainty and 100 high uncertainty.

To illustrate the resulting uncertainties, the five criteria and the global score are computed for single-class grassland SenRVM models (Sec. 4.2.2). Figure 4.15 provides examples of two SenRVM time series predicted by the same model. The five criteria computed are shown. For visual assessment, the global uncertainty score is also displayed with colors from green to red, respectively, for low to high uncertainties.

It can be noted that the three upper histograms, associated with the criteria Cr.1, 2, and 3, are identical for both parcels. This is expected, as the same model is used and both parcels are on the same area and the three criteria are computed from all samples. They will thus only vary between different datasets. On the contrary, the two following histograms (Cr.4 and 5) vary for each sample.

Figure 4.15a illustrates a time series for which the global uncertainty scores are low for the entire observed time range. Visually, these good scores are explained by the presence of numerous labels for training, distributed throughout the entire time series.

Conversely, Figure 4.15b depicts a grassland time series located on a high altitude in the Pyrenees mountains. Frequent snow during winter and clouds during spring and summer leads to a very poor number of valid Sentinel-2 acquisitions to be available for learning. Thus, the uncertainties related to the temporal availability (Cr.4 and 5) are very high for the first and last parts of the time series, reflecting the lack of supervision and the potential errors in the predictions. Especially, a sudden drop observed in the SenRVM predictions is accurately associated with a very high uncertainty score (red color) at the beginning of March. This drop can be explained by the unavailability of any valid samples (*i.e.*, 100% cloud cover) for training at this date, and

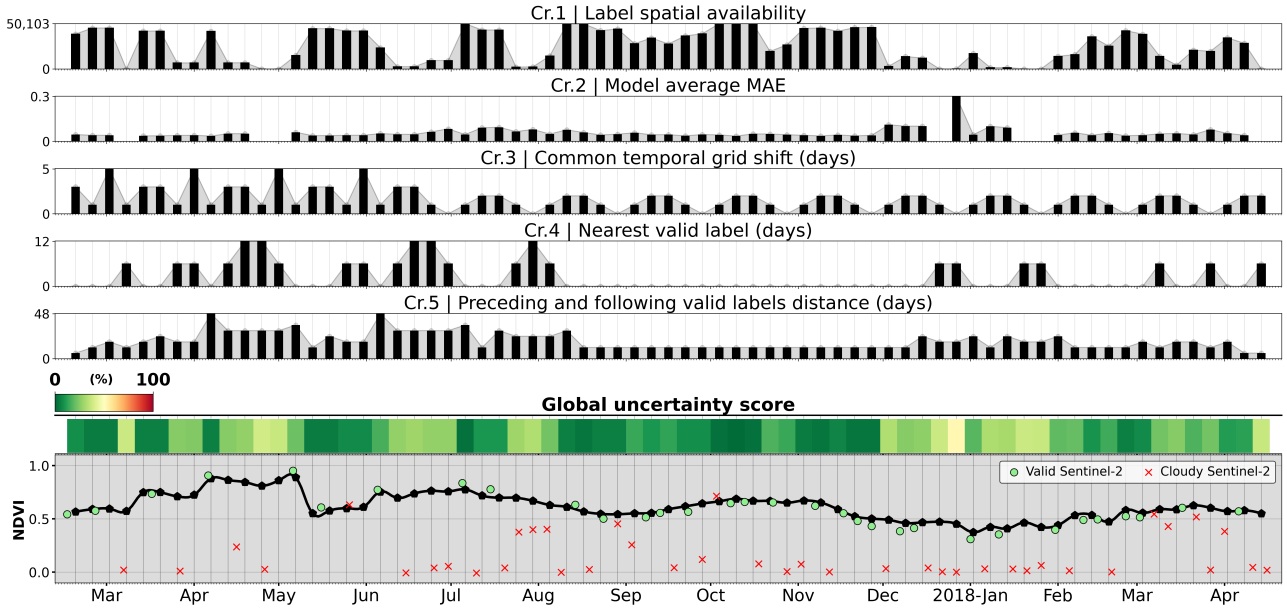

(a) Example of low uncertainties throughout the agricultural season associated to SenRVM predictions.

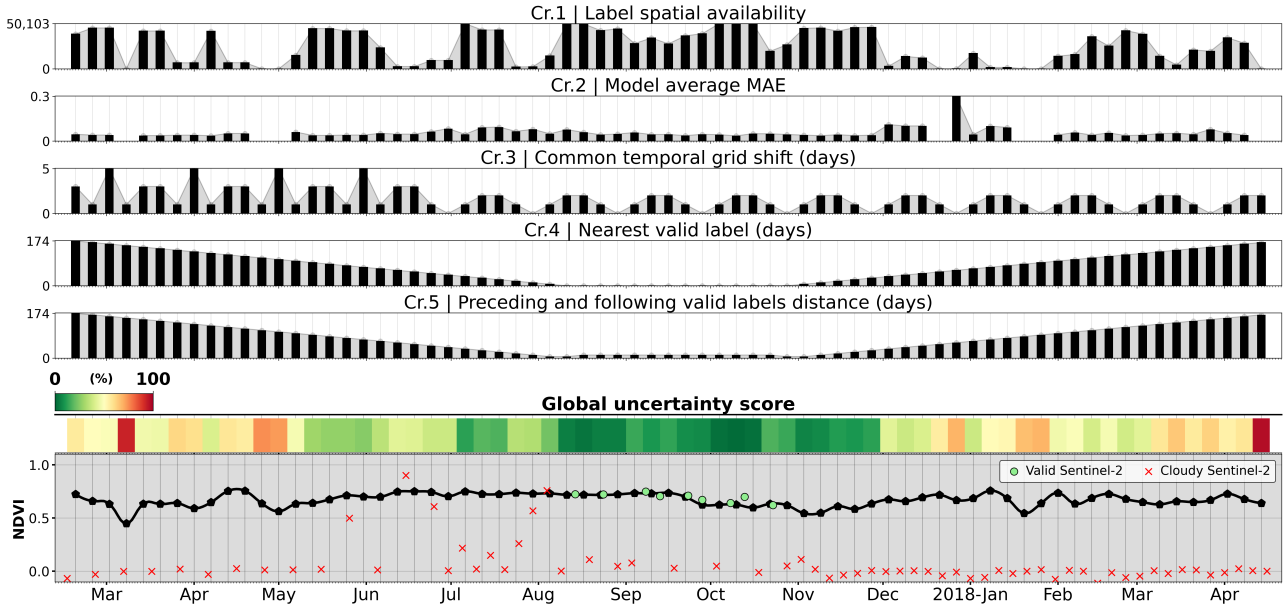

(b) Example of high uncertainties throughout the agricultural season associated to SenRVM predictions.

Figure 4.15: Visualization of SenRVM time series and uncertainty scores for two permanent grassland parcels over the Toulouse area.

the high temporal distance to valid labels.

Although the resulting criteria rely on basic information, the proposed approach illustrates the potential of deriving uncertainties associated to predictions. Additional criteria tailored with respect to a specific decision-based task or the incorporation of weighting strategies in the global score can be proposed. This could improve the computation of the uncertainties introduced here and move from a visual perspective to an operational solution.

4.6 Concluding remarks

This chapter has proposed the study of the results of the SenRVM approach previously presented. The results were analyzed both quantitatively and qualitatively. The different experiments have illustrated the satisfactory results of the proposed SenRVM method and demonstrated the relevance of the resulting time series for grassland monitoring.

The accuracy of the regression towards NDVI was first evaluated on datasets grouping grasslands, crops and forests as well as separately (multi-class and mono-class). Satisfactory results were obtained in both cases, with an accurate stability in the results between vegetation types. The influence of the temporal and spatial distribution of the data on the regression performances has been illustrated, with a noticeable impact of the persistent cloud cover and the size of the reference parcels on the obtained errors. Taking into account the different nature of the data used as input, an ablation study was proposed to underline the importance of SAR time series and the relevance of both backscatter coefficient and coherence features. A divergent outcome was nevertheless reported for forests, with an increased contribution of the cloud & shadow masks used to discard cloudy acquisitions. The performances of SenRVM with respect to several existing regression and interpolation methods have been assessed for the reconstruction over short- and long-term data gaps. The comparison has allowed to illustrate the satisfactory results of the proposed approach.

The generalization capabilities of the SenRVM approach were then explored. Spatial (*i.e.*, between different areas) and temporal (*i.e.*, between different years) shifts were considered. The results have highlighted some generalization limitations, which nevertheless do not affect the results previously obtained, but rather point out potential areas for improvement. For instance, models learned on samples extracted from tiles integrating different climatic contexts or the implementation of strategies allowing a better robustness to temporal shifts are in particular to be considered to improve the generalization of the proposed models.

Finally, post-processing steps allowing to improve the SenRVM results have been briefly presented. The correction of cloud masks, the integration of Sentinel-2 NDVI data, and the generation of uncertainties associated with the predictions have been discussed.

Part III

MONITORING GRASSLANDS

Chapter 5

Detecting and quantifying grassland management practices

5.1 Challenges and related work

Previous chapters have demonstrated that grassland management is varied, both in its effects on biomass and in its temporal calendar. Mowing, grazing, and ploughing have major impacts on ecosystemic services, that hold an important part of capital environmental goods. Consequently, having a comprehensive knowledge of management practices, in the context of environmental changes and sustainable management, is a crucial factor.

The expected provisioning services and subsequent seeded agronomic species will mainly define the nature of technical acts performed on a grassland during the growing season. In order to achieve optimal management of the grass resource of a parcel, a mix of mowing, grazing, and ploughing practices is often encountered. Beyond these three technical acts, several commonly employed management practices are performed. These practices do not necessarily imply the grass resource to be harvested, but do influence its growth. Early spring mowing and grazing which favor vigorous grass regrowth, are for example frequent. The choice between mowing or grazing does not have to be permanent for the rest of the growing season. The number of following technical acts will varies. Grassland maintenance (which can take several forms) is possible before the beginning of winter, to prepare for the next season. During the growing season, several re-seedings can also take place after ploughing. Over-seeding, which involves adding seeds to regenerate the grass, is also routinely performed. It generally occurs at the end of winter or at the end of summer. This technique is often combined with harrowing or rolling to remove weeds and influence soil structure, respectively. Fertilization (organic, nitrogen, phosphorus, and potassium mainly) can also be carried out from February onwards to encourage growth and favor certain species. Grassland botanical composition and phenology therefore reflect a combination of environmental factors and farming practices. The strategies mentioned above will imply different impacts on the above-ground biomass varying in intensity and duration. This consequently also leads to high variability in the temporal and spatial management of grasslands.

Most of the work studying the detection of practices on grasslands with remote sensing focuses on detecting the three main types of technical acts (*i.e.*, mowing, grazing, and ploughing). The strong correlation with the ecosystemic quality of a grassland due to the drastic change they induce explains why these three practices are mainly considered. In recent years, the interest in developing methods to detect grassland management practices is greatly increasing (see Section 1.2.2.2). First, due to the growing environmental concerns. The second reason is the arrival of the high spatial and temporal time series from the Sentinel constellation. From the existing literature, two main categories are recovered: (i) classification-based approaches, aiming the discrimination of grassland management (*e.g.*, mowed, grazed); (ii) detection-based approaches, which intend to gather information on management practice frequencies. This last category often aims to estimate the exact date at which technical acts occur.

The following paragraphs present the existing literature on management practices. The works based on the classification of practices are first discussed. Close to the objectives followed in this chapter, the methods for detecting practices are then thoroughly presented. Data and methods used by works considering only optical time series are first introduced. Works relying on the use of SAR features or integrating both optical and SAR features are then addressed. The considerations and limitations of the different works will then be discussed.

Mapping the nature of management practices

Methods that target grassland classification according to management practices make the common assumption that different technical acts have a distinct impact on grassland phenology and therefore are distinguishable. The classes recovered are mainly related to *usage intensity*, *e.g.*, extensively, intensively, with certain degrees. Grasslands that are intensively exploited are generally assumed to be mowed, while grazing is asso-

ciated with extensive usage. For instance, Guo et al., 2000b propose to map six different classes of management practices according to different usage intensities. The study exploits three Landsat-5 images acquired at different seasons of a year and thresholding techniques to differentiate the classes. Likewise, thresholding techniques are employed in Asam et al., 2015 on LAI time series obtained from 9 RapidEye images to distinguish four classes of usage intensity. In Sibanda et al., 2017, a single WorldView-3 image is classified with k-means clustering based on the spectral separability of the expected classes. Random Forest and Gradient boosting algorithms are applied on a set of 200 images from Sentinel-1 (backscatter coefficient and Gray Level Co-occurrence Matrices (GLCM)) and Sentinel-2 (NDVI, EVI, Normalized Difference Water Index and GLCM of Band 8) spanning 24 months to separate 3 classes of grassland management in O'Hara et al., 2021. Meadow and pastures, which have different usage intensities, are classified at a national scale in Stumpf et al., 2020. For this purpose, a strategy based on thresholding of NDVI composites from Landsat ETM+ and OLI is proposed. In Bastin et al., 2012, grazed grasslands are retrieved with Landsat TM and ETM+ images through a comparison of minimum ground-cover on grasslands between the different years. Gaussian Mean Map Kernels are proposed in Lopes et al., 2017 for mapping management practices (mowed, grazed, or both) from FORMOSAT-2 times series spanning three years. Deep-based networks are also employed (D'Andrimont et al., 2018) to separate crops from grasslands by detecting ploughing activities. Time series from Sentinel-1 (backscatter coefficient and coherence) and Sentinel-2 (Bare Soil Index) are used.

While dealing with management practices, these works are more related to land-cover mapping. They allow for an estimation of adopted management regimes but rarely inform about the frequency of management practices which are identified as of particular interest.

Exploiting optical time series for the detection of practices

Traditionally, the detection-based approaches study the evolution of image time series. Due to the temporal and quantitative variability of technical acts, gathering exhaustive validation data describing the exact dates of management practices is complex and costly. As a consequence, works dealing with the detection of management practices and their frequency are relatively limited and mainly rely on unsupervised approaches. Existing work considers that technical acts can be associated with abrupt changes in the time series. The magnitude of the change is usually related to the type of management practice. Mowing or ploughing generally induce an important and abrupt removal of grass cover, therefore implying a high magnitude of change in the time series. On the contrary, grazing can last longer and often affect vegetation only gradually. Due to the temporal resolution of satellite time series, most of the works are therefore focusing on detecting mowing or ploughing, while grazing is rarely considered.

In the Earth Observation community, different change point detection methods exploiting low- and moderate spatial resolution times series are specifically proposed. For instance, the Breaks For Additive Seasonal and Trend (BFAST, Verbesselt et al., 2010) or Landsat-based detection of trends in disturbance and recovery (LandTrendr, Kennedy et al., 2010) approaches are commonly adopted to monitor trends or seasonal changes in vegetation surfaces. They provide good performance for tasks such as identifying forest disturbances. However, frequent and varied technical acts prevent any long-term trend in grasslands from being extracted. Therefore, these methods are not adapted to retrieve these rapidly evolving phenomena and characterize the technical acts. This explains why they are not exploited in the related literature.

Optical imagery is identified as the most commonly used to monitor grassland vegetation status in Section 1.2.2.2. The temporal resolution remains a driving factor for accurate detection of practices. Consequently, work exploiting optical imagery only, either rely on short very high resolution time series such as from SPOT-5 (Dusseux et al., 2014c), RapidEye (Franke et al., 2012; Gómez-Giménez et al., 2017), FORMOSAT-2 (Hadj Said et al., 2011), or span multiple years with a lower intra-year repetitivity (Lopes et al., 2017). Some works propose to exploit coarse-spatial resolution images from MODIS (Estel et al., 2018; Halabuk et al., 2015) to increase the temporal resolution, at the cost of spatial resolution. More recently, Sentinel-2 (Kolecka et al.,

2018) or Harmonized Landsat Sentinel-2 (HLS) products combining Sentinel-2 and Landsat-8 (Griffiths et al., 2019; Schwieder et al., 2021) are explored to obtain higher temporal resolutions.

Most of the works that aim the detection of practices from optical imagery use hard fixed thresholding methods. Time series of NDVI (Franke et al., 2012; Estel et al., 2018; Kolecka et al., 2018; Griffiths et al., 2019) and EVI (Schwieder et al., 2020) features, or spectral bands (Hadj Said et al., 2011), are also proposed. For these approaches, the thresholds are largely defined by visual interpretation and applied directly to the feature time series. In Kolecka et al., 2018, management practices are detected by comparing first-order derivatives computed on neighboring parcels. A threshold is defined to assess the dissimilarity of the resulting time series to perform the detection. Taking into account the 10-day equidistant NDVI time series constructed from the HLS products, 1 to 5 mowings between April and November are detected at the country scale in Griffiths et al., 2019. In this last work, a idealized non-managed time series (*i.e.*, unaffected by management practices) is first constructed by fitting a polynomial model with a set of vertices corresponding to high NDVI values. To detect mowings corresponding to contrasting trends between the fitted model and the time series, a fixed threshold is applied on residual errors. The same strategy is employed for multiple years in Schwieder et al., 2021, using EVI rather than NDVI. Instead of a polynomial fit, this work proposes a linear interpolation applied on the selected EVI vertices. To set the threshold, the authors use the mean value of all absolute residuals within the time series of each parcel. As for the previous work, the residuals are computed from the difference between the fitted model and the observed time series. A two-stage adaptive threshold, defined for each parcel independently, is used in Gómez-Giménez et al., 2017. The authors exploit a bi-temporal vegetation index and propose to use the mean and the 95% percentile value of the time series of each parcel in the threshold strategy.

Besides thresholding approaches, some works are adopting the supervised classification of multi-temporal optical data. Different classifier methods are proposed such as Dynamic Time Warping with Support Vector Machines (Dusseux et al., 2014c) or CART decision trees (Halabuk et al., 2015). However, due to the previously mentioned scarcity of validation data, only a few parcels, dozens at most, are included in these proposed approaches, preventing a conclusive evaluation of their relevance.

Increasing interest in SAR time series for the detection of practices

Especially since the arrival of Sentinel-1 SAR time series, some works propose the exploitation of frequent and regular SAR acquisitions. SAR approaches mainly rely on the backscattering coefficient, calibrated to Sigma0 (σ^0, see Section 2.4.2) (Schuster et al., 2011; Siegmund et al., 2016; Stendardi et al., 2019b; Taravat et al., 2019), Gamma0 (γ^0) which is a σ^0 normalized with the local incidence (De Vroey et al., 2021a; Lobert et al., 2021), or coherence (see Section 2.4.3) (De Vroey et al., 2021a; Lobert et al., 2021; Komisarenko et al., 2022). Besides most of the works exploiting Sentinel-1, the use of TerraSAR-X Schuster et al., 2011 and COSMO-SkyMed Siegmund et al., 2016 is also explored.

Nevertheless, due to the complexity of interpreting the SAR feature time series (Sections 1.2.1.2 and 2.4), the majority of work relying only on SAR data is exploratory and does not perform statistical validation or report a specific methodology for the detection of practices. Instead, these works to analyze the behavior of different SAR features time series in response to technical acts. For example, Sentinel-1 backscatter coefficient (Chiboub et al., 2019; Zhou et al., 2021) and coherence (Chiboub et al., 2019; Tamm et al., 2016; Voormansik et al., 2016; Voormansik et al., 2020) temporal behavior with respect to mowing or ploughing, reported from field campaigns, are thoroughly analyzed. Several polarimetric features, such as eigenbased entropy, anisotropy, or alpha decomposition from high spatial resolution TanDEM-X (dual-polarimetric) and RADARSAT-2 (fully polarimetric) are also assessed (Voormansik et al., 2016). Optical imagery is sometimes used alongside SAR features to facilitate the interpretation. In Voormansik et al., 2020, the discrimination of mowing and ploughing acts using Sentinel-1 backscatter coefficient and Sentinel-2 NDVI 6-month time series is explored at a national scale. The authors in Zhou et al., 2021 observe the response over a single alfalfa parcel being monitored on the ground. The backscattering coefficient from Sentinel-1, together with NDVI

and EVI obtained from Sentinel-2, Landsat-8, and MODIS satellites, as well as HLS products are considered. SAR and optical responses to technical acts on mountain pastures are also explored using NDVI and RGB images recorded from on-ground pheno-cameras (Rossi et al., 2019; Stendardi et al., 2019a).

As mentioned, few works perform statistical validation or propose a methodology for the detection of practices from SAR features time series. These few works, as for optical-based approaches, rely for the most part on fixed thresholding approaches (Schuster et al., 2015; Siegmund et al., 2016). Adaptive thresholding is also proposed by some works in the litterature. For example, several detection methods are proposed on either γ^0 time series or coherence time series in De Vroey et al., 2021a. The authors propose three different methods to detect a signal increase followed by a signal decrease which is related to mowing events (see Section 2.4.3). The first method is a mean shift approach with a sliding averaging window whose size varies with the local variance. Fixed or adaptive thresholds (*e.g.*, related to the standard deviation) are applied to each window. The second assessed method is a linear regression approach with an asymmetrical sliding windows and thresholds applied on the resulting regression coefficients. The third method follows a two-mean strategy, which relies on a fixed-size sliding window. A statistical hypothesis test verifies if there is a significant change in each window, and a threshold on the significance of the p-value of this hypothesis is used to detect a candidate mowing. In Taravat et al., 2019 a deep-based approach is also adopted. The authors consider the detection of mowings as a binary classification problem. A shallow MLP with 1 hidden layer using as input Sentinel-1 backscattering coefficient, from which second-order texture metrics are also computed (homogeneity, contrast, entropy, and dissimilarity). In this work, network training is done using mowing events with exact dates reported for ten grassland parcels.

Joint optical and SAR exploitation for the detection of practices

A small number of works finally propose to jointly exploit the strengths of both optical and SAR time series. Section 2.4 and the previous paragraph highlighted the complex interpretation of SAR time series for detecting practices. Exploiting SAR and optical features furthermore implies a high dimensionality of the data. Hence, Machine Learning (ML) approaches are favored. Deep-based methods are adopted here as providing accurate results such as reported in Chapter 3. In the two identified works, data from the Sentinel-1 and 2 missions are used. Furthermore, 1D-CNN strategies are proposed in both approaches.

In (Lobert et al., 2021), Sentinel-1 gamma backscattering coefficient and GLCM, interferometric coherence, and NDVI from Sentinel-2 and Landsat-8 are exploited. Median values are computed from the features at parcel level and used as input data. Labeled sub-sequences of the time series are fed into a 1D-CNN yielding a binary output corresponding to the presence or absence of mowing. In this study, a reference dataset composed of 257 mowings from 64 parcels is used to supervise model training and validate the results. The 64 grassland parcels are distributed across three different and spatially distant sites in Germany. The second work uses temporally smoothed interferometric coherence and filtered NDVI time series from Sentinel-1 and Sentinel-2 acquired between April and October Komisarenko et al., 2022. Both time series are resampled to a 1-day temporal grid to feed the network with equidistant observations. As for the last work, a binary classification of mown / not mown for each time series date is performed using a 1D-CNN. Furthermore, a rejection mechanism in case of uncertainty is furthermore tested. The latter strategy relies on the rejection of a detection when the distance to a discrimination plan is lower than a particular set threshold. The network supervision and validation uses a dataset containing the technical acts, manually labeled, of 2,000 grassland parcels distributed at a country-scale in Estonia.

Characteristics of the most recent notable works

Starting in 2010, only about seventeen peer-reviewed journal research works, reporting a detection method and assessing the results using optical or SAR features are identified. These works, have been introduce

din the previous paragraphs. Among these works, important differences are nevertheless observed and are illustrated here. In particular, the extent of grassland surfaces (km^2), and the number of validation points (*i.e.*, technical acts) considered for the different works vary significantly.

Figure 5.1 illustrates these two features for the seventeen notable works. It can be remarked that the extent of considered surfaces ranges from a few contiguous parcels to twenty-seven European countries. It must be noted that as the grassland extend is not always explicitly given, some of the reported numbers concerning the considered extent can be approximate. In the case where this information was not explicitly reported in the works, similar information is used to retrieve the total extent considered, such as the number of parcels and their average size. The number of validations points varies between 4 and 2,000. These relatively low numbers highlight the complexity and scarcity of gathering large-scale validation datasets.

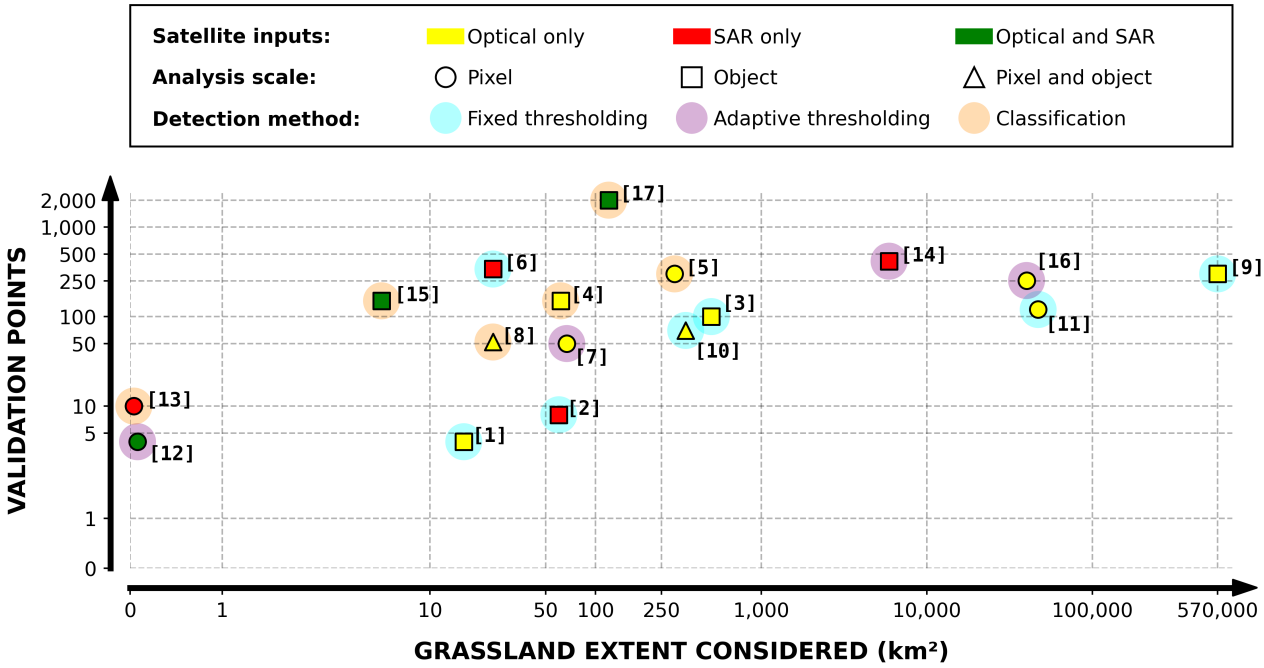

References included in the figure

[1]	Hadj Said et al., 2011	[11]	Griffiths et al., 2019
[2]	Schuster et al., 2011	[12]	Stendardi et al., 2019a
[3]	Franke et al., 2012	[13]	Taravat et al., 2019
[4]	Dusseux et al., 2014c	[14]	De Vroey et al., 2021a
[5]	Halabuk et al., 2015	[15]	Lobert et al., 2021
[6]	Siegmund et al., 2016	[16]	Schwieder et al., 2021
[7]	Gómez-Giménez et al., 2017	[17]	Komisarenko et al., 2022
[8]	Lopes et al., 2017		
[9]	Estel et al., 2018		
[10]	Kolecka et al., 2018		

Figure 5.1: *Top:* Summary of the reviewed work by considering different criteria : grassland extent and number of included validation points (both in logarithmic scales), input data type, scale of analysis and type of methodologies; *Bottom:* reference list of the reviewed works.

Three other characteristics are also reported in Figure 5.1:

(i) the type of satellite input data: optical, SAR or using both;

(ii) the analysis scale: pixel-, object-based or both;

(iii) the categorization of the proposed methodology : fixed/adaptive thresholds or defining a classification problem.

From these three additional characteristics, it is observed that ten out of the seventeen studies only exploit optical imagery, while only four exploit SAR images and three rely on both data sources. Regarding the analysis scale, six works are pixel-based while nine are object-based and two provide both pixel- and object-based analysis. The summary shows how fixed thresholds are employed in the majority, as only four studies employ adaptive thresholds. Finally, only six works propose classification strategies to detect management practices.

Outcomes of the literature review

Despite the efforts mentioned above, the results obtained for the detection of management practices on grasslands still exhibit some limitations. In the following, it is proposed to summarize these limitations and identify important aspects that can be discussed in further detail.

Regarding the choice of data, the temporal resolution they allow considering the rapidly evolving grasslands is the main driving factor. Optical data is initially preferred until the availability of Sentinel-1 SAR data. Due to the speckle noise and the temporal fluctuations of SAR feature, additional filtering steps are commonly adopted. Temporal smoothing is for example often performed which can be detrimental to the detection of practices as outlined by the rapid regrowth on grasslands. Additionally, the choices required to use SAR features are numerous. As SAR data are characterized by several incidence angles, polarizations or drastically different feature types, their adoption can add many open parameters to the detection task. The different works thus rely on distinct pre-procesing and feature selection steps that can be discussed. The recent availability of products that integrate Sentinel-2 and Landsat-8 facilitates the processing, but the temporal repetitivity is remaining conditioned by cloud cover. Geographical considerations can prevent these approaches to be effective. Overall, the data coming from different sensors (*i.e.*, optical and SAR or multiple optical sensors) are generally exploited independently, as the main objective of these multi-sensor approaches is to increase the temporal resolution of the time series.

Threshold-based approaches allow simple interpretations of the results and also the integration of expert knowledge. Incorporating expect knowledge, regarding features or temporal aspects, appears to be necessary to address complex phenologies and variable grassland management calendars. Threshold-based approaches are consequently largely favored. However, setting thresholds is challenging and considerably influences the reliability of these methods, especially due to missing data in optical time series and variety and fluctuations of SAR features. The threshold-based approach can be prone to poor spatial generalization capabilities.

Still, most of the existing works are found to validate their approach on a relatively small number of parcels due to the complexity of acquiring reference data. Moreover, the parcels are generally in the same climate-wise area, implying low heterogeneity in the used datasets and potential spatial correlation. Taking into account the work presented in Figure 5.1, the mean number of validation points is only 254. The different validation datasets are mainly constructed from photo-interpretation of time series of optical data and, to some extent, from field visits. The low number of validation points reflects the difficulty in obtaining exhaustive data to allow effective validation of the different proposed methodologies. In addition, the geographical areas covered by the validation seem insufficient with respect to the large areas covered by grasslands.

Finally, in the literature, both pixel- and object-based approaches are proposed. Pixel-based analysis is mainly adopted by optical-based studies. The main advantage of this strategy is the spatial accuracy it allows. However, pixel-based analysis is sensitive to noise, as the accuracy of the analysis depends on the radiometric quality of the data to separate adjacent pixels responses to changes. This type of analysis is also computationally resource intensive. Furthermore, as mentioned previously, the pixel-based approach is challenging when integrating SAR data, especially due to speckle noise. To address the existing drawbacks, object-based

approaches are found in the literature. Traditionally, these strategies propose the use of LPIS information to perform analysis at the parcel scale. Integrating object-based knowledge allows to propose a more robust statistical analysis to detect changes, for example, taking into account the mean, median, or standard deviation of the pixels in the parcel. However, object-based analysis greatly reduces spatial information and does not account for large parcels with heterogeneous cover, which can be found in the case of grasslands. Although the choice of the analysis scale is mainly initiated by the type of data used (*i.e.*, optical or SAR imagery), it is rarely thematically justified.

To address the limitations of the existing work, a new approach for the detection of technical act frequencies on grasslands is developed and assessed. The proposed approach will assess different methodologies that are based on the exploitation of highly sampled NDVI time series obtained from the SenRVM approach. This will allow us to capitalize on the temporal resolution of SAR time series and the favorable spectral response of the NDVI to management practices. On the contrary of the presented related works, it is furthermore proposed to discuss and define an alternative to the pixel- and parcel-based analysis scales. To assess the different detection methods and to overcome the scarcity of validation datasets, the construction of large-scale validation datasets is introduced.

5.2 The proposed methodology

A three-step workflow is proposed in the following. The first step of the methodology aims to address the spatial specificities of grasslands and discuss the relevant scale of analysis. This will lead to the definition of a new analysis scale based on superpixels (Section 5.2.1). As a second step, hyper-temporal NDVI time series at the superpixel scale obtained with the SenRVM methodology are introduced (Section 5.2.2). They must allow for better characterization of abrupt changes and avoid missed management practices due to clouds. Finally, different detection strategies that are applied to the time series obtained from SenRVM are proposed as a last step (Section 5.2.3).

5.2.1 Monitoring grasslands: the importance of the spatial scale

Existing object-based approaches have proposed the detection of grassland management practices at the parcel object-level. The proposed parcel-based analysis, although computationally efficient and allowing the integration of often robust reference data on the location of grassland parcels, includes important limitations.

It was explained in Section 1.1.4 that administratively declared parcels are subject to management practices that are carried out on finer scales. In particular, rotational management, aiming at spreading the availability of the grass resource over time, brings farmers to conduct technical acts that are not performed uniformly on the parcel. As a result, the parcel is splitted into smaller areas that are managed with distinct calendars. From a methodological point of view, this process can be related to an over-segmentation (*i.e.*, defining multiple and smaller parts) of the parcel boundaries.

Two main factors will induce the spatial distribution of the smaller intra-parcel areas:

- *location-induced* parcel segmentation is performed when environmental factors, such as topographical or pedological factors, are inducing the spatial distribution. For instance, some areas may for example be affected by a lower water retention capacity in the case of a steep slope, or be affected by different soil properties, *e.g.*, with sandier areas or disparate clay concentrations. Therefore, the phenology of grasses, potential yields, and growth rates of these areas will differ. The segmentation of the parcel is in this case naturally influenced by these environmental factors, resulting in distinct management practices and calendars of the different areas.

- *management-induced* parcel segmentation refers to the use of parcel properties, beyond environmental factors, to define smaller intra-parcel areas. Accessibility to livestock, potential for mechanization, or temporally expected yields are among the properties commonly used to perform such segmentation.

To highlight the importance of the analysis scale, an example of multiple intra-parcel behaviors in a parcel extracted from the RPG is shown in Figure 5.2. Three consecutive non-cloudy Sentinel-2 acquisitions illustrate the management practices performed on this permanent grassland.

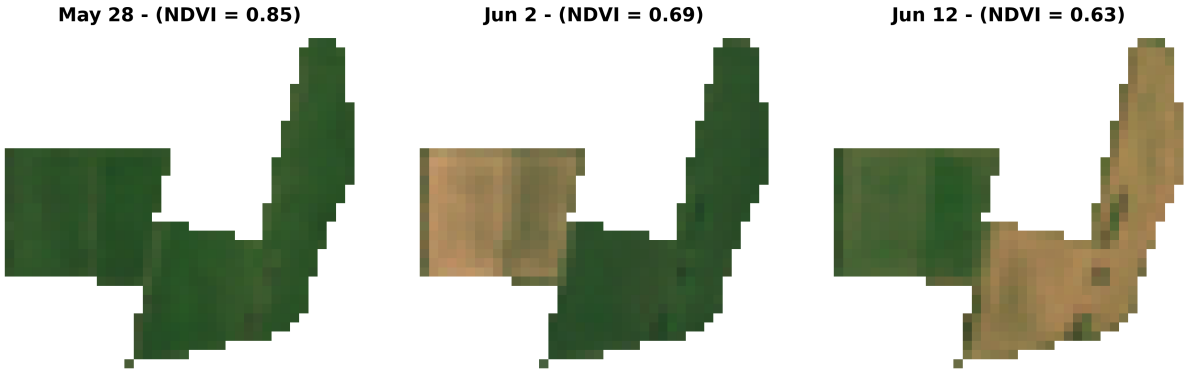

(a) (b) (c)

Figure 5.2: Example of Rotational management of a permanent grassland parcel extracted from the RPG. The three consecutive non-cloudy Sentinel-2 images illustrate how two technical acts are performed at different dates for a single parcel.

Another important remark is that the larger the parcel, the more likely and possible rotational management will be adopted. Hence, the larger the parcel, the more the parcel object-scale analysis is inappropriate. To corroborate this, Figure 5.3 illustrates three RPG declared parcels for which rotational managements are applied. First, it clearly appears that, as previously observed, the height of the vegetation is not homogeneous on the overall surface of these parcels. Furthermore, two areas are distinguished in the first parcel which is 6.24 ha, 5 areas is the second parcel of 14.41 ha and up to a dozen of differently managed areas are visible in the third parcel of 44.8 ha.

(a) (b) (c)

Figure 5.3: Three examples of administratively declared parcels for which technical acts are performed only on local areas of the parcel. Parcel (a) is 6.24 ha, parcel (b) is 14.41 ha and parcel (c) is 44.8 ha.

Considering all the above, a single decision at the parcel scale about the occurrence of a technical act therefore can not be appropriate. Taking into account the spatial specificities of grassland management prac-

tices can lead to more robust and reliable methodologies. In this way, several considerations can be taken for the segmentation of the parcels:

- very small regions in the parcel of the order of a few pixels can occur, due to the strong response of grasslands to topographic and soil conditions. The small regions will have characteristics different from those of a more homogeneous neighborhood. These isolated pixels, which are seen as a kind of outliers, can result in a too detailed over-segmentation.
- a minimum size can be assumed for the distinction of homogeneous regions managed in a similar way. In fact, constraints on accessibility, profitability or potential mechanization would prevent too small regions from being defined by farmers.
- effects on the vegetation of management practices are non-persistent as the grass growth back. Relying only sparse temporal information to differentiate the small areas is therefore not sufficient. As observed in Figure 5.2, the average NDVI of both separately managed areas is similar if the three dates are only considered (*e.g.*, two dates with high vegetation cover and one date with bare ground for each area). Thus, longer time series should be considered alongside spatial features to distinguish the areas.

Superpixel scale definition

One solution to the limitations of pixel- and parcel-based analysis is to define an intermediate analysis scale. In this work, the partitioning of administratively declared RPG parcels into *superpixels* (Ren and Malik, 2003) is proposed. Superpixels are defined as perceptually meaningful atomic regions (*i.e.*, parts of the original object), which are obtained from feature and spatial characteristics. The underlying idea is to identify regions of parcels that have the same behavior throughout the year and, by extension, are managed in the same manner.

Superpixels are automatically obtained from segmentation techniques, aiming the full partition of a digital image into multiple regions. A rich and prolific literature covers image segmentation techniques from multiple sources and for various applications. Historically and still today, for some applications, techniques based on thresholding or edge detection are employed. The threshold-based techniques are the simplest approaches to image segmentation. They mainly investigate intensity histograms to apply thresholds to perform segmentation. Local and global threshold methods can be found, either with fixed or adaptive thresholds. Threshold methods are used, for example, to create binary segmentation that highlights a single class of interest. Otsu (Otsu, 1979), Niblack (Niblack, 1985) or Sauvola (Sauvola and Pietikäinen, 2000) methods are among the most widely used threshold segmentation techniques. Edge-base techniques look for discontinuities in the local features of an image. They return collections of points, lines, that are then used to obtain a continuous segmentation. Examples of edge-based techniques are the well-known Sobel (Kittler, 1983), Prewitt (Prewitt, 1970), Laplacian (Marr et al., 1980) or Canny (Canny, 1986) operators.

Recent advances in remote sensing sensors allow Earth observation images to provide abundant spatial information and complex spectral information. Threshold and edge detection techniques are sensitive to noise and generally only take into account very local spatial information. Furthermore, these techniques are not necessarily applicable to multispectral data. Hence, region-based approaches that expand the previously mentioned techniques are preferred for the segmentation of multispectral satellite images. Region-based techniques are separated between region growing methods and region splitting with merging methods. Starting from seed pixels, these methods are sought for similarities or discontinuities between adjacent pixels. Predefined rules, including thresholds, are used as a criterion to differentiate the different regions in an iterative process. Statistical Region Merging methods (Nock and Nielsen, 2004), Watershed-based methods (Beucher and Lantuéjoul, 1979) or Mean Shift methods (Fukunaga and Hostetler, 1975) are region-based techniques that

are extensively used.

Superpixels (Ren and Malik, 2003) are region-based methods that are gaining interest in various segmentation tasks (Wang et al., 2017a; Stutz et al., 2018). Two constraints are imposed to the superpixels and not necessarily to region-based approaches. The size must be similar for the set of superpixels which must also follow an equidistribution throughout the image. Similar sizes limit the creation of very small areas, which can be implausible in the case of agricultural management practices. Furthermore, this allows the integration of some spectral diversity in a more globally homogeneous region (*e.g.*, isolated pixels), as it can be the case for grasslands. The Simple Linear Iterative Clustering (SLIC) algorithm introduced in Achanta et al., 2012, is a clustering region-based algorithm and belongs to the most commonly used superpixel generation methods (Zhou et al., 2013; Csillik, 2017; Mahajan and Fataniya, 2020; Derksen et al., 2020; Yin et al., 2021). It adapts the k-means clustering approach (MacQueen et al., 1967) to efficiently generate superpixels with a combined spatial-feature distance to encourage compact segments.

SLIC algorithm takes as input the number of superpixels to be generated by setting the k parameter. The average size of the superpixels $S \times S$ is then calculated with k and the total number of image pixels N of the image. Superpixel centers C_k are initialized on a regular grid spaced $S = \sqrt{N/k}$ pixels apart. The pixels in a $2S \times 2S$ window around C_k are then iteratively aggregated while updated superpixel centers are calculated. Iterations are repeated until convergence, reached when C_k coordinates are no longer changing. The aggregation of pixels is verified with the D metric. D is based on a weighted sum of the spatial d_s and feature d_f distances:

$$d_s = \sqrt{(x_k - x_i)^2 + (y_k - y_i)^2}\,, \tag{5.1}$$

$$d_f = \sqrt{\sum_{b=1}^{B} (G_k^b - g_i^b)^2}\,, \tag{5.2}$$

$$D = \sqrt{(d_f)^2 + \left(\frac{d_s}{S}\right)^2 \times m^2}\,, \tag{5.3}$$

where $[x, y]$ are the image coordinates and G_b^k and g_b^k are respectively the superpixel mean features and the pixel feature for the bth feature-channels $\in B$ channels of the image. m is a compactness weighting value to prioritize either the spatial or feature distances. This permits to relax the size and equidistribution constraints. A post-processing step, based on a connected component algorithm, allows the inclusion of isolated pixels in the final segmentation.

Initializing C_k on a fixed and evenly spaced grid involves segmenting the entire image (*e.g.*, a rectangular shaped raster). In the case where solely a region of interest wants to be segmented, such as a parcel with non-rectangular boundaries, the number of superpixels and an adequate border adherence cannot be achieved. The maskSLIC approach (Irving, 2016) allows to apply the SLIC method only to the region of interest. The initialization of C_k is done taking into account the distance to the borders of a provided mask and to the respective centers of the superpixels. Figure 5.4 shows an original grassland raster, the results of a SLIC segmentation in the middle which segments the entire raster, and the maskSLIC segmentation on the right, applied to the region of interest. Both SLIC and maskSLIC segmentation are performed with the same parameters ($k = 10$ and $m = 5$).

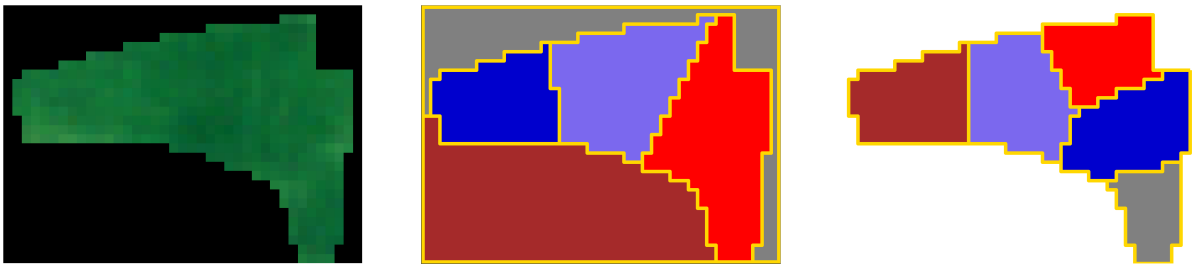

(a) (b) (c)

Figure 5.4: (a): Grassland raster retrieved from the LPIS. (b): Original SLIC segmentation, which does not suppresses the background of the input image resulting in a poor segmentation within the region of interest. (c): Segmentation with maskSLIC which performs segmentation only in the region of interest.

5.2.2 Estimation of hyper-temporal NDVI time series

The estimation of hyper-temporal NDVI time series is performed by the SenRVM regression methodology presented in Chapter 3. As previously observed, the temporal resolution of the SenRVM time series allows a better characterization of vegetation changes, which is essential to detect fast changes in grasslands.

To improve the SenRVM predictions, the blending post-processing strategy denoted as *AND-S2* and presented in Section 4.5.2 is considered. This strategy proposes to combine NDVI time series obtained from SenRVM and Sentinel-2 acquired NDVI time series. The *AND-S2* strategy permits to obtain densely sampled time series with a temporal resolution varying between 2 and 6 days (*i.e.*, the original SenRVM temporal resolution). The resulting temporal resolution appears suitable for the task of detecting the frequency of technical acts. It allows frequent monitoring, which is mandatory in the case of rapid regrowth, as illustrated in the objectives of the manuscript.

Chapter 4 has shown satisfactory results of SenRVM for monitoring grassland at the parcel level. However, Section 5.2.1 has illustrated that this scale is not adapted to the specific task of detecting technical acts. Thus, SenRVM is applied at the superpixel scale. Working at such a scale offers two main advantages. On the one hand, it allows a convenient trade-off between preserving the spatial information within a parcel and the reduction of the speckle effect affecting the SAR-based SenRVM inputs by averaging over clusters of pixels. On the other hand, it has been seen that the superpixel scale is relevant to distinguish the rotational management of grasslands. Finally, the pre-processing steps (*i.e.*, object-based statistics, building of a common temporal grid) described in Section 2.5 defined at the parcel-scale are valid for the superpixel scale and do not need any adaptation.

5.2.3 Detection of changes in the reconstructed NDVI time series

Different strategies are proposed to exploit the time series obtained from the SenRVM methodology for detecting technical acts. As outlined in the literature, they assume that grassland management practices are considered as changes in time series inducing a decrease in biomass. The lack of significant reference data first requires the adoption of unsupervised methods. Furthermore, this limitation prevents the semantic distinction of the different management practices. Indeed, both the complex visual interpretation and the temporal resolution of Sentinel-2 images used for annotations do not allow such distinction. Methods that require calibration (*e.g.*, based on phenology) are also discarded, as highly variable grassland phenologies are found. Change detection methods can also be divided into two categories: *offline* and *online*. An offline algorithm considers the entire time series and determines whether a change occurred using information from preced-

ing and following data. In contrast, online (*i.e.*, or near real-time) methods will concurrently perform their monitoring and process each data point as it becomes available. Thus, these online methods have no need, but also no knowledge, of the incoming acquisitions of the time series. Both types of methods are considered here, but it is worth mentioning that online methods have the advantage of being able to be applied in more operational contexts, often requiring decisions to be made quickly. The relevant methods finally must be able to capture different behaviors in the time series. The decrease induced by technical acts can be abrupt (*e.g.*, ploughing) or gradual (*e.g.*, extensive grazing). Furthermore, they can be successive, such as in the case of rapid regrowth with a new technical act, or ploughing following a mowing.

The time series obtained from the SenRVM methodology are denoted as $\widehat{N} = \{\hat{n}_1, \hat{n}_2, ..., \hat{n}_T\}$. $\widehat{N}$ is of variable length T, with $t \in T$, considering the blending step with non-cloudy Sentinel-2 acquisitions. The baseline method, referred to as **THR**, applies a threshold α on the first derivative of $\widehat{N}$, denoted as $dt(\widehat{N})$. The first derivative is computed as the difference between two consecutive points in a time series of length T. As proposed in the related work, the threshold value is considered either fixed (*i.e.*, same for all $\widehat{N}$), or adaptive (*i.e.*, taking into account the variance of $\widehat{N}$).

Rather than considering only two successive dates, as done with **THR**, the **THR-WIN** proposed method takes into account the cumulative sum value of successive decreasing $\widehat{N}$ time intervals as denoted by:

$$\int_{t_i}^{t_j} dt(\widehat{N})_t < \alpha \;\Big|\; dt(\widehat{N})_t < 0,\ t \in [t_i, t_j]\,, \tag{5.4}$$

where t_i and t_j are respectively the first and last dates of the decreasing time interval.

The second proposed strategy is denoted as the **THR-OLS** method. This methods idea is to use the slope of a linear regression line to depict the change rate in the time series. A rolling fixed temporal window applied on the $\widehat{N}$ time series is considered to calculate the slope. The slope parameter is computed using the classical ordinary least squares (OLS) algorithm. If the slope is exceeding some value, it can be considered that a change has occurred between the mid-point of the current temporal windows and the mid-point of the previous one. The change is detected by thresholding the estimated slope coefficient. This method requires the setting of two parameters: the size of the rolling temporal window W and the thresholding value α. Following the strategy presented in Griffiths et al., 2019 and Schwieder et al., 2021, the **THR-POLY** method is proposed. This third strategy computes an idealized time series of the growing season (*e.g.*, unaffected by changes due to technical acts). This time series is obtained by fitting a polynomial model (Po) over some selected vertices ($vert$). The primary vertices include the first, maximum and last values of $\widehat{N}$. The maximum values of $\widehat{N}$ selected within a rolling temporal window of size W are then used as supplementary vertices (sv). The number of such supplementary vertices depends on the size of W. The algorithm then calculates the residual values for each $t \in T$ as the deviation of $\widehat{N}_t$ from the idealized growing season trajectory at the corresponding date t. A threshold value α is applied on the residuals to iteratively detect the candidate technical acts. The size of the rolling window W and the threshold value α are defined by the user.

$$\begin{aligned}
sv_t &= max(\widehat{N}_{t:t+W}) \;\Big|\; t \in \{W,\ W \times 2,\ W \times 3, ..., W \times \frac{T}{W}\}\,,\\
vert &= [\widehat{N}_0,\ max(\widehat{N}),\ \widehat{N}_T,\ \{sv_1, sv_2, ..., sv_W\}] \;\Big|\; W \leqslant \frac{T}{W}\,,\\
Po &= c_0 + c_1 \cdot vert. + c_2 \cdot vert.^2\,,\\
|Po_t - \widehat{N}_t| &> \alpha \;\Big|\; t \in [0, T]\,,
\end{aligned} \tag{5.5}$$

Lastly, the use of the **THR-PELT** method is proposed, which relies on the Pruned Exact Linear Time (PELT, Killick et al., 2012) algorithm. PELT is a common change-point detection approach which minimizes

a cost function (cost) over both the number of change-points and their location in the time series. A change-point is defined as a rupture between several regimes of the time series. These regimes are obtained by iteratively segmenting the time series into sub-sequences. PELT is based on the dynamic programming approach (Bellman and Dreyfus, 1962) which allows to skip some iterations aiming at retrieving sub-sequences if the cost function satisfies some properties. This allows the PELT approach to be considerably much faster than other change-point detection methods. Furthermore, as a dynamic approach, PELT does not require the number of change-points to be specified. To account for possible noise in the time series, PELT allows for a minimum sub-sequence length W to be defined. A ρ penalty term, mostly linear, associated with the cost function further guards against overfitting and regulates the number of change-points detected.

Figure 5.5 provides a schematic illustration of the five different strategies applied on the same $\widehat{N}$ time series (green dots). The time intervals taken into account by the different methods for the candidate technical acts are marked by a grey background. The magnitude of the change thresholded during the change detection process is illustrated with red lines.

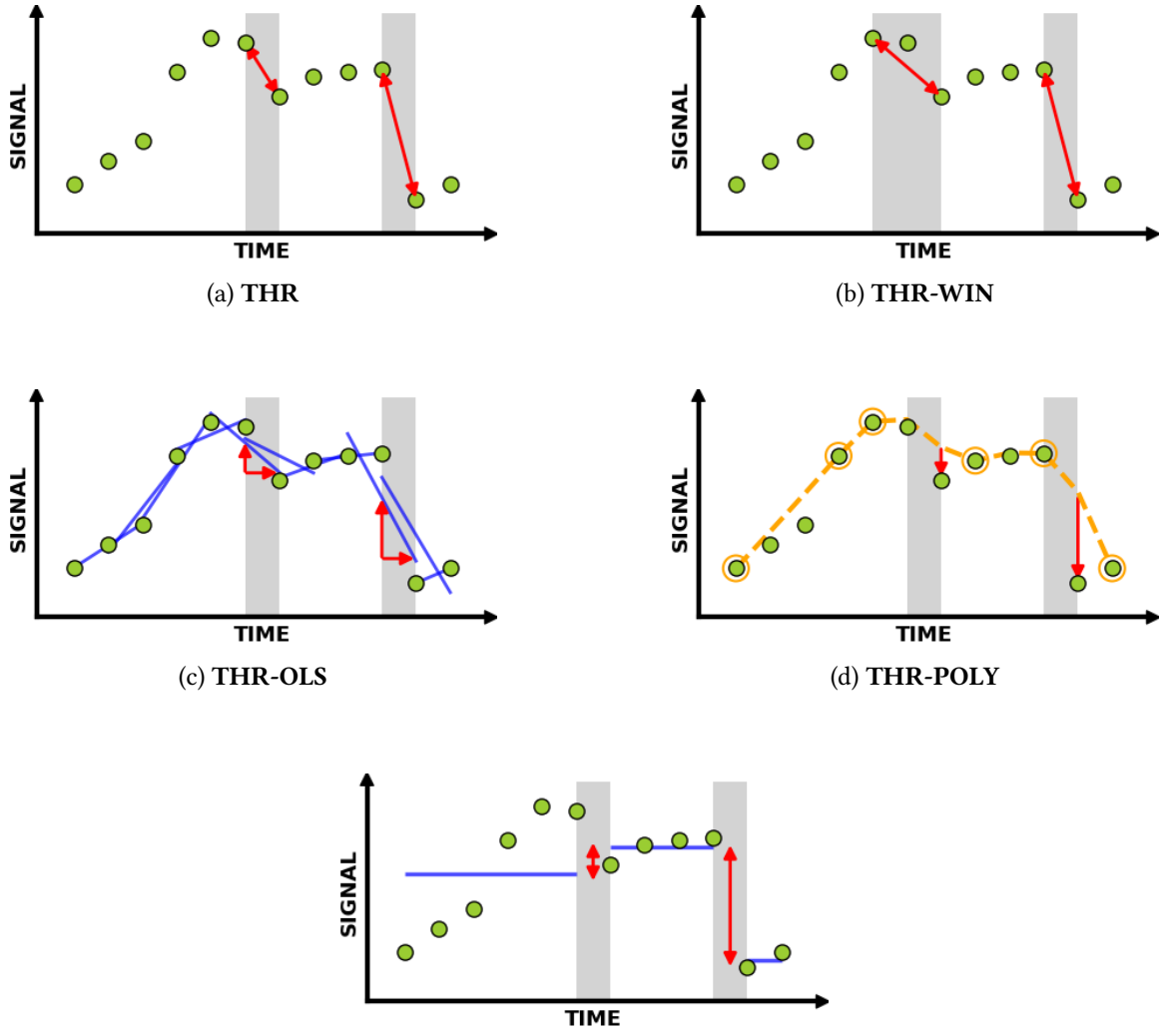

(a) **THR** (b) **THR-WIN**

(c) **THR-OLS** (d) **THR-POLY**

(e) **THR-PELT**

Figure 5.5: Schematic illustration of the five management practices detection strategies introduced in Section 5.2.3. Detection is performed on a time series signal (green dots). Candidates change-point time intervals are highlighted by grey background. The red lines represent the magnitude of change assessed by the different methods.

For the first **THR** method illustrated in Figure 5.5a, only consecutive dates are compared. For the second candidate technical act, the decrease magnitude is important, and this method should easily detect the change. The first technical act, which has a substantially lower impact on the decrease, is more challenging. In this latter case, the second method **THR-WIN** shown in Figure 5.5b might be more appropriate for detecting the change. As the magnitude of the change is assessed over decreasing time intervals of $\widehat{\mathrm{N}}$, a high magnitude of change is obtained by accounting for the sum of two consecutive decreases. For the **THR-OLS** method (Figure 5.5c), the OLS-regressed lines with a temporal window W of 3 are illustrated by the blue lines. The slope coefficient used for detecting the technical acts is shown by the red lines. Accurately, the second technical act with a larger drop of $\widehat{\mathrm{N}}$ exhibits a much more negative slope coefficient than the first technical act. In Figure 5.5d, the **THR-POLY** method is illustrated with a rolling temporal windows W of 3 $\widehat{\mathrm{N}}$ data points. The candidate technical acts are searched on the residuals calculated between the fitted polynomial curve (yellow line) constructed from selected vertices (orange outlined points) and the corresponding values of $\widehat{\mathrm{N}}$. Finally, the **THR-PELT** method based on the segmentation of $\widehat{\mathrm{N}}$ is shown in Figure 5.5e. Three sub-sequences are detected by the method (blue lines) using a cost function, a penalty term, and a minimal sub-sequence length W set here at 4. Differences between these observed sub-sequences defining distinct time series regimes are used to detect the candidates technical acts. At last, it can noted that **THR**, **THR-WIN** and **THR-OLS** methods are almost online methods as they only rely on the previous, or a few previous data points to perform their detection. The two remaining **THR-POLY** and **THR-PELT** methods are conversely offline, as they need the entire time series to be effective, respectively, to fit a polynomial curve and segment the time series.

5.3 Description of validation data

As outlined in Chapter 1, despite the clear and growing interest, a large-scale database (*e.g.*, regional, national, European) collecting information about technical acts currently does not exist (see also Section 5.1). Such a database is tedious to construct, as grasslands cover vast areas, and calendars of technical acts are neither regular nor predictable. The works in the literature are presenting several strategies to create validation datasets, which are illustrating the complexity of the task, especially regarding the highly varied grasslands agronomic species, and phenologies. To evaluate the methods presented in Section 5.2.3, a large validation data set is constructed considering the protocol defined in Section 5.3.1.

5.3.1 Protocol for data collection

Three possible ways of constructing such a dataset have been designed in the literature. First, by administrative means, as done in the framework of the Common Agricultural Policy (CAP) where farmers are required to report their main crop for each parcel. Unfortunately, the legal framework, the implementation of guidelines and tools are an arduous task that requires significant efforts to be implemented and were not realistic on the time scale of a PhD. A second possibility relies in field campaigns. Nevertheless, the possibility of rapid regrowth and the varying and unknown agricultural calendar on grasslands makes the collection of in situ data from field visits a very tedious task. As already illustrated, management practices monitoring would require at least weekly visits, which very quickly becomes time consuming. Lastly, the visual interpretation of satellite remote sensing images available at large scales is the solution proposed by most of the related works.

Visual interpretation is selected as the most practical of the three different solutions. The use of SAR images and features for visualization of technical acts has already been discarded as suffering from temporal fluctuations that can be misinterpreted as management practice (discussed in Section 2.4). Optical satellite imagery appears to be the best solution for the construction of a validation dataset. The illustrations provided earlier in this manuscript have already shown that observing the differences in true-color RGB compositions

is efficient. However, using optical remote sensing time series for the construction of the validation dataset involves certain limitations that must be outlined:

- the recurrent presence of clouds and the temporal resolution of satellite images prevents the exact date of the technical act from being known. Likewise, stability (*i.e.*, no technical act was performed) ;
- if the cloud cover is persistent, several technical acts may occur during the obstructed time interval. Thus, a single technical act can be annotated while two - or more - actually occurred;
- exhaustiveness of annotated technical acts can not be guaranteed and the evaluation of the results can not be entirely robust. The false positive or true negative rates of a method are only indicative.

In our case, Sentinel-2 images are used to construct a dataset recording all technical acts observed. Annotations are performed by considering the superpixel scale defined in Section 5.2.1. A technical act is considered when a significant change in reflectance in two successive non-cloudy RGB images is observed. In this case, the date preceding and the date for which the change is observed are annotated as the time interval during which a technical act was performed. To perform the annotation task, a python-based annotation module is subsequently developed (Figure. 5.6). The tool allows one to visualize all non-cloudy images acquired over the superpixel polygon. To help the annotation of technical acts, the first-order derivative of Sentinel-2 NDVI is thresholded as a pre-filtering step. The thresholding, using a user-defined value (*e.g.*, 0.1, 0.2), helps to identify potential technical acts (red boxes and orange temporal window in Figure 5.6), which can then be accepted, refuted, and supplementary technical acts added.

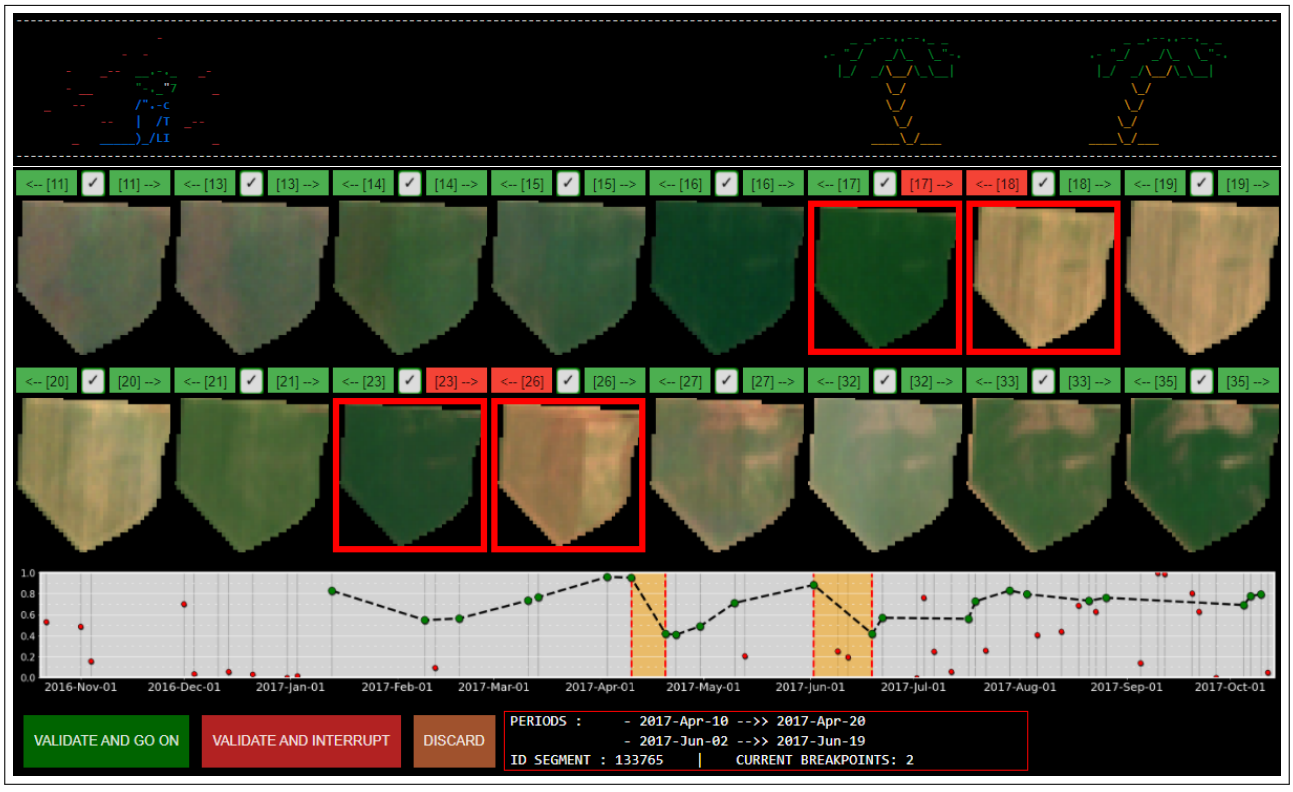

Figure 5.6: Screenshot of the interactive annotation module used to construct the validation data set. The module allows for visual interpretation of Sentinel-2 RGB images and time series analysis. Two technical acts are annotated for this grassland parcel. For each technical act, the two dates highlighted by red boxes (*top*) and by the orange temporal windows showing the NDVI decrease between the two consecutive images (*bottom*) are retained.

The use of complementary optical imagery acquired from other optical sensors could be used to reduce data uncertainty and the number of potentially missed technical acts for the construction of the validation dataset. Nevertheless, the likelihood of cloud obstruction similar to Sentinel-2 outweighs the data acquisition and curation efforts, and this possibility was discarded.

5.3.2 Characteristics of the validation dataset

The visual interpretation protocol described above is applied on 1,000 segments, *i.e.*, the superpixels obtained by the method described in Section 5.2.1, for both Mâcon and Toulouse areas. The 1,000 segments are geographically distributed across the areas and have sizes ranging from 0.28 ha to 25.6 ha. For Mâcon, 1,625 annotations corresponding to time intervals (*i.e.*, the date before the change, and the date of change) are obtained. For Toulouse, 1,641 technical acts are annotated. Only the technical acts for which there is little doubt are annotated, with a clear change in reflectance between both observed images and a decrease in the corresponding Sentinel-2 NDVI time series. One may consider that this artificially increases the performance score of the proposed methods. Yet, this remains the best solution for retrieving the less erroneous validation dataset possible.

Figure 5.7 provides the main properties of the two constructed validation datasets. It can be observed that for a large majority of the annotated segments, only 1 technical act is reported. This number goes up to 4 for some segments associated with more productive agronomic varieties.

Regarding the temporal properties of the annotations, a high propensity of technical acts is observed in late spring. Note that most of the annotations are contained on the months of June and May, respectively, for Mâcon and Toulouse. The length in days of the annotated time intervals is disparate, depending on the cloud cover and the area. For Mâcon, the time intervals range from 2 to 45 days, with a mode of 23 days. For Toulouse, time intervals ranging from 5 to 90 days are annotated, with a mode equal to 10 days. The drop magnitude (*i.e.*, difference in NDVI) for each annotated time interval is also calculated. For Mâcon and Toulouse, most technical acts induce a drop in NDVI ranging from 0.3 to 0.4. For Mâcon, the second most observed drop is between 0.2 and 0.3. However, for Toulouse, the second most observed drop is ranging from 0.4 to 0.5.

5.4 Experimental setup

The experimental setup of the proposed three-step methodology presented in Section 5.2, *i.e.*, superpixel gathering, calculation of SenRVM models, and evaluation of technical act detection methods is presented here. The metrics used to assess the accuracies of the different methods are also introduced.

Generation of superpixels from the grassland datasets

Segmentation with maskSLIC is performed on Mâcon and Toulouse grassland datasets. Two strategies to apply the maskSLIC algorithm are possible: performing mono-temporal (*i.e.*, renewed at each date) or multi-temporal segmentation (valid and unchanged for the whole time series). The latter approach is selected, as technical acts have an impact on both the spatial and temporal domains. Furthermore, varying the location of the superpixel for each data would require an important adaptation to the SenRVM approach, which requires full time series to perform the regression task.

Superpixel segmentation is performed for each parcel of the Mâcon and Toulouse grassland datasets presented in Section 2.3.1.1. For each area, the entire stack of NDVI images marked as valid by the cloud &

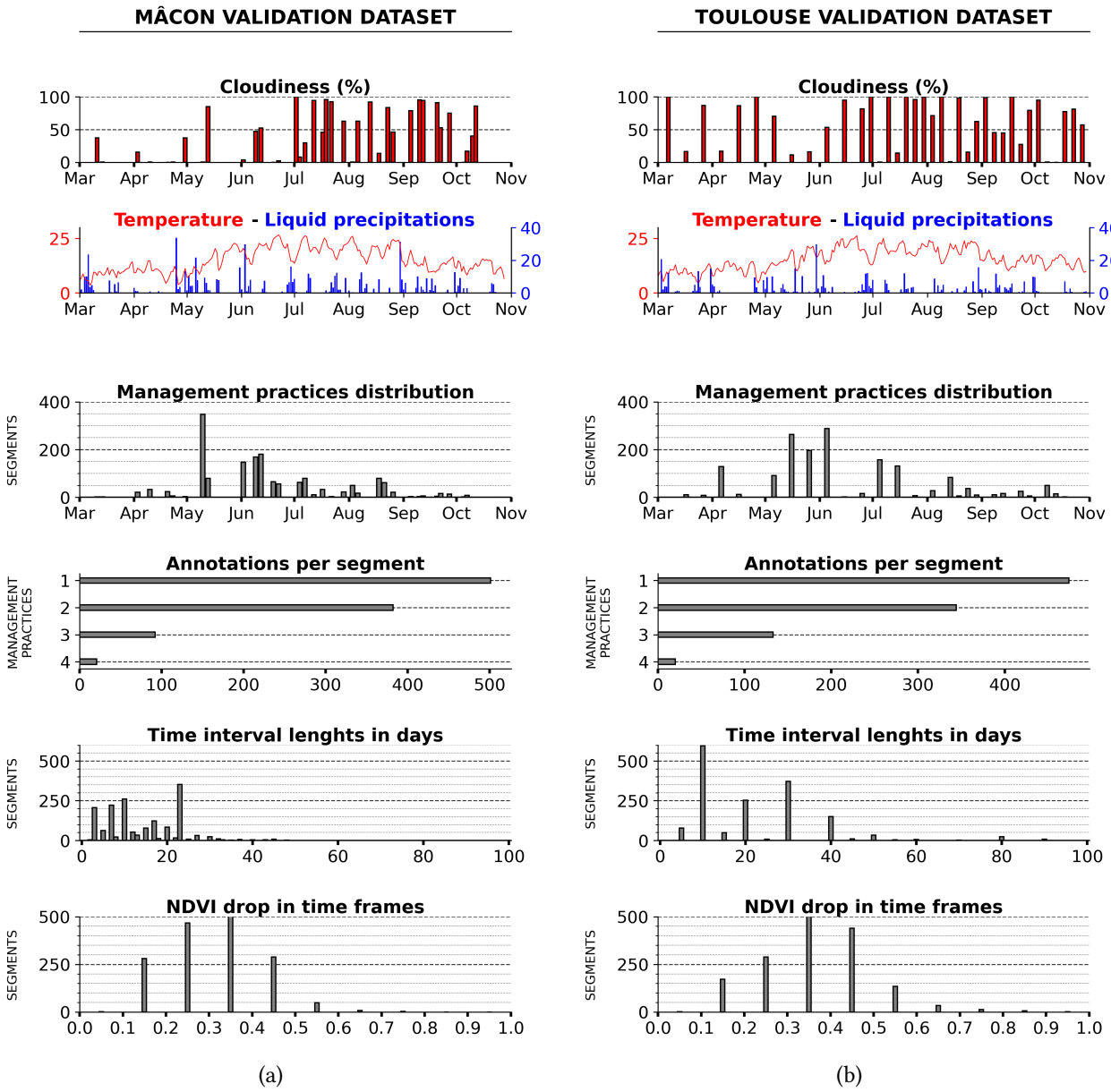

Figure 5.7: Mâcon (*left*) and Toulouse (*right*) validation dataset statistics. From *top* to *bottom*: cloud cover per date, temperature and liquid precipitation, temporal distribution of management practices, number of acts annotated by the different segments, length in days of annotated time intervals and drop of NDVI in the annotated time intervals.

shadow masks is used. This temporal stack is fed to the maskSLIC algorithm. The NDVI stack corresponds then to the previously described feature channels of Equation 5.2. Thus a spatio-temporal segmentation is performed by the maskSLIC algorithm. Same parameters are used for both areas. The m parameter is empirically set to 0.2 to encourage feature homogeneity within the superpixels. Indeed, the shapes of the individual areas within the parcel that wants to be retrieved can greatly vary. The parameter k is set accordingly to the size in hectares (s) of each parcel: k is (2,5,10) for the intervals ($s < 5$ ha, 5 ha $< s <$ 30 ha, $s >$ 30 ha).

An additional post-processing step is performed to filter the segments whose sizes are smaller than 0.15 ha. This value has been chosen to allow for the balance between the minimum spatial size of the superpixels and

the gathering of enough pixels for the computation of spatial statistics. Based on boundaries, the small segments are iteratively merged with the smallest neighbor segment until all segments are larger than 0.15 ha. However, the segments are not always connected to each other due to the complex grassland shapes and, furthermore, due to the negative buffering performed on the initial grassland polygons as a pre-processing step (Chapter 2, Section 2.5). In the case where no other segments are contiguous, the small segment is merged with the geographically closest segment according to their centroids.

Training SenRVM models at the superpixel-scale

SenRVM models are independently learned on the complete set of superpixels obtained from the previous step. Models are learned for the Mâcon and Toulouse areas. The same experimental setup previously used for parcel-based models (*i.e.*, same train/test/validation proportion, 5 models each having 5 folds, see Section 4.1.1) are used for the superpixel-scale models. Minor adjustments in hyperparameters are considered, accounting for the changes induced by the scale-shift (*e.g.*, number of samples in the datasets, sub-classes distribution, etc.). These changes are reported in Table 5.1.

Table 5.1: Comparison of SenRVM hyperparameters considered for parcel- and superpixel-based datasets.

	Mâcon		Toulouse	
	PARCELS	SUPERPIXELS	PARCELS	SUPERPIXELS
Batch Size	256	128	256	128
Learning rate	0.0005	0.0001	0.0001	0.0001
GRU hidden size	256	512	256	512

Parameters of the technical acts detection methods

The parameters tested for each of the five methods presented in Section 5.2.3 are provided in Table 5.2.

For all five methods, the threshold (or penalty value in the case of **THR-PELT**) α is tested considering twenty different values. For **THR**, **THR-WIN** and **THR-POLY**, the range [-3,-1] is empirically defined considering the observed NDVI drops induced by technical acts and reported for the validation datasets. Steps of 0.01 are considered. For **THR-OLS**, the range considered as well as the step values are divided by 2. For the **THR-PELT** method, the penalty term ρ is in the range [0,0.5] with steps of 0.025.

For the **THR-OLS** and **THR-PELT** methods, a temporal window size W is defined. For **THR-OLS**, W, which describes the fixed number of consecutive data points taken into account to perform the OLS regression. Values of 3, 4, and 5 are tested. For **THR-POLY**, the temporal window W describes the temporal interval in which vertices are selected. Values of 3, 5, 10, and 20 are considered. The W parameter of **THR-PELT** is different, as it constrains the minimal size of sub-sequences and thus the minimal distance between potential technical acts. Low values of 2, 3, and 4 are tested, as it has been previously demonstrated that rapid regrowth and thus temporally close technical acts are occurring. For the **THR-POLY** method, orders of 2 and 3 are tested for the polynomial fit between the selected vertices. For the implementation of the PELT algorithm, the *Ruptures* package is used (Truong et al., 2020). It provides different cost functions from which the L1 norm, L2 norm, and a Radial Basis Function (RBF) kernel are selected.

During the dormancy of the grass, technical acts are generally not performed. Thus, the time series considered as input to the different detection methods are restricted to the temporal interval between March 1^{st} and October 31^{st}. This consideration has been extensively used in the literature as mentioned in Section 5.1, and allows us to eliminate any significant decrease in vegetative activity or biomass due to climate factors.

Finally, time intervals are considered as outputs of the detection methods. As in the two validation datasets, the date preceding the detection and the date detected are kept as the time interval in which the technical act potentially occurred. Any intersecting date between a detected and an annotated time interval is subsequently considered as an accurate detection. Consecutive detected time intervals are merged as a single detection. Furthermore, it should be noted that the annotated time interval can be relatively long due to cloud cover (Section 5.3.2). Therefore, if several technical acts are detected during a single annotation time interval, as cloud cover prevents any further assessment, these detections are counted as only one accurate detection.

Table 5.2: Description of the parameters tested for the different methodologies detailed in Section 5.2.3. α refers to a threshold, ρ to a penalty value, W to a temporal window size, σ to the standard deviation of the time series, ord. to the order of the polynomial fit, and cost to a cost function.

METHOD	PARAMETERS
THR	α = [-0.1 , -0.3] with steps of 0.01 or $\sigma \times \alpha$, α=[0.75 , 1.75] with steps of 0.05
THR-WIN	α = [-0.1 , -0.3] with steps of 0.01
THR-OLS	α = [-0.05 , -0.15] with steps of 0.005 | W = [3 , 4 , 5]
THR-POLY	α = [-0.1 , -0.3] with steps of 0.01 | W = [3 , 5 , 10 , 20] | ord. = [2 , 3]
THR-PELT	ρ = [0 , 0.5] with steps of 0.025 | W = [2 , 3 , 4] | cost = [L1 , L2 , RBF]

Accuracy metrics

The two constructed validation datasets are used to evaluate the five proposed technical act detection methods. Detecting technical acts is a binary classification problem. For each date, the method informs on the presence (*positive* outcome) or absence (*negative* outcome) of the technical act. Precision, Recall, and F-Score metrics are thus used to evaluate the detection performances:

$$\text{Precision} = \frac{\text{TP}}{\text{TP} + \text{FP}}\,, \tag{5.6}$$

$$\text{Recall} = \frac{\text{TP}}{\text{TP} + \text{FN}}\,, \tag{5.7}$$

$$\text{F-Score} = 2 \cdot \frac{\text{Precision} \cdot \text{Recall}}{\text{Precision+Recall}} \in [0, 1]\,, \tag{5.8}$$

where TP (True Positive) = correctly detected management practices
FP (False Positive) = supplementary detected management practices
FN (False Negative) = missed management practices.

Precision informs on how often a technical act detection is accurate, while recall informs about the proportion of accurate detection with respect to the total of detections. The F-score combines both precision and recall in a single metric assessing the accuracy and sensitivity of the predictions. The three metrics of Equations 5.6, 5.7 and 5.8 are in the range [0,1] and high values indicate accurate predictions.

It must be once again noted that due to the shortcomings described in Section 5.3.1 (*e.g.*, temporal resolution of Sentinel-2 or persistent cloud cover), the FP are only indicative. The lack of satellite data used in the visual interpretation does not guarantee that management practices have not occurred. Thus, the precision metric can be influenced downward by a large number of FP, without the guarantee of error. Nevertheless, the methods can be efficiently compared since missing technical acts due to cloud cover are considered in all detection methods.

5.5 Assessment of the proposed method

The results of the three-step methodology are presented in the following. The relevance of the proposed superpixel scale is assessed and illustrated on managed grasslands with technical acts in Section 5.5.1. The results of the newly obtained SenRVM models at the superpixel scale are presented in Section 5.5.2. Finally, Section 5.5.3 will present the results obtained by the different detection methods by using the constructed validation datasets. The detection methods are applied to the resulting SenRVM NDVI time series obtained from the the two previous steps.

5.5.1 Evaluation of the superpixel scale

For Mâcon, 68,974 segments (*i.e.*, the superpixels) are obtained from the 27,832 grassland parcels described in Section 2.3.1.1. For Toulouse, 137,378 segments from 50,103 parcels are obtained.

Figure 5.8 indicates the number of segments obtained per parcel (ordinate in logarithmic scale). Two segments are mostly obtained from the segmentation task. An important number of parcels, corresponding to small-sized parcels and for which the maskSLIC algorithm could not differentiate spectral and temporal patterns, are not segmented. On the other hand, and mainly for Toulouse, some parcels are divided into a large number of segments. Two parcels in the Toulouse area are, for example segmented into 30 superpixels. These parcels correspond to very large pastoral areas in the Pyrenees, the largest of which is 1,733 ha. The average size of the resulting segments is 0.89 ha for the Mâcon area and 1.07 ha for Toulouse, which is roughly about 100 Sentinel-2 10×10 pixels. The median values are 0.65 ha and 0.50 ha for Mâcon and Toulouse, respectively. The similar size of the superpixels observed between the Mâcon and Toulouse areas, in spite of the originally very different parcel sizes (Table 2.6), illustrates the size and shape constraints imposed by the maskSLIC algorithm.

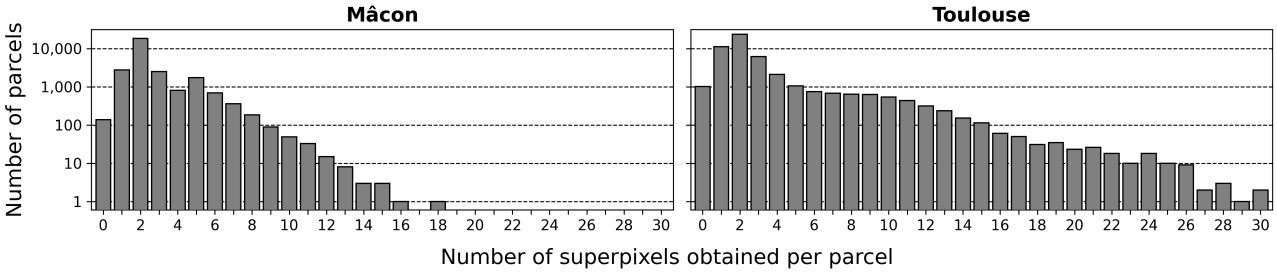

Figure 5.8: Number of superpixels obtained per parcel of the Mâcon and Toulouse grassland datasets. The number ranges from 1 (not segmented) to 30 in the case of large pastoral areas.

The superpixel segmentation task aimed at obtaining more homogeneous surfaces in terms of biomass, and therefore management practices. A comparison of the standard deviation of the pixels belonging to either the parcel or the superpixel-scale thus can inform on the obtained improvements. The standard deviation of the Sentinel-2 NDVI, averaged on all non-cloudy dates, is calculated at both the parcel- and superpixel-scale. Results are illustrated in Figure 5.9. For the parcels of the Mâcon area, the average standard deviation of the NDVI is 0.0375. This value drops to 0.0280 when using the superpixels to evaluate the standard deviation of the pixels. Similarly, for Toulouse, the NDVI standard deviation drops from 0.0493 to 0.0377 with the segmentation to a superpixel scale. The obtained standard deviation values of the pixels at the parcel-scale may already appear relatively low. Nevertheless, it must be recalled that a large corpus of several millions of pixels is taken into account for the computation. Thus, parcels depicting a homogeneous cover were probably already widely represented. Furthermore, the decrease of standard deviation achieved by the superpixel scale

corresponds to a significant decrease of 25.33% and 23.53% for Mâcon and Toulouse, respectively.

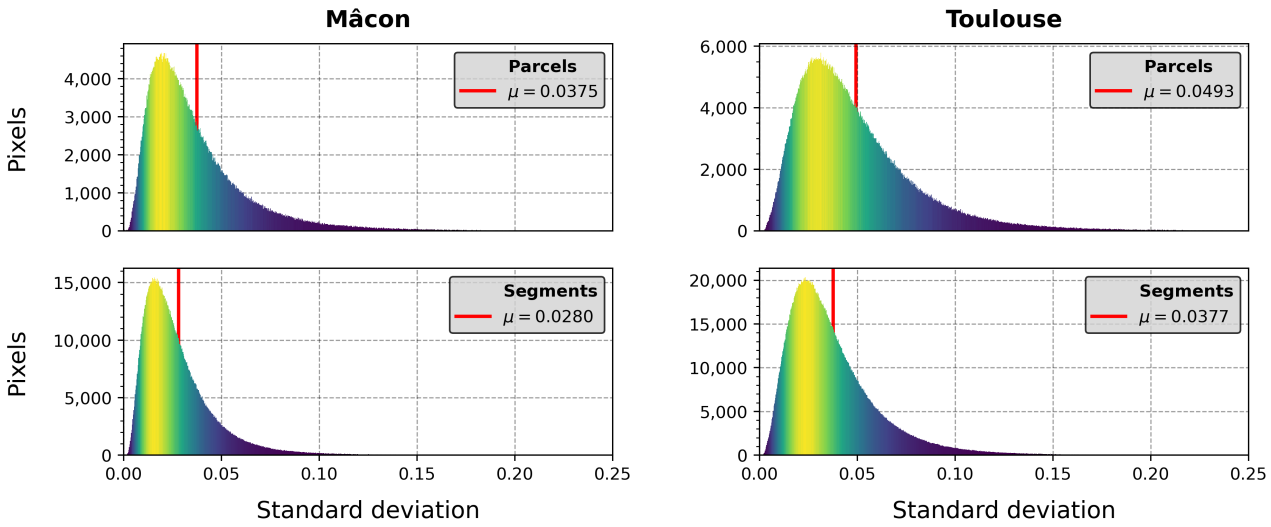

Figure 5.9: Standard deviation of pixels belonging to a given polygon (either parcel or superpixel scales). All the polygons of the grasslands datasets are considered. The standard deviation is illustrated with 1,000 bins and report a decrease of 25.33% and 23.53% for Mâcon and Toulouse, respectively, when using superpixels compared to parcels. Yellow colors surround the mode of the distribution.

To qualitatively demonstrate the interest of the superpixel scale obtained, Figure 5.10 illustrates two grasslands parcels from the Mâcon area over which a technical act (June 16) is observed. The technical acts do not impact the entire parcels, but rather some distinct areas that have been defined for rotational management.

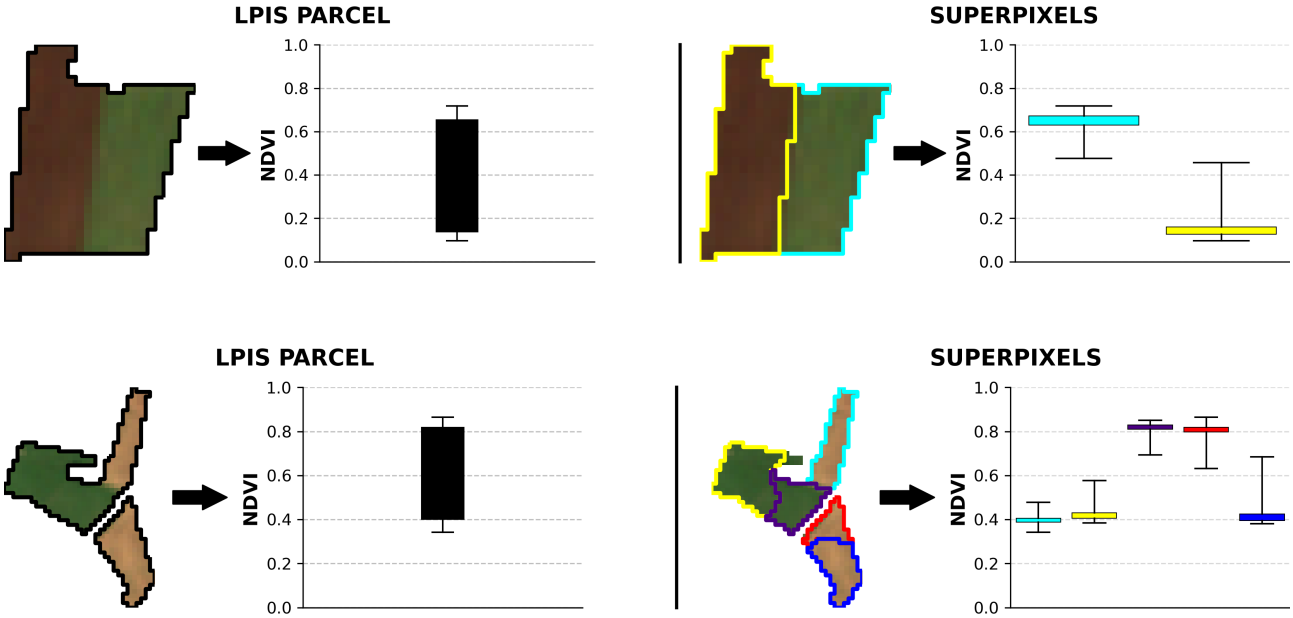

Figure 5.10: Two examples of resulting satisfactory parcel segmentation. Both parcels have technical acts performed only on sub-areas of the parcel. NDVI distribution at the RPG parcel level exhibits high variability as shown in black (*left*). Considering superpixels depicted as colored boxes, an accurate distinction of the different vegetation states is possible (*right*).

On the left column, the boxplots showing the quartiles (minimum and maximum values, first and last quartile) of the pixels belonging to the LPIS RPG declared parcel are illustrated in black. It can be seen that for both parcels, the pixels depict a large dispersion. This is due to the two states of vegetation inside the parcel, *i.e.*, a part being ploughed and the other still having a grass cover. On the right column, the same information is provided for pixels belonging to superpixels obtained from the segmentation step. For the upper and lower parcels, respectively, 2 and 6 segments are obtained. The color of the boxplots denotes the dispersion of pixels belonging to the corresponding superpixel. For both parcels, a clear contrast of pixels belonging to one of the two vegetation states is visible. The average NDVI of the cyan segments on the top parcel and the cyan, yellow, and blue segments of the lower parcels are accurately much lower than the other segments. In both cases, the dispersion of pixels at the superpixel-scales are much lower, allowing for a clear spatial distinction.

5.5.2 SenRVM results at the superpixel scale

The results obtained by the maskSLIC segmentation are used to regress NDVI at the superpixel scale. The pre-processing steps of the optical, SAR, and ancillary data described in Chapter 2 are subsequently repeated on the new superpixels datasets of Mâcon and Toulouse. As a recall, the two datasets contain 68,974 and 137,378 superpixels, respectively, for Mâcon and Toulouse. This allows for larger datasets to be used in the SenRVM methodology and perform validation over a wider number of samples. However, a strong correlation between regression performances and polygon size has been identified in Section 4.3.1 of Chapter 4.

Comparison of the regression results between single-class SenRVM models at the parcel scale presented in Section 4.2.2 and SenRVM models obtained at the superpixel scale are reported in Table 5.3. Obtained results show that despite a change of scale, the regression scores achieved from parcel- and superpixel-scales datasets are similar for both Mâcon and Toulouse areas. This confirms the stability of SenRVM results. Regarding the observed correlation between poorer performances and small-sized parcels highlighted in Chapter 4, the post-processing step that allowed one to obtain segments larger than 0.15 ha may have partially addressed this limitation and explain the satisfactory results.

Table 5.3: Comparison of SenRVM results over grasslands using parcel- and superpixel-based datasets.

	Mâcon		Toulouse	
	PARCELS	SUPERPIXELS	PARCELS	SUPERPIXELS
R^2	0.8384 ± 0.0152	0.8421 ± 0.0151	0.8464 ± 0.0115	0.8492 ± 0.0108
MAE	0.0418 ± 0.0058	0.0412 ± 0.0042	0.0443 ± 0.0029	0.0441 ± 0.0033
MSE	0.0040 ± 0.0009	0.0041 ± 0.0011	0.0037 ± 0.0006	0.0036 ± 0.0006
RMSE	0.0629 ± 0.0069	0.0618 ± 0.0072	0.0606 ± 0.0049	0.0608 ± 0.0053

Figure 5.11 provides a visual example of the NDVI time series obtained by SenRVM considering the superpixel scale. The two segments obtained in these parcels have previously been shown in Figure 5.10 (top). The two segments (red and blue color) are from the same administratively declared parcel but are separately managed, attested by the acquired Sentinel-2 cloudless images. Two mowings occur in June and July, affecting in both cases only one of the two segments. The corresponding time series accurately show either stability or decrease of NDVI. Likewise, ploughing of both segments is undergone separately with different calendars in the end of September and beginning of October. The time series of the two segments correctly follow the temporal calendars of the ploughing and allow for a spatial separation of technical acts performed on this declared parcel. Finally, the resulting time series are blended with Sentinel-2 acquisitions with the *AND-S2* strategy (Section 4.5.2), to allow the retrieval of the original magnitude of the decrease of NDVI and to further increase the temporal resolution.

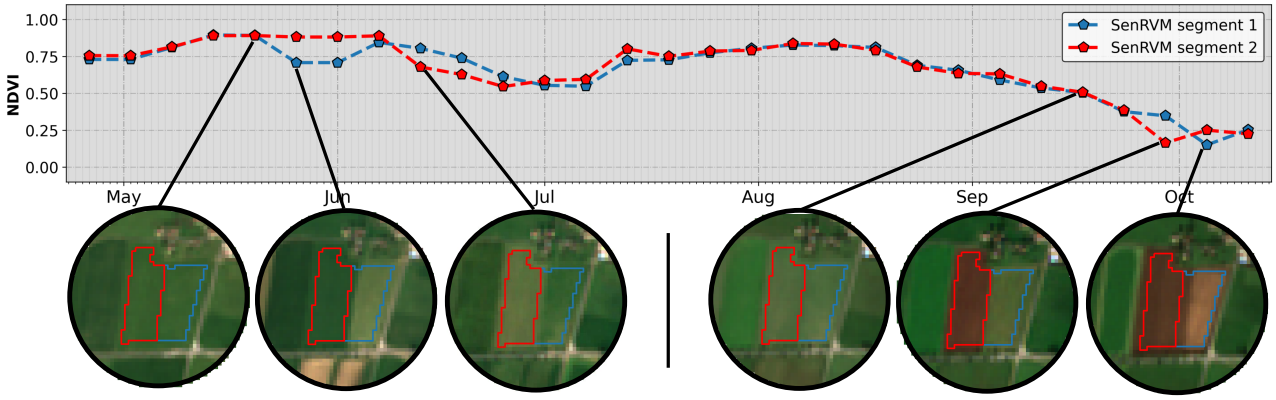

Figure 5.11: NDVI times series obtained by applying SenRVM on two maskSLIC segments belonging to the same RPG declared parcel. Sub-parcel management is accurately retrieved in the time series, attested by Sentinel-2 images.

5.5.3 Detection of management practices

5.5.3.1 Comparative analysis of the different methods

To compare and evaluate the five different technical acts detection methods, the two validation datasets constructed over Mâcon and Toulouse and described in Section 5.3.2 are considered. The methods are applied to each superpixel-scale SenRVM time series blended with Sentinel-2 of the annotated segments. As presented in Section 5.4, different parameters are tested for each of the methods. The metrics presented in Section 5.4 are used to compare the results. As a wide range of parameters are tested, the F-score is used to select the best parameter setting for each method. The results that achieve the highest performances are presented in Table 5.4.

Table 5.4: Highest F-score results of the five detection methods among a range of tested parameters described in Table 5.2. Results for Mâcon (*top*) and Toulouse (*bottom*) areas are given and the highest and lowest performance are highlighted in green and red, respectively.

Mâcon

	Rank	F-score	Precision	Recall	α/ρ	W	ord.	cost	Detected	Missed	Supplementary
THR	3	0.894	0.885	0.903	-0.14	-	-	-	1467	158	190
THR - WIN	1	0.917	0.925	0.909	-0.20	-	-	-	1478	147	120
THR - OLS	2	0.907	0.911	0.903	-0.085	3	-	-	1467	158	144
THR - POLY	5	0.792	0.778	0.806	-0.22	5	2	-	1310	315	374
THR - PELT	4	0.893	0.878	0.909	0.025	2	-	L2	1477	148	206

Toulouse

	Rank	F-score	Precision	Recall	α/ρ	W	ord.	cost	Detected	Missed	Supplementary
THR	4	0.765	0.721	0.814	-0.16	-	-	-	1336	305	517
THR - WIN	1	0.842	0.784	0.909	-0.23	-	-	-	1492	149	411
THR - OLS	3	0.786	0.749	0.828	-0.105	3	-	-	1358	283	456
THR - POLY	5	0.678	0.627	0.738	-0.21	5	2	-	1211	430	721
THR - PELT	2	0.836	0.821	0.851	0.05	2	-	L2	1396	245	304

As observed, the **THR-WIN** method, with a fixed threshold value, obtains the best performances for both test sites. F-scores of 0.917 and 0.842 are achieved, respectively, for the Mâcon and Toulouse areas. In contrast to **THR-WIN**, the **THR-POLY** method obtains the lowest results. A decrease in the F-score is observed for both areas, with 0.792 (-13.67%) obtained for Mâcon and 0.678 (-19.49%) obtained for Toulouse using the **THR-POLY** method. From 1,625 technical acts annotated for Mâcon, 1,478 are correctly detected with the **THR-WIN** method, 147 are missed and 120 supplementary technical acts are found. For Toulouse, 1,492 of the 1,641 annotated technical acts are detected, 149 are missed, and 411 are supplementary detected.

It can first be noted that very similar results are obtained for the two areas with $\approx$ 91% of the technical acts detected and $\approx$ 9% missed. Different but close threshold values α are used for the two areas: -0.20 for Mâcon and -0.23 for Toulouse. It was previously reported that the drops induced by the technical acts annotated for the Toulouse area (Figure 5.7) are somewhat higher than for the Mâcon area. This potentially explains the lower α value obtaining the best results. The close α values used for **THR-WIN** hints at the good generalization capability. The F-score for the Toulouse area is also slightly lower as a smaller precision score is achieved. The 411 supplementary detections correspond to 25% of the total annotated technical acts. The higher percentage of cloud cover that affects the Toulouse area compared to Mâcon (top of Figure 5.7) nevertheless could prevent numerous technical acts from being annotated during the assessed time interval. Consequently, the number of supplementary technical acts obtained for the two areas of Mâcon and Toulouse does not appear unreasonable.

The satisfactory results obtained by the **THR-WIN** method can be confirmed by comparing the results obtained from some of the related works presented in Table 5.1b. In Schwieder et al., 2021, the frequency of mowings is assessed on parcels dispatched across the main natural regions of Germany. Three years are taken into account, with 92 parcels in 2018, 81 in 2019, and 180 in 2020 being annotated with mowings. Mean F-scores of 0.58, 0.64, and 0.67 are obtained for 2018, 2019, and 2020, respectively. The authors report a clear correlation between the number of satellite acquisitions and the performances, which explains the relatively low results obtained. Indeed, as the authors are using optical time series obtained from the HLS product, the lowest F-scores are obtained in areas where orbit-overlap is not available. Based on optical and SAR time series, an F-score of 0.84 is reached in Lobert et al., 2021 on 64 parcels for which 257 mowings are recorded. Using a 1D-CNN method, the authors found a recall of 0.859 and a precision of 0.824. In this work, an underestimation of mowings for intensively managed grasslands caused by insufficient temporal resolution of the time series to detect close events is also observed. The authors in Komisarenko et al., 2022 are reporting the accuracy, which does not penalize false positives such as done by the F-score, for the detection of mowing events over 2,000 parcels located across Estonia. A 73% accuracy is achieved for mowing detection using a 1D-CNN neural network and optical and SAR-based features as input. The lower results obtained in the latter work are, as in the two previous works, due to the unequal temporal resolution of the optical time series used. Furthermore, most of the incorrectly predicted events are reported for parcels whose sizes are bellow 1 ha. This limitation appears to be important, since it has been shown that technical acts on grassland parcels can occur on small intra-parcel areas. While the results obtained by the three previous works are all integrating optical time series in their methodology, lower results are reported when SAR features are solely used. The authors in De Vroey et al., 2021a exploit Sentinel-1 backscattering coefficient and coherence features derived from Sentinel-1. As previously presented (see Section 5.1), three detection methods are evaluated with 196 parcels in Belgium for which mowing events are reported from field visits. Precision and recall, respectively, of 0.42 and 0.54 are found for the best performing method. Poor results are obtained for small-sized parcels, due to the SAR geometry, and for grazed grasslands, possibly related to the important fluctuations in the SAR signal. The results obtained by these different works first allow to highlight the interest of using the SenRVM approach to obtain densely sampled time series to overcome the optical data scarcity limitation reported. As NDVI time series are obtained, the complexity of SAR integration and exploitation is also reduced. Furthermore, albeit not on the same datasets, the high performances obtained from the **THR-WIN** method on a large number of technical acts can be underlined. Especially, an adequate balance between precision and recall is observed

compared to the mentioned related works.

The results obtained here from the five detection methods are presenting some differences for the Mâcon and Toulouse areas. In Mâcon, apart from the **THR-WIN** method, the three **THR**, **THR-OLS**, and **THR-PELT** methods obtain very similar results. In the case of Toulouse, distinct results are observed with **THR-PELT** performing significantly better than the **THR** and **THR-OLS** methods.

The **THR-OLS** method obtains the second best F-score for Mâcon with a temporal rolling window W of size 3 and a α value of -0.085. This first indicates that the methods perform more efficiently taking into account longer time intervals (either fixed in the case of **THR-OLS** or variable in the case of **THR-WIN**). In these cases, both abrupt and gradual technical acts can be detected. Similar results are obtained on Toulouse, where the most accurate W size is also 3. However, threshold α requires a lower value of -0.105.

The **THR-PELT** method achieves the second highest F-score among the five methods (while it ranks 4^{th} in Mâcon). Furthermore, this method reports the lowest number of supplementary detections. The use of time intervals that could be larger than for **THR-WIN** and **THR-OLS** by segmenting the entire time series can explain this result. Because of the persistent cloud cover resulting in large data-gaps, the annotations may have larger time intervals (Figure 5.7) over the Toulouse area. The segmentation proposed by the PELT algorithm permits to decrease the potential local variability in the time series leading to less supplementary detections. It can also be noted that for both areas, the penalty values (ρ) guarding from ovefitting and the minimum segment length between detections (W) are low. Low penalty values indicate that accurate time series segmentations are obtained. The W value that obtains the best F-score is 2. As it has been illustrated that rapid regrowth is common and consecutive technical acts can occur, a low value allows for temporally near detection. Lastly, although close performances are achieved, the L2-norm as the cost function of the PELT algorithm is found to be more efficient than the L1-norm or a Gaussian RBF kernel.

It is also found that the baseline method **THR** performs relatively well in both areas. As for the **THR-WIN** method, close α threshold values are achieving the best results, respectively, -0.14 and -0.16 for Mâcon and Toulouse. For Mâcon, only 11 technical acts are not detected compared to **THR-WIN** with 70 supplementary detections. For the Toulouse area, compared to the **THR-WIN** method, 156 technical acts are additionally missed and 327 more supplementary detections are found. As mentioned above, the longer time intervals used for the annotations and the higher magnitude of NDVI drops observed in Toulouse explain the poorer results obtained by **THR**. Fixed and adaptive (based on the standard deviation σ of the time series) thresholds were also tested. A fixed threshold obtains better results. The best F-scores obtained with an adaptive threshold are 0.869 ($\sigma \times 1.2$) for Mâcon and 0.722 ($\sigma \times 1.045$) for Toulouse.

Among the five detection methods, the **THR-POLY** method achieves substantially less accurate results for both areas. The highest results are obtained with a temporal window W equal to 5 and a polynomial fit of order 2. Results using a 3^{rd} order polynomial show a very large number of additional detections. The poor results obtained by **THR-POLY** can be explained by the bi-temporal detection strategy that only considers two dates. The limitations of bi-temporal strategies are also observed by the **THR** method. Nevertheless, the **THR-POLY** method appears less reliable as it is sensitive to the setting of multiple parameters. In particular, the construction of an idealized time series from the selection of vertices can be complex and strongly influence the performances. The choice of the time window W size used for the selection of the vertices also have limitations. A fixed value affects the vertices selections and can greatly constrain the trend of the idealized time series. Thus, despite that similar threshold values α are used for **THR-WIN**, the results obtained by the **THR-POLY** method are significantly poorer.

Figure 5.12 illustrates the results obtained by the five methods on the same superpixel that belongs to a grassland parcel in the Mâcon area. The optimal parameters reported in Table 5.4 are used. For this example, two technical acts are annotated, which are highlighted by gray windows. Different patterns can be associated with the two practices. In the first technical act, the NDVI drop magnitude is important whereas the second

technical act corresponds to a gradual decrease of NDVI.

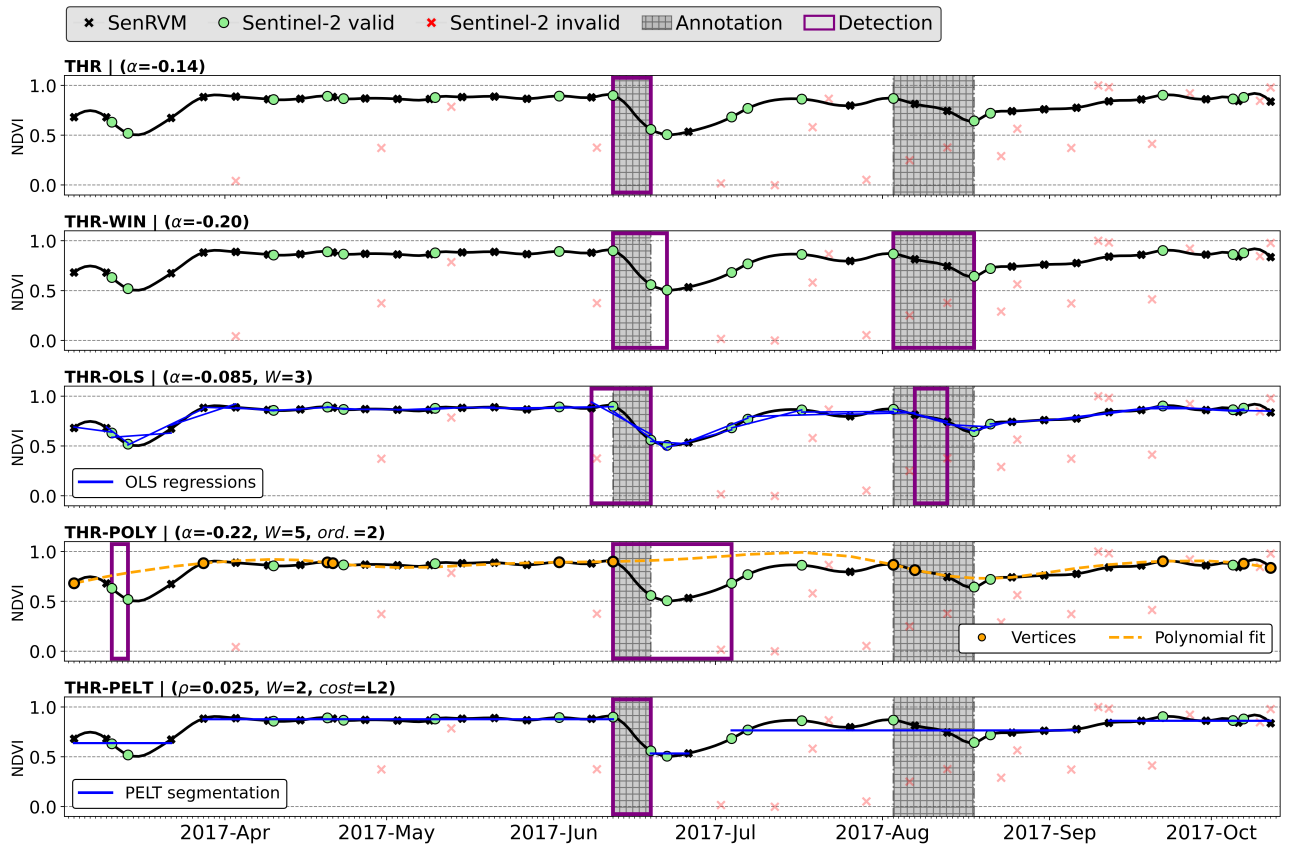

Figure 5.12: Example of results for all methods using the parameter configuration reaching the highest F-score. The same time series containing two annotated time intervals is considered. The first management practices occurring mid-June is retrieved by all methods. The second one, depicted by gradual decrease of NDVI, is only retrieved by two methods relying on temporal windows to perform the detection.

The figure shows that the first technical act is detected accurately by all the methods. On the other hand, the second technical act is only retrieved by the **THR-WIN** and **THR-OLS** methods by integrating multiple dates to assess the change. In the case of the **THR** method, the detection of the second practice having a gradual NDVI decrease would require low threshold values which in return would greatly increase the number of supplementary detections. The polynomial fit of the **THR-POLY** method, is, as previously explained, influenced by the choice of vertices. As the gradual decrease does not exhibit a clear rupture in the time series trend, the second technical act is missed. Furthermore, a quick vegetation growth occurring in March lead the **THR-POLY** method to detect a supplementary technical act. The selection of vertices corresponding to high NDVI values in temporal windows produces a discrepancy with the actual evolution of the NDVI time series. Thus, high residuals are considered by the method, falsely triggering a technical act detection. While a decrease of NDVI is observed with two temporally close Sentinel-2 NDVI acquisitions, the decrease is weak and this supplementary detection unlikely occurred. Finally, the **THR-PELT** method does not perform an adequate segmentation of the time series. The gradual decrease of the second technical act is observed as too low to define a new regime in the time series, leading to its omission.

Next, the qualitative and quantitative analysis of the supplementary detections permits to highlight the accuracy of the proposed methods and the interest in using the time series obtained by the SenRVM approach. A visual photo-interpretation is first performed of the 142 and 411 technical acts detected by the **THR-WIN** method for Mâcon and Toulouse areas, respectively. For the Mâcon area, 23% of the supplementary detections

are in fact accurate detections corresponding to technical acts. For Toulouse, accurate detections corresponds to 16% of the supplementary detections. These valid supplementary detections are overwhelmingly due to cloud mask commissions. These commissions are removing a valid image that shows a technical act or a grass regrowth and prevent an annotation to be made. These statistics further reduce the margin of error of the results obtained from the **THR-WIN** method. They also again underline the interest of the SenRVM approach allowing the detection of technical acts not detected by the use of optical time series or dependent on the masks quality. Concerning the remaining 77% and 84% of supplementary detections in Mâcon and Toulouse, the cloud cover prevents the photo-interpretation to be conclusive. Nevertheless it was observed that a significant number of these additional detections occurred during time intervals with persistent cloud cover, especially during July and September on the Toulouse area. These two months are particularly cloudy with few valid acquisitions (Figure 2.2). This supports the fact that the number of supplementary detections found by most of the methods is coherent with the potential number of performed technical acts.

Figure 5.13 illustrates the results that contain a supplementary detection of the different methods on an intensively exploited parcel.

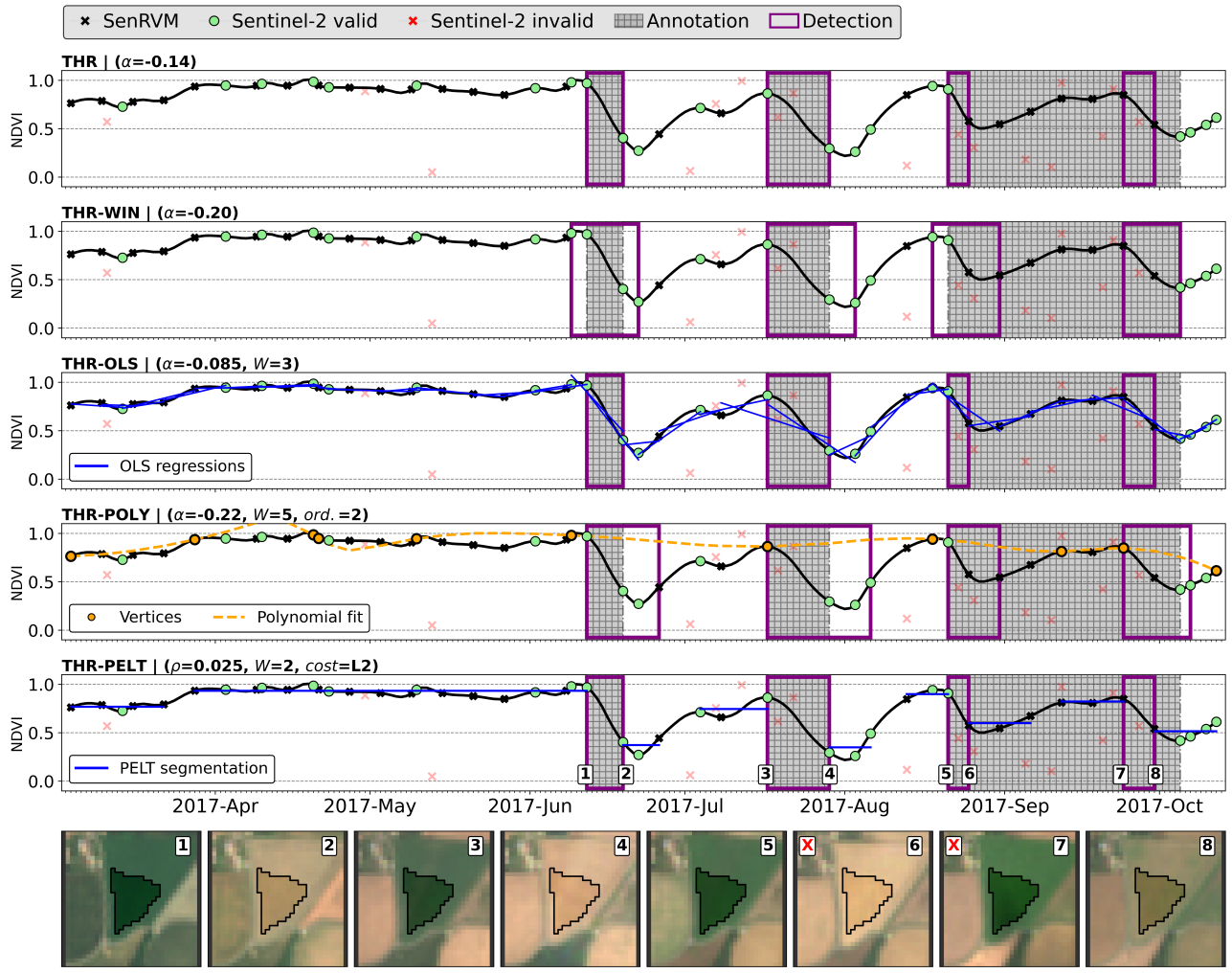

Figure 5.13: Example of an accurate supplementary technical act detection performed by all the methods. Two images (number 6 and 7 at the bottom) are falsely marked as invalid by the cloud & shadow mask preventing their use for an annotation. Relying on Sentinel-2 and masks, this technical act would have been missed.

This example shows three annotated technical acts from the validation dataset. However, it can be observed that the third technical act corresponds to a long time interval defined between two successive valid Sentinel-2 acquisitions. This annotated time interval spans more than a month, from the end of August to the beginning of October. However, the results obtained from the five methods show two detections during the annotated time interval. The first is found at the end of August and the second at the end of September. The visual inspection of the Sentinel-2 images acquired over this superpixel illustrate the commissions errors previously found during the quantitative analysis. Two successive images (numbers 6 and 7 at the bottom of the figure) are marked as invalid by the corresponding cloud & shadow masks. Nevertheless, these two images are actually valid and show a technical act performed and the subsequent regrowth of the vegetation cover. These two images confirm the validity of the two detections made by the five methods and illustrate the interest of the reconstructed SenRVM time series accurately depicting this supplementary technical act. This additional technical act would indeed not be observable with the sole use of Sentinel-2 time series associated with the masks.

Finally, despite most of the supplementary detections could not be assessed, it is worth mentioning that using the optimal parameters described in Table 5.4, solely 6 technical acts out of the 1,625 annotated for the Mâcon area are missed by all the five methods. For Toulouse, 15 technical acts are missed by all methods from a total of 1,641. These technical acts correspond to very gradual and low decreases of NDVI and mainly in long time intervals.

Figure 5.14 illustrates two annotations (top in Mâcon, bottom in Toulouse) that are missed by all methods. The undetected annotation is marked in red and the two corresponding Sentinel-2 images used for the annotation are shown on the right part of the Figure. While the visual interpretation clearly hints at a change in reflectance, a poor decrease of NDVI both in Sentinel-2 and SenRVM obtained time series is observed. Thus, unless very low threshold values are used, which would lead to other supplementary detections, the methods are unable to retrieve this annotated technical act. This discrepancy between visual interpretation and patterns observed on the time series evolution illustrates the complexity of annotating technical acts from satellite images. The observed change in reflectance may for example be induced by atmospheric conditions resulting in the decrease in NDVI to be underestimated.

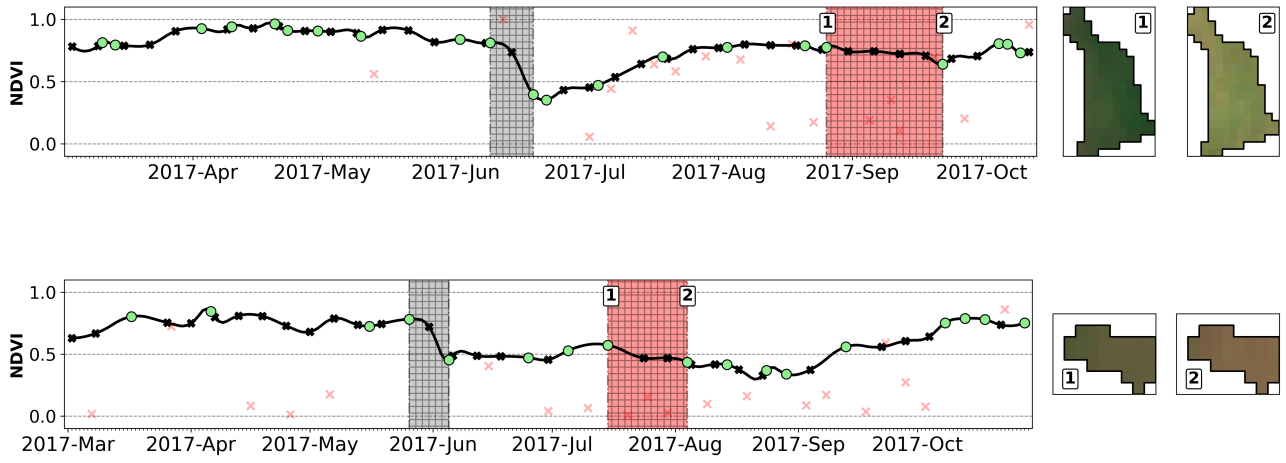

Figure 5.14: Two examples of annotations missed by all the detection methods on Mâcon (*top*) and Toulouse (*bottom*). In both cases, the visual interpretation of Sentinel-2 images suggests a change in vegetation status. Nevertheless, NDVI time series both from Sentinel-2 and obtained with SenRVM show a low decrease during the annotated time interval (red frame). Consequently, the methods do not detect the change.

5.5.3.2 Sensitivity analysis for parameter setting

The 6 and 15 technical acts missed by all methods in Mâcon and Toulouse, respectively, show on one hand the good overall performance of the proposed methods. On the other hand, compared to the respective number of missed annotations of the different methods, this low number indicates that the technical acts missed are not necessarily the same depending on the method. It was explained earlier that a distinction in the approach to detecting technical acts (*e.g.*, in temporal windows, in online or offline ways) explains these differences. Therefore, to estimate the sensitivity of selecting method parameters according to the area under study, the evolution of the number of missed annotations and supplementary detected technical acts can be reported.

Figure 5.15 and Figure 5.16 illustrate the sensitivity of the five different methods to a range of threshold values α and penalty values ρ (for **THR-PELT**) reported in Table 5.2. The missed annotations are depicted by brown bars, supplementary detection by the purple lines, and the F-scores by red lines. The highest F-score (Table 5.4) achieved by the methods is shown with a red vertical line and a black outlined dot. To ease the comparison between the methods, other parameters, *e.g.*, the size of the temporal window W, and the other cost function `cost`, the polynomial order, as well as the adaptive threshold for **THR**, are not shown as performing poorly. For these additional parameters, the parameter that achieves the highest performance (Table 5.2) is selected for visualization.

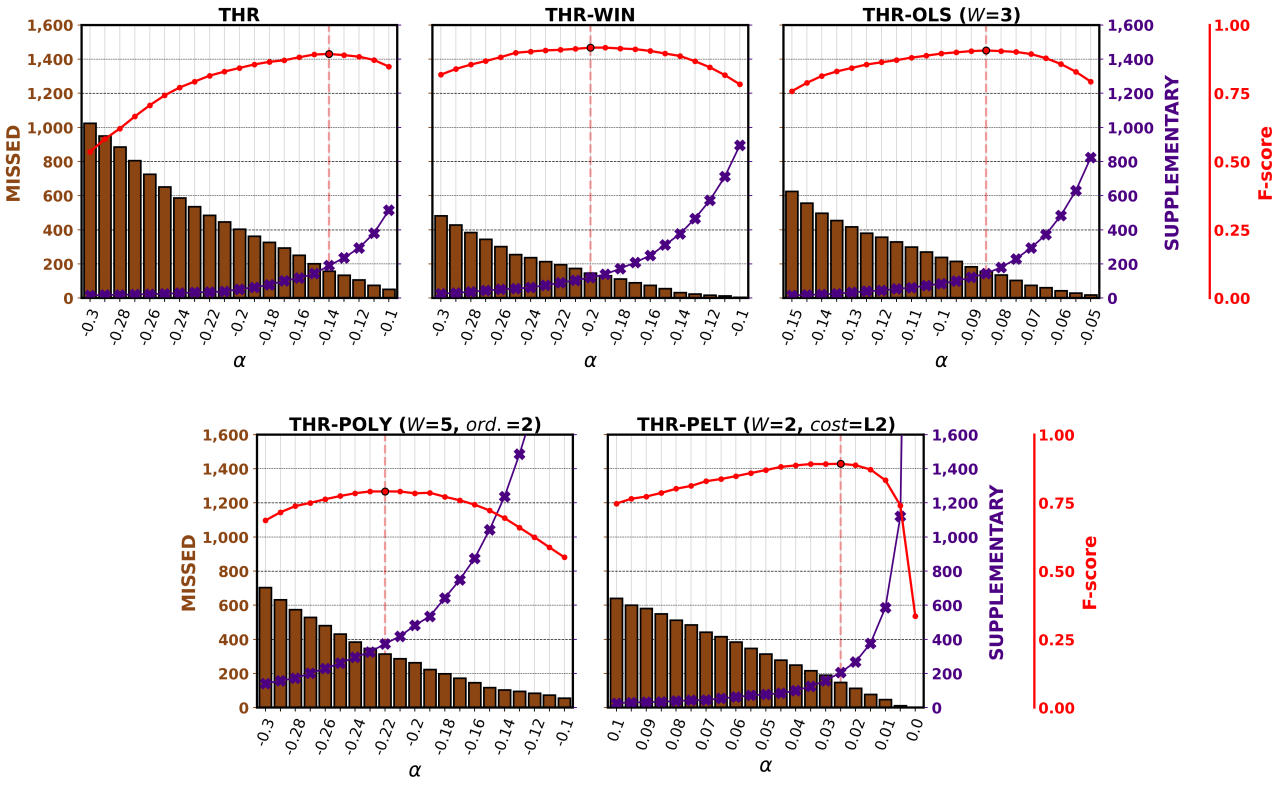

Figure 5.15: Sensitivity of the five methods to a threshold value α or ρ to missed (brown bars) and supplementary detections (purple line) in the Mâcon area. The red vertical lines indicate the highest F-score obtained among the different thresholds. Regarding additional parameters to concerned methods (window size, W, cost function, `cost`), the best parameter reported in Table 5.4 is used.

It can be observed in Figure 5.15 that for the Mâcon area, the evolution of the F-score with respect to the threshold values is very similar for the **THR-WIN** and **THR-OLS** methods. However, greater stability is observed for the **THR-WIN** method with important threshold values, synonymous with fewer missed an-

notations. In comparison, the baseline method **THR** only achieves satisfactory results with lower threshold values, due to its date-to-date detection. The **THR-POLY** method, as previously reported, obtains a significant number of missed annotations and additional detections and consequently much lower F-scores. The evolution of the F-score allows to visualize the higher difficulty in choosing the right parameters for this method, with a plateau of high values less important than for the **THR-WIN** and **THR-OLS** methods. We can also note the very large number of supplementary detections obtained by this method with low threshold values, despite the short temporal windows and the second-order polynomial fitting, which promotes reasonable distance to the selected vertices. The **THR-PELT** method appears to be relatively similar to the **THR-OLS** method, but with a substantial decrease in accuracy when using low ρ penalty values. This decrease is due to an exponential number of supplementary detections as the penalty values are aimed at regulating the number of detections.

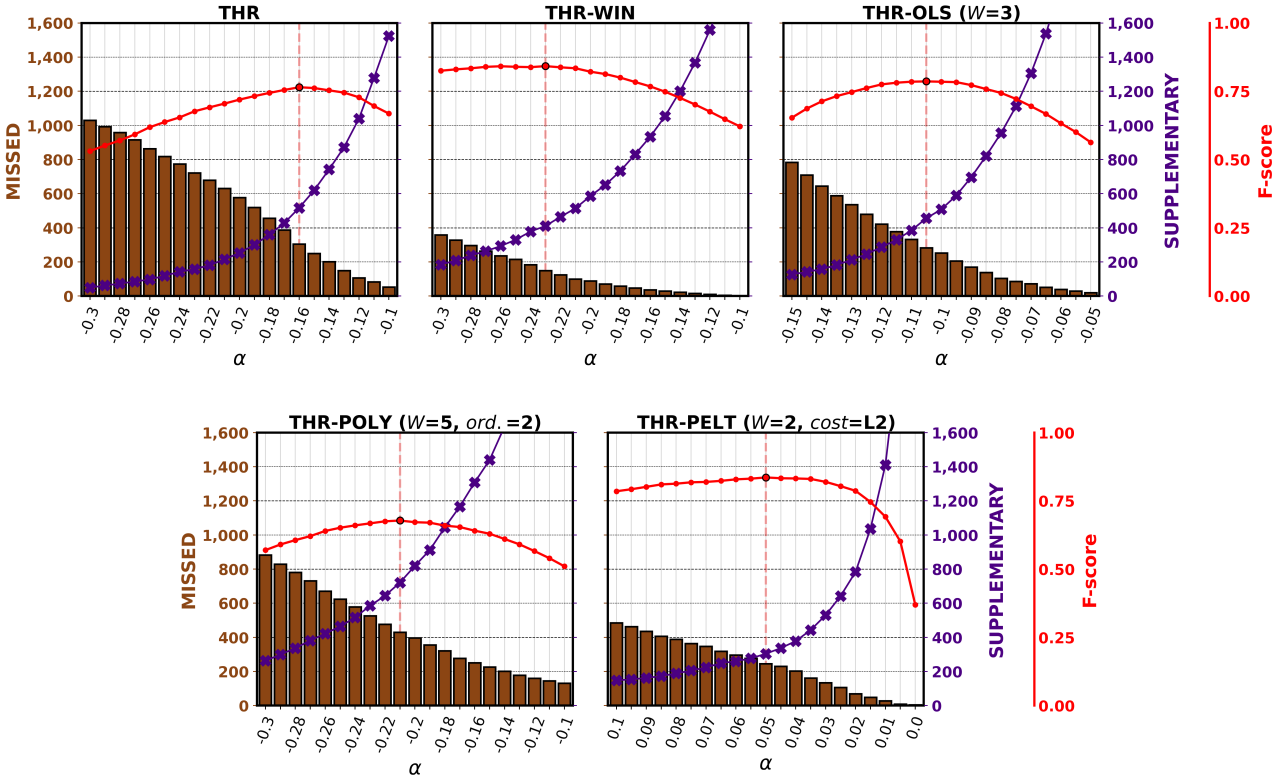

Figure 5.16: Sensitivity of the five methods to a threshold value α or ρ to missed (brown bars) and supplementary detections (purple line) in the Toulouse area. The red vertical lines indicate the highest F-score obtained among the different thresholds. Regarding additional parameters to concerned methods (window size, *W*, cost function, cost), the best parameter reported in Table 5.4 is used.

Compared to the Mâcon area, Figure 5.16 shows that for Toulouse, the**THR** and **THR-POLY** exhibit same F-score trends with nevertheless lower performance. While for these last two methods, the number of supplementary detections is somewhat similar to the Mâcon area, the **THR** method shows exponentially higher numbers when using low α values. As previously explained, the higher drops in NDVI observed on the Toulouse area explain this result. Again, the accuracy of these detections cannot be verified, but this large number compared to other methods seems to indicate an over-detection. The **THR-PELT** method, on the other hand, has fewer annotations missed for large ρ penalty values compared to the Mâcon area but more supplementary detections. For Toulouse, the **THR-PELT** method obtains the highest apparent stability regarding the tested range of penalty values, along with the **THR-WIN** method. However, the two **THR-WIN** and **THR-OLS** methods appear less stable when low or high threshold values are used than in the case

of Mâcon. This is again probably due to the important number of supplementary detections found for the Toulouse area, which nevertheless unfortunately can not be validated.

From a parameter setting point of view, the results obtained in the previous Section 5.5.3.1 are confirmed. Methods relying on temporal windows to perform the detection appear to be more stable for a range of threshold values. The **THR-WIN** method, especially, requires a single parameter to be set and achieves the overall best results compared to the four other methods.

5.6 Potential outcomes

The two tasks of reconstructing time series for frequent and regular monitoring and detecting management practices were determined in response to the issues of grassland conservation and sustainable management. The methodologies presented in this manuscript have incorporated data that favor their large-scale deployment. Therefore, information on the intensity of grassland exploitation can be derived and observed in large areas, allowing a better understanding of existing spatial and temporal distinctions. Using the time series obtained at the superpixel-scale by the SenRVM approach (Section 5.5.2), the THR-WIN method (Section 5.2.3) is applied to the entire areas of Mâcon and Toulouse. The optimal threshold values obtained from the validation datasets are used.

It was emphasized (Chapter 1) that the frequency of technical acts, their earliness, and their impact on biomass are the main aspects to estimate the quality of ecosystem services provided by grasslands. A subset of the results, which provides these three information for the growing season from March to October 2017, is presented in Figure 5.17 for Mâcon and Figure 5.18 for Toulouse. The two figures provide the RPG cultural codes on top left and three key features: the number of technical acts detected on top right, the month of the first technical act on bottom left, and the amplitude in NDVI (*i.e.*, between the maximum and minimum values) on bottom right.

The derived key features, albeit illustrated at a local scale, permit to draw several observations regarding the different agronomic species and their related management practices. It can, for example, be noted that the detected number of performed technical acts is accurately related to the agronomic type of the grassland. Permanent grasslands (*PPH*, *PRL*, *SPH*), are more prone to extensive exploitation, making up almost all segments for which no or at most one technical act has been detected. The first technical act on these segments is also generally done later in the season, mostly in June and July, when the grass reaches its maximum yield. Consequently, the NDVI amplitude during the season is low, mainly varying with climate, as there is little or no anthropological pressure. Fallow lands (*J5M*, *J6P*, *J6S*) are similarly managed as commonly associated with low production areas. On the contrary, temporary grassy areas (*LU5*, *LU6*, *LU7*, *LUZ*, *MLG*, *RGA*) and forage legumes (*TR5*, *TR6*, *TR7*, *TRE*) are clearly subject to more performed technical acts. For Mâcon, the number of detected acts reaches four for some temporary grassy areas and a ryegrass parcel, and up to five for Toulouse for alfalfa parcels. The illustrated information also allows one to observe that a first mowing is performed earlier on these types of grasslands, mainly in April and, for some, even in March. The NDVI amplitude derived from the NDVI time series obtained from SenRVM also accurately depicts the distinction between extensively and intensively exploited grasslands.

This visual interpretation of these value-added features about grassland management, moreover, once again demonstrate the accuracy of the SenRVM obtained time series. The different segments belonging to the same parcel very often display similar and stable information, for the three provided key features. It must lastly noted that for the Mâcon area, only 6 segments out of 68,974 are found with more than 5 technical acts (up to seven), furthermore solely from 5 unique RPG parcels. For Toulouse, 68 segments (from 57 RPG parcels) of a total of 137,378 have more than 5 detected technical acts (up to six). This largely confirms the satisfactory results obtained on the validation datasets, this time at large scale.

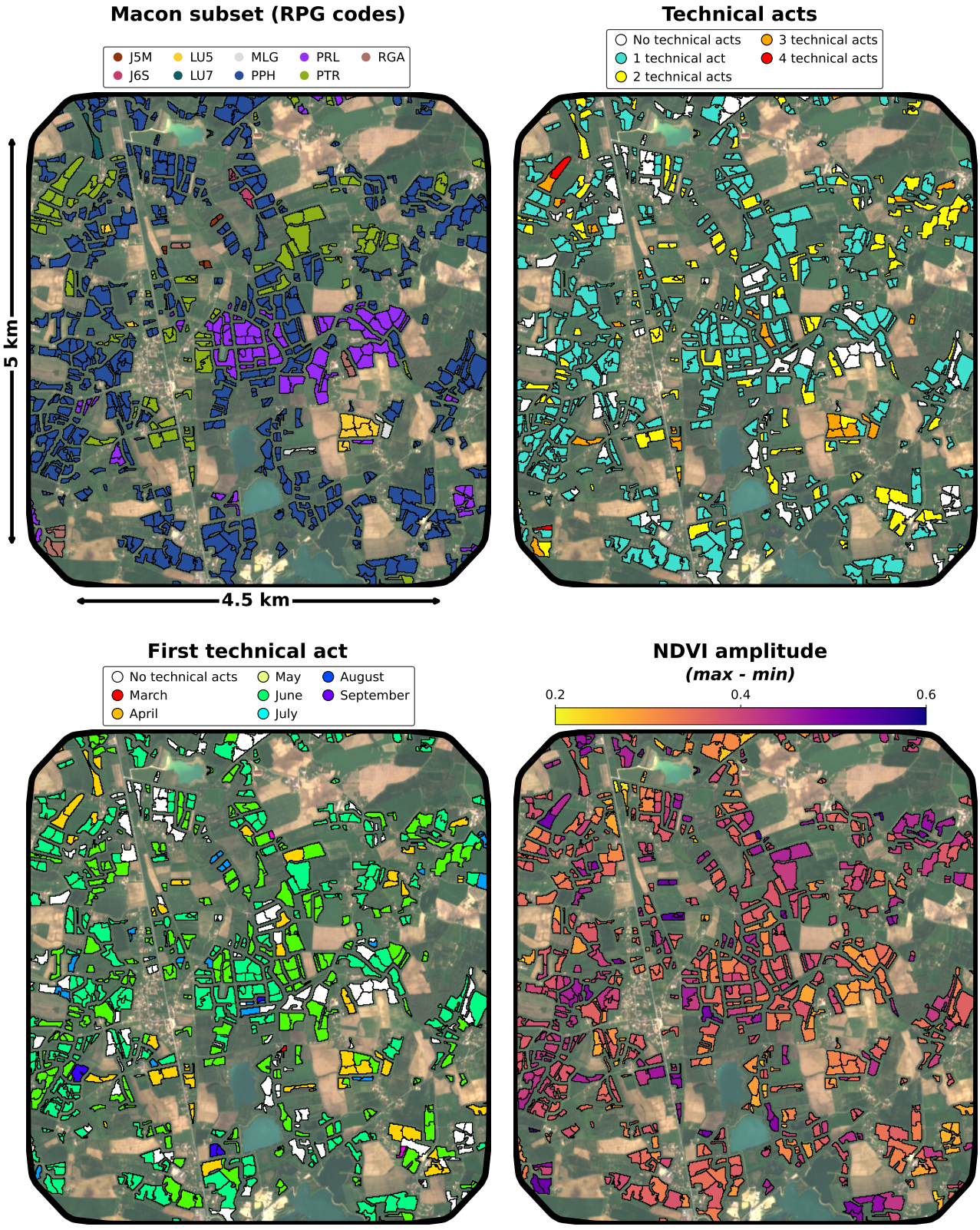

Figure 5.17: Information derived about grassland management practices for the growing season between March and October 2017 for a subset of the Mâcon area. *Top left*: RPG codes; *Top right*: number of detected technical acts; *Bottom left*: month of the first technical act; *Bottom right*: NDVI amplitude.

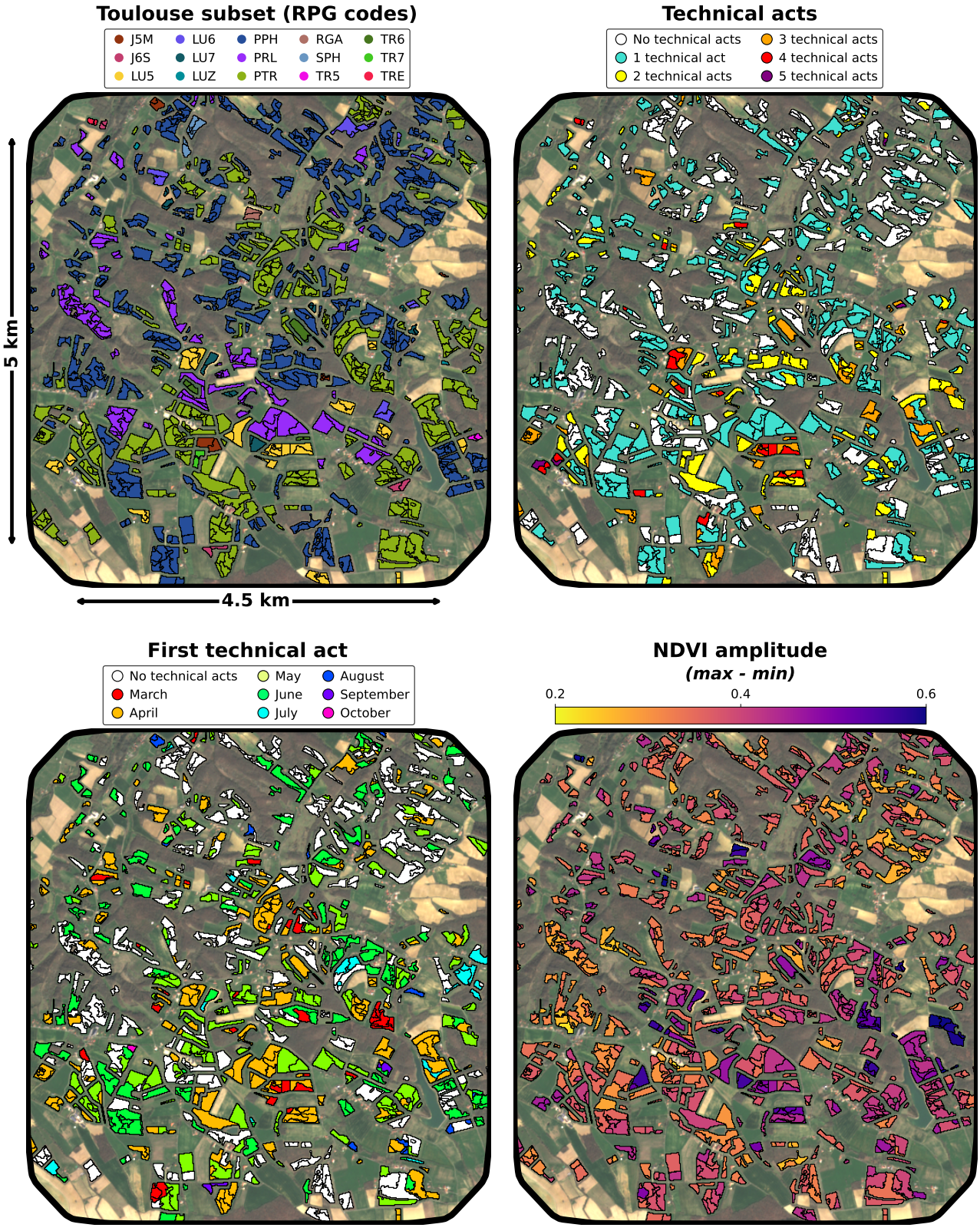

Figure 5.18: Information derived about grassland management practices for the growing season between March and October 2017 for a subset of the Toulouse area. *Top left*: RPG codes; *Top right*: number of detected technical acts; *Bottom left*: month of the first technical act; *Bottom right*: NDVI amplitude.

The number of technical acts found for the two areas of Macon and Toulouse demonstrates the high quality of the results obtained by the proposed method, since they are fully coherent with the expected number of technical acts performed.

These examples illustrate the potential applications of the proposed methodology in monitoring grassland dynamics. Reliable and large-scale information can then be used to derive spatial analyses related to various factors that influence the environment. The earliness of technical acts can be linked to climate change, monitoring of grassland overexploitation can indicate potential environmental degradation, or the intra-seasonal amplitude of NDVI can indicate the resilience of certain soils, species or practices.

5.7 Concluding remarks

This chapter has established a three-step approach for detecting management practices on grasslands. A review of the related literature has first allowed us to analyze the strengths and especially the weaknesses of the existing approaches. Drawbacks associated with the spatial and temporal scales were identified and improvements regarding the scale of analysis and the temporal resolution of the data have been proposed.

A new analysis scale was proposed to take into account the specificities of rotational management encountered on grasslands. The superpixels segmentation strategy has permitted to retrieve intra-parcel areas being homogeneously managed, favoring an adequate NDVI time series response to technical acts. To overcome the temporal resolution limitations for detecting temporally close technical acts, the time series obtained by the SenRVM method have proven to enable a substantial revisit and therefore frequent monitoring. Subsequently, validation datasets with a total of more than 3,000 technical acts have been constructed and presented. This high number and the diversity of annotations has allowed us to perform a comprehensive and large-scale validation.

Several bi- and multi-temporal detection strategies have been proposed and studied. The change detection problem has also be tackled by segmentation and error fitting methods. These several methods have corroborated that there exists a high variability of temporal patterns, number of the practices, and dates at which technical acts are performed. Using the constructed validation datasets, the proposed methods have been compared and their stability with respect to parameter settings has been explored. More reliable results were obtained by thresholding methods performing the detection in temporal windows both in terms of overall accuracy and parameter setting configurations. These approaches have achieved the detection of different types of managements with abrupt or more gradual decreases. A method performing the detection on decreasing time intervals of time series first-order derivative retrieved 91% of the annotated technical acts accurately. The lowest results, with 77% of detected annotations, have been obtained by a error fitting method relying on the comparison between a constructed idealized fitted time series and the real time series.

The satisfactory results have been confirmed by comparing them with those obtained in several related works. Furthermore, a low number of supplementary detections (about 150 for the best-performing method) have been obtained. Among the supplementary, 20% were valid detections that cloud & shadow masks error prevented to be annotated.

Finally, this chapter has corroborated the interest in continuous monitoring and mapping of grassland management practices through different illustrated examples. The achieved results allow to foresee the potential of the developed approach to support the conservation and sustainable management of grasslands through satellite monitoring.

Part IV

GENERAL CONCLUSION

Chapter 6

Conclusion and perspectives

6.1 Summary

Overview of challenges and contributions

Grasslands were recognized as complex ecosystems, as evidenced by the lack of consensus on their definition. The monitoring of grassland dynamics was presented as a challenging task due to the multitude of agronomic species, varied topographic and climatic contexts they cover. The temperate grasslands, with a large majority of agricultural vocation, were identified as subject to the greatest threats. Their conversion into other types of surfaces such as crops, but especially their increasing overexploitation was pointed out. The frequency of management practices (*i.e.*, mowing, grazing, and ploughing) was presented as closely linked to grasslands capacities to provide multiple ecosystem services. In a context where grasslands took an increasingly important place in environmental issues, the development of methods to retrieving information on this frequency appeared as necessary.

To account for the heterogeneity of grasslands, a large-scale analysis was performed. The French Land Parcel Identification System (RPG) was used to recover the location of grasslands polygons. Two main areas, around Mâcon and Toulouse, and two additional areas (divided into several sub-areas) north of Paris and around Nantes in Western France were defined to develop and assess the proposed methodologies. In total, more than 284,000 parcels with various agronomic species and geographical context were gathered to compose the grassland datasets. The study areas cover more than 67,000 km^2, while the variety of grasslands leads most of the related work to integrate only local scales (a few parcels, watershed, etc.). To allow a transverse interpretation of the results, similar datasets on crops ($> 47,000$ polygons) and forests ($> 19,000$ polygons) were also obtained over the two main areas.

To conduct large-scale analysis, satellite missions offer an efficient and accessible tool for continuous vegetation monitoring. Freely available optical and Synthetic Aperture Radar (SAR) imagery from Sentinel-2 and Sentinel-1 can provide significant information to monitor vegetation changes over wide areas at high spatial and temporal resolution. Sentinel time series were considered over all areas on an annual basis to cover a complete agricultural season. Subsequently, different satellite-based features were computed, *i.e.*, the Normalized Difference Vegetation Index (NDVI), the backscattering coefficient, and the interferometric coherence. Therefore, a first objective of this thesis was to assess the distinct strengths and weaknesses of the different satellite features for grassland monitoring. The evolution of NDVI has shown its interest in monitoring management practices. However, the effective temporal resolution of optical data, due to cloudy conditions, appeared to be insufficient. Observing the management practices using SAR features was more complex, because of their temporal fluctuations due to external effects. Nevertheless, the temporal repetitivity of SAR features, ensured by their weather independent acquisition, proved to be a major asset. To exploit the information provided by SAR time series, this thesis proposed the integration of ancillary data. Topographic and climatic data were incorporated in the proposed methodologies to address the limitations related to the acquisition geometry and dielectric conditions of the SAR signal.

Under the grassland monitoring goal, the analysis of features derived from Sentinel images performed in this thesis highlighted two majors challenges. The first challenge stemmed from the fact that grassland exhibit highly varied and quickly evolving dynamics. In particular, it was illustrated that vegetation regrowth after a management practice was often fast. A possible complete recovery of the biomass was observed even in less than a week. Besides the challenge of rapid regrowth, grasslands also presented the particularity of being managed at a fine and intra-parcel scale. Rotational management was observed as a common strategy established by farmers to favor the temporal availability of the grass resource. Thus, relying on the polygons recovered from the RPG to detect a management practice turned out not to be adapted. In particular, the use of large polygons could lead to significant errors as they were enclosing very different grass cover states.

The irregular temporal resolution of optical Sentinel acquisitions was, with respect to rapid regrowth of

the grass, a strong limitation to its use. To address this concern, this thesis proposed the Sentinel Regression for Vegetation Monitoring (SenRVM) approach. SenRVM is a new deep learning strategy to provide dense temporal resolution NDVI time series describing the phenological evolution of vegetation covers. The high temporal resolution of SAR acquisitions was exploited to recover NDVI time series on a regular temporal grid of 6 days, coping with the observed requirements of frequent revisit. The proposed SenRVM methodology relied on a highly supervised recurrent deep learning architecture, using the cloudless Sentinel-2 NDVI acquisitions to perform the regression task. Furthermore, the architecture proposed to integrate the ancillary data to address the weaknesses of the SAR signal and its sensitivity to fluctuations. The fusion of climate, topography, and SAR features allowed the extraction of complex relationships and the achievement of accurate results. Instead of studying grasslands on the classical polygon scale, this thesis proposed the segmentation to superpixels of the RPG polygons. This allowed smaller and homogeneously managed areas to be obtained within the different grassland parcels, addressing the challenge of rotational management. The analysis of NDVI times series at the superpixel scale has corroborated that management practices are performed on different areas in a single grassland parcel with different timings.

The challenges of specific spatio-temporal management of grasslands have been addressed by proposing new methodologies. These methodologies were the first important contributions of this thesis which allowed to achieve novel accurate spatial and temporal scales for detecting grassland management practices. The second important contribution of this work was the development of new detection methodologies exploiting the the superpixel spatial scale and the SenRVM obtained time series temporal scale. These methodologies were tailored to cope with the high diversity of time series patterns associated with grassland management practices. In fact, a diverse number of management practices, with different timings and abrupt or gradual decreases in grass cover, had to be taken into account. Finally, the construction of large validation datasets covering different geographical contexts was used to corroborate the satisfactory results achieved.

SenRVM for continuous vegetation monitoring

The SenRVM performances were first evaluated on two test sites, Mâcon and Toulouse. Large datasets covering three vegetation classes (grassland, crop and forest) exhibiting many agronomic subclasses and distinct landscapes were used. This comprehensive evaluation was a novelty, as most of the similar existing works aiming the recovery of NDVI from SAR features focused exclusively on crops. Among the three classes ($> \ 144,000$ vegetation polygons) and two areas ($> \ 20,000$ km^2), R^2 above 0.83 and MAE below 0.05 were obtained. Despite the high phenological variability of the different classes, satisfactory generalization capabilities of SenRVM were obtained with respect to vegetation type.

Class-oriented results were analyzed on different temporal scales (per date and season). The temporal stability of the results was corroborated by the low errors. The highest MAE errors of about 0.25 were observed during winter, which is more prone to long-term data gaps due to heavy cloud cover. Besides the lack of supervision due to clouds, these results were explained by fluctuations in SAR measurements during winter, due to the presence of bare soil or very little vegetation cover. A spatial evaluation of the results was also performed to investigate whether the reconstruction accuracies were affected by the polygon sizes and their respective locations. This study showed that there is a significant correlation between the size of the polygons (ranging from 0.12 to several hundreds of hectares) and their prediction accuracies. Pearson correlation coefficients above 0.71 were found for the three vegetation classes. The results highlighted that large homogeneous polygons achieve the best accuracies. Among others, large polygons benefit from strong speckle filtering, which could explain the increase in performance. Concerning the location of the polygons, a slight decrease in performance was observed on high-relief geographical regions. This could be explained by the particular side-looking geometry and the strong local incidence angle effects induced by surface topography. It is well-known that these effects degrade the usefulness of SAR images. In the presence of steep topography, it may even prevent information extraction. The SenRVM method proposed a solution to reduce

these undesirable topographic effects by incorporating DTM-derived data. The incorporation of such data as input to the SenRVM architecture helped mitigating the topographic effects which nevertheless cannot be discarded.

The performances of multi-class and single-class SenRVM models were also evaluated and compared by performing an ablation study. The study investigated the impact of different input feature scenarios on the SenRVM performances. The results have suggested different conclusions for agricultural and forest classes. For instance, ancillary data (*e.g.*, climatic and topographic information) could not provide sufficient information for the prediction of NDVI time series on grassland and crop classes (R^2 between 0.5 and 0.7), driven by anthropic activities and phenological stages. Conversely, these features seemed of utmost importance for accurate predictions on forests, achieving R^2 above 0.83 when discarding SAR features. This result was explained by the lower impact of human activities, which leads forest time series to be defined by a more stable and seasonal evolution. The removal of the cloud & shadow mask information allowed another distinction among vegetation classes. The use of these masks permitted a performance gain in all cases (on average 0.07 of R^2), which was considerable on forests (0.13 of R^2).

Different experiments were carried out to evaluate SenRVM performances with respect to several existing machine learning regression algorithms and standard interpolation methods. Random Forest, Gaussian Processes and Multilayer Perceptron supervised regression approaches were considered. Concerning interpolation methods, a Whittaker smoother and a weighted linear interpolation method were considered. Two different scenarios were investigated to confirm the advantages of the SenRVM approach for regular vegetation monitoring. The reconstruction of short- and long-term data gaps showed that the SenRVM approach obtained satisfactory results. SenRVM reached similar absolute errors with classical mono-sensor methodologies and even the lowest in many cases. The advantages of SenRVM were more noticeable in recovering long-term data gaps. Especially, the SenRVM performances were remarkable when vegetation changes occur during the missing data period. In this situation, standard interpolation methods obtained low accuracies and failed to capture vegetation cover changes. The good performance of SenRVM was mainly explained by two factors: its ability to extract complex features and relations between SAR and ancillary data and the efficient extraction of temporal information through recurrent cells.

The generalization capabilities of the SenRVM approach to predict NDVI over grasslands were also explored using the two additional areas ($> 46,000$ km^2) divided in five sub-areas. Models trained on these test sites have corroborated the stability of SenRVM results with $R^2 > 0.80$ and MAE < 0.054 over $205,000$ grassland polygons. The results showed that spatial generalization capabilities of models trained and inferred in distinct sub-areas with similar climatic conditions gave promising results with decreases of R^2 below 0.18. Furthermore, a model using a limited number of training polygons ($10,000$) from the five sub-areas has obtained reliable predictions. R^2 ranging from 0.69 to 0.86 were obtained when this multi-area learned model was applied to the five sub-areas. Temporal generalization was briefly explored by applying a model trained on a specific year (*i.e.*, 2017) to another year (*e.g.*, 2019). Unfortunately, learning and inference from one year to another showed very deteriorated results with R^2 drops of about 0.6.

Finally, some post-processing strategies were proposed to improve SenRVM results. The detection of cloud mask errors by comparing SenRVM and Sentinel-2 discrepancies allowed to improve the results. The blending of SenRVM time series with cloudless Sentinel-2 NDVI was proposed to obtain time series with an even higher temporal resolution. A strategy to obtain a measure of uncertainty associated with SenRVM predictions was also discussed. Relying on spatial and temporal criteria describing the input features, the proposed uncertainties criteria have allowed to illustrate how such additional information could improve the interpretation or integration of the results.

Detection of grassland management practices

A literature review has first allowed us to identify the strengths and especially the weaknesses of the existing approaches. Drawbacks associated to the spatial and temporal scales were identified as the two main challenges to detect management practices on grasslands.

The limitations of object-based studies considering the parcel scale have been presented. This scale was found inadequate due rotational management and the distinction of small intra-parcel areas. To address the limitations, a new scale of analysis between the commonly adopted pixel and parcel-scales was adopted to detect the management practices. A spatio-temporal segmentation of Sentinel-2 times series was proposed to divide into superpixels the grassland parcels recovered from the RPG. Superpixels are intended at providing segments of close size and relatively similar shapes. These two constraints can be counterintuitive in natural environments such as grasslands. Consequently, the maskSLIC algorithm, an alternative to the commonly used SLIC, was proposed to perform the segmentation task. The segmentation with maskSLIC is performed only in a region of interest. Thus, irregular parcel shapes of grasslands were taken into account during the segmentation and the shape constraint was relaxed. The size constraint turned out to be adequate as intra-parcel areas are mainly defined according to practicality of management (accessibility, potential mechanization, etc.). This strategy allowed to avoid the presence of isolated and small-sized segment in the results. The spatio-temporal segmentation was subsequently performed on the Mâcon and Toulouse areas using the complete available set of non-cloudy Sentinel-2 NDVI images. An average size of 0.98 ha was obtained for more than 206,000 superpixels obtained from approximately 78,000 RPG parcels. The resulting superpixel scale has shown satisfactory spatial homogeneity, illustrated by several examples. The standard deviations computed at superpixel scale were found to be lower than those computed at the parcel scale. The analysis of results has corroborated that the different superpixel segments within a grassland parcel can be associated to different management practices. Concerning limitations regarding the temporal scales proposed in the existing methodologies, they were addressed by developing the SenRVM approach. The blended time series (*i.e.*, with non-cloudy Sentinel-2 NDVI) was proven to be an excellent tool to obtain frequent and regular observations to monitor vegetation conditions. The SenRVM method, previously assessed at the parcel scale, was applied at the superpixel scale. The results obtained on Mâcon and Toulouse demonstrated the satisfactory performances achieved by SenRVM by obtaining similar results. The relevance of the obtained time series was illustrated by the good contrasting temporal trends of adjacent superpixels managed separately.

The lack of in-situ reference data describing the frequency and dates of management practices was a third limitation highlighted through this thesis. Poor and spatially local statistical validations was presented by existing works which have, on average, use approximately 250 known technical acts for validation. To develop robust and reliable methodologies, the construction of a large dataset has been a mandatory step in this thesis. The photo-interpretation of Sentinel-2 images has been proposed to manually annotate multiple technical acts on $2,000$ superpixels covering the Mâcon and Toulouse areas. Time intervals were annotated considering the non-cloudy Sentinel-2 acquisitions preceding and displaying the observed technical act. The resulting data sets contained a wide variety of technical acts performed throughout the growing season. For each study area, more than $1,600$ technical acts were annotated.

The exploitation of the hyper-temporal NDVI times series at the superpixel-scale was finally proposed to develop different methodologies aiming the management practices detection. Unsupervised methods were considered because there was not enough reference data available to adopt supervised strategies. Offline and online detection methods were proposed and compared with strategies adapted from the literature. Some methods have considered bi-temporal strategies by only evaluating two consecutive time series values. In contrast, other methods have proposed to study temporal windows to perform a detection.

Five different methods were compared using the two constructed validation datasets. Their performances were measured with the F-score, Precision, and Recall metrics. Different parameter configurations were studied for the different methods. The performances of the different methods were compared by considering the

parameter configurations obtaining the highest F-Score. A method (THR-WIN) based on a fixed threshold applied on the sum of the first derivative in decreasing values intervals achieved the highest F-scores in both areas. F-scores of 0.917 and 0.842 were obtained by this method, missing only about 9% (150 of more than 1,600) annotated technical acts in each area. Comparatively, the rest of the methods obtained more or less similar results. The lowest results were found using a bi-temporal method based on time series polynomial fitting and thresholding of residual errors. This strategy obtained F-scores of 0.792 and 0.678 on the Mâcon and Toulouse test areas. Different experiments were carried out to analyze the sensitivity of the parameter settings of the different methods. The results obtained have corroborated that strategies performing detection in temporal windows provided more reliable and robust results.

A comparison with results obtained by similar works confirmed the excellent results of the THR-WIN method. The main limitations reported in these works have been overcome by addressing in this thesis the spatio-temporal constraints related to grassland monitoring (super-pixel scale and especially hyper-temporal NDVI time series). The generalization capabilities of THR-WIN were demonstrated by the similar results obtained for both test sites. Furthermore, close optimal threshold parameters were found for Mâcon and Toulouse. To understand the limitation of the THR-WIN method, the missed technical acts were analyzed. Some examples showed that practices characterized by a very gradual decrease of NDVI over long time intervals (several weeks or even months) were causing these omissions. The good performances of the THR-WIN method were also corroborated by the low over-detection of technical acts, with only 120 and 411 non-annotated detections for the Mâcon and Toulouse areas. A study was carried out to analyze if these supplementary detections were due to the method or to the construction protocol of the validation dataset. To address this, the supplementary detected technical acts were qualitatively analyzed through photo-interpretation. Approximately 20% of the supplementary detections were correct detections of technical acts that were not annotated. Mostly, these technical acts were not annotated due to cloud & shadow mask commission errors. This result outlined the interest in using the time series obtained from the multi-modal SenRVM approach, as these supplementary technical acts would have been missed by the sole use of Sentinel-2 time series. For the remaining 80% of the supplementary detections, any conclusion could not be reached, since cloud cover prevent to confirm the occurrence of a technical act.

Finally, some visual results allowed to corroborate the interest of the proposed methodologies. These results were obtained by applying the THR-WIN method with optimal parameter setting on the entire Mâcon and Toulouse test sites. Three different informations were extracted from the hyper-temporal NDVI time series and detection results and mapped. The key features, closely related to the quality of the ecosystem services of a grassland, involving the frequency of technical acts, the date of the first detected technical act, and the seasonal amplitude of NDVI were proposed. Accurate and coherent results have confirmed the relevance and interest of the methods developed in this thesis. Acquiring and monitoring on large scales information such as provided by these key features, and potentially others, allow to foresee efficient tools for grassland monitoring.

6.2 Perspectives

The perspectives presented hereafter should help to identify potential future improvements of the proposed methodologies aiming: (i) the recovery of dense NDVI time series and (ii) the detection of grassland management practices.

Methodological perspectives involving the SenRVM framework

Improvements of the SenRVM method could be proposed involving the selection of the input data, the pre-processing steps, and the neural network architecture. Concerning the SenRVM input data proposed in this

thesis, two main limitations could be mentioned. The first concerns the important computational costs that are required to obtain the interferometric coherence features. Nevertheless, this feature has been found essential, as it provides temporal information and is less prone to climate-induced noise than the backscattering coefficient. Efforts are underway to allow large-scale calculation of interferometric coherence images on clusters (for example, through PEPS, 2021) or provide platform services for its systematic distribution (such as through ForM@Ter, 2021). This will eventually allow in the near future to minor the computational constraints linked to interferometric coherence. The second limitation is the use of proprietary data for climate features. These data, acquired daily under the authority of the French national meteorological service, provide calibrated and highly accurate measurements. However, their acquisition can be costly and limit the large-scale deployment of the SenRVM approach. Alternatives can be proposed to acquire large-scale and free climate data based on remote sensing (Liu, 2015; Baghdadi et al., 2020). These last data also provide better spatial resolution than the 8 km grid used in this thesis. Unfortunately, the quality of these data is often much lower, and the variety of climate measurements they propose is limited. Hence, a trade-off between spatial resolution, quality of data and availability is for now required to exploit climate features. The pre-processing step of building a common temporal grid to align the different Sentinels acquisition can also be discussed. First, in this thesis, a nearest-neighbor interpolation was proposed to preserve the dynamics of the NDVI time series. This was motivated by the grassland management practice detection goal. However, other interpolation methods (Lepot et al., 2017) could also be proposed, which could allow a better characterization of the gradual temporal evolution generally observed in vegetation cover. Another solution could be the exploitation of different neural network architectures that do not require the use of regular temporal sampling. Strategies such as the positional encoding traditionally used in Transformers architectures (Vaswani et al., 2017; Li et al., 2020a; Rußwurm and Körner, 2020; Sainte Fare Garnot et al., 2020; Wang et al., 2021) could be implemented to process time series with irregular and asynchronous sampling. Another improvement that could be proposed to improve the regression results is the incorporation of Sentinel-2 information. Indeed, optical measurements have only been used for network supervision. Taking into account past and future Sentinel-2 observations from the current sample or from neighborhood samples may help to improve the predictions of SenRVM. This temporal trajectory could be incorporated by proposing new loss functions based on the assessment of trajectory similarity between predicted and expected time series. For instance, losses based on Dynamic Time Warping (Sakoe and Chiba, 1990), Temporal Distortion Index (Gastón et al., 2017) or Shape and Time Distortion Loss (Guen and Thome, 2019) were already proposed to integrate temporal constraints. However, such strategies must take into account that due to potential long-term data gaps in optical imagery, past and future observations may be temporally very distant.

Besides the improvements mentioned above, heading towards a large-scale application of the SenRVM approach is one of the main perspectives of the work presented in this thesis. Excellent results were obtained by models learned and inferred during an agricultural season (*e.g.*, October 2016 to October 2017) and a specific location (*e.g.*, on a Sentinel-2 tile). The trained models, when confronted with a single spatio-temporal domain, have demonstrated satisfactory generalization capabilities over several vegetation types. Further spatio-temporal generalization experiments have been proposed. Encouraging results of spatial generalization of the SenRVM approach have been found for two experiments. Within broader areas with same climate, the learning on one area and inference on another area gave reliable results. In addition, by integrating data from several areas for learning, the trained models achieved good results in all areas. In contrast, the temporal generalization (*e.g.*, training on one year and inference on another year) which have been explored for a single area, has revealed some limitations. Therefore, to train more generalizable SenRVM models robust to spatial and temporal shifts, different strategies need to be considered.

For spatial generalization, the multi-area learning experiment could be be extended. For instance, if the objective is to develop a model for large scales in France, the construction of a consistent and balanced dataset containing geographically distributed parcels is the first step. Spatial sampling of parcels in numerous areas (*e.g.*, such as Sentinel-2 tiles) or at least in each eco-climatic region would be appropriate (Inglada et al., 2017;

Verde et al., 2020). This would allow the integration of different phenologies, spatial contexts, and especially to gather sufficient samples of infrequent grassland classes at the scale of a single smaller area. The availability of Land Parcel Identification Systems such as the RPG allows to recover the location of grassland parcels on a country-scale. Training SenRVM from spatially distributed samples on large scales could also help mitigate the effects of cloud cover on predictions (Sudmanns et al., 2020b). Higher SenRVM errors have been found in winter due to the lack of supervision. A large and spatially dispatched sampling would increase the chances of gathering non-cloudy NDVI acquisitions over the winter period. Incorporating more training labels during this cloudy period will allow to train more robust models (Che et al., 2018). Some important considerations for training SenRVM at large scale are the computation costs and training times. It should be noted that the reconstruction task in this thesis has taken about an hour for a complete Sentinel-2 tile (*i.e.*, $1/90^{\text{th}}$ of metropolitan France), which seems reasonable for country-wide operational deployment.

To promote the SenRVM temporal generalization capabilities of a large scale model, several strategies could be possible. Data augmentation methods for time series could first be implemented (Guennec et al., 2016; Iwana and Uchida, 2021). Among others, introducing small temporal shifts in the time series of SAR, ancillary, or NDVI features could be a simple and efficient proposed strategy (Sainte Fare Garnot et al., 2022). A modality-dropout could also be employed (Gibert et al., 2020), by randomly removing certain dates during training. Training SenRVM models by using data acquired from several years is also a simple and obvious prospect. A yearly time series containing dates from the different years would increase the integration of more varied weather conditions. Alternatively, training over longer time series composed of several years could be proposed. In this thesis, relatively short time series were extracted. The sequential processing of RNNs was found to be sufficient for the proposed regression task. Short-term memory was favored to describe the rapidly evolving vegetation cover of grasslands. Training over longer time series, on the other hand, could favor long-term memory, for example, to learn patterns of specific seasons seen multiple times. In this case, the use of architectures with self-attention such as Transformers would allow to extract long-term memory and also through parallel learning, greatly reduce training times.

Beyond generalization capabilities, another important consideration is that the SenRVM performances have been only evaluated on NDVI predictions. As previously discussed, this choice was made because of its versatility and simplicity. Nevertheless it is worth noting that the SenRVM methodology is not specifically designed for NDVI. Depending on the application and output modality required by the intended reconstruction task, the presented approach could be applied to different vegetation indices (*e.g.*, EVI, MSAVI, NDMI), biophysical variables (*e.g.*, LAI, faPAR, fCOVER) or even raw optical spectral bands. Such experiments would require little change in the proposed SenRVM architecture. The changes would occur at the last decoding block of the architecture, which would require a different output layer size (*e.g.*, 4 instead of 1 for NDVI, for the prediction of the blue, green, red and infrared bands). In this sense, simultaneous reconstructions of multiple and various vegetation indices (*e.g.*, NDVI and NDMI) potentially exhibiting complex correlations could be considered. Considering the prediction of multiple indices as a multi-task learning problem (Zhang and Yang, 2021; Ilteralp et al., 2022), it would require the definition of weighted combination of task-specific losses (Kendall et al., 2018).

The predictive capacity of RNNs could also be exploited in a near real-time or forecast scenario. A pre-trained model over a sufficient time interval could be used to predict NDVI, from the latest acquired SAR data without retraining. Using such a pre-trained model would allow to obtain NDVI values regardless of climatic conditions by overcoming the need for non-cloudy conditions for network supervision data. A fine-tuning (Sćepanović et al., 2021) of the model, for example, on a monthly basis with the new acquired data, could also be considered to improve the prediction results.

Taking into account all the above, the developed SenRVM methodology could be considered as one of the main contributions of this thesis. The proposed regression method has opened the door to the development of methodologies that jointly exploit optical and SAR data from different satellites. In fact, it must be noticed

that the proposed methodology is nearly invariant to the satellites from which the features are obtained. The NDVI, the backscattering coefficient, or the interferometric coherence statistical descriptors could be computed from other satellites than the Sentinels. Optical data coming from Landsat or Planet, SAR data retrieved from RADARSAT-2 or TerraSAR-X, with different spatial and temporal resolutions could be considered. The growing availability of Earth observation data will thus probably allow the integration of data from various sensors, increasing the scope of applications of an approach such as SenRVM. Furthermore, the imminent arrival of SAR and optical satellites expanding the Sentinel-1 and Sentinel-2 constellations may also permit to apply the SenRVM framework with a temporal resolution higher than 6 days. Such improvements will be beneficial for the regular monitoring of vegetation through satellite time series.

Improvements on detecting grassland management practices

An essential aspect of any scientific work is the validation of the proposed approaches. The lack of validation data on technical acts on grasslands has been a very limiting aspect in the development of the constructed methods. Despite the solicitation of several agriculture chambers, different public research institutes and institutions working on grasslands, and even farmers, no data beyond a few parcels could be obtained. This lack of in situ reference data prevented, for example, assessing the temporal accuracy of the detection methods or distinguishing the management practices (*i.e.*, mowing, grazing, ploughing). In this thesis, the constitution of a dataset by photo-interpretation of optical satellite images has allowed the validation of the methods to some extent. However, some limitations have been highlighted in the constructed datasets (*e.g.*, the impact of clouds, and the temporal resolution of satellite acquisitions). Obtaining expert data on grasslands would certainly allow a more exhaustive validation of the proposed approaches. Therefore, any work that seeks to study grassland management should consider the acquisition of validation data as a priority.

A dataset containing details about the nature (grazed, mowed, mixed, ploughed) and at least the frequency – and at best the exact dates of the technical acts for each grasslands would therefore be essential to improve the results obtained. Above all, for large-scale (country, continent) grassland monitoring, the constitution of such reference data on several geographical contexts is fundamental. It would be possible, for example, to have farmers themselves provide this information via their annual Common Agricultural Policy declarations, in the same way as for the majority crop of their parcels.

Despite the lack of large-scale reference data, it must be noted that satisfactory results have already been achieved for the detection of management practices. By considering accurate spatial (superpixels) and temporal (SenRVM time series) scales, the exploitation of simple methodologies have been found effective. Extending the methods proposed in this thesis could improve the results and promote their large-scale application. One possibility would be to integrate an uncertainty measure, such as the one explored in this thesis to characterize SenRVM predictions, in the change detection decision. This uncertainty could inform on the predictive quality of NDVI but also integrate thematic expert knowledge on management practices. Integrating constraints on the temporal proximity of technical acts, on the probability of a technical act according to climatic conditions, according to the agronomic species or the their spatial proximity could also be considered. This expert knowledge could be defined according to geographical areas or legislative constraints, allowing to obtain tailored results. Another possible improvement would be to exploit the information, illustrated as relevant, from the interferometric coherence features to confirm or deny the detection of a change. Performing change detection with multimodal data could improve the results by limiting the weaknesses of each data.

The collection of large in-situ reference data could promote the development of more integrated and complex methods, based particularly on supervised learning. In particular, such supervised approach would make it possible to avoid the threshold calibration step of methods such as the one proposed in this thesis. These thresholds can vary from one geographical context to another and prevent to obtain a generic change detection model applicable on a large scale. In the case of possible supervision, multi-task methodologies could especially be proposed. This thesis allowed to outline through different illustrations and results that

evolution of NDVI, management practices, and agronomic type of a grassland are closely linked. For example, a ryegrass parcel will have higher temporal fluctuations and numerous and temporally close management practices, whereas a permanent grassland may only be managed once whit otherwise a stable vegetation cover.

Therefore, multi-task approaches aiming the reconstruction of NDVI and classification of grassland types could be proposed. Similarly, a multi-task learning of NDVI reconstruction and change detection could be considered. The idea behind multi-task models is that since NDVI, grassland type and technical acts are highly correlated, the embeddings obtained by the first two blocks of the SenRVM architecture (encoding and recurrent block) could subsequently be used as a pivot variable for one or more prediction tasks (Adsuara et al., 2021; Rolf et al., 2021). Providing as input to the SenRVM approach information related to the grassland type alongside the ones used for NDVI reconstruction could allow training on both tasks simultaneously. This strategy would potentially improve the results by capitalizing on the correlation between the two tasks. If sufficient reference data is acquires describing technical acts, a similar strategy could be implemented to both reconstruct NDVI and detect a change. In addition, if adequate reference data were available, the semantic distinction of management types (*e.g.*, mowed, grazed, mixed, etc.) could also be a novel outcome of such strategies (Daudt et al., 2019). As in the case of multiple output of vegetation indices, separate losses should be considered for these multi-tasks strategies, *e.g.*, for the reconstruction of the NDVI and the probability of change.

Furthermore, depending on the amount of reference data available, transfer-learning strategies could be explored. Indeed, the tasks of NDVI reconstruction and grasslands type classification are both highly supervised. Examples of SAR, ancillary data and NDVI are countless to perform the reconstruction task and the availability of Land Parcel Identification Systems providing class information of grassland parcels on a large-scale are available. Accounting for the high correlation of the different tasks, fine-tuning (Sćepanović et al., 2021) or few shot learning (Rußwurm et al., 2020; Sun et al., 2021b) strategies could be considered. The idea would be, for example, to first train a model for the reconstruction or classification task with strong supervision. The networks weights of the encoder and recurrent block of the SenRVM architecture could then be freezed. The embeddings of the pre-trained recurrent block describing SAR and ancillary time series could next be used to propose a fine-tuning task of the decoder block for the task of change detection, supervised with scarce in-situ reference data. These strategies could provide reliable results with limited validation data which, as seen above, are complex and costly to obtain.

Finally, from a thematic point of view, the results obtained over grasslands in this thesis could be exploited for various applications. The key indicators proposed as examples that are the frequency of the technical acts, the precocity of their occurrence, and the amplitude of variation of the biomass via the NDVI could be used at a large-scale. Their large-scale retrieval could be used to corroborate different environmental studies, for example, related to climate change. Different spatio-temporal analysis could be used to observe or highlight global trends directly linked to different environmental aspects. Lastly, the methods proposed in this thesis could be applied to other similar problems that require frequent and regular monitoring. The retrieval of crop phenological parameters could be proposed by exploiting SenRVM time series. Forest monitoring applications, such as cutting detection, could be considered, especially in environments with high cloud cover. Given the successful and promising result obtained in this thesis for grassland monitoring, the use of the proposed methodologies presented should be beneficial for accurate monitoring and forecasting of vegetation conditions.

Appendix A. Thesis publications

This appendix provides a list of publications made during this PhD or soon to be published.

Peer-reviewed journal papers

- A. Garioud, S. Valero, S. Giordano, C. Mallet. *Recurrent-based regression of Sentinel time series for continuous vegetation monitoring.* Remote Sensing of Environment, vol. 263, pp. 112419, 2021.
- A. Garioud, S. Valero, C. Mallet. *Exploiting the synergy of Sentinel's times series for accurate grassland management practices detection at new spatial and temporal scales. In prep.*, 2023.

Peer-reviewed conferences

- A. Garioud, S. Giordano, S. Valero, C. Mallet. *Challenges in grassland mowing event detection with multimodal sentinel images.* IEEE 10th International Workshop on the Analysis of Multitemporal Remote Sensing Images (MultiTemp), pp. 1–4, 2019. (*oral communication with proceedings*)
- A. Garioud, S. Valero, S. Giordano, C. Mallet. *Joint analysis of SAR and optical satellite images time series for grassland mowing event detection.* ILUS International Land Use Symposium 2019, Land use changes: Trends and projections, 2019. (*oral communication with proceedings*)
- A. Garioud, S. Valero, S. Giordano, C. Mallet. *On the joint exploitation of optical and SAR imagery for grassland monitoring.* The International Archives of the Photogrammetry, Remote Sensing and Spatial Information Sciences XLIII-B3-2020, pp.591-598, 2020. (*oral communication with proceedings*)
- A. Garioud, S. Valero and C. Mallet. *Assessing the interest of a multi-modal gap-filling strategy for monitoring changes in grassland parcels.* IEEE International Geoscience and Remote Sensing Symposium (IGARSS), pp. 3105-3108, 2021. (*oral communication with proceedings*)
- A. Garioud, S. Valero and C. Mallet. *Superpixel-based identification of grassland management practices from dense SenRVM-NDVI time series.* IEEE International Geoscience and Remote Sensing Symposium (IGARSS), pp. 3105-3108, 2022. (*oral communication with proceedings*)
- A. Garioud, S. Valero and C. Mallet. *Detecting management frequency in grasslands from multi-modal Sentinel time series.* The International Archives of the Photogrammetry, Remote Sensing and Spatial Information Sciences, 2022. (*poster presentation*)
- A. Garioud, S. Valero and C. Mallet. *SenRVM: A multi-modal deep learning regression methodology for continuous vegetation monitoring with dense temporal NDVI time series.* ESA Living Planet Symposium (LPS), 2022. (*poster presentation*)
- A. Garioud, S. Valero and C. Mallet. *Superpixel-based identification of grassland management practices from dense NDVI time series.* ESA Living Planet Symposium (LPS), 2022. (*poster presentation*)

Appendix B. LPIS and BD-Forêt cultural and species codes

A full description of declarative codes used in the French *Registre Parcellaire Graphique* within the Common Agricultural Policy is available at Telepac, 2021. Forest polygon species of the *BD Forêt* V2 and related codes are available at (IGN, 2021).

Grassland-related declarative codes:

Permanent grassland or pasture (PM):

- *PPH* = Permanent grassland - predominantly grass (no or limited woody forage resources)
- *PRL* = Long rotation grassland (6 years or more)
- *SPH* = Pastoral surface - predominantly grass and woody forage resources present

Temporary grassy areas (TG):

- *BRH* = Borage, 5 years old or less
- *BRO* = Brome, 5 years old or less
- *CRA* = Garden Cress, 5 years old or less
- *DTY* = Orchad grass, 5 years old or less
- *FET* = Fescue, 5 years old or less
- *FLO* = Timothy grass, 5 years old or less
- *PAT* = Rough bluegrass, 5 years old or less
- *PCL* = Phacelia, 5 years old or less
- *RGA* = Ryegrass, 5 years old or less
- *XFE* = X-Festolium, 5 years old or less
- *GFP* = Other pure forage grass, 5 years old or less
- *MLG* = Mixture of predominantly leguminous plants at seeding and forage grasses, 5 years old or less
- *PTR* = Other temporary grassland of 5 years or less

Fallow land (FA):

- *J5M* = Fallow land of 5 years or less
- *J6P* = Fallow land of 6 years or more
- *J6S* = Fallow land of 6 years or more declared as an ecological interest area

Forage legumes (FL):

- *FFO* = Fodder beans
- *JOS* = Grass peas
- *LFH* = Winter forage lupin
- *LFP* = Spring forage lupin
- *LUZ* = Alfalfa
- *MEL* = Melilot
- *PFH* = Other winter field peas
- *PFP* = Other spring field peas
- *SAI* = Common sainfoin
- *SER* = Serradella
- *TRE* = Clover
- *VES* = Vetches

Crops-related declarative codes:

- *BTH* = Winter wheat
- *MIS* = Maize
- *ORH* = Winter barley

Forest-related species:

- *FF_1* = Closed forest with a mixture of predominantly coniferous and deciduous trees
- *FF_2* = Closed forest of pure black pine or Laricio pine
- *FF_3* = Closed pure Scots pine forest
- *FF_4* = Closed forest with a mixture of other conifers
- *FF_5* = Closed fir or spruce forest
- *FF_6* = Closed forest of another pure pine
- *FF_7* = Closed pure Douglas fir forest
- *FF_8* = Closed forest of pure coniferous patches
- *FF_9* = Closed forest of another deciduous tree
- *FF_10* = Closed forest with pure pine mix
- *FF_11* = Closed forest with a mixture of deciduous trees
- *FF_12* = Closed pure deciduous oak forest
- *FF_13* = Closed forest of another pure conifer other than pine
- *FF_14* = Closed forest with a mixture of predominantly deciduous trees and coniferous
- *FF_15* = Closed pure beech forest
- *FF_16* = Closed pure Robinia forest
- *FF_17* = Closed forest with a mixture of other conifers in patches
- *FF_18* = Closed forest of another pure hardwood
- *FF_19* = Closed pure chestnut forest

Appendix C. SenRVM regression results for Mâcon and Toulouse

per vegetation sub-class

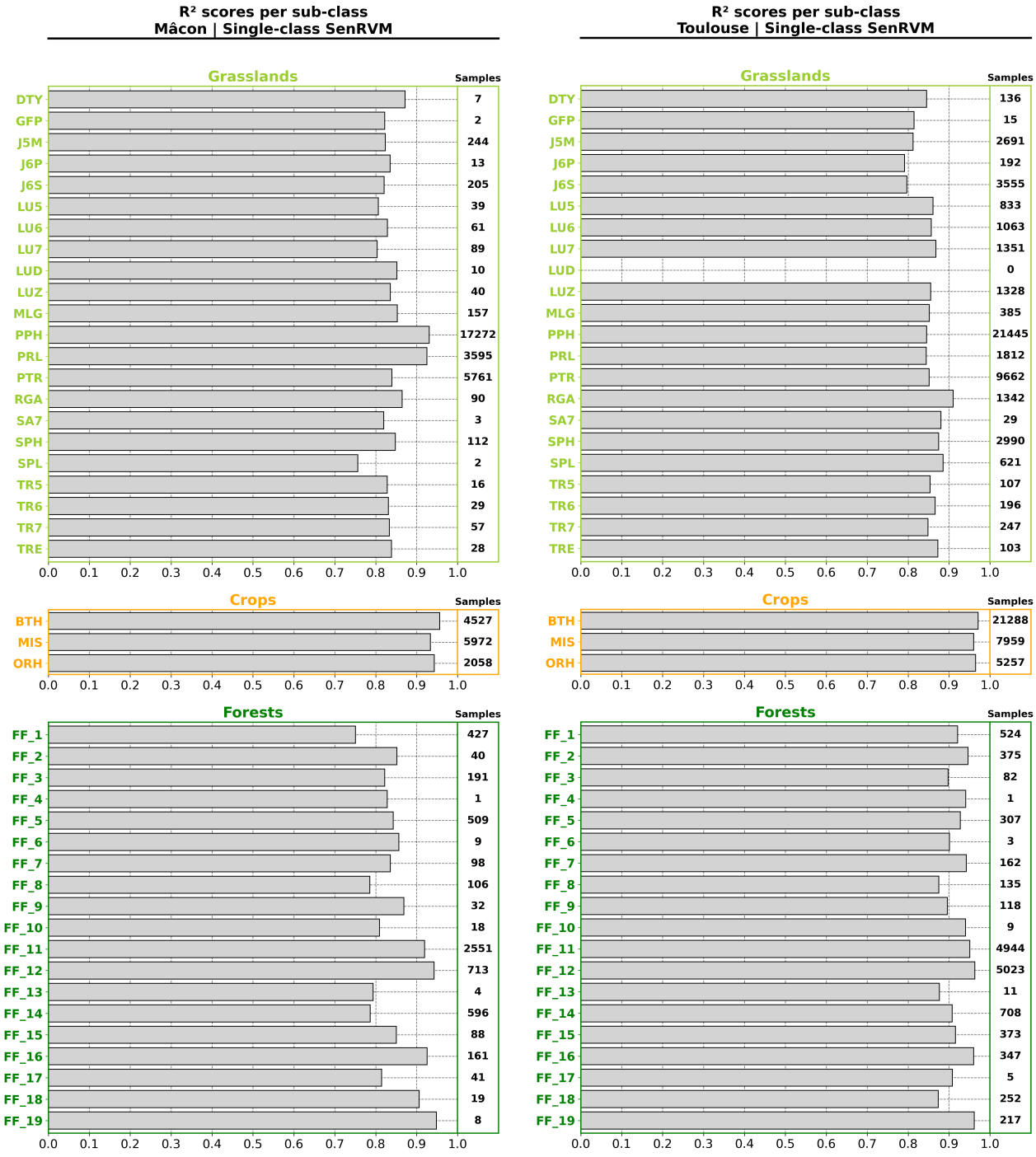

(a) (b)

Figure APP. 1: R^2 scores obtained for each sub-class of the three grasslands, crops and forests vegetation classes, for Mâcon (a) and Toulouse (b) study areas. Results are averages obtained from the test datasets of 5 folds and 5 runs of single-class SenRVM models presented in Section 4.2.2.

Bibliography

Abdar, Moloud, Farhad Pourpanah, Sadiq Hussain, Dana Rezazadegan, Li Liu, Mohammad Ghavamzadeh, Paul Fieguth, Xiaochun Cao, Abbas Khosravi, U. Rajendra Acharya, Vladimir Makarenkov, and Saeid Nahavandi (2021). "A review of uncertainty quantification in deep learning: Techniques, applications and challenges". In: *Information Fusion*, 76, pp. 243–297.

Abdel-Hamid, Ayman, Olena Dubovyk, Valerie Graw, and Klaus Greve (2020). "Assessing the impact of drought stress on grasslands using multi-temporal SAR data of Sentinel-1: a case study in Eastern Cape, South Africa". In: *European Journal of Remote Sensing*, 53.sup2, pp. 3–16.

Abuzar, Mohammad, Desmond M. Whitfield, and Andy McAllister (2017). "Farm Level Assessment of Irrigation Performance for Dairy Pastures in the Goulburn-Murray District of Australia by Combining Satellite-Based Measures with Weather and Water Delivery Information". In: *ISPRS Int. J. Geo Inf.*, 6, p. 239.

Achanta, Radhakrishna, Appu Shaji, Kevin Smith, Aurelien Lucchi, Pascal Fua, and Sabine Süsstrunk (2012). "SLIC Superpixels Compared to State-of-the-Art Superpixel Methods". In: *IEEE Transactions on Pattern Analysis and Machine Intelligence*, 34.11, pp. 2274–2282.

Adamo, Maria, Valeria Tomaselli, Cristina Tarantino, Saverio Vicario, Giuseppe Veronico, Richard Lucas, and Palma Blonda (2020). "Knowledge-Based Classification of Grassland Ecosystem Based on Multi-Temporal WorldView-2 Data and FAO-LCCS Taxonomy". In: *Remote Sensing*, 12.9.

Adsuara, Jose E., Manuel Campos-Taberner, Javier García-Haro, Carlo Gatta, Adriana Romero, and Gustau Camps-Valls (2021). "Learning Unsupervised Feature Representations of Remote Sensing Data with Sparse Convolutional Networks". In: *Deep Learning for the Earth Sciences*. John Wiley & Sons, Ltd. Chap. 2, pp. 13–23.

Agreste, Ministère de l'Agriculture et de l'Alimentation (2021). *L'agriculture, la forêt, la pêche et les industries agroalimentaires - GRAPH'AGRI 2021*. URL: https://agreste.agriculture.gouv.fr/agreste-web/download/publication/publie/GraFra2021Integral/GraFra2021_integral.pdf (visited on 12/10/2021).

Ali, Iftikhar, Brian Barrett, Fiona Cawkwell, Stuart Green, Edward Dwyer, and Maxim Neumann (2017a). "Application of Repeat-Pass TerraSAR-X Staring Spotlight Interferometric Coherence to Monitor Pasture Biophysical Parameters: Limitations and Sensitivity Analysis". In: *IEEE Journal of Selected Topics in Applied Earth Observations and Remote Sensing*, 10.7, pp. 3225–3231.

Ali, Iftikhar, Fiona Cawkwell, Edward Dwyer, Brian Barrett, and Stuart Green (2016). "Satellite remote sensing of grasslands: from observation to management". In: *Journal of Plant Ecology*, 9.6, pp. 649–671.

Ali, Iftikhar, Fiona Cawkwell, Edward Dwyer, and Stuart Green (2017b). "Modeling Managed Grassland Biomass Estimation by Using Multitemporal Remote Sensing Data—A Machine Learning Approach". In: *IEEE Journal of Selected Topics in Applied Earth Observations and Remote Sensing*, 10, pp. 3254–3264.

Ali, Iftikhar, Fiona Cawkwell, Stuart Green, and Ned Dwyer (2014). "Application of statistical and machine learning models for grassland yield estimation based on a hypertemporal satellite remote sensing time series". In: *2014 IEEE Geoscience and Remote Sensing Symposium*, pp. 5060–5063.

Allaby, M. (1998). *A Dictionary of Plant Sciences*. Oxford Paperbacks. Oxford University Press.

Almeida-Ñauñay, Andrés F., Rosa M. Benito, Miguel Quemada, Juan C. Losada, and Ana M. Tarquis (2022). "Recurrence plots for quantifying the vegetation indices dynamics in a semi-arid grassland". In: *Geoderma*, 406, p. 115488.

Alom, Md. Zahangir, Tarek Taha, Chris Yakopcic, Stefan Westberg, Paheding Sidike, Mst Nasrin, Mahmudul Hasan, Brian Essen, Abdul Awwal, and Vijayan Asari (2019). "A State-of-the-Art Survey on Deep Learning Theory and Architectures". In: *Electronics*, 8, p. 292.

An, Nan, Kevin P. Price, and John M. Blair (2013). "Estimating above-ground net primary productivity of the tallgrass prairie ecosystem of the Central Great Plains using AVHRR NDVI". In: *International Journal of Remote Sensing*, 34, pp. 3717 –3735.

Anaya, Jesús A., Emilio Chuvieco, and Alicia Palacios-Orueta (2009). "Aboveground biomass assessment in Colombia: a remote sensing approach." In: *Forest Ecology and Management*, 257, pp. 1237–1246.

Anderson, Gerald L., J. D. Hanson, and Robert H. Haas (1993). "Evaluating Landsat Thematic Mapper derived vegetation indices for estimating above-ground biomass on semiarid rangelands". In: *Remote Sensing of Environment*, 45, pp. 165–175.

Antoran, Javier, James Allingham, and José Miguel Hernández-Lobato (2020). "Depth Uncertainty in Neural Networks". In: *Advances in Neural Information Processing Systems*. Ed. by H. Larochelle, M. Ranzato, R. Hadsell, M. F. Balcan, and H. Lin. Vol. 33. Curran Associates, Inc., pp. 10620–10634.

Asam, Sarah, Doris Klein, and Stefan W. Dech (2015). "Estimation of grassland use intensities based on high spatial resolution LAI time series". In: *ISPRS - International Archives of the Photogrammetry, Remote Sensing and Spatial Information Sciences*, pp. 285–291.

Aschbacher, Josef and Maria P. M. Pérez (2010). "GMES — Status review and policy developments". In: *Yearbook on Space Policy 2008/2009: Setting New Trends*. Ed. by Kai-Uwe Schrogl, Wolfgang Rathgeber, Blandina Baranes, and Christophe Venet. Vienna: Springer Vienna, pp. 188–207.

Askari, Mohammad Sadegh, Timothy McCarthy, Aidan Magee, and Darren J. Murphy (2019). "Evaluation of Grass Quality under Different Soil Management Scenarios Using Remote Sensing Techniques". In: *Remote Sensing*, 11.15.

Asmuß, Tina, Michel Bechtold, and Bärbel Tiemeyer (2019). "On the Potential of Sentinel-1 for High Resolution Monitoring of Water Table Dynamics in Grasslands on Organic Soils". In: *Remote Sensing*, 11, p. 1659.

Atanov, Andrei, Arsenii Ashukha, Dmitry Molchanov, Kirill Neklyudov, and Dmitry P. Vetrov (2018). "Uncertainty Estimation via Stochastic Batch Normalization". In: *6th International Conference on Learning Representations, ICLR 2018, Vancouver, BC, Canada, April 30 - May 3, 2018, Workshop Track Proceedings*.

Atkinson, P. M., C. Jeganathan, Jadu Dash, and Clement Atzberger (2012). "Inter-comparison of four models for smoothing satellite sensor time-series data to estimate vegetation phenology". In: *Remote Sensing of Environment*, 123, pp. 400 –417.

Atkinson, P. M. and A. R. L. Tatnall (1997). "Introduction: Neural networks in remote sensing". In: *International Journal of Remote Sensing*, 18.4, pp. 699–709.

Atwood, Donald, David Small, and R. Gens (2012). "Improving PolSAR Land Cover Classification With Radiometric Correction of the Coherency Matrix". In: *IEEE Journal of Selected Topics in Applied Earth Observations and Remote Sensing*, 5, pp. 848–856.

Atzberger, Clement (2004). "Object-based retrieval of biophysical canopy variables using artificial neural nets and radiative transfer models". In: *Remote Sensing of Environment*, 93.1, pp. 53–67.

— (2013). "Advances in Remote Sensing of Agriculture: Context Description, Existing Operational Monitoring Systems and Major Information Needs". In: *Remote Sensing*, 5.2, 949–981.

Baetens, Louis, Camille Desjardins, and Olivier Hagolle (2019). "Validation of Copernicus Sentinel-2 Cloud Masks Obtained from MAJA, Sen2Cor, and FMask Processors Using Reference Cloud Masks Generated with a Supervised Active Learning Procedure". In: *Remote Sensing*, 11.4.

Baeza, Santiago, Felipe Lezama, Gervasio Piñeiro, Alice Altesor, and José M. Paruelo (2010). "Spatial variability of above-ground net primary production in Uruguayan grasslands: a remote sensing approach". In: *Applied Vegetation Science*, 13, pp. 72–85.

Baghdadi, Nicolas, Hassan Bazzi, Mohammad El Hajj, and Mehrez Zribi (2020). "Comparison between Theïa and Copernicus surface soil moisture products over southern France". In: *IEEE Geoscience and Remote Sensing Society (M2GARSS 2020)*.

Baghdadi, Nicolas, Mohamad El Hajj, Mehrez Zribi, and Ibrahim Fayad (2016). "Coupling SAR C-Band and Optical Data for Soil Moisture and Leaf Area Index Retrieval Over Irrigated Grasslands". In: *IEEE Journal of Selected Topics in Applied Earth Observations and Remote Sensing*, 9.3, pp. 1229–1243.

Baghi, Naghmeh Gholami and Jens Oldeland (2019). "Do soil-adjusted or standard vegetation indices better predict above ground biomass of semi-arid, saline rangelands in North-East Iran?" In: *International Journal of Remote Sensing*, 40, pp. 8223 –8235.

Bardgett, Richard, James Bullock, Sandra Lavorel, Pete Manning, Urs Schaffner, Nicholas Ostle, Mathilde Chomel, Giselda Durigan, Ellen Fry, David Johnson, Jocelyn Lavallee, Gaëtane Le Provost, Shan Luo, Kenny Png, Mahesh Sankaran, Xiangyang Hou, Huakun Zhou, Li Ma, Weibo Ren, and Hongxiao Shi (2021). "Combatting global grassland degradation". In: *Nature Reviews Earth & Environment*, 2.

Barrachina, Maria, Jordi Cristóbal, and Antoni Francesc Tulla (2015). "Estimating above-ground biomass on mountain meadows and pastures through remote sensing". In: *Int. J. Appl. Earth Obs. Geoinformation*, 38, pp. 184–192.

Barrett, Brian, Ingmar Nitze, Stuart Green, and Fiona Cawkwell (2014). "Assessment of multi-temporal, multi-sensor radar and ancillary spatial data for grasslands monitoring in Ireland using machine learning approaches". In: *Remote Sensing of Environment*, 152, pp. 109–124.

Barsi, Julia A., Bahjat Alhammoud, Jeffrey Czapla-Myers, Ferran Gascon, Md. Obaidul Haque, Morakot Kaewmanee, Larry Leigh, and Brian L. Markham (2018). "Sentinel-2A MSI and Landsat-8 OLI radiometric cross comparison over desert sites". In: *European Journal of Remote Sensing*, 51.1, pp. 822–837.

Bastin, G. N., Peter Scarth, Vanessa H. Chewings, Ashley D. Sparrow, Robert Denham, Michael Schmidt, Peter O'Reagain, Ross W. Shepherd, and Brett N Abbott (2012). "Separating grazing and rainfall effects at regional scale using remote sensing imagery: A dynamic reference-cover method". In: *Remote Sensing of Environment*, 121, pp. 443–457.

Beck, Pieter S.A., Clement Atzberger, Kjell Arild Høgda, Bernt Johansen, and Andrew K. Skidmore (2006). "Improved monitoring of vegetation dynamics at very high latitudes: A new method using MODIS NDVI". In: *Remote Sensing of Environment*, 100.3, pp. 321–334.

Begon, Michael, Colin R. Townsend, and John L. Harper (2006). *Ecology: from individuals to ecosystems*. MA : Blackwell Publishing, Malden, 416 pp.

Bekkema, Marijke and Marieke Eleveld (2018). "Mapping Grassland Management Intensity Using Sentinel-2 Satellite Data". In: *GI Forum*, 1, pp. 194–213.

Belda, Santiago, Luca Pipia, Pablo Morcillo-Pallarés, Juan Pablo Rivera-Caicedo, Eatidal Amin, Charlotte De Grave, and Jochem Verrelst (2020a). "DATimeS: A machine learning time series GUI toolbox for gap-filling and vegetation phenology trends detection". In: *Environmental Modelling & Software*, 127, p. 104666.

Belda, Santiago, Luca Pipia, Pablo Morcillo-Pallarés, and Jochem Verrelst (2020b). "Optimizing Gaussian Process Regression for Image Time Series Gap-Filling and Crop Monitoring". In: *Agronomy*, 10.5.

Belgiu, Mariana and Lucian Drăguţ (2016). "Random forest in remote sensing: A review of applications and future directions". In: *ISPRS Journal of Photogrammetry and Remote Sensing*, 114, pp. 24–31.

Bellini, Edoardo, Giovanni Argenti, Marco Moriondo, Nicolina Staglianò, Carolina Pugliese, Andrea Confessore, Chiare Aquilani, Lapo Nannucci, Ricardo Bozzi, and Camilla Dibari (2021). "Use of Sentinel-2 images

for biomass assessment in extensive pastures in the Apennines (Central Italy)". In: *Grassland Science in Europe, 21th EGF symposium 2021 : Sensing - New Insights into Grassland Science and Practice*, 26, p. 231.

Bellman, Richard E. and Stuart E. Dreyfus (1962). *Applied Dynamic Programming*. Princetown University Press.

Bengio, Yoshua, Patrice Simard, and Paolo Frasconi (1994). "Learning long-term dependencies with gradient descent is difficult". In: *IEEE Transactions on Neural Networks*, 5.2, pp. 157–166.

Bengtsson, Jan, James M. Bullock, Benis Egoh, Colin Everson, Terry Everson, Thomas O'Connor, Patrick O'Farrell, Henrik G. Smith, and Regina Lindborg (2019). "Grasslands—more important for ecosystem services than you might think". In: *Ecosphere*, 10.2, e02582.

Bénié, Goze B., Séraphine Sawadogo Kaboré, Kalifa Goïta, and Marie-Françoise Courel (2005). "Remote sensing-based spatio-temporal modeling to predict biomass in sahelian grazing ecosystem". In: *Ecological Modelling*, 184, pp. 341–354.

Beucher, Serge and Christian Lantuéjoul (1979). "Use of Watersheds in Contour Detection". In: *International Workshop on Image Processing: Real-time Edge and Motion Detection/Estimation*, 132.

Bishop, Joshua (2012). "The economics of ecosystems and biodiversity in business and enterprise /". In: "An output of TEEB: The Economics of Ecosystems and Biodiversity"., xxv, 269 p.

Blanco, Lisandro J., Carlos A. Ferrando, and Fernando N. Biurrun (2009). "Remote Sensing of Spatial and Temporal Vegetation Patterns in Two Grazing Systems". In: *Rangeland Ecology & Management*, 62.5, pp. 445–451.

Boland, D H P (1976). *Trophic classification of lakes using LANDSAT-1 (ERTS-1) multispectral scanner data*. U.S. Environmental Protection Agency, Office of Research and Development.

Bolton, Douglas K., Josh M. Gray, Eli K. Melaas, Minkyu Moon, Lars Eklundh, and Mark A. Friedl (2020). "Continental-scale land surface phenology from harmonized Landsat 8 and Sentinel-2 imagery". In: *Remote Sensing of Environment*, 240, p. 111685.

Bongaarts, John (2019). "IPBES, 2019. Summary for policymakers of the global assessment report on biodiversity and ecosystem services of the Intergovernmental Science-Policy Platform on Biodiversity and Ecosystem Services". In: *Population and Development Review*, 45.3, pp. 680–681.

Boschetti, Mirco, Stefano Bocchi, and Pietro Brivio (2007). "Assessment of pasture production in the Italian Alps using spectrometric and remote sensing information". In: *Agriculture, Ecosystems & Environment*, 118, pp. 267–272.

Boval, Maryline and R.M. Dixon (2012). "The importance of grasslands for animal production and other functions: A review on management and methodological progress in the tropics". In: *Animal : an international journal of animal bioscience*, 6, pp. 748–62.

Brandt, Martin, Jean-Pierre Wigneron, Jerome Chave, Torbern Tagesson, Josep Penuelas, Philippe Ciais, Kjeld Rasmussen, Feng Tian, Cheikh Mbow, Amen Al-Yaari, Nemesio Rodriguez-Fernandez, Guy Schurgers, Wenmin Zhang, Jinfeng Chang, Yann Kerr, Aleixandre Verger, Compton Tucker, Arnaud Mialon, Laura Vang Rasmussen, Lei Fan, and Rasmus Fensholt (2018). "Satellite passive microwaves reveal recent climate-induced carbon losses in African drylands". In: *Nature Ecology & Evolution*, 2.5, pp. 827–835.

Brinkmann, Katja, Uta Dickhoefer, Eva Schlecht, and Andreas Buerkert (2011). "Quantification of aboveground rangeland productivity and anthropogenic degradation on the Arabian Peninsula using Landsat imagery and field inventory data". In: *Remote Sensing of Environment*, 115, pp. 465–474.

Buddeberg, Marion, Marcel Sciwieder, A. Orthofer, Katja Kowalski, Kira Pfoch, Patrick Hostert, and Heike Bach (2021). "Estimating grassland biomass from Sentinel 2 – a study on model transferability". In: vol. 26, p. 231.

Buono, G., Martin Oesterheld, Viviana Nakamatsu, and José M. Paruelo (2010). "Spatial and temporal variation of primary production of Patagonian wet meadows". In: *Journal of Arid Environments*, 74, pp. 1257–1261.

Cai, Zhanzhang, Per Jönsson, Hongxiao Jin, and Lars Eklundh (2017). "Performance of Smoothing Methods for Reconstructing NDVI Time-Series and Estimating Vegetation Phenology from MODIS Data". In: *Remote Sensing*, 9.12.

Campos-Taberner, Manuel, Francisco Javier García-Haro, Beatriz Martínez, Emma Izquierdo-Verdiguier, Clement Atzberger, Gustau Camps-Valls, and María Amparo Gilabert (2020). "Understanding deep learning in land use classification based on Sentinel-2 time series". In: *Scientific Reports*, 10.1, p. 17188.

Canny, John (1986). "A Computational Approach to Edge Detection". In: *IEEE Transactions on Pattern Analysis and Machine Intelligence*, 8.6, pp. 679–698.

Cao, Xin, Yongchang Meng, and Jin Chen (2015). "Mapping Grassland Wildfire Risk of the World". In: *World Atlas of Natural Disaster Risk*. Ed. by Peijun Shi and Roger Kasperson. Berlin, Heidelberg: Springer Berlin Heidelberg, pp. 277–283.

Carlos Marcelo, Di Bella, Robert Faivre, Françoise Ruget, Bernard Seguin, Martine Guérif, Bruno Combal, Marie Weiss, and Cesar Rebella (2004). "Remote sensing capabilities to estimate pasture production in France". In: *International Journal of Remote Sensing*, 25.23, pp. 5359–5372.

Chaivaranont, Wasin, Jason P. Evans, Yi Y. Liu, and Jason J. Sharples (2018). "Estimating grassland curing with remotely sensed data". In: *Natural Hazards and Earth System Sciences*, 18.6, pp. 1535–1554.

Chang, Jinfeng, Philippe Ciais, Thomas Gasser, Pete Smith, Mario Herrero, Petr Havlík, Michael Obersteiner, Bertrand Guenet, Daniel S. Goll, Wei Li, Victoria Naipal, Shushi Peng, Chunjing Qiu, Hanqin Tian, Nicolas Viovy, Chao Yue, and Dan Zhu (2021). "Climate warming from managed grasslands cancels the cooling effect of carbon sinks in sparsely grazed and natural grasslands". In: *Nature Communications*, 12.1, p. 118.

Che, Zhengping, Sanjay Purushotham, Kyunghyun Cho, David Sontag, and Yan Liu (2018). "Recurrent Neural Networks for Multivariate Time Series with Missing Values". In: *Scientific Reports*, 8.1, p. 6085.

Chen, Bao-Xiong, Xianzhou Zhang, Jian Tao, Jianshuang Wu, Jingsheng Wang, Pei li Shi, Yangjian Zhang, and Chengqun Yu (2014). "The impact of climate change and anthropogenic activities on alpine grassland over the Qinghai-Tibet Plateau". In: *Agricultural and Forest Meteorology*, 189, pp. 11–18.

Chen, Fang, Keith T. Weber, and Bhushan Gokhale (2011). "Herbaceous Biomass Estimation from SPOT 5 Imagery in Semiarid Rangelands of Idaho". In: *GIScience & Remote Sensing*, 48, pp. 195 –209.

Chen, Jin, Per. Jönsson, Masayuki Tamura, Zhihui Gu, Bunkei Matsushita, and Lars Eklundh (2004). "A simple method for reconstructing a high-quality NDVI time-series data set based on the Savitzky–Golay filter". In: *Remote Sensing of Environment*, 91.3, pp. 332 –344.

Chen, Yong, Wei He, Naoto Yokoya, and Ting-Zhu Huang (2019). "Blind cloud and cloud shadow removal of multitemporal images based on total variation regularized low-rank sparsity decomposition". In: *ISPRS Journal of Photogrammetry and Remote Sensing*, 157, pp. 93 –107.

Chen, Yun, Juan Guerschman, Yuri Shendryk, Dave Henry, and Matthew Tom Harrison (2021). "Estimating Pasture Biomass Using Sentinel-2 Imagery and Machine Learning". In: *Remote Sensing*, 13.4.

Chi, Dengkai, Hong Max Wang, Xiaobing Li, Honghai Liu, and Xiaohui Li (2018). "Assessing the effects of grazing on variations of vegetation NPP in the Xilingol Grassland, China, using a grazing pressure index". In: *Ecological Indicators*, 88, pp. 372–383.

Chiboub, Ons, Amjad Kallel, Pierre-Louis Frison, and Maïlys Lopes (2019). "Monitoring of Grasslands Management Practices Using Interferometric Products Sentinel-1". In: *Advances in Remote Sensing and Geo Informatics Applications*. Ed. by Hesham M. El-Askary, Saro Lee, Essam Heggy, and Biswajeet Pradhan. Springer International Publishing, pp. 239–242.

Cho, Kyunghyun, Bart van Merriënboer, Dzmitry Bahdanau, and Yoshua Bengio (2014). "On the Properties of Neural Machine Translation: Encoder-Decoder Approaches". In: pp. 103–111.

Cimbelli, Alessandro and Valerio Vitale (2017). "Grassland Height Assessment by Satellite Images". In: *Advances in Remote Sensing*, 06, pp. 40–53.

Claverie, Martin, Junchang Ju, Jeffrey G. Masek, Jennifer L. Dungan, Eric F. Vermote, Jean-Claude Roger, Sergii V. Skakun, and Christopher Justice (2018). "The Harmonized Landsat and Sentinel-2 surface reflectance data set". In: *Remote Sensing of Environment*, 219, pp. 145 –161.

Clementini, Chiara, Andrea Pomente, Daniele Latini, Hideki Kanamaru, Maria Raffaella Vuolo, Ana Heureux, Mariko Fujisawa, Giovanni Schiavon, and Fabio Del Frate (2020). "Long-Term Grass Biomass Estimation of Pastures from Satellite Data". In: *Remote Sensing*, 12.13.

Courault, Dominique, Rachid Hadria, Françoise Ruget, Albert Olioso, Benoît Duchemin, Olivier Hagolle, and Gérard Dedieu (2010). "Combined use of FORMOSAT-2 images with a crop model for biomass and water monitoring of permanent grassland in Mediterranean region". In: *Hydrology and Earth System Sciences*, 14, pp. 1731–1744.

Crabbe, Richard Azu, David William Lamb, Clare Edwards, Karl Andersson, and Derek Schneider (2019). "A Preliminary Investigation of the Potential of Sentinel-1 Radar to Estimate Pasture Biomass in a Grazed Pasture Landscape". In: *Remote Sensing*, 11.7.

Cresson, Rémi, Dino Ienco, Raffaele Gaetano, Kenji Ose, and Dinh Ho Tong Minh (2019). "Optical image gap filling using deep convolutional autoencoder from optical and radar images". In: *IGARSS 2019 - 2019 IEEE International Geoscience and Remote Sensing Symposium*, pp. 218–221.

Csillik, Ovidiu (2017). "Fast Segmentation and Classification of Very High Resolution Remote Sensing Data Using SLIC Superpixels". In: *Remote Sensing*, 9.3.

Cui, Xia, Zheng Gang Guo, Tiangang Liang, Yu ying Shen, Xing Liu, and Yong Liu (2012). "Classification management for grassland using MODIS data: a case study in the Gannan region, China". In: *International Journal of Remote Sensing*, 33, pp. 3156 –3175.

Dabrowska-Zielinska, Katarzyna, M. Budzynska, M. Gatkowska, W. Kowalik, M. Bartold, and M. Kiryla (2017). "Importance of grasslands monitoring applying optical and radar satellite data in perspective of changing climate". In: *2017 IEEE International Geoscience and Remote Sensing Symposium (IGARSS)*, pp. 5782–5785.

Dara, Andrey, Matthias Baumann, Martin Freitag, Norbert Hölzel, Patrick Hostert, Johannes Kamp, Daniel Müller, Alexander V. Prishchepov, and Tobias Kuemmerle (2020). "Annual Landsat time series reveal post-Soviet changes in grazing pressure". English. In: *Remote Sensing of Environment*, 239.

Das, Monidipa and Soumya K. Ghosh (2016). "A cost-efficient approach for measuring Moran's index of spatial autocorrelation in geostationary satellite data". In: *2016 IEEE International Geoscience and Remote Sensing Symposium (IGARSS)*, pp. 5913–5916.

Dass, Pawlok, Benjamin Z Houlton, Yingping Wang, and David Warlind (2018). "Grasslands may be more reliable carbon sinks than forests in California". In: *Environmental Research Letters*, 13.7, p. 074027.

Daudt, Rodrigo Caye, Bertrand Le Saux, Alexandre Boulch, and Yann Gousseau (2019). "Multitask learning for large-scale semantic change detection". In: *Computer Vision and Image Understanding*, 187, p. 102783.

De Grave, Charlotte, Jochem Verrelst, Pablo Morcillo-Pallarés, Luca Pipia, Juan Pablo Rivera-Caicedo, Eatidal Amin, Santiago Belda, and José Moreno (2020). "Quantifying vegetation biophysical variables from the Sentinel-3/FLEX tandem mission: Evaluation of the synergy of OLCI and FLORIS data sources". In: *Remote Sensing of Environment*, 251, p. 112101.

De Vroey, Mathilde, Julien Radoux, and Pierre Defourny (2021a). "Grassland Mowing Detection Using Sentinel-1 Time Series: Potential and Limitations". In: *Remote Sensing*, 13.3.

De Vroey, Mathilde, Julien Radoux, Massimo Zavagli, Laura De Vendictis, Diane Heymans, Sophie Bontemps, and Pierre Defourny (2021b). "Performance Assessment of the Sen4CAP Mowing Detection Algorithm

on a Large Reference Data Set of Managed Grasslands". In: *2021 IEEE International Geoscience and Remote Sensing Symposium IGARSS*, pp. 743–746.

De Winter, Joost C. F., Gosling Samuel D., and Potter Jeff (2016). "Comparing the Pearson and Spearman correlation coefficients across distributions and sample sizes: A tutorial using simulations and empirical data." In: *Psychological methods*, 21 3, pp. 273–90.

de Wit, Allard and Bob Su (2005). "Deriving phenological indicators from SPOT-VGT data using the HANTS algorithm". English. In: *Proceedings of the 2nd international VEGETATION user conference; 1998-2004: 6 years of operational activities*. Ed. by F. Veroustraete, E. Bartholomé, and W.W. Verstraeten. 2nd international VEGETATION user conference; Antwerp (Belgium) ; Conference date: 24-03-2004 Through 26-03-2004. EC, pp. 195–201.

Defourny, Pierre, Sophie Bontemps, Nicolas Bellemans, Cosmin Cara, Gérard Dedieu, Eric Guzzonato, Olivier Hagolle, Jordi Inglada, Laurentiu Nicola, Thierry Rabaute, Mickael Savinaud, Cosmin Udroiu, Silvia Valero, Agnès Bégué, Jean-François Dejoux, Abderrazak El Harti, Jamal Ezzahar, Nataliia Kussul, Kamal Labbassi, Valentine Lebourgeois, Zhang Miao, Terrence Newby, Adolph Nyamugama, Norakhan Salh, Andrii Shelestov, Vincent Simonneaux, Pierre Sibiry Traore, Souleymane S. Traore, and Benjamin Koetz (2019). "Near real-time agriculture monitoring at national scale at parcel resolution: Performance assessment of the Sen2-Agri automated system in various cropping systems around the world". In: *Remote Sensing of Environment*, 221, pp. 551 –568.

Derksen, Dawa, Jordi Inglada, and Julien Michel (2020). "Geometry Aware Evaluation of Handcrafted Superpixel-Based Features and Convolutional Neural Networks for Land Cover Mapping Using Satellite Imagery". In: *Remote Sensing*, 12.3.

Desai, M. and A. Ganatra (2012). "Survey on Gap Filling in Satellite Images and Inpainting Algorithm". In: *International Journal of Computer Theory and Engineering*, 4.3, pp. 341–345.

Dinerstein, Eric, David Olson, Anup Joshi, Carly Vynne, Neil D. Burgess, Eric Wikramanayake, Nathan Hahn, Suzanne Palminteri, Prashant Hedao, Reed Noss, Matt Hansen, Harvey Locke, Erle C Ellis, Benjamin Jones, Charles Victor Barber, Randy Hayes, Cyril Kormos, Vance Martin, Eileen Crist, Wes Sechrest, Lori Price, Jonathan E. M. Baillie, Don Weeden, Kierán Suckling, Crystal Davis, Nigel Sizer, Rebecca Moore, David Thau, Tanya Birch, Peter Potapov, Svetlana Turubanova, Alexandra Tyukavina, Nadia de Souza, Lilian Pintea, José C. Brito, Othman A. Llewellyn, Anthony G. Miller, Annette Patzelt, Shahina A. Ghazanfar, Jonathan Timberlake, Heinz Klöser, Yara Shennan-Farpón, Roeland Kindt, Jens-Peter Barnekow Lillesø, Paulo van Breugel, Lars Graudal, Maianna Voge, Khalaf F. Al-Shammari, and Muhammad Saleem (2017). "An Ecoregion-Based Approach to Protecting Half the Terrestrial Realm". In: *BioScience*, 67.6, pp. 534–545.

Ding, Chao, Xiangnan Liu, and Fang Huang (2017). "Temporal Interpolation of Satellite-Derived Leaf Area Index Time Series by Introducing Spatial-Temporal Constraints for Heterogeneous Grasslands". In: *Remote Sensing*, 9.9.

Diouf, Abdoul Aziz, Martin Brandt, Aleixandre Verger, Moussa El Jarroudi, Bakary Djaby, Rasmus Fensholt, Jacques André Ndione, and Bernard Tychon (2015). "Fodder Biomass Monitoring in Sahelian Rangelands Using Phenological Metrics from FAPAR Time Series". In: *Remote Sensing*, 7, pp. 9122–9148.

Donald, G. E., S. G. Gherardi, A. Edirisinghe, S. P. Gittins, D. A. Henry, and G. Mata (2010). "Using MODIS imagery, climate and soil data to estimate pasture growth rates on farms in the south-west of Western Australia". In: *Animal Production Science*, 50.6, pp. 611–615.

Donald, Graham E., J. Michael Scott, and Peter J. Vickery (2013). "Satellite derived evidence of whole farmlet and paddock responses to management and climate". In: *Animal Production Science*, 53, pp. 699–710.

Dong, Taifeng, Jiangui Liu, Budong Qian, Liming He, Jane Liu, Rong Wang, Qi Jing, Catherine Champagne, Heather McNairn, Jarrett Powers, Yichao Shi, Jing M. Chen, and Jiali Shang (2020). "Estimating crop biomass using leaf area index derived from Landsat 8 and Sentinel-2 data". In: *ISPRS Journal of Photogrammetry and Remote Sensing*, 168, pp. 236 –250.

Doxani, Georgia, Eric Vermote, Jean-Claude Roger, Ferran Gascon, Stefan Adriaensen, David Frantz, Olivier Hagolle, André Hollstein, Grit Kirches, Fuqin Li, Jérôme Louis, Antoine Mangin, Nima Pahlevan, Bringfried Pflug, and Quinten Vanhellemont (2018). "Atmospheric Correction Inter-Comparison Exercise". In: *Remote Sensing*, 10.2.

Drusch, Matthias, Umberto Del Bello, Simon Carlier, Olivier Colin, Valérie Fernandez, Ferran Gascon, Bianca Hoersch, Claudia Isola, Paolo Laberinti, Philippe Martimort, Aimé Meygret, Francois Spoto, Omar Sy, Franco Marchese, and Pier Bargellini (2012). "Sentinel-2: ESA's Optical High-Resolution Mission for GMES Operational Services". In: *Remote Sensing of Environment*, 120, 25–36.

Dube, Opha Pauline and Geoff Pickup (2001). "Effects of rainfall variability and communal and semi-commercial grazing on land cover in southern African rangelands". In: *Climate Research*, 17, pp. 195–208.

Dusseux, Pauline, Thomas Corpetti, Laurence Hubert-Moy, and Samuel Corgne (2014a). "Combined Use of Multi-Temporal Optical and Radar Satellite Images for Grassland Monitoring". In: *Remote Sensing*, 6.7, pp. 6163–6182.

Dusseux, Pauline, Xing Gong, Laurence Hubert-Moy, and Thomas Corpetti (2014b). "Identification of grassland management practices from leaf area index time series". In: *Journal of Applied Remote Sensing*, 8.

Dusseux, Pauline, Laurence Hubert-Moy, Thomas Corpetti, and Françoise Vertès (2015). "Evaluation of SPOT imagery for the estimation of grassland biomass". In: *Int. J. Appl. Earth Obs. Geoinformation*, 38, pp. 72–77.

Dusseux, Pauline, Françoise Vertès, Thomas Corpetti, Samuel Corgne, and Laurence Hubert-Moy (2014c). "Agricultural practices in grasslands detected by spatial remote sensing". In: *Environmental Monitoring and Assessment*, 186, pp. 8249–8265.

Dwyer, John L., David P. Roy, Brian Sauer, Calli B. Jenkerson, Hankui K. Zhang, and Leo Lymburner (2018). "Analysis Ready Data: Enabling Analysis of the Landsat Archive". In: *Remote Sensing*, 10.9.

D'Andrimont, Raphaël, Guido Lemoine, and Marijn Van der Velde (2018). "Targeted Grassland Monitoring at Parcel Level Using Sentinels, Street-Level Images and Field Observations". In: *Remote Sensing*, 10.8.

d'Andrimont, Raphaël, Matthieu Taymans, Guido Lemoine, Andrej Ceglar, Momchil Yordanov, and Marijn van der Velde (2020). "Detecting flowering phenology in oil seed rape parcels with Sentinel-1 and -2 time series". In: *Remote Sensing of Environment*, 239, p. 111660.

Edirisinghe, Asoka, Da Clark, and Deanne Waugh (2012). "Spatio-temporal modelling of biomass of intensively grazed perennial dairy pastures using multispectral remote sensing". In: *Int. J. Appl. Earth Obs. Geoinformation*, 16, pp. 5–16.

Edirisinghe, Asoka, Michael J. Hill, Graham E. Donald, and M. W. Hyder (2011). "Quantitative mapping of pasture biomass using satellite imagery". In: *International Journal of Remote Sensing*, 32, pp. 2699 –2724.

Ehrlich, Paul and Anne Ehrlich (1981). "Extinction: the causes and consequences of the disappearance of species". In: *New York: Random House*, 305 p.

Eisfelder, Christina, Igor Klein, Aruzhan Asankulovna Bekkuliyeva, Claudia Kuenzer, Manfred F. Buchroithner, and Stefan W. Dech (2017). "Above-ground biomass estimation based on NPP time-series - A novel approach for biomass estimation in semi-arid Kazakhstan". In: *Ecological Indicators*, 72, pp. 13–22.

El Hajj, Mohammad, Nicolas Baghdadi, Hassan Bazzi, and Mehrez Zribi (2019). "Penetration Analysis of SAR Signals in the C and L Bands for Wheat, Maize, and Grasslands". In: *Remote Sensing*, 11.1.

Elman, Jeffrey L. (1990). "Finding structure in time". In: *Cognitive Science*, 14.2, pp. 179–211.

ESA, Serco Gael consortium (2021a). *Copernicus Sentinel Data Access Annual Report Y2020*. URL: https://scihub.copernicus.eu/reportsandstats/ (visited on 11/12/2021).

ESA, SNAP (2021b). *ESA Sentinel Application Platform*. URL: http://step.esa.int (visited on 01/10/2021).

Esch, Thomas, Annekatrin Metz, Mattia Marconcini, and Manfred Keil (2014). "Combined use of multi-seasonal high and medium resolution satellite imagery for parcel-related mapping of cropland and grassland". In: *Int. J. Appl. Earth Obs. Geoinformation*, 28, pp. 230–237.

Estel, Stephan, Sebastian Mader, Christian Levers, Peter H. Verburg, Matthias Baumann, and Tobias Kuemmerle (2018). "Combining satellite data and agricultural statistics to map grassland management intensity in Europe". In: *Environmental Research Letters*, 13, pp. 1–11.

European Union (2018). "Copernicus Land Monitoring Service:" in: *European Environment Agency (EEA)*.

Eurostat, the statistical office of the European Union (2021). *Land cover and land use, landscape (LUCAS)*. URL: https://ec.europa.eu/eurostat/web/lucas/data/database (visited on 12/10/2021).

Everitt, J.H, D.E Escobar, and A.J Richardson (1989). "Estimating grassland phytomass production with near-infrared and mid-infrared spectral variables". In: *Remote Sensing of Environment*, 30.3, pp. 257–261.

Fan, Jiang wen, Quanqin Shao, Ji-Yuan Liu, Jun bang Wang, Warwick Harris, Zhuoyuan Chen, Huaping Zhong, Xinliang Xu, and Rong Liu (2010). "Assessment of effects of climate change and grazing activity on grassland yield in the Three Rivers Headwaters Region of Qinghai–Tibet Plateau, China". In: *Environmental Monitoring and Assessment*, 170, pp. 571–584.

Fassnacht, Fabian E., Christopher Schiller, Jiapeng Qu, Teja Kattenborn, and Xinquan Zhao (2018). "Modis-Based Grassland Trends Within and Around the Kekexili Core Protection Zone of the Sanjiangyuan Nature Reserve". In: *IGARSS 2018 - 2018 IEEE International Geoscience and Remote Sensing Symposium*, pp. 2880–2882.

Fauvel, Mathieu, Mailys Lopes, Titouan Dubo, Justine Rivers-Moore, Pierre-Louis Frison, Nicolas Gross, and Annie Ouin (2020). "Prediction of plant diversity in grasslands using Sentinel-1 and -2 satellite image time series". In: *Remote Sensing of Environment*, 237, 13 p.

Fazzini, Paolo, Giuseppina De Felice Proia, Maria Adamo, Palma Blonda, Francesco Petracchini, Luigi Forte, and Cristina Tarantino (2021). "Sentinel-2 Remote Sensed Image Classification with Patchwise Trained ConvNets for Grassland Habitat Discrimination". In: *Remote Sensing*, 13.12.

Feng, Xiaoming and Yu Zhao (2011). "Grazing intensity monitoring in Northern China steppe: Integrating CENTURY model and MODIS data". In: *Ecological Indicators*, 11, pp. 175–182.

Feng, Yunfei, Jianshuang Wu, Jing Zhang, Xianzhou Zhang, and Chunqiao Song (2017). "Identifying the Relative Contributions of Climate and Grazing to Both Direction and Magnitude of Alpine Grassland Productivity Dynamics from 1993 to 2011 on the Northern Tibetan Plateau". In: *Remote Sensing*, 9, p. 136.

Fern, Rachel R., Elliott A. Foxley, Andrea Bruno, and Michael L. Morrison (2018). "Suitability of NDVI and OSAVI as estimators of green biomass and coverage in a semi-arid rangeland." In: *Ecological Indicators*, 94, pp. 16–21.

Fernández-Habas, Jesús, Alma María García Moreno, M. Teresa Hidalgo-Fernández, José Ramón Leal-Murillo, Begoña Abellanas Oar, Pedro J. Gómez-Giráldez, María P. González-Dugo, and Pilar Fernández-Rebollo (2021). "Investigating the potential of Sentinel-2 configuration to predict the quality of Mediterranean permanent grasslands in open woodlands". In: *Science of The Total Environment*, 791, p. 148101.

Fontana, Fabio, Christian Rixen, Tobias Jonas, Gabriel Aberegg, and Stefan Wunderle (2008). "Alpine Grassland Phenology as Seen in AVHRR, VEGETATION, and MODIS NDVI Time Series - a Comparison with In Situ Measurements". In: *Sensors (Basel, Switzerland)*, 8, pp. 2833 –2853.

ForM@Ter, CNRS et CNES (2021). *Pôle Terre solide*. URL: https://www.poleterresolide.fr/ (visited on 11/25/2021).

Franke, Jonas, Vanessa Keuck, and Florian Siegert (2012). "Assessment of grassland use intensity by remote sensing to support conservation schemes". In: *Journal for Nature Conservation*, 20, 125–134.

Friedl, M. A., D. S. Schimel, J. Michaelsen, F. W. Davis, and H. Walker (1994). "Estimating grassland biomass and leaf area index using ground and satellite data". In: *International Journal of Remote Sensing*, 15.7, pp. 1401–1420.

Frolking, Steve, Mark A. Fahnestock, Tom Milliman, Kyle McDonald, and John S. Kimball (2005). "Interannual variability in North American grassland biomass/productivity detected by SeaWinds scatterometer backscatter". In: *Geophysical Research Letters*, 32.

Fu, Xinyu, Chuanjiang Tang, Xuxiao Zhang, Jingying Fu, and Dong Jiang (2014). "An improved indicator of simulated grassland production based on MODIS NDVI and GPP data: A case study in the Sichuan province, China". In: *Ecological Indicators*, 40, pp. 102–108.

Fukunaga, K. and L. Hostetler (1975). "The estimation of the gradient of a density function, with applications in pattern recognition". In: *IEEE Transactions on Information Theory*, 21.1, pp. 32–40.

Gaffney, Rowan, Lauren M. Porensky, Feng Gao, J Gonzalo N Irisarri, Martin Durante, Justin D. Derner, and David J. Augustine (2018). "Using APAR to Predict Aboveground Plant Productivity in Semi-Arid Rangelands: Spatial and Temporal Relationships Differ". In: *Remote Sensing*, 10, p. 1474.

Gal, Yarin and Zoubin Ghahramani (2016). "Dropout as a Bayesian Approximation: Representing Model Uncertainty in Deep Learning". In: *Proceedings of the 33rd International Conference on International Conference on Machine Learning - Volume 48*. ICML'16. New York, NY, USA: JMLR.org, 1050–1059.

Gang, Chengcheng, Wei Zhou, Yizhao Chen, Zhaoqi Wang, Zhengguo Sun, Jianlong Li, Jiaguo Qi, and Inakwu Odeh (2014). "Quantitative assessment of the contributions of climate change and human activities on global grassland degradation". In: *Environmental Earth Sciences*, 72.11, pp. 4273–4282.

Gao, Feng, Martha C. Anderson, Xiaoyang Zhang, Zhengwei Yang, Joseph G. Alfieri, William P. Kustas, Rick Mueller, David M. Johnson, and John H. Prueger (2017). "Toward mapping crop progress at field scales through fusion of Landsat and MODIS imagery". In: *Remote Sensing of Environment*, 188, pp. 9 –25.

Gao, Jianhao, Qiangqiang Yuan, Jie Li, Hai Zhang, and Xin Su (2020). "Cloud Removal with Fusion of High Resolution Optical and SAR Images Using Generative Adversarial Networks". In: *Remote Sensing*, 12.1.

Gao, Qingzhu, Mark W. Schwartz, Wenquan Zhu, Yunfan Wan, Xiaobo Qin, Xin Ma, Shuo Liu, Matthew A. Williamson, Casey B. Peters, and Yue Li (2016). "Changes in Global Grassland Productivity during 1982 to 2011 Attributable to Climatic Factors". In: *Remote Sensing*, 8, p. 384.

Gao, Tian, Bin Xu, Xiuchun Yang, Yunxiang Jin, Hailong Ma, Jinya Li, and Haida Yu (2013). "Using MODIS time series data to estimate aboveground biomass and its spatio-temporal variation in Inner Mongolia's grassland between 2001 and 2011". In: *International Journal of Remote Sensing*, 34, pp. 7796 –7810.

Gascoin, S., M. Grizonnet, M. Bouchet, G. Salgues, and O. Hagolle (2019). "Theia Snow collection: high-resolution operational snow cover maps from Sentinel-2 and Landsat-8 data". In: *Earth System Science Data*, 11.2, pp. 493–514.

Gastón, Martín, Laura Frías-Paredes, F. Mallor, and Teresa Leon (2017). "Assessing energy forecasting inaccuracy by simultaneously considering temporal and absolute errors". In: *Energy Conversion and Management*, 142.

Gerber, Florian, Rogier de Jong, Michael E. Schaepman, Gabriela Schaepman-Strub, and Reinhard Furrer (2018). "Predicting Missing Values in Spatio-Temporal Remote Sensing Data". In: *IEEE Transactions on Geoscience and Remote Sensing*, 56.5, pp. 2841–2853.

Gibert, Daniel, Carles Mateu, and Jordi Planes (2020). "HYDRA: A multimodal deep learning framework for malware classification". In: *Computers & Security*, 95, p. 101873.

Gibson, David J. (2009). "Grasses and Grassland Ecology". In: *Oxford University Press*.

Glenn, Edward P., Alfredo R. Huete, Pamela L. Nagler, and Stephen G. Nelson (2008). "Relationship Between Remotely-sensed Vegetation Indices, Canopy Attributes and Plant Physiological Processes: What Vegetation Indices Can and Cannot Tell Us About the Landscape". In: *Sensors*, 8.4, pp. 2136–2160.

Gómez-Giménez, Marta, Rogier Jong, Raniero Della Peruta, Armin Keller, and Michael Schaepman (2017). "Determination of grassland use intensity based on multi-temporal remote sensing data and ecological indicators". In: *Remote Sensing of Environment*, 198, pp. 126–139.

Goodfellow, Ian J., Yoshua Bengio, and Aaron Courville (2016). *Deep Learning*. Cambridge, MA, USA: MIT Press.

Govender, Megandhren, Kershani Chetty, and Hartley Bulcock (2007). "A review of hyperspectral remote sensing and its application in vegetation and water resource studies". In: *Water S.A*, 33.

Grant, Kerstin, Robert Siegmund, Marian Wagner, and Stephan Hartmann (2015). "Satellite-based assessment of grassland yields". In: *ISPRS - International Archives of the Photogrammetry, Remote Sensing and Spatial Information Sciences*, pp. 15–18.

Grant, Kristin, Daniel L. Johnson, David V. Hildebrand, and Derek R. Peddle (2013). "Quantifying biomass production on rangeland in southern Alberta using SPOT imagery". In: *Canadian Journal of Remote Sensing*, 38, pp. 695 –708.

Griffiths, Patrick, Claas Nendel, Jürgen Pickert, and Patrick Hostert (2019). "Towards national-scale characterization of grassland use intensity from integrated Sentinel-2 and Landsat time series". In: *Remote Sensing of Environment*, 238, p. 111124.

Grizonnet, Manuel, Julien Michel, Victor Poughon, Jordi Inglada, Mickaël Savinaud, and Rémi Cresson (2017). "Orfeo ToolBox: Open source processing of remote sensing images". In: *Open Geospatial Data, Software and Standards*, 2.1, p. 15.

Gu, Yingxin, Bruce K. Wylie, and Norman B. Bliss (2013). "Mapping grassland productivity with 250-m eMODIS NDVI and SSURGO database over the Greater Platte River Basin, USA". In: *Ecological Indicators*, 24, pp. 31–36.

Guen, Vincent Le and Nicolas Thome (2019). "Shape and Time Distortion Loss for Training Deep Time Series Forecasting Models". In: *Advances in Neural Information Processing Systems 32 (NeurIPS 2019)*. Vol. 4191–4203. Advances in Neural Information Processing Systems 32 (NIPS 2019) proceedings.

Guennec, Arthur Le, Simon Malinowski, and Romain Tavenard (2016). "Data Augmentation for Time Series Classification using Convolutional Neural Networks". In.

Guerini Filho, Marildo, Tatiana Mora Kuplich, and Fernando Luiz Ferreira de Quadros (2019). "Estimating natural grassland biomass by vegetation indices using Sentinel 2 remote sensing data". In: *International Journal of Remote Sensing*, 41, pp. 2861 –2876.

Guido, Anaclara, Ramón Díaz Varela, Pablo Baldassini, and José Paruelo (2014). "Spatial and Temporal Variability in Aboveground Net Primary Production of Uruguayan Grasslands". In: *Rangeland Ecology & Management*, 67.1, pp. 30–38.

Guo, Jian, Xiuchun Yang, Jianming Niu, Yunxiang Jin, Bin Xu, Ge Shen, Wenbo Zhang, Fen Zhao, and Yujing Zhang (2019). "Remote sensing monitoring of green-up dates in the Xilingol grasslands of northern China and their correlations with meteorological factors". In: *International Journal of Remote Sensing*, 40, pp. 2190 –2211.

Guo, Qun, Zhongmin Hu, Shenggong Li, Xuanran Li, Xiaomin Sun, and Guirui Yu (2012). "Spatial variations in aboveground net primary productivity along a climate gradient in Eurasian temperate grassland: effects of mean annual precipitation and its seasonal distribution". In: *Global Change Biology*, 18, pp. 3624–3631.

Guo, Xulin, Kevin P. Price, and James M. Stiles (2000a). "Biophysical and Spectral Characteristics of Cool- and Warm-Season Grasslands under Three Land Management Practices in Eastern Kansas". In: *Natural Resources Research*, 9, pp. 321–331.

Guo, Xulin, Kevin P. Price, and James M. Stiles (2000b). "Biophysical and Spectral Characteristics of Cool- and Warm-Season Grasslands under Three Land Management Practices in Eastern Kansas". In: *Natural Resources Research*, 9, pp. 321–331.

Guo, Xulin, Kevin P. Price, and James M. Stiles (2003). "Grasslands discriminant analysis using Landsat TM single and multitemporal data". In: *Photogrammetric Engineering and Remote Sensing*, 69, pp. 1255–1262.

Guo, Xulin, John F. Wilmshurst, Stephen J. McCanny, Patrick J. Fargey, and Pierre J. H. Richard (2004). "Measuring Spatial and Vertical Heterogeneity of Grasslands Using Remote Sensing Techniques". In: *Journal of Environmental Informatics*, 3, pp. 24–32.

Gutiérrez-Guzmán, Ulises Noel, Edmundo Edmundo Castellanos-Pérez, J. Santos Serrato-Corona, Juan José Martínez-Ríos, and isaías Chairez-hernández (2017). "Satellite and field radiometry for the estimation of biomass production in a grassland site in state of Durango, Mexico". In: *Range Management and Agroforestry*, 38, pp. 158–164.

Hadj Said, Malika, Mourad Laghrouche, Mokrane Malek, Rachid Hadria, Albert Olioso, Dominique Courault, and Soltane Ameur (2011). "Détection supervisée des dates des opérations de fauche des prairies irriguées dans la plaine de la Crau, France." In: *Teledetection*, 10.2-3, pp. 129–136.

Hagolle, Olivier, Mireille Huc, David Villa Pascual, and Gerard Dedieu (2015). "A multi-temporal and multi-spectral method to estimate aerosol optical thickness over land, for the atmospheric correction of FormoSat-2, LandSat, VENμS and Sentinel-2 images". In: *Remote Sensing*, 7.3, pp. 2668–2691.

Halabuk, Andrej, Matej Mojses, Marek Halabuk, and Stanislav David (2015). "Towards Detection of Cutting in Hay Meadows by Using of NDVI and EVI Time Series". In: *Remote Sensing*, 7.5, pp. 6107–6132.

Hall, Karin, Lotten J. Johansson, Martin T. Sykes, Triin Reitalu, Karin Larsson, and Honor C. Prentice (2010). "Inventorying management status and plant species richness in semi-natural grasslands using high spatial resolution imagery". In: *Applied Vegetation Science*, 13, pp. 221–233.

Hancock, John and Taghi Khoshgoftaar (2020). "Survey on categorical data for neural networks". In: *Journal of Big Data*, 7.

Hardy, Tom, Lammert Kooistra, Marston Domingues Franceschini, Sebastiaan Richter, Erwin Vonk, Gé van den Eertwegh, and Dion van Deijl (2021). "Sen2Grass: A Cloud-Based Solution to Generate Field-Specific Grassland Information Derived from Sentinel-2 Imagery". In: *AgriEngineering*, 3.1, pp. 118–137.

He, Honglin, Min Liu, Xiangming Xiao, Xiaoli Ren, Li Zhang, Xiaomin Sun, Yuanhe Yang, Yingnian Li, Liang Zhao, Pei li Shi, Mingyuan Du, Yaoming Ma, Mingguo Ma, Y. Zhang, and Guirui Yu (2014). "Large-scale estimation and uncertainty analysis of gross primary production in Tibetan alpine grasslands". In: *Journal of Geophysical Research*, 119, pp. 466–486.

He, Li, Ainong Li, Gaofei Yin, Xi Nan, and Jinhu Bian (2019). "Retrieval of Grassland Aboveground Biomass through Inversion of the PROSAIL Model with MODIS Imagery". In: *Remote Sensing*, 11.13.

He, Qibin, Xian Sun, Zhiyuan Yan, and Kun Fu (2022). "DABNet: Deformable Contextual and Boundary-Weighted Network for Cloud Detection in Remote Sensing Images". In: *IEEE Transactions on Geoscience and Remote Sensing*, 60, pp. 1–16.

He, Wei and Naoto Yokoya (2018). "Multi-Temporal Sentinel-1 and -2 Data Fusion for Optical Image Simulation". In: *ISPRS International Journal of Geo-Information*, 7.10.

Hebb, D.O. (1949). "The Organization of Behavior". In: *Brain Research Bulletin*, 50.5, p. 437.

Heymann, Yuri, Chris Steenmans, G. Croisille, and M. Bossard (1994). "CORINE Land Cover. Technical Guide". In: *Commission of the European Communities*.

Hibbard, Kathy, David Schimel, Steven Archer, Dennis Ojima, and And Parton (2003). "Grassland to woodland transitions: Integrating changes in landscape structure and biogeochemistry". In: *Ecological Applications*, 13, pp. 911–926.

Hill, Michael J., Graham E. Donald, M. W. Hyder, and R. G. Smith (2004). "Estimation of pasture growth rate in the south west of Western Australia from AVHRR NDVI and climate data". In: *Remote Sensing of Environment*, 93, pp. 528–545.

Hochreiter, Sepp and Jürgen Schmidhuber (1997). "Long short-term memory". In: *Neural computation*, 9.8, pp. 1735–1780.

Holtgrave, Ann-Kathrin, Andrea Ackermann, Norbert Röder, and Birgit Kleinschmit (2020). "Towards a dual-polarisation radar vegetation index for Sentinel-1 for grassland monitoring". In: *Grassland Science in Europe, Proceedings of the 28th General Meeting of the European Grassland Federation : Meeting the future demands for grassland production*, 25, p. 807.

Hou, Jing, Lingtong Du, Ke Liu, Yue Hu, and Yuguo Zhu (2019). "Characteristics of vegetation activity and its responses to climate change in desert/grassland biome transition zones in the last 30 years based on GIMMS3g". In: *Theoretical and Applied Climatology*, 136.

Hubert-Moy, Laurence, Jeanne Thibault, Elodie Fabre, Clémence Rozo, Damien Arvor, Thomas Corpetti, and Sébastien Rapinel (2019). "Mapping Grassland Frequency Using Decadal MODIS 250 m Time-Series: Towards a National Inventory of Semi-Natural Grasslands". In: *Remote Sensing*, 11.24.

Hubert-Moy, Laurence, Jeanne Thibault, Elodie Fabre, Clémence Rozo, Damien Arvor, Thomas Corpetti, and Sébastien Rapinel (2019). "Mapping Grassland Frequency Using Decadal MODIS 250 m Time-Series: Towards a National Inventory of Semi-Natural Grasslands". In: *Remote Sensing*, 11.24.

Huffman, George J., David T. Bolvin, Eric J. Nelkin, David B. Wolff, Robert F. Adler, Guojun Gu, Yang Hong, Kenneth P. Bowman, and Erich F. Stocker (2007). "The TRMM Multisatellite Precipitation Analysis (TMPA): Quasi-Global, Multiyear, Combined-Sensor Precipitation Estimates at Fine Scales". In: *Journal of Hydrometeorology*, 8.1, pp. 38 –55.

Hufkens, Koen, Trevor F. Keenan, Lawrence B. Flanagan, Russell L. Scott, Carl J. Bernacchi, Eva Joo, Nathaniel A. Brunsell, Joseph Verfaillie, and Andrew D. Richardson (2016). "Productivity of North American grasslands is increased under future climate scenarios despite rising aridity". In: *Nature Climate Change*, 6.7, pp. 710–714.

IGN, Institut national de l'information géographique et forestière (2021). *BD Forêt*. URL: https://geoservices.ign.fr/bdforet (visited on 12/02/2021).

Ikeda, Haruhiko, Katsuo Okamoto, and Michikazu Fukuhara (1999). "Estimation of aboveground grassland phytomass with a growth model using Landsat TM and climate data". In: *International Journal of Remote Sensing*, 20, pp. 2283–2294.

Ilteralp, Melike, Sema Ariman, and Erchan Aptoula (2022). "A Deep Multitask Semisupervised Learning Approach for Chlorophyll-a Retrieval from Remote Sensing Images". In: *Remote Sensing*, 14.1.

Inglada, Jordi, Arthur Vincent, Marcela Arias, Benjamin Tardy, David Morin, and Isabel Rodes (2017). "Operational High Resolution Land Cover Map Production at the Country Scale Using Satellite Image Time Series". In: *Remote Sensing*, 9.1.

Irisarri, J Gonzalo N, Martin Oesterheld, José M. Paruelo, and Marcos Texeira (2012). "Patterns and controls of above-ground net primary production in meadows of Patagonia. A remote sensing approach". In: *Journal of Vegetation Science*, 23, pp. 114–126.

Irving, B. (2016). "maskSLIC: Regional Superpixel Generation with Application to Local Pathology Characterisation in Medical Images". In: *arXiv: Computer Vision and Pattern Recognition*.

Iwana, Brian Kenji and Seiichi Uchida (2021). "An empirical survey of data augmentation for time series classification with neural networks". In: *PLOS ONE*, 16.7. Ed. by Friedhelm Schwenker, e0254841.

Jackson, Hasan and Stephen D. Prince (2016). "Degradation of net primary production in a semiarid rangeland". In: *Biogeosciences*, 13, pp. 4721–4734.

Jansen, Vincent S., Crystal A. Kolden, and Heidi J. Schmalz (2018). "The Development of Near Real-Time Biomass and Cover Estimates for Adaptive Rangeland Management Using Landsat 7 and Landsat 8 Surface Reflectance Products". In: *Remote Sensing*, 10, p. 1057.

Jia, Wenxiao, Min Liu, Duoduo Wang, Honglin He, Pei li Shi, Yingnian Li, and Yanfen Wang (2018). "Uncertainty in simulating regional gross primary productivity from satellite-based models over northern China grassland". In: *Ecological Indicators*, 88, pp. 134–143.

Jia, Xiaoxu, Baoni Xie, Mingan Shao, and Chunlei Zhao (2015). "Primary Productivity and Precipitation-Use Efficiency in Temperate Grassland in the Loess Plateau of China". In: *PLoS ONE*, 10.

Jiang, Yanbin, Jian Tao, Yong qi Huang, Juntao Zhu, Li Tian, and Yang jian Zhang (2015). "The spatial pattern of grassland aboveground biomass on Xizang Plateau and its climatic controls". In: *Journal of Plant Ecology*, 8, pp. 30–40.

Jianlong, Li, Liang Tian-gang, and Chen Quan-gong (1998). "Estimating grassland yields using remote sensing and GIS technologies in China". In: *New Zealand Journal of Agricultural Research*, 41, pp. 31–38.

Jiao, Xianfeng, Heather McNairn, Jiali Shang, and J. Liu (2010). "The sensitivity of multi-frequency (X, C and L-band) radar backscatter signatures to bio-physical variables (LAI) over corn and soybean fields". In: *International Archives of the Photogrammetry, Remote Sensing and Spatial Information Sciences - ISPRS Archives*, 38, pp. 317–321.

Jin, Jiaxin, Xuanlong Ma, Huai Chen, Han Wang, Xiaoming Kang, Xufeng Wang, Ying Wang, Bin Yong, and Fengsheng Guo (2019). "Grassland production in response to changes in biological metrics over the Tibetan Plateau." In: *The Science of the total environment*, 666, pp. 641–651.

Jin, Yunxiang, Xiuchun Yang, Jianjun Qiu, Jinya Li, Tian Gao, Qiong Wu, Fen Zhao, Hailong Ma, Haida Yu, and Bin Xu (2014). "Remote Sensing-Based Biomass Estimation and Its Spatio-Temporal Variations in Temperate Grassland, Northern China". In: *Remote Sensing*, 6, pp. 1496–1513.

Jobbágy, Esteban G., Osvaldo E. Sala, and José M. Paruelo (2002). "Patterns and controls of primary production in the Patagonian steppe: a remote sensing approach". In: *Ecology*, 83, pp. 307–319.

John, Ranjeet, Jiquan Chen, Vincenzo Giannico, Hogeun Park, Jingfeng Xiao, Gabriela Shirkey, Zutao Ouyang, Changliang Shao, Raffaele Lafortezza, and Jiaguo Qi (2018). "Grassland canopy cover and aboveground biomass in Mongolia and Inner Mongolia: Spatiotemporal estimates and controlling factors". In: *Remote Sensing of Environment*, 213, pp. 34–48.

Jonsson, Per and Lars Eklundh (2002). "Seasonality extraction by function fitting to time-series of satellite sensor data". In: *IEEE Transactions on Geoscience and Remote Sensing*, 40.8, pp. 1824–1832.

JORF (1980). "Arrêté du 28 novembre 1980 relatif à la terminologie de la télédétection aérospatiale". In: *Journal officiel*, n°288 du Jeudi 11 Décembre 1980, pp. 10818–10868.

Ju, Junchang and David P. Roy (2008). "The availability of cloud-free Landsat ETM+ data over the conterminous United States and globally". In: *Remote Sensing of Environment*, 112.3, pp. 1196–1211.

Julien, Yves and José A. Sobrino (2019). "Optimizing and comparing gap-filling techniques using simulated NDVI time series from remotely sensed global data". In: *International Journal of Applied Earth Observation and Geoinformation*, 76, pp. 93 –111.

Justice, Christopher O. and Pierre Hiernaux (1986). "Monitoring the grasslands of the Sahel using NOAA AVHRR data: Niger 1983". In: *International Journal of Remote Sensing*, 7, pp. 1475–1497.

Jönsson, Per and Lars Eklundh (2004). “"TIMESAT—a program for analyzing time-series of satellite sensor data"”. In: *Computers & Geosciences*, 30.8, pp. 833 –845.

Kamilaris, Andreas and Francesc X. Prenafeta-Boldú (2018). “Deep learning in agriculture: A survey”. In: *Computers and Electronics in Agriculture*, 147, pp. 70 –90.

Kamir, Elisa, François Waldner, and Zvi Hochman (2020). “Estimating wheat yields in Australia using climate records, satellite image time series and machine learning methods”. In: *ISPRS Journal of Photogrammetry and Remote Sensing*, 160, pp. 124 –135.

Kandasamy, S., F. Baret, A. Verger, P. Neveux, and M. Weiss (2013). “A comparison of methods for smoothing and gap filling time series of remote sensing observations; application to MODIS LAI products”. In: *Biogeosciences*, 10.6, pp. 4055–4071.

Kang, S., S. W. Running, M. Zhao, J. S. Kimball, and J. Glassy (2005). “Improving continuity of MODIS terrestrial photosynthesis products using an interpolation scheme for cloudy pixels”. In: *International Journal of Remote Sensing*, 26.8, pp. 1659–1676.

Kath, Jarrod, Andrew F. Le Brocque, Kathryn Reardon-Smith, and Armando Apan (2019). “Remotely sensed agricultural grassland productivity responses to land use and hydro-climatic drivers under extreme drought and rainfall”. In: *Agricultural and Forest Meteorology*.

Kavats, Olena, D. A. Khramov, Kateryna Sergieieva, and Volodymyr V. Vasyliev (2019). “Monitoring Harvesting by Time Series of Sentinel-1 SAR Data”. In: *Remote Sensing*, 11, p. 2496.

Kawamura, Kensuke, Tsuyoshi Akiyama, Hiromi Yokota, Michio Tsutsumi, Taisuke Yasuda, Osamu Watanabe, and Shiping Wang (2005a). “Comparing MODIS vegetation indices with AVHRR NDVI for monitoring the forage quantity and quality in Inner Mongolia grassland, China”. In: *Grassland Science*, 51, pp. 33–40.

— (2005b). “Quantifying grazing intensities using geographic information systems and satellite remote sensing in the Xilingol steppe region, Inner Mongolia, China”. In: *Agriculture, Ecosystems & Environment*, 107, pp. 83–93.

Kellogg, Elizabeth A. (2015). *Flowering Plants. Monocots : Poaceae*. Springer International Publishing, 752 pp.

Kendall, Alex and Yarin Gal (2017). “What Uncertainties Do We Need in Bayesian Deep Learning for Computer Vision?” In: *Proceedings of the 31st International Conference on Neural Information Processing Systems*. NIPS’17. Long Beach, California, USA: Curran Associates Inc., 5580–5590.

Kendall, Alex, Yarin Gal, and Roberto Cipolla (2018). “Multi-task Learning Using Uncertainty to Weigh Losses for Scene Geometry and Semantics”. In: *2018 IEEE/CVF Conference on Computer Vision and Pattern Recognition*, pp. 7482–7491.

Kennedy, Robert E, Zhiqiang Yang, and Warren B Cohen (2010). “Detecting trends in forest disturbance and recovery using yearly Landsat time series: 1. LandTrendr—Temporal segmentation algorithms”. In: *Remote Sensing of Environment*, 114.12, pp. 2897–2910.

Killick, Rebecca, Paul Fearnhead, and Idris A. Eckley (2012). “Optimal Detection of Changepoints With a Linear Computational Cost”. In: *Journal of the American Statistical Association*, 107.500, pp. 1590–1598.

Kingma, Diederik P. and Jimmy Ba (2017). *Adam: A Method for Stochastic Optimization*.

Kittler, Josef (1983). “On the accuracy of the Sobel edge detector”. In: *Image and Vision Computing*, 1.1, pp. 37–42.

Kloucek, Tomás, David Moravec, Jan Komárek, Ondřej Lagner, and Premysl Stych (2018). “Selecting appropriate variables for detecting grassland to cropland changes using high resolution satellite data”. In: *PeerJ*, 6.

Knyazikhin, Yuri, Mitchell A. Schull, Pauline Stenberg, Matti Mõttus, Miina Rautiainen, Yan Yang, Alexander Marshak, Pedro Latorre Carmona, Robert K. Kaufmann, Philip Lewis, Mathias I. Disney, Vern Vanderbilt, Anthony B. Davis, Frédéric Baret, Stéphane Jacquemoud, Alexei Lyapustin, and Ranga B. Myneni (2013).

"Hyperspectral remote sensing of foliar nitrogen content". In: *Proceedings of the National Academy of Sciences*, 110.3, E185–E192.

Kogan, Felix N., R. Stark, Anatoly A. Gitelson, L. Jargalsaikhan, C. Dugrajav, and Sh. Tsooj (2004). "Derivation of pasture biomass in Mongolia from AVHRR-based vegetation health indices". In: *International Journal of Remote Sensing*, 25, pp. 2889 –2896.

Kolecka, Natalia, Christian Ginzler, Robert Pazur, Bronwyn Price, and Peter H. Verburg (2018). "Regional Scale Mapping of Grassland Mowing Frequency with Sentinel-2 Time Series". In: *Remote Sensing*, 10.8.

Komisarenko, Viacheslav, Kaupo Voormansik, Radwa Elshawi, and Sherif Sakr (2022). "Exploiting time series of Sentinel-1 and Sentinel-2 to detect grassland mowing events using deep learning with reject region". In: *Scientific Reports*, 12.1, p. 983.

Krieger, Gerhard, Konstantinos Panagiotis Papathanassiou, and Shane R. Cloude (2005). "Spaceborne Polarimetric SAR Interferometry: Performance Analysis and Mission Concepts". In: *EURASIP Journal on Advances in Signal Processing*, 2005.20, p. 354018.

Kuenzer, Claudia, Marco Ottinger, Martin Wegmann, Huadong Guo, Changlin Wang, Jianzhong Zhang, Stefan Dech, and Martin Wikelski (2014). "Earth observation satellite sensors for biodiversity monitoring: potentials and bottlenecks". In: *International Journal of Remote Sensing*, 35.18, pp. 6599–6647.

Kurtz, Ditmar Bernardo, Jürgen Schellberg, and Matthias H. Braun (2010). "Ground and satellite based assessment of rangeland management in sub-tropical Argentina". In: *Applied Geography*, 30, pp. 210–220.

Lakshminarayanan, Balaji, Alexander Pritzel, and Charles Blundell (2017). "Simple and Scalable Predictive Uncertainty Estimation Using Deep Ensembles". In: *Proceedings of the 31st International Conference on Neural Information Processing Systems*. NIPS'17. Long Beach, California, USA: Curran Associates Inc., 6405–6416.

Lamy, Jérôme and Arnaud Saint-Martin (2013). "Faire politique d'un système d'observation de la Terre : l'élaboration du programme européen Copernicus/GMES (Global monitoring for environment and security)". FR. In: *L'Année sociologique*, 63.2, pp. 429–472.

Lara, Bruno and Marcelo Gandini (2016). "Assessing the performance of smoothing functions to estimate land surface phenology on temperate grassland". In: *International Journal of Remote Sensing*, 37.8, pp. 1801–1813.

Lathuilière, Sté, Pablo Mesejo, Xavier Alameda-Pineda, and Radu Horaud (2019). "A Comprehensive Analysis of Deep Regression". In: *IEEE Transactions on Pattern Analysis and Machine Intelligence*, 42.9, pp. 2065–2081.

Le Quéré, C., R. J. Andres, T. Boden, T. Conway, R. A. Houghton, J. I. House, G. Marland, G. P. Peters, G. R. van der Werf, A. Ahlström, R. M. Andrew, L. Bopp, J. G. Canadell, P. Ciais, S. C. Doney, C. Enright, P. Friedlingstein, C. Huntingford, A. K. Jain, C. Jourdain, E. Kato, R. F. Keeling, K. Klein Goldewijk, S. Levis, P. Levy, M. Lomas, B. Poulter, M. R. Raupach, J. Schwinger, S. Sitch, B. D. Stocker, N. Viovy, S. Zaehle, and N. Zeng (2013). "The global carbon budget 1959–2011". In: *Earth System Science Data*, 5.1, pp. 165–185.

LeCun, Yann, Yoshua Bengio, and Geoffrey Hinton (2015). "Deep learning". In: *Nature*, 521.7553, pp. 436–444.

Lee, J. S., L. Jurkevich, P. Dewaele, P. Wambacq, and A. Oosterlinck (1994). "Speckle filtering of synthetic aperture radar images: A review". In: *Remote Sensing Reviews*, 8.4, pp. 313–340.

Lei, Guangbin, Ainong Li, Zhengjian Zhang, Jinhu Bian, Guyue Hu, Changbo Wang, Xi Nan, Jiyan Wang, Jianbo Tan, and Xiaohan Liao (2020). "The Quantitative Estimation of Grazing Intensity on the Zoige Plateau Based on the Space-Air-Ground Integrated Monitoring Technology". In: *Remote Sensing*, 12.9.

Leimgruber, Peter, William J. McShea, Christopher J. Brookes, Lhamsuren Bolor-Erdene, Chris Wemmer, and Chris J. Larson (2001). "Spatial patterns in relative primary productivity and gazelle migration in the Eastern Steppes of Mongolia". In: *Biological Conservation*, 102, pp. 205–212.

Lepot, Mathieu, Jean-Baptiste Aubin, and François H.L.R. Clemens (2017). "Interpolation in Time Series: An Introductive Overview of Existing Methods, Their Performance Criteria and Uncertainty Assessment". In: *Water*, 9.10.

Li, Fa, Zhipeng Gui, Zhaoyu Zhang, Dehua Peng, Siyu Tian, Kunxiaojia Yuan, Yunzeng Sun, Huayi Wu, Jianya Gong, and Yichen Lei (2020a). "A hierarchical temporal attention-based LSTM encoder-decoder model for individual mobility prediction". In: *Neurocomputing*, 403, pp. 153–166.

Li, Fei, Jiquan Chen, Yi cheng Zeng, Bin Wu, and Xuelei Zhang (2017). "Renewed Estimates of Grassland Aboveground Biomass Showing Drought Impacts". In: *Journal of Geophysical Research*, 123, pp. 138–148.

Li, Fei, Lei Jiang, Xufeng Wang, Xiaoqiang Zhang, Jiajia Zheng, and Qianjun Zhao (2013a). "Estimating grassland aboveground biomass using multitemporal MODIS data in the West Songnen Plain, China". In: *Journal of Applied Remote Sensing*, 7.

Li, Fei, Jiajia Zheng, Hao Wang, Juhua Luo, Yingming Zhao, and R Zhao (2016). "Mapping grazing intensity using remote sensing in the Xilingol steppe region, Inner Mongolia, China". In: *Remote Sensing Letters*, 7, pp. 328 –337.

Li, Nan, Pei Zhan, Yaozhong Pan, Xiufang Zhu, Muyi Li, and Dujuan Zhang (2020b). "Comparison of Remote Sensing Time-Series Smoothing Methods for Grassland Spring Phenology Extraction on the Qinghai–Tibetan Plateau". In: *Remote Sensing*, 12.20.

Li, Tong, Lizhen Cui, Zhihong Xu, Ronghai Hu, Pawan Joshi, Xiufang Song, Li Tang, Anquan Xia, Yanfen Wang, Da Guo, Jiapei Zhu, Yanbin Hao, Lan Song, and Xiaoyong Cui (2021). "Quantitative Analysis of the Research Trends and Areas in Grassland Remote Sensing: A Scientometrics Analysis of Web of Science from 1980 to 2020". In: *Remote Sensing*, 13, p. 1279.

Li, Yingchang, Mingyang Li, Chao Li, and Zhenzhen Liu (2020c). "Forest aboveground biomass estimation using Landsat 8 and Sentinel-1A data with machine learning algorithms". In: *Scientific Reports*, 10.1, p. 9952.

Li, Zhe, Ted Huffman, Brian McConkey, and Lawrence Townley-Smith (2013b). "Monitoring and modeling spatial and temporal patterns of grassland dynamics using time-series MODIS NDVI with climate and stocking data". In: *Remote Sensing of Environment*, 138, pp. 232–244.

Liang, Tiangang, Shuxia Yang, Qisheng Feng, Baokang Liu, Renping Zhang, Xiaodong Huang, and Hongjie Xie (2016). "Multi-factor modeling of above-ground biomass in alpine grassland: A case study in the Three-River Headwaters Region, China". In: *Remote Sensing of Environment*, 186, pp. 164–172.

Lim, Bryan, Sercan Ö. Arık, Nicolas Loeff, and Tomas Pfister (2021). "Temporal Fusion Transformers for interpretable multi-horizon time series forecasting". In: *International Journal of Forecasting*, 37.4, pp. 1748–1764.

Linnainmaa, Seppo (1976). "Taylor expansion of the accumulated rounding error". In: *BIT Numerical Mathematics*, 16, pp. 146–160.

Liu, Dong C. and Jorge Nocedal (1989). "On the limited memory BFGS method for large scale optimization". In: *Mathematical Programming*, 45.1, pp. 503–528.

Liu, H., P. Gong, J. Wang, N. Clinton, Y. Bai, and S. Liang (2020a). "Annual dynamics of global land cover and its long-term changes from 1982 to 2015". In: *Earth System Science Data*, 12.2, pp. 1217–1243.

Liu, Han, Randy A. Dahlgren, Royce E. Larsen, Scott M. Devine, Leslie M. Roche, Anthony T. OǴeen, Andy J. Y. Wong, Sarah Covello, and Yufang Jin (2019). "Estimating Rangeland Forage Production Using Remote Sensing Data from a Small Unmanned Aerial System (sUAS) and PlanetScope Satellite". In: *Remote Sensing*, 11, p. 595.

Liu, Jianhong, Clement Atzberger, Xin Huang, Kejian Shen, Yongmei Liu, and Lei Wang (2020b). "Modeling grass yields in Qinghai Province, China, based on MODIS NDVI data-an empirical comparison". In: *Frontiers of Earth Science*, 14.2, pp. 413–429.

Liu, Shiliang, Xu kun Su, Shi kui Dong, Fangyan Cheng, Haidi Zhao, Xiaoyu Wu, Xiang Kui Zhang, and Junran Li (2015). "Modeling aboveground biomass of an alpine desert grassland with SPOT-VGT NDVI". In: *GIScience & Remote Sensing*, 52, pp. 680 –699.

Liu, Zhong (2015). "Comparison of precipitation estimates between Version 7 3-hourly TRMM Multi-Satellite Precipitation Analysis (TMPA) near-real-time and research products". In: *Atmospheric Research*, 153, pp. 119–133.

Lobert, Felix, Ann-Kathrin Holtgrave, Marcel Schwieder, Marion Pause, Juliane Vogt, Alexander Gocht, and Stefan Erasmi (2021). "Mowing event detection in permanent grasslands: Systematic evaluation of input features from Sentinel-1, Sentinel-2, and Landsat 8 time series". In: *Remote Sensing of Environment*, 267, p. 112751.

Long, Yushan, Zengkui Li, Liu Wei, and Zhou Hua-kun (2010). "Using Remote Sensing and GIS Technologies to Estimate Grass Yield and Livestock Carrying Capacity of Alpine Grasslands in Golog Prefecture, China". In: *Pedosphere*, 20, pp. 342–351.

Lopes, Mailys, Mathieu Fauvel, Stéphane Girard, and David Sheeren (2017). "Object-Based Classification of Grasslands from High Resolution Satellite Image Time Series Using Gaussian Mean Map Kernels". In: *Remote Sensing*, 9, p. 688.

Luo, Yanyun, Xixi Wang, Fengling Li, Ruizhong Gao, Limin Duan, and Tingxiang Liu (2014). "Responses of Grass Production to Precipitation in a Mid-Latitude Typical Steppe Watershed". In: *Transactions of the ASABE*, 57, pp. 1595–1610.

Luyssaert, Sebastiaan, Mathilde Jammet, Paul C. Stoy, Stephan Estel, Julia Pongratz, Eric Ceschia, Galina Churkina, Axel Don, KarlHeinz Erb, Morgan Ferlicoq, Bert Gielen, Thomas Grünwald, Richard A. Houghton, Katja Klumpp, Alexander Knohl, Thomas Kolb, Tobias Kuemmerle, Tuomas Laurila, Annalea Lohila, Denis Loustau, Matthew J. McGrath, Patrick Meyfroidt, Eddy J. Moors, Kim Naudts, Kim Novick, Juliane Otto, Kim Pilegaard, Casimiro A. Pio, Serge Rambal, Corinna Rebmann, James Ryder, Andrew E. Suyker, Andrej Varlagin, Martin Wattenbach, and A. Johannes Dolman (2014). "Land management and land-cover change have impacts of similar magnitude on surface temperature". In: *Nature Climate Change*, 4.5, pp. 389–393.

López-Puigdollers, Dan, Gonzalo Mateo-García, and Luis Gómez-Chova (2021). "Benchmarking Deep Learning Models for Cloud Detection in Landsat-8 and Sentinel-2 Images". In: *Remote Sensing*, 13.5.

Ma, Qingqing, Linrong Chai, Fujiang Hou, Shenghua Chang, Yushou Ma, Atsushi Tsunekawa, and Yunxiang Cheng (2019). "Quantifying Grazing Intensity Using Remote Sensing in Alpine Meadows on Qinghai-Tibetan Plateau". In: *Sustainability*, 11, p. 417.

MacQueen, James et al. (1967). "Some methods for classification and analysis of multivariate observations". In: *Proceedings of the fifth Berkeley symposium on mathematical statistics and probability*. Vol. 1. 14. Oakland, CA, USA, pp. 281–297.

Magiera, Anja, Hannes Feilhauer, Rainer Waldhardt, Martin Wiesmair, and Annette Otte (2017). "Modelling biomass of mountainous grasslands by including a species composition map". In: *Ecological Indicators*, 78, pp. 8–18.

Mahajan, Seema and Bhavin Fataniya (2020). "Cloud detection methodologies: variants and development—a review". In: *Complex & Intelligent Systems*, 6.2, pp. 251–261.

Main-Knorn, Magdalena, Bringfried Pflug, Jerome Louis, Vincent Debaecker, Uwe Müller-Wilm, and Ferran Gascon (2017). "Sen2Cor for Sentinel-2". In: *Image and Signal Processing for Remote Sensing XXIII*. Ed. by Lorenzo Bruzzone. Vol. 10427. International Society for Optics and Photonics. SPIE, pp. 37 –48.

Mallet, Clément and Frédéric Bretar (2009). "Full-waveform topographic lidar: State-of-the-art". In: *ISPRS Journal of Photogrammetry and Remote Sensing*, 64.1, pp. 1–16.

Mallet, Clément and Arnaud Le Bris (2020). "Current challenges in operational very high resolution land-cover mapping". In: *The International Archives of the Photogrammetry, Remote Sensing and Spatial Information Sciences*, XLIII-B2-2020.

Mansour, Khalid, Onisimo Mutanga, Elhadi Adam, and Elfatih M. Abdel-Rahman (2016). "Multispectral remote sensing for mapping grassland degradation using the key indicators of grass species and edaphic factors". In: *Geocarto International*, 31.5, pp. 477–491.

Mao, Dehua, Zongming Wang, Lin Li, and Wenhong Ma (2014). "Spatiotemporal dynamics of grassland aboveground net primary productivity and its association with climatic pattern and changes in Northern China". In: *Ecological Indicators*, 41, pp. 40–48.

Mardian, Jacob, Aaron A. Berg, and Bahram Daneshfar (2021). "Evaluating the temporal accuracy of grassland to cropland change detection using multitemporal image analysis". In: *Remote Sensing of Environment*, 255, p. 112292.

Marr, D., E. Hildreth, and Sydney Brenner (1980). "Theory of edge detection". In: *Proceedings of the Royal Society of London. Series B. Biological Sciences*, 207.1167, pp. 187–217.

Marsett, Robert C., Jiaguo Qi, Philip Heilman, Sharon H. Biedenbender, M. Carolyn Watson, Saud Amer, Mark Weltz, David Goodrich, and Roseann Marsett (2006). "Remote Sensing for Grassland Management in the Arid Southwest". In: *Rangeland Ecology & Management*, 59.5, pp. 530–540.

Martínez-Ferrer, L., M. Piles, and G. Camps-Valls (2020). "Crop Yield Estimation and Interpretability With Gaussian Processes". In: *IEEE Geoscience and Remote Sensing Letters*, pp. 1–5.

Marwaha, R., F. Cawkwell, D. Hennessy, and S. Green (2020). "Machine learning forecasting model for grass yield estimation in Ireland". In: vol. 25, p. 807.

Maselli, Fabio, Giovanni Argenti, Marta Chiesi, Luca Angeli, and Dario Papale (2013). "Simulation of grassland productivity by the combination of ground and satellite data". In: *Agriculture, Ecosystems & Environment*, 165, pp. 163–172.

Mateus, Balduíno César, Mateus Mendes, José Torres Farinha, Rui Assis, and António Marques Cardoso (2021). "Comparing LSTM and GRU Models to Predict the Condition of a Pulp Paper Press". In: *Energies*, 14.21.

McCulloch, Warren S. and Walter Pitts (1943). "A logical calculus of the ideas immanent in nervous activity". In: *The bulletin of mathematical biophysics*, 5.4, pp. 115–133.

McNairn, Heather and Brian Brisco (2004). "The application of C-band polarimetric SAR for agriculture: a review". In: *Canadian Journal of Remote Sensing*, 30.3, pp. 525–542.

Meng, Baoping, Jing Ge, Tiangang Liang, Shuxia Yang, Jinglong Gao, Qisheng Feng, X. Cui, Xiaodong Huang, and Hongjie Xie (2017). "Evaluation of Remote Sensing Inversion Error for the Above-Ground Biomass of Alpine Meadow Grassland Based on Multi-Source Satellite Data". In: *Remote Sensing*, 9, p. 372.

Meng, Chunlei and Huoqing Li (2019). "Assimilating Satellite Land Surface States Data from Fengyun-4A". In: *Scientific Reports*, 9.1, p. 19567.

Meraner, Andrea, Patrick Ebel, Xiao Xiang Zhu, and Michael Schmitt (2020). "Cloud removal in Sentinel-2 imagery using a deep residual neural network and SAR-optical data fusion". In: *ISPRS Journal of Photogrammetry and Remote Sensing*, 166, pp. 333 –346.

Mercier, Audrey, Julie Betbeder, Sébastien Rapinel, Nicolas Jegou, Jacques Baudry, and Laurence Hubert-Moy (2020). "Evaluation of Sentinel-1 and -2 time series for estimating LAI and biomass of wheat and rapeseed crop types". In: *Journal of Applied Remote Sensing*, 14.2, pp. 1 –21.

Meroni, Michele, Raphaël d'Andrimont, Anton Vrieling, Dominique Fasbender, Guido Lemoine, Felix Rembold, Lorenzo Seguini, and Astrid Verhegghen (2021). "Comparing land surface phenology of major European crops as derived from SAR and multispectral data of Sentinel-1 and-2". In: *Remote sensing of environment*, 253, p. 112232.

Meshesha, Derege Tsegaye, Muhyadin Mohammed Ahmed, Dahir Yosuf Abdi, and Nigussie Haregeweyn (2020). "Prediction of grass biomass from satellite imagery in Somali regional state, eastern Ethiopia". In: *Heliyon*, 6.10, e05272.

Mestre-Quereda, Alejandro, Juan M. Lopez-Sanchez, Fernando Vicente-Guijalba, Alexander W. Jacob, and Marcus E. Engdahl (2020). "Time-Series of Sentinel-1 Interferometric Coherence and Backscatter for Crop-Type Mapping". In: *IEEE Journal of Selected Topics in Applied Earth Observations and Remote Sensing*, 13, pp. 4070–4084.

Michalk, David L., David R. Kemp, Warwick B. Badgery, Jianping Wu, Yingjun Zhang, and Paul J. Thomassin (2019). "Sustainability and future food security—A global perspective for livestock production". In: *Land Degradation & Development*, 30.5, pp. 561–573.

Mohite, Jay, Suryakant Sawant, Ankur Pandit, and Srinivasu Pappula (2020). "Investigating the performance of Random Forest and Support Vector Regression for estimation of cloud-free NDVI using Sentinel-1 SAR data". In: *ISPRS - International Archives of the Photogrammetry, Remote Sensing and Spatial Information Sciences*, XLIII-B3-2020, pp. 1379–1383.

Mooney, H. and P. Ehrlich (1997). "Ecosystem services: A fragmentary history". In: *Nature's Services. Societal Dependence on Natural Ecosystems*.

Moreau, Sophie, Roland Bosseno, Xing fa Gu, and Frédéric Baret (2003). "Assessing the biomass dynamics of Andean bofedal and totora high-protein wetland grasses from NOAA/AVHRR". In: *Remote Sensing of Environment*, 85, pp. 516–529.

Moreno, Álvaro, Francisco Javier García-Haro, Beatriz Martínez, and María Amparo Gilabert (2014). "Noise Reduction and Gap Filling of fAPAR Time Series Using an Adapted Local Regression Filter". In: *Remote Sensing*, 6.9, pp. 8238–8260.

Moreno-Martínez, Álvaro, Emma Izquierdo-Verdiguier, Marco P. Maneta, Gustau Camps-Valls, Nathaniel Robinson, Jordi Muñoz-Marí, Fernando Sedano, Nicholas Clinton, and Steven W. Running (2020). "Multispectral high resolution sensor fusion for smoothing and gap-filling in the cloud". In: *Remote sensing of environment*, 247, pp. 111901–111901.

Motta, Jaíza, César Encina, Eliane Guaraldo, Ariadne Barbosa Goncalves, Roberto Gamarra, and Antonio Paranhos Filho (2021). "Analysis of the degree of grassland degradation using remote sensing". In: *Caminhos de Geografia*, 22, pp. 201–219.

Munyati, Christopher and D. Makgale (2009). "Multitemporal Landsat TM imagery analysis for mapping and quantifying degraded rangeland in the Bahurutshe communal grazing lands, South Africa". In: *International Journal of Remote Sensing*, 30, pp. 3649 –3668.

Myrgiotis, Vasileios, Thomas Luke Smallman, and Mathew Williams (2021). "The carbon budget of the managed grasslands of Great Britain constrained by earth observations". In: *Biogeosciences Discussions*, 2021, pp. 1–35.

Na, Yin tai, Jinxia Li, Buho Hoshino, Saixialt Bao, Fu ying Qin, and P. Myagmartseren (2018). "Effects of Different Grazing Systems on Aboveground Biomass and Plant Species Dominance in Typical Chinese and Mongolian Steppes". In: *Sustainability*, 10, p. 4753.

Nadon, Brian and Scott Jackson (2020). "Chapter Seven - The polyploid origins of crop genomes and their implications: A case study in legumes". In: ed. by Donald L. Sparks. Vol. 159. Academic Press, pp. 275–313.

Nagler, Thomas, Helmut Rott, Elisabeth Ripper, Gabriele Bippus, and Markus Hetzenecker (2016). "Advancements for Snowmelt Monitoring by Means of Sentinel-1 SAR". In: *Remote Sensing*, 8.4.

Nasrallah, Ali, Nicolas Baghdadi, Mohammad El Hajj, Talal Darwish, Hatem Belhouchette, Ghaleb Faour, Salem Darwich, and Mario Mhawej (2019). "Sentinel-1 Data for Winter Wheat Phenology Monitoring and Mapping". In: *Remote Sensing*, 11.19.

Ndikumana, Emile, Dinh Ho Tong Minh, Nicolas Baghdadi, Dominique Courault, and Laure Hossard (2018). "Deep Recurrent Neural Network for Agricultural Classification using multitemporal SAR Sentinel-1 for Camargue, France". In: *Remote Sensing*, 10.8.

Niblack, Wayne (1985). *An Introduction to Digital Image Processing*. DNK: Strandberg Publishing Company.

Nickmilder, Charles, Anthony Tedde, Isabelle Dufrasne, Françoise Lessire, Bernard Tychon, Yannick Curnel, Jérome Bindelle, and Hélene Soyeurt (2021). "Development of Machine Learning Models to Predict Compressed Sward Height in Walloon Pastures Based on Sentinel-1, Sentinel-2 and Meteorological Data Using Multiple Data Transformations". In: *Remote Sensing*, 13.3.

Nicula, Alexandru-Sabin (2019). "Analysis of Changes in Grassland Surfaces in Mountain Areas Assisted by Remote Sensing and GIS". In.

Nock, R. and F. Nielsen (2004). "Statistical region merging". In: *IEEE Transactions on Pattern Analysis and Machine Intelligence*, 26.11, pp. 1452–1458.

Numata, Izaya, Dar A. Roberts, Oliver A. Chadwick, Joshua P. Schimel, Fernando Antônio Rebouças Sampaio, Francisco das Chagas Leonidas, and João Vianei Soares (2007). "Characterization of pasture biophysical properties and the impact of grazing intensity using remotely sensed data". In: *Remote Sensing of Environment*, 109, pp. 314–327.

O'Hara, Rob, Mohamed Saadeldin, Jesko Zimmermann, Stuart Green, John Finn, Brian MacNamee, Kevin McGuinness, and Noel O'Connor (2021). "Mapping grassland management and habitats with satellite and ground level imagery through machine learning". In: vol. 26, p. 231.

O'Mara, Frank P. (2012). "The role of grasslands in food security and climate change". In: *Annals of Botany*, 110.6, pp. 1263–1270.

Otgonbayar, Munkhdulam, Clement Atzberger, Jonathan Chambers, and Amarsaikhan Damdinsuren (2019). "Mapping pasture biomass in Mongolia using Partial Least Squares, Random Forest regression and Landsat 8 imagery". In: *International Journal of Remote Sensing*, 40, pp. 3204 –3226.

Otsu, Nobuyuki (1979). "A Threshold Selection Method from Gray-Level Histograms". In: *IEEE Transactions on Systems, Man, and Cybernetics*, 9.1, pp. 62–66.

Palmer, Anthony R., Alan Short, and Isa A. M. Yunusa (2010). "Biomass production and water use efficiency of grassland in KwaZulu-Natal, South Africa". In: *African Journal of Range & Forage Science*, 27, pp. 163 –169.

Parente, Leandro, Vinícius Mesquita, Fausto Miziara, Luis Baumann, and Laerte Ferreira (2019). "Assessing the pasturelands and livestock dynamics in Brazil, from 1985 to 2017: A novel approach based on high spatial resolution imagery and Google Earth Engine cloud computing". In: *Remote Sensing of Environment*, 232, p. 111301.

Paruelo, José M., Martin Oesterheld, Carlos M. Di Bella, Martin Arzadum, J.R.C. Lafontaine, Miguel Cahuepé, and Cesar M. Rebella (2000). "Estimation of primary production of subhumid rangelands from remote sensing data". In: *Applied Vegetation Science*, 3, pp. 189–195.

Paudel, Keshav Prasad and Per-Øivin Berg Andersen (2010). "Assessing rangeland degradation using multi temporal satellite images and grazing pressure surface model in Upper Mustang, Trans Himalaya, Nepal". In: *Remote Sensing of Environment*, 114, pp. 1845–1855.

Pausas, Juli G. and William J. Bond (2019). "Humboldt and the reinvention of nature". In: *Journal of Ecology*, 107.3, pp. 1031–1037.

Pazúr, R., N. Huber, D. Weber, C. Ginzler, and B. Price (2021). "A national extent map of cropland and grassland for Switzerland based on Sentinel-2 data". In: *Earth System Science Data Discussions*, 2021, pp. 1–14.

Pelletier, Charlotte, Silvia Valero, Jordi Inglada, Nicolas Champion, and Gérard Dedieu (2016). "Assessing the robustness of Random Forests to map land cover with high resolution satellite image time series over large areas". In: *Remote Sensing of Environment*, 187, pp. 156–168.

PEPS, CNES (2021). *French Platform for Sentinel Product*. URL: https://peps.cnes.fr/ (visited on 06/10/2021).

Peratoner, G., F. Greifeneder, M. Castelli, A. Crespi, P.J. Zellner, A. Vianello, M. Morlacchi, L. Pasolli, P. Bartkowiak, C. Notarnicola, R. Monsorno, and M. Zebisch (2021). "Evaluation of a grassland drought index based on LAI from remote sensing and meteorological data". In: *Grassland Science in Europe, 21th EGF symposium 2021 : Sensins - New Insights into Grassland Science and Practice*, 26, p. 231.

Perissin, Daniele and Teng Wang (2012). "Repeat-Pass SAR Interferometry With Partially Coherent Targets". In: *IEEE Transactions on Geoscience and Remote Sensing*, 50.1, pp. 271–280.

Petermann, Jana S. and Oksana Y. Buzhdygan (2021). "Grassland biodiversity". In: *Current Biology*, 31.19, R1195–R1201.

Piao, Shilong, Jingyun Fang, Liming Zhou, Kun Tan, and Shu Tao (2007). "Changes in biomass carbon stocks in Chinaś grasslands between 1982 and 1999". In: *Global Biogeochemical Cycles*, 21.

Picard, Ghislain, Thuy Le Toan, and Francesco Mattia (2003). "Understanding C-band radar backscatter from wheat canopy using a multiple-scattering coherent model". In: *IEEE Transactions on Geoscience and Remote Sensing*, 41.7, pp. 1583–1591.

Piñeiro, Gervasio, Martin Oesterheld, and José M. Paruelo (2005). "Seasonal Variation in Aboveground Production and Radiation-use Efficiency of Temperate rangelands Estimated through Remote Sensing". In: *Ecosystems*, 9, pp. 357–373.

Pipia, Luca, Jordi Muñoz-Marí, Eatidal Amin, Santiago Belda, Gustau Camps-Valls, and Jochem Verrelst (2019). "Fusing optical and SAR time series for LAI gap filling with multioutput Gaussian processes". In: *Remote Sensing of Environment*, 235, p. 111452.

Plummer, Stephen, Pascal Lecomte, and Mark Doherty (2017). "The ESA Climate Change Initiative (CCI): A European contribution to the generation of the Global Climate Observing System". In: *Remote Sensing of Environment*, 203. Earth Observation of Essential Climate Variables, pp. 2–8.

Porter, Tucker Fredrick., Chengci Chen, John A. Long, Rick L. Lawrence, and Bok F. Sowell (2014). "Estimating biomass on CRP pastureland: A comparison of remote sensing techniques". In: *Biomass & Bioenergy*, 66, pp. 268–274.

Poschlod, Peter, André Baumann, and Petr Karlik (2009). "Origin and development of grasslands in Central Europe". In: *Grasslands in Europe of high nature value*. Leiden, The Netherlands: KNNV Publishing, pp. 15 –25.

Potin, P., B. Rosich, N. Miranda, P. Grimont, I. Shurmer, A. O'Connell, M. Krassenburg, and J. Gratadour (2019). "Copernicus Sentinel-1 Constellation Mission Operations Status". In: *IGARSS 2019 - 2019 IEEE International Geoscience and Remote Sensing Symposium*, pp. 5385–5388.

Powers, Ryan P. and Walter Jetz (2019). "Global habitat loss and extinction risk of terrestrial vertebrates under future land-use-change scenarios". In: *Nature Climate Change*, 9.4, pp. 323–329.

Prata, Fred, V. Caselles, C. Coll, Jose A. Sobrino, and Catherine Ottlé (1995). "Thermal remote sensing of land surface temperature from satellites: Current status and future prospects". In: *Remote Sensing Reviews*, 12.3-4, pp. 175–224.

Prats-Iraola, Pau, Rolf Scheiber, Marc Rodriguez-Cassola, Josef Mittermayer, Steffen Wollstadt, Francesco De Zan, Benjamin Bräutigam, Marco Schwerdt, Andreas Reigber, and Alberto Moreira (2014). "On the Processing of Very High Resolution Spaceborne SAR Data". In: *IEEE Transactions on Geoscience and Remote Sensing*, 52.10, pp. 6003–6016.

Prewitt, Judith M. S. (1970). "Object enhancement and extraction". In: *Picture Processing and. Psychopictorics*.

Punalekar, Suvarna, Anne Verhoef, Tristan Quaife, David Humphries, Louise Bermingham, and Christopher Reynolds (2018). "Application of Sentinel-2A data for pasture biomass monitoring using a physically based radiative transfer model". In: *Remote Sensing of Environment*, 218, pp. 207–220.

Qamer, Faisal Mueen, Chen Xi, Sawaid Abbas, M. S. R. Murthy, Wu Ning, and Bao Anming (2016). "An Assessment of Productivity Patterns of Grass-Dominated Rangelands in the Hindu Kush Karakoram Region, Pakistan". In: *Sustainability*, 8, pp. 1–15.

Qin, Pengyao, Bin Sun, Zengyuan Li, Zhihai Gao, Yifu Li, Ziyu Yan, and Ting Gao (2021). "Estimation of Grassland Carrying Capacity by Applying High Spatiotemporal Remote Sensing Techniques in Zhenglan Banner, Inner Mongolia, China". In: *Sustainability*, 13.6.

Quan, Xingwen, Binbin He, Marta Yebra, Changming Yin, Zhanmang Liao, Xueting Zhang, and Xing Li (2017). "A radiative transfer model-based method for the estimation of grassland aboveground biomass". In: *Int. J. Appl. Earth Obs. Geoinformation*, 54, pp. 159–168.

Quintana-Seguí, Pere, Patrick Le Moigne, Yves Durand, Eric Martin, Florence Habets, Martine Baillon, Claire Canellas, Laurent Franchisteguy, and Sophie Morel (2008). "Analysis of Near-Surface Atmospheric Variables: Validation of the SAFRAN Analysis over France". In: *Journal of Applied Meteorology and Climatology*, 47.1, pp. 92–107.

Raab, Christoph, Friederike Riesch, Bettina Tonn, Brian W. Barrett, Marcus Meißner, Niko Balkenhol, and Johannes Isselstein (2020). "Target-oriented habitat and wildlife management: estimating forage quantity and quality of semi-natural grasslands with Sentinel-1 and Sentinel-2 data". In: *Remote Sensing in Ecology and Conservation*, 6, pp. 381–398.

Radkowski, A., I. Radkowska, W. Drzewiecki, T. Pirowski, and W. Szewczyk (2021). "Initial evaluation of PlanetScope nanosatellite images applicability for identification of grazed plant communities". In: vol. 26, p. 231.

Ramankutty, Navin, Amato T. Evan, Chad Monfreda, and Jonathan A. Foley (2010). *Global Agricultural Lands: Pastures, 2000*. Palisades, NY.

Ramoelo, Abel, Moses Cho, Renaud Mathieu, Sabelo Madonsela, Ruben van de Kerchove, Zaneta Kaszta, and Eleonore Wolff (2015a). "Monitoring grass nutrients and biomass as indicators of rangeland quality and quantity using random forest modelling and WorldView-2 data". In: *International Journal of Applied Earth Observation and Geoinformation*, 43. Special Issue on "Advances in remote sensing of vegetation function and traits", pp. 43–54.

Ramoelo, Abel, Moses Cho, Renaud Mathieu, and Andrew K. Skidmore (2015b). "Potential of Sentinel-2 spectral configuration to assess rangeland quality". In: *Journal of Applied Remote Sensing*, 9.1, pp. 1 –11.

Raney, Russell K., Tony Freeman, Robert W. Hawkins, and Richard Bamler (1994). "A plea for radar brightness". In: *Proceedings of IGARSS '94 - 1994 IEEE International Geoscience and Remote Sensing Symposium*. Vol. 2, 1090–1092 vol.2.

Reeves, Matt C. and Larry Scott Baggett (2014). "A remote sensing protocol for identifying rangelands with degraded productive capacity". In: *Ecological Indicators*, 43, pp. 172–182.

Reeves, Matt C., Jerome C. Winslow, and Steven W. Running (2001). "Mapping Weekly Rangeland Vegetation Productivity Using MODIS Algorithms". In: *Journal of Range Management*, 54.

Reichstein, Markus, Gustau Camps-Valls, Bjorn Stevens, Martin Jung, Joachim Denzler, Nuno Carvalhais, and Prabhat (2019). "Deep learning and process understanding for data-driven Earth system science". In: *Nature*, 566.7743, pp. 195–204.

Reinermann, Sophie, Sarah Asam, Ursula Gessner, Anne Schucknecht, and Claudia Kuenzer (2021). "Detection of grassland mowing events with optical satellite time series data". In: vol. 26, p. 231.

Reinermann, Sophie, Sarah Asam, and Claudia Kuenzer (2020). "Remote Sensing of Grassland Production and Management—A Review". In: *Remote Sensing*, 12.12.

Reinfelds, Ivars V. (2011). "Monitoring and Assessment of Surface Water Abstractions for Pasture Irrigation from Landsat Imagery: Bega–Bemboka River, NSW, Australia". In: *Water Resources Management*, 25, pp. 2319–2334.

Ren, Hongrui and Gao Feng (2015). "Are soil-adjusted vegetation indices better than soil-unadjusted vegetation indices for above-ground green biomass estimation in arid and semi-arid grasslands?" In: *Grass and Forage Science*, 70, pp. 611–619.

Ren, Xiaofeng and Jitendra Malik (2003). "Learning a classification model for segmentation". In: *Proceedings Ninth IEEE International Conference on Computer Vision*, 10–17 vol.1.

Ricotta, Carlo, Bradley C. Reed, and Larry L. Tieszen (2003). "The role of C3 and C4 grasses to interannual variability in remotely sensed ecosystem performance over the US Great Plains". In: *International Journal of Remote Sensing*, 24, pp. 4421 –4431.

Robinson, Nathaniel P., Matthew O. Jones, Álvaro Moreno, Tyler A. Erickson, David E. Naugle, and Brady W. Allred (2019). "Rangeland Productivity Partitioned to Sub-Pixel Plant Functional Types". In: *Remote Sensing*, 11, p. 1427.

Röder, Achim, Thomas Udelhoven, Joachim Hill, Gabriel del Barrio, and Georgios Tsiourlis (2008). "Trend analysis of Landsat-TM and -ETM+ imagery to monitor grazing impact in a rangeland ecosystem in Northern Greece". In: *Remote Sensing of Environment*, 112, pp. 2863–2875.

Rolf, Esther, Jonathan Proctor, Tamma Carleton, Ian Bolliger, Vaishaal Shankar, Miyabi Ishihara, Benjamin Recht, and Solomon Hsiang (2021). "A generalizable and accessible approach to machine learning with global satellite imagery". In: *Nature Communications*, 12.1, p. 4392.

Rosenblatt, Frank (1958). "The perceptron: A probabilistic model for information storage and organization in the brain." In: *Psychological Review*, 65.6, pp. 386–408.

Rossi, Mattia, Georg Niedrist, Sarah Asam, Giustino Tonon, Enrico Tomelleri, and Marc Zebisch (2019). "A Comparison of the Signal from Diverse Optical Sensors for Monitoring Alpine Grassland Dynamics". In: *Remote Sensing*, 11, p. 296.

Rossi, Mattia, Georg Niedrist, Sarah Asam, Giustino Tonon, and Marc Zebisch (2018). "Optical Responses on Multiple Spatial Scales for Assessing Vegetation Dynamics - A Case Study for Alpine Grasslands". In: *IGARSS 2018 - 2018 IEEE International Geoscience and Remote Sensing Symposium*, pp. 2992–2995.

Rossini, Micol, Sergio Cogliati, Michele Meroni, Mirco Migliavacca, Marta Galvagno, Lorenzo Busetto, Edoardo Cremonese, Tommaso Julitta, Consolata Siniscalco, Umberto Morra di Cella, and Roberto Colombo (2012). "Remote sensing-based estimation of gross primary production in a subalpine grassland". In: *Biogeosciences*, 9, pp. 2565–2584.

Roumiguié, Antoine, Anne Jacquin, Grégoire Sigel, Hervé Poilvé, Olivier Hagolle, and Jean Daydé (2015). "Validation of a Forage Production Index (FPI) Derived from MODIS fCover Time-Series Using High-Resolution Satellite Imagery: Methodology, Results and Opportunities". In: *Remote Sensing*, 7.9, pp. 11525–11550.

Roumiguié, Antoine, Grégoire Sigel, Hervé Poilvé, Bruno Bouchard, Anton Vrieling, and Anne Jacquin (2017). "Insuring forage through satellites: testing alternative indices against grassland production estimates for France". In: *International Journal of Remote Sensing*, 38.7, pp. 1912–1939.

Rouse, J. W. Jr., R. H. Haas, J. A. Schell, and D. W. Deering (1974). "Monitoring vegetation systems in the Great Plains with ERTS". In: *NASA Special Publication*. Vol. 351, p. 309.

Roy, David P., Junchang Ju, Philip Lewis, Crystal Schaaf, Feng Gao, Matt Hansen, and Erik Lindquist (2008). "Multi-temporal MODIS–Landsat data fusion for relative radiometric normalization, gap filling, and prediction of Landsat data". In: *Remote Sensing of Environment*, 112.6, pp. 3112 –3130.

Rudant, Jean-Paul and Pierre-Louis Frison (2019). "Télédétection radar : de l'image d'intensité initiale au choix du mode de calibration des coefficients de diffusion beta 0, sigma 0, gamma 0". In: *Revue Française de Photogrammétrie et de Télédétection*, 219-220, 19–28.

Rufin, Philippe, Hannes Müller, Dirk Pflugmacher, and Patrick Hostert (2015). "Land use intensity trajectories on Amazonian pastures derived from Landsat time series". In: *Int. J. Appl. Earth Obs. Geoinformation*, 41, pp. 1–10.

Rumelhart, David E. and James L. McClelland (1987). "Learning Internal Representations by Error Propagation". In: *Parallel Distributed Processing: Explorations in the Microstructure of Cognition: Foundations*, pp. 318–362.

Rußwurm, Marc and Marco Körner (2020). "Self-attention for raw optical Satellite Time Series Classification". In: *ISPRS Journal of Photogrammetry and Remote Sensing*, 169, pp. 421 –435.

Rußwurm, Marc, Sherrie Wang, Marco Korner, and David Lobell (2020). "Meta-Learning for Few-Shot Land Cover Classification". In: *2020 IEEE/CVF Conference on Computer Vision and Pattern Recognition Workshops (CVPRW)*. IEEE Computer Society, pp. 788–796.

Sainte Fare Garnot, Vivien, Loic Landrieu, and Nesrine Chehata (2022). "Multi-modal temporal attention models for crop mapping from satellite time series". In: *ISPRS Journal of Photogrammetry and Remote Sensing*, 187, pp. 294–305.

Sainte Fare Garnot, Vivien, Loic Landrieu, Sebastien Giordano, and Nesrine Chehata (2020). "Satellite Image Time Series Classification with Pixel-Set Encoders and Temporal Self-Attention". In: *Proceedings of the IEEE/CVF Conference on Computer Vision and Pattern Recognition*, pp. 12325–12334.

Sakoe, Hiroaki and Seibi Chiba (1990). "Dynamic programming algorithm optimization for spoken word recognition". In: *IEEE Transactions on Acoustics, Speech, and Signal Processing*, pp. 159–224.

Salinero-Delgado, Matías, José Estévez, Luca Pipia, Santiago Belda, Katja Berger, Vanessa Paredes Gómez, and Jochem Verrelst (2022). "Monitoring Cropland Phenology on Google Earth Engine Using Gaussian Process Regression". In: *Remote Sensing*, 14.1.

Samrat, Abhishek, Soubadra Devy, and T. Ganesh (2021). "Delineating fragmented grassland patches in the tropical region using multi-seasonal synthetic aperture radar (SAR) and optical satellite images". In: *International Journal of Remote Sensing*, 42.10, pp. 3938–3954.

Sankey, Temuulen Tsagaan, Joel Brown Sankey, Keith T. Weber, and Cliff Montagne (2009). "Geospatial Assessment of Grazing Regime Shifts and Sociopolitical Changes in a Mongolian Rangeland". In: *Rangeland Ecology & Management*, 62.6, pp. 522–530.

Sauvola, Jaakko Jari and Matti Pietikäinen (2000). "Adaptive document image binarization". In: *Pattern Recognition*, 33.2, pp. 225–236.

Scarpa, Giuseppe, Massimiliano Gargiulo, Antonio Mazza, and Raffaele Gaetano (2018). "A CNN-Based Fusion Method for Feature Extraction from Sentinel Data". In: *Remote Sensing*, 10.2.

Schino, Gabriele, Flavio Borfecchia, Luigi De Cecco, Camilla Dibari, Massimo Iannetta, Sandro Martini, and Franco Pedrotti (2003). "Satellite estimate of grass biomass in a mountainous range in central Italy". In: *Agroforestry Systems*, 59.2, pp. 157–162.

Schmidt, Kersten, Marco Schwerdt, Nuno Miranda, and Jens Reimann (2020). "Radiometric Comparison within the Sentinel-1 SAR Constellation over a Wide Backscatter Range". In: *Remote Sensing*, 12.5.

Schmitt, Michael and Xiao Xiang Zhu (2016). "Data Fusion and Remote Sensing: An ever-growing relationship". In: *IEEE Geoscience and Remote Sensing Magazine*, 4.4, pp. 6–23.

Schmitz, Anja and Johannes Isselstein (2020). "Effect of Grazing System on Grassland Plant Species Richness and Vegetation Characteristics: Comparing Horse and Cattle Grazing". In: *Sustainability*, 12.8.

Schucknecht, Anne, Michele Meroni, François Kayitakire, and Amadou Boureima (2017). "Phenology-Based Biomass Estimation to Support Rangeland Management in Semi-Arid Environments". In: *Remote Sensing*, 9, p. 463.

Schuster, Christian, Iftikhar Ali, Peter Lohmann, Annett Frick, Michael Förster, and Birgit Kleinschmit (2011). "Towards Detecting Swath Events in TerraSAR-X Time Series to Establish NATURA 2000 Grassland Habitat Swath Management as Monitoring Parameter". In: *Remote Sensing*, 3, pp. 1308–1322.

Schuster, Christian, Tobias Schmidt, Christopher Conrad, Birgit Kleinschmit, and Michael Förster (2015). "Grassland habitat mapping by intra-annual time series analysis - Comparison of RapidEye and TerraSAR-X satellite data". In: *International Journal of Applied Earth Observation and Geoinformation*, 34, pp. 25–34.

Schuster, Mike and Kuldpi K. Paliwal (1997). "Bidirectional recurrent neural networks". In: *IEEE Transactions on Signal Processing*, 45.11, pp. 2673–2681.

Schwieder, Marcel, Marion Buddeberg, Katja Kowalski, Kira Pfoch, Julia Bartsch, Heike Bach, Jürgen Pickert, and Patrick Hostert (2020). "Estimating Grassland Parameters from Sentinel-2: A Model Comparison Study". In: *PFG - Journal of Photogrammetry, Remote Sensing and Geoinformation Science*, 88.5, pp. 379–390.

Schwieder, Marcel, Maximilian Wesemeyer, David Frantz, Kira Pfoch, Stefan Erasmi, Jürgen Pickert, Claas Nendel, and Patrick Hostert (2021). "Mapping grassland mowing events across Germany based on combined Sentinel-2 and Landsat 8 time series". In: *Remote Sensing of Environment*, 269, p. 112795.

Scurlock, Jonathan M. O. and David O. Hall (1998). "The global carbon sink: a grassland perspective". In: *Global Change Biology*, 4, pp. 229–233.

Seaquist, Jonathan W., Lennart Olsson, and Jonas Ardö (2003). "A remote sensing-based primary production model for grassland biomes". In: *Ecological Modelling*, 169, pp. 131–155.

Selva, Daniel and David Krejci (2012). "A survey and assessment of the capabilities of Cubesats for Earth observation". In: *Acta Astronautica*, 74, pp. 50–68.

Serrano, João, Shakib Shahidian, Luis Paixão, José Marques da Silva, Tiago Morais, Ricardo Teixeira, and Tiago Domingos (2021). "Spatiotemporal Patterns of Pasture Quality Based on NDVI Time-Series in Mediterranean Montado Ecosystem". In: *Remote Sensing*, 13.19.

Shao, Yun, Qingrong Hu, Huadong Guo, Yuan Lu, Qing Dong, and Chunming Han (2003). "Effect of dielectric properties of moist salinized soils on backscattering coefficients extracted from RADARSAT image". In: *IEEE Transactions on Geoscience and Remote Sensing*, 41.8, pp. 1879–1888.

Shaw, Peter, Jakob Uszkoreit, and Ashish Vaswani (2018). "Self-Attention with Relative Position Representations". In: *Proceedings of the 2018 Conference of the North American Chapter of the Association for Computational Linguistics: Human Language Technologies, Volume 2 (Short Papers)*. New Orleans, Louisiana: Association for Computational Linguistics, pp. 464–468.

Shen, H., X. Li, Q. Cheng, C. Zeng, G. Yang, H. Li, and L. Zhang (2015). "Missing Information Reconstruction of Remote Sensing Data: A Technical Review". In: *IEEE Geoscience and Remote Sensing Magazine*, 3.3, pp. 61–85.

Shen, Huanfeng, Xiangchao Meng, and Liangpei Zhang (2016). "An Integrated Framework for the Spatio–Temporal– Spectral Fusion of Remote Sensing Images". In: *IEEE Transactions on Geoscience and Remote Sensing*, 54.12, pp. 7135–7148.

Shewalkar, Apeksha, Deepika Nyavanandi, and Simone Ludwig (2019). "Performance Evaluation of Deep Neural Networks Applied to Speech Recognition: RNN, LSTM and GRU". In: *Journal of Artificial Intelligence and Soft Computing Research*, 9, pp. 235–245.

Shukla, Priyadarshi R., Jim Skea, Eduardo Calvo Buendia, Valérie Masson-Delmotte, Hans-Otto Pörtner, Debra Roberts, Panmao Zhai, Raphael Slade, Sarah Connors, Renée van Diemen, Marion Ferrat, Eamon Haughey, Sigourney Luz, Suvadip Neogi, Minal Pathak, Jan Petzold, Joana Portugal Pereira, Purvi Vyas, Elizabeth Huntley, Katie Kissick, Malek Belkacemi, and (eds.) Juliette Malley (2019). *Climate Change and Land - An IPCC special report on climate change, desertification, land degradation, sustainable land management, food security, and greenhouse gas fluxes in terrestrial ecosystems. Chapter 1: Framing and Context.*

Si, Yali, Martin Schlerf, Raúl Zurita-Milla, Andrew K. Skidmore, and Tiejun Wang (2012). "Mapping spatio-temporal variation of grassland quantity and quality using MERIS data and the PROSAIL model". In: *Remote Sensing of Environment*, 121, pp. 415–425.

Sibanda, Mbulisi, Onisimo Mutanga, and Mathieu Rouget (2016). "Comparing the spectral settings of the new generation broad and narrow band sensors in estimating biomass of native grasses grown under different management practices". In: *GIScience & Remote Sensing*, 53, pp. 614 –633.

— (2017). "Testing the capabilities of the new WorldView-3 space-borne sensor's red-edge spectral band in discriminating and mapping complex grassland management treatments". In: *International Journal of Remote Sensing*, 38, pp. 1 –22.

Siegmund, Robert, Kerstin Grant, Marian Wagner, and Stephan Hartmann (2016). "Satellite-based monitoring of grassland: assessment of harvest dates and frequency using SAR". In: *Remote Sensing for Agriculture, Ecosystems, and Hydrology XVIII*. Ed. by Christopher M. U. Neale and Antonino Maltese. Vol. 9998. International Society for Optics and Photonics. SPIE, pp. 9 –25.

Silva, Carlos Alberto, Sassan Saatchi, Mariano Garcia, Nicolas Labrière, Carine Klauberg, António Ferraz, Victoria Meyer, Kathryn J. Jeffery, Katharine Abernethy, Lee White, Kaiguang Zhao, Simon L. Lewis, and Andrew T. Hudak (2018). "Comparison of Small- and Large-Footprint Lidar Characterization of Tropical Forest Aboveground Structure and Biomass: A Case Study From Central Gabon". In: *IEEE Journal of Selected Topics in Applied Earth Observations and Remote Sensing*, 11.10, pp. 3512–3526.

Silverman, N. L., Brady W. Allred, J Patrick Donnelly, Teresa B. Chapman, Jeremy D. Maestas, Joseph M. Wheaton, Jeff White, and David E. Naugle (2019). "Low-tech riparian and wet meadow restoration increases vegetation productivity and resilience across semiarid rangelands". In: *Restoration Ecology*, 27, pp. 269–278.

Simard, Marc, Naiara Pinto, Joshua B. Fisher, and Alessandro Baccini (2011a). "Mapping forest canopy height globally with spaceborne lidar". In: *Journal of Geophysical Research: Biogeosciences*, 116.G4.

Simard, Marc, Naiara Pinto, Joshua B. Fisher, and Alessandro Baccini (2011b). "Mapping forest canopy height globally with spaceborne lidar". In: *Journal of Geophysical Research: Biogeosciences*, 116.G4.

Singh, Prabhishek and Raj Shree (2016). "Analysis and effects of speckle noise in SAR images". In: *2016 2nd International Conference on Advances in Computing, Communication, Automation (ICACCA)*, pp. 1–5.

Small, David and Adrian Schubert (2019). "Guide to Sentinel-1 Geocoding". In: *University of Zurich. P*, 42.

Smit, Harm J., Marc Metzger, and Frank Ewert (2008). "Spatial distribution of grassland productivity and land use in Europe". In: *Agricultural Systems*, 98.3, pp. 208–219.

Smith, Richard Linn, M. Adams, S. P. Gittins, Steve Gherardi, Duncan Wood, Stefan W. Maier, Richard Stovold, Graham E. Donald, Sarfraz Khohkar, and A. C. B. Allen (2011). "Near real-time Feed On Offer (FOO) from MODIS for early season grazing management of Mediterranean annual pastures". In: *International Journal of Remote Sensing*, 32, pp. 4445 –4460.

Sobrino, José A., Fabio Del Frate, Matthias Drusch, Juan C. Jiménez-Muñoz, Paolo Manunta, and Amanda Regan (2016). "Review of Thermal Infrared Applications and Requirements for Future High-Resolution Sensors". In: *IEEE Transactions on Geoscience and Remote Sensing*, 54.5, pp. 2963–2972.

Solano-Correa, Yady Tatiana, Francesca Bovolo, Lorenzo Bruzzone, and Diego Fernández-Prieto (2020). "A Method for the Analysis of Small Crop Fields in Sentinel-2 Dense Time Series". In: *IEEE Transactions on Geoscience and Remote Sensing*, 58.3, pp. 2150–2164.

Soubry, Irini, Thuy Doan, Thuan Chu, and Xulin Guo (2021). "A Systematic Review on the Integration of Remote Sensing and GIS to Forest and Grassland Ecosystem Health Attributes, Indicators, and Measures". In: *Remote Sensing*, 13, p. 3262.

Spagnuolo, Olivia S.B., Julie C. Jarvey, Michael J. Battaglia, Zachary M. Laubach, Mary Ellen Miller, Kay E. Holekamp, and Laura L. Bourgeau-Chavez (2020). "Mapping Kenyan Grassland Heights Across Large Spatial Scales with Combined Optical and Radar Satellite Imagery". In: *Remote Sensing*, 12.7.

Stendardi, Laura, Stein Rune Karlsen, Georg Niedrist, Renato Gerdol, Marc Zebisch, Mattia Rossi, and Claudia Notarnicola (2019a). "Exploiting Time Series of Sentinel-1 and Sentinel-2 Imagery to Detect Meadow Phenology in Mountain Regions". In: *Remote Sensing*, 11, p. 542.

— (2019b). "Exploiting Time Series of Sentinel-1 and Sentinel-2 Imagery to Detect Meadow Phenology in Mountain Regions". In: *Remote Sensing*, 11, p. 542.

Stumpf, Felix, Manuel K. Schneider, Armin Keller, Andreas Mayr, Tobias Rentschler, Reto G. Meuli, Michael Schaepman, and Frank Liebisch (2020). "Spatial monitoring of grassland management using multi-temporal satellite imagery". In: *Ecological Indicators*, 113, p. 106201.

Stutz, David, Alexander Hermans, and Bastian Leibe (2018). "Superpixels: An evaluation of the state-of-the-art". In: *Computer Vision and Image Understanding*, 166, pp. 1–27.

Sudmanns, Martin, Dirk Tiede, Hannah Augustin, and Stefan Lang (2020a). "Assessing global Sentinel-2 coverage dynamics and data availability for operational Earth observation (EO) applications using the EO-Compass". In: *International Journal of Digital Earth*, 13.7, pp. 768–784.

— (2020b). "Assessing global Sentinel-2 coverage dynamics and data availability for operational Earth observation (EO) applications using the EO-Compass". In: *International Journal of Digital Earth*, 13.7, pp. 768–784.

Sun, Bin, Zeng yuan Li, Zhihai Gao, Zhongyang Guo, Bengyu Wang, Xiaolong Hu, and Lina Bai (2017). "Grassland degradation and restoration monitoring and driving forces analysis based on long time-series remote sensing data in Xilin Gol League". In: *Acta Ecologica Sinica*, 37, pp. 219–228.

Sun, Bin, Zengyuan Li, Wentao Gao, Yuanyuan Zhang, Zhihai Gao, Zhangliang Song, Pengyao Qin, and Xin Tian (2019). "Identification and assessment of the factors driving vegetation degradation / regeneration in drylands using synthetic high spatiotemporal remote sensing Data— A case study in Zhenglanqi, Inner Mongolia, China". In: *Ecological Indicators*, 107, p. 105614.

Sun, Liang, Feng Gao, Donghui Xie, Martha Anderson, Ruiqing Chen, Yun Yang, Yang Yang, and Zhongxin Chen (2021a). "Reconstructing daily 30 m NDVI over complex agricultural landscapes using a crop reference curve approach". In: *Remote Sensing of Environment*, 253, p. 112156.

Sun, Xian, Bing Wang, Zhirui Wang, Hao Li, Hengchao Li, and Kun Fu (2021b). "Research Progress on Few-Shot Learning for Remote Sensing Image Interpretation". In: *IEEE Journal of Selected Topics in Applied Earth Observations and Remote Sensing*, 14, pp. 2387–2402.

Sun, Zheng guo, Xiaohua Long, Chengming Sun, Wei Zhou, Weimin Ju, and Jianlong Li (2013). "Evaluation of net primary productivity and its spatial and temporal patterns in southern China's grasslands". In: *Rangeland Journal*, 35, pp. 331–338.

Suttie, J, S Reynolds, and Caterina Batello (2005). *Grasslands of the World*. Food and Agriculture Organization of the United Nations.

Sćepanović, Sanja, Oleg Antropov, Pekka Laurila, Yrjo Rauste, Vladimir Ignatenko, and Jaan Praks (2021). "Wide-Area Land Cover Mapping With Sentinel-1 Imagery Using Deep Learning Semantic Segmentation Models". In: *IEEE Journal of Selected Topics in Applied Earth Observations and Remote Sensing*, 14, pp. 10357–10374.

Tamm, Tanel, Karlis Zalite, Kaupo Voormansik, and Liina Talgre (2016). "Relating Sentinel-1 Interferometric Coherence to Mowing Events on Grasslands". In: *Remote Sensing*, 8.10.

Tan, Kun, Philippe Ciais, Shilong Piao, Xiaopu Wu, Yanhong Tang, Nicolas Vuichard, Shuang Liang, and Jingyun Fang (2010). "Application of the ORCHIDEE global vegetation model to evaluate biomass and soil carbon stocks of Qinghai-Tibetan grasslands". In: *Global Biogeochemical Cycles*, 24.

Tang, Chuanjiang, Xinyu Fu, Dong Jiang, Jingying Fu, Xinyue Zhang, and Su Zhou (2014). "Simulating Spatiotemporal Dynamics of Sichuan Grassland Net Primary Productivity Using the CASA Model and In Situ Observations". In: *The Scientific World Journal*, 2014.

Tarantino, Cristina, Luigi Forte, Palma Blonda, Saverio Vicario, Valeria Tomaselli, Carl Beierkuhnlein, and Maria Adamo (2021). "Intra-Annual Sentinel-2 Time-Series Supporting Grassland Habitat Discrimination". In: *Remote Sensing*, 13.2.

Taravat, Alireza, Matthias P. Wagner, and Natascha Oppelt (2019). "Automatic Grassland Cutting Status Detection in the Context of Spatiotemporal Sentinel-1 Imagery Analysis and Artificial Neural Networks". In: *Remote Sensing*, 11.6.

TEEB (2010). "The Economics of Ecosystems and Biodiversity: Mainstreaming the Economics of Nature". In: *A synthesis of the approach, conclusions and recommendations of TEEB*.

Telepac, site des téléservices des aides de la PAC (2021). *Cultures et précisions*. URL: https://www.telepac.agriculture.gouv.fr/ (visited on 01/10/2021).

Tiscornia, Guadalupe, Walter E. Baethgen, Andrea Ruggia, Martin Do Carmo, and Pietro Ceccato (2019). "Can we Monitor Height of Native Grasslands in Uruguay with Earth Observation?" In: *Remote Sensing*, 11, p. 1801.

Todd, Stella W., Roger M. Hoffer, and Daniel G. Milchunas (1998). "Biomass estimation on grazed and ungrazed rangelands using spectral indices". In: *International Journal of Remote Sensing*, 19, pp. 427–438.

Toivonen, Tuuli, Miska Toivonen, and Miska Luoto (2003). "Landsat TM images in mapping of semi-natural grasslands and analysing of habitat pattern in an agricultural landscape in south-west Finland". In: *Fennia*, 181.

Tong, Alexander and Yuhong He (2017). "Estimating and mapping chlorophyll content for a heterogeneous grassland: Comparing prediction power of a suite of vegetation indices across scales between years". In: *ISPRS Journal of Photogrammetry and Remote Sensing*, 126, pp. 146–167.

Touzi, Ridha, Armand Lopes, Jérôme Bruniquel, and Paris W. Vachon (1999). "Coherence estimation for SAR imagery". In: *IEEE Transactions on Geoscience and Remote Sensing*, 37.1, pp. 135–149.

Transon, Julie, Raphaël D'Andrimont, Alexandre Maugnard, and Pierre Defourny (2018). "Survey of Hyperspectral Earth Observation Applications from Space in the Sentinel-2 Context". In: *Remote Sensing*, 10.2.

Truong, Charles, Laurent Oudre, and Nicolas Vayatis (2020). "Selective review of offline change point detection methods". In: *Signal Processing*, 167, p. 107299.

Tsai, Ya-Lun, Dietz Andreas, Natascha Oppelt, and Claudia Kuenzer (2019). "Remote Sensing of Snow Cover Using Spaceborne SAR: A Review". In: *Remote Sensing*, 11, p. 1456.

Tsalyuk, Miriam, Maggi Kelly, Kevin Koy, Wayne M. Getz, and H. Scott Butterfield (2015). "Monitoring the Impact of Grazing on Rangeland Conservation Easements Using MODIS Vegetation Indices". In: *Rangeland Ecology & Management*, 68.2, pp. 173–185.

Tucker, Compton J. (1979). "Red and photographic infrared linear combinations for monitoring vegetation". In: *Remote Sensing of Environment*, 8.2, pp. 127–150.

Tucker, Compton J., C. L. Vanpraet, Margaret Sharman, and G. Van Ittersum (1985). "Satellite remote sensing of total herbaceous biomass production in the Senegalese Sahel - 1980-1984". In: *Remote Sensing of Environment*, 17, pp. 233–249.

Ullah, Saleem, Yali Si, Martin Schlerf, Andrew K. Skidmore, Muhammad Shafique, and Irfan Akhtar Iqbal (2012). "Estimation of grassland biomass and nitrogen using MERIS data". In: *International Journal of Applied Earth Observation and Geoinformation*, 19, pp. 196–204.

UN, United Nations (2015). *Transforming our World: the 2030 Agenda for Sustainable Development*. Working Papers. eSocialSciences.

United Nations Office for Outer Space Affairs (UNOOSA) (2021). *Online Index of Objects Launched into Outer Space*. URL: https://www.unoosa.org/oosa/osoindex/search-ng.jspx?lf_id= (visited on 10/10/2021).

United States (1956). *Key to meteorological records documentation*. Washington, D. C: U. S. Dept. of Commerce, Weather Bureau.

Van der Sanden, J.J., P. Budkewitsch, D. Flett, R. Landry, T.I. Lukowski, H. McNairn, T.J. Pultz, V. Singhroy, J. Sokol, R. Touzi, and P.W. Vachon (2001). "Applications potential of planned C-band SAR satellites: leading to Radarsat-2". In: *IGARSS 2001. Scanning the Present and Resolving the Future. Proceedings. IEEE 2001 International Geoscience and Remote Sensing Symposium*. Vol. 1, 488–492 vol.1.

Van Tricht, Kristof, Anne Gobin, Sven Gilliams, and Isabelle Piccard (2018). "Synergistic use of radar Sentinel-1 and optical Sentinel-2 imagery for crop mapping: a case study for Belgium". In: *Remote Sensing*, 10.10, p. 1642.

Vaswani, Ashish, Noam Shazeer, Niki Parmar, Jakob Uszkoreit, Llion Jones, Aidan N. Gomez, Lukasz Kaiser, and Illia Polosukhin (2017). *Attention Is All You Need*.

Veloso, Amanda, Stéphane Mermoz, Alexandre Bouvet, Thuy Le Toan, Milena Planells, Jean-François Dejoux, and Eric Ceschia (2017). "Understanding the temporal behavior of crops using Sentinel-1 and Sentinel-2-like data for agricultural applications". In: *Remote Sensing of Environment*, 199, pp. 415–426.

Venter, Zander S. and Markus A. K. Sydenham (2021). "Continental-Scale Land Cover Mapping at 10 m Resolution Over Europe (ELC10)". In: *Remote Sensing*, 13.12.

Verbesselt, Jan, Rob Hyndman, Glenn Newnham, and Darius Culvenor (2010). "Detecting trend and seasonal changes in satellite image time series". In: *Remote Sensing of Environment*, 114.1, pp. 106–115.

Verde, Natalia, Ioannis P. Kokkoris, Charalampos Georgiadis, Dimitris Kaimaris, Panayotis Dimopoulos, Ioannis Mitsopoulos, and Giorgos Mallinis (2020). "National Scale Land Cover Classification for Ecosystem Services Mapping and Assessment, Using Multitemporal Copernicus EO Data and Google Earth Engine". In: *Remote Sensing*, 12.20.

Verrelst, Jochem, Juan Pablo Rivera, Frank Veroustraete, Jordi Muñoz-Marí, Jan G.P.W. Clevers, Gustau Camps-Valls, and José Moreno (2015). "Experimental Sentinel-2 LAI estimation using parametric, non-parametric and physical retrieval methods – A comparison". In: *ISPRS Journal of Photogrammetry and Remote Sensing*, 108, pp. 260–272.

Vescovo, Loris and Damiano Gianelle (2008). "Using the MIR bands in vegetation indices for the estimation of grassland biophysical parameters from satellite remote sensing in the Alps region of Trentino (Italy)". In: *Advances in Space Research*, 41, pp. 1764–1772.

Vidal, Jean-Philippe, Eric Martin, Laurent Franchistéguy, Martine Baillon, and Jean-Michel Soubeyroux (2010). "A 50-year high-resolution atmospheric reanalysis over France with the Safran system". In: *International Journal of Climatology*, 30.11, pp. 1627–1644.

Voormansik, Kaupo, Thomas Jagdhuber, Aire Olesk, Irena Hajnsek, and Konstantinos P. Papathanassiou (2013). "Towards a detection of grassland cutting practices with dual polarimetric TerraSAR-X data". In: *International Journal of Remote Sensing*, 34, pp. 8081 –8103.

Voormansik, Kaupo, Thomas Jagdhuber, Karlis Zalite, Mart Noorma, and Irena Hajnsek (2016). "Observations of Cutting Practices in Agricultural Grasslands Using Polarimetric SAR". In: *IEEE Journal of Selected Topics in Applied Earth Observations and Remote Sensing*, 9, pp. 1382–1396.

Voormansik, Kaupo, Karlis Zalite, Indrek Sünter, Tanel Tamm, Kalev Koppel, Tarvi Verro, Agris Brauns, Dainis Jakovels, and Jaan Praks (2020). "Separability of Mowing and Ploughing Events on Short Temporal Baseline Sentinel-1 Coherence Time Series". In: *Remote Sensing*, 12, p. 3784.

Vreugdenhil, Mariette, Claudio Navacchi, Bernhard Bauer-Marschallinger, Sebastian Hahn, Susan Steele-Dunne, Isabella Pfeil, Wouter Dorigo, and Wolfgang Wagner (2020). "Sentinel-1 Cross Ratio and Vegetation Optical Depth: A Comparison over Europe". In: *Remote Sensing*, 12.20.

Vreugdenhil, Mariette, Wolfgang Wagner, Bernhard Bauer-Marschallinger, Isabella Pfeil, Irene Teubner, Christoph Rüdiger, and Peter Strauss (2018). "Sensitivity of Sentinel-1 backscatter to vegetation dynamics: An Austrian case study". In: *Remote Sensing*, 10.9, p. 1396.

Vuolo, Francesco, Wai-Tim Ng, and Clement Atzberger (2017). "Smoothing and gap-filling of high resolution multi-spectral time series: Example of Landsat data". In: *International Journal of Applied Earth Observation and Geoinformation*, 57, pp. 202 –213.

Wang, Benyou, Lifeng Shang, Christina Lioma, Xin Jiang, Hao Yang, Qun Liu, and Jakob Grue Simonsen (2021). "On Position Embeddings in BERT". In: *International Conference on Learning Representations*.

Wang, Guoqiang, Shuman Liu, Tingxiang Liu, Zhiyuan Fu, Jingshan Yu, and Baolin Xue (2019a). "Modelling above-ground biomass based on vegetation indexes: a modified approach for biomass estimation in semi-arid grasslands". In: *International Journal of Remote Sensing*, 40, pp. 3835 –3854.

Wang, Jia-Wen and Ching-Hsue Cheng (2007). "Information Fusion Technique for Weighted Time Series Model". In: *2007 International Conference on Machine Learning and Cybernetics*. Vol. 4, pp. 1860–1865.

Wang, Jie, Xiangming Xiao, Rajen Bajgain, Patrick Starks, Jean Steiner, Russell B. Doughty, and Qing Chang (2019b). "Estimating leaf area index and aboveground biomass of grazing pastures using Sentinel-1, Sentinel-2 and Landsat images". In: *ISPRS Journal of Photogrammetry and Remote Sensing*, 154, pp. 189 –201.

Wang, Jie, Xiangming Xiao, Rajen Bajgain, Patrick J. Starks, Jean L. Steiner, Russell B. Doughty, and Qing Chang (2019c). "Estimating leaf area index and aboveground biomass of grazing pastures using Sentinel-1, Sentinel-2 and Landsat images". In: *ISPRS Journal of Photogrammetry and Remote Sensing*.

Wang, Jiyan, Ainong Li, and Jinhu Bian (2016). "Simulation of the Grazing Effects on Grassland Aboveground Net Primary Production Using DNDC Model Combined with Time-Series Remote Sensing Data - A Case Study in Zoige Plateau, China". In: *Remote Sensing*, 8, p. 168.

Wang, Murong, Xiabi Liu, Yixuan Gao, Xiao Ma, and Nouman Q. Soomro (2017a). "Superpixel segmentation: A benchmark". In: *Signal Processing: Image Communication*, 56, pp. 28–39.

Wang, Qian, Yue Yang, Yangyang Liu, Linjing Tong, Qi peng Zhang, and Jianlong Li (2019d). "Assessing the Impacts of Drought on Grassland Net Primary Production at the Global Scale". In: *Scientific Reports*, 9.

Wang, Ran, John A. Gamon, Craig A. Emmerton, Kyle R. Springer, Rong Yu, and Gabriel Hmimina (2020). "Detecting intra- and inter-annual variability in gross primary productivity of a North American grassland using MODIS MAIAC data". In: *Agricultural and Forest Meteorology*, 281, p. 107859.

Wang, Xiaoyi, Tao Wang, Dan Liu, Taotao Zhang, JinFeng Xu, Guishan Cui, Guanting Lv, and Huabing Huang (2019e). "Multisatellite Analyses of Spatiotemporal Variability in Photosynthetic Activity Over the Tibetan Plateau". In: *Journal of Geophysical Research*, 124, pp. 3778–3797.

Wang, Yinyin, Gaolin Wu, Lei Deng, Zhuangsheng Tang, Kaibo Wang, Wenyi Sun, and Zhouping Shangguan (2017b). "Prediction of aboveground grassland biomass on the Loess Plateau, China, using a random forest algorithm". In: *Scientific Reports*, 7.

Watkinson, A.R. and S.J. Ormerod (2001). "Grasslands, grazing and biodiversity: editors' introduction". In: *Journal of Applied Ecology*, 38.2, pp. 233–237.

Wehlage, Donald C., John A. Gamon, Donnette R. Thayer, and David V. Hildebrand (2016). "Interannual Variability in Dry Mixed-Grass Prairie Yield: A Comparison of MODIS, SPOT, and Field Measurements". In: *Remote Sensing*, 8, p. 872.

Wei, Sun, Li Meng, Wang Junhao, and Fu Gang (2019). "Driving Mechanism of Gross Primary Production Changes and Implications for Grassland Management on the Tibetan Plateau". In: *Journal of Resources and Ecology*, 10, pp. 472 –480.

Werbos, Paul and Paul John (1974). "Beyond regression : new tools for prediction and analysis in the behavioral sciences /". In.

Wesemeyer, M., M. Schwieder, J. Pickert, and P. Hostert (2021). "Identifying areas of homogeneous grassland management based on iterative segmentation of Sentinel-1 and Sentinel-2 data". In: vol. 26, p. 231.

Whitcraft, Alyssa K., Eric F. Vermote, Inbal Becker-Reshef, and Christopher O. Justice (2015). "Cloud cover throughout the agricultural growing season: Impacts on passive optical earth observations". In: *Remote Sensing of Environment*, 156, pp. 438–447.

White, Robin P., Siobhan Murray, and Mark Rohweder (2000). "Pilot analysis of global ecosystems : grassland ecosystems". In: *World Ressources Institute (WRI)*.

Widrow, B. and M. E. Hoff (1960). "Adaptive Switching Circuits". In: *1960 IRE WESCON Convention Record*. Reprinted in *Neurocomputing* MIT Press, 1988 ., pp. 96–104.

Wilsey, Brian (2018). "The biology of grasslands". In: *The Biology of Grasslands*, pp. 1–195.

Winkler, Karina, Richard Fuchs, Mark Rounsevell, and Martin Herold (2021). "Global land use changes are four times greater than previously estimated". In: *Nature Communications*, 12.1, p. 2501.

Wu, Chaoyang (2012). "Use of a vegetation index model to estimate gross primary production in open grassland". In: *Journal of Applied Remote Sensing*, 6.

Wu, Weixing, Shaoqiang Wang, Xiangming Xiao, Guirui Yu, Yu ling Fu, and Yanbin Hao (2008). "Modeling gross primary production of a temperate grassland ecosystem in Inner Mongolia, China, using MODIS imagery and climate data". In: *Science in China Series D: Earth Sciences*, 51, pp. 1501–1512.

Wu, Xinhong, Peng Li, Chao Jiang, Pengtao Liu, Jing He, and Xiangyang Hou (2014). "Climate changes during the past 31 years and their contribution to the changes in the productivity of rangeland vegetation in the Inner Mongolian typical steppe". In: *Rangeland Journal*, 36, pp. 519–526.

Wylie, Bruce K., John A. Harrington, Stephen D. Prince, and Issa Denda (1991). "Satellite and ground-based pasture production assessment in Niger: 1986-1988". In: *International Journal of Remote Sensing*, 12, pp. 1281–1300.

Wylie, Bruce K., Daniel M. Howard, Devendra Dahal, Tagir Gilmanov, Lei Ji, Li Zhang, and Kelcy Smith (2016). "Grassland and Cropland Net Ecosystem Production of the U.S. Great Plains: Regression Tree Model Development and Comparative Analysis". In: *Remote Sensing*, 8, p. 944.

Wylie, Bruce K., David J. Meyer, Larry L. Tieszen, and Sylvio Mannel (2002). "Satellite mapping of surface biophysical parameters at the biome scale over the North American grasslands a case study". In: *Remote Sensing of Environment*, 79, pp. 266–278.

Xia, Jiangzhou, Shuguang Liu, Shunlin Liang, Yang Chen, Wenfang Xu, and Wenping Yuan (2014). "Spatio-Temporal Patterns and Climate Variables Controlling of Biomass Carbon Stock of Global Grassland Ecosystems from 1982 to 2006". In: *Remote Sensing*, 6, pp. 1783–1802.

Xie, Yichun, Zongyao Sha, Mei Yu, Yongfei Bai, and Lianchang Zhang (2009). "A comparison of two models with Landsat data for estimating above ground grassland biomass in Inner Mongolia, China". In: *Ecological Modelling*, 220, pp. 1810–1818.

Xing, Xiao ru, Xingliang Xu, Xianzhou Zhang, Cai ping Zhou, Minghua Song, Bin Shao, and Hua Ouyang (2010). "Simulating net primary production of grasslands in northeastern Asia using MODIS data from 2000 to 2005". In: *Journal of Geographical Sciences*, 20, pp. 193–204.

Xiong, Qinli, Yang Xiao, Marwa Waseem A. Halmy, Mohammed A Dakhil, Pinghan Liang, Cheng gang Liu, Linxiu Zhang, Bikram Pandey, Kaiwen Pan, Sameh B. El Kafraway, and Jun Chen (2019). "Monitoring the impact of climate change and human activities on grassland vegetation dynamics in the northeastern Qinghai-Tibet Plateau of China during 2000–2015". In: *Journal of Arid Land*, 11, pp. 637 –651.

Xu, B., X. C. Yang, Weiguo Tao, J. M. Miao, Z. W. Yang, Haiqing Liu, Y. X. Jin, Xi Zhu, Zhihao Qin, Haitao Lv, and Jinya Li (2013). "MODIS-based remote-sensing monitoring of the spatiotemporal patterns of Chinaś grassland vegetation growth". In: *International Journal of Remote Sensing*, 34, pp. 3867 –3878.

Xu, Bin, Xiuchun Yang, Weiguo Tao, Zhihao Qin, Haiqi Liu, and J. M. Miao (2007). "Remote sensing monitoring upon the grass production in China". In: *Acta Ecologica Sinica*, 27, pp. 405–413.

Xu, Dandan, Nicola Koper, and Xulin Guo (2018). "Quantifying the influences of grazing, climate and their interactions on grasslands using Landsat TM images". In: *Grassland Science*, 64, pp. 118–127.

Xu, Dawei, Baorui Chen, Beibei Shen, Xu Wang, Yuchun Yan, Lijun Xu, and Xiaoping Xin (2019a). "The Classification of Grassland Types Based on Object-Based Image Analysis with Multisource Data". In: *Rangeland Ecology and Management*, 72, pp. 318 –326.

Xu, Dawei, Baorui Chen, Ruirui Yan, Yuchun Yan, Xinbo Sun, Lijun Xu, and Xiaoping Xin (2019b). "Quantitative monitoring of grazing intensity in the temperate meadow steppe based on remote sensing data". In: *International Journal of Remote Sensing*, 40.5-6, pp. 2227–2242.

Xu, Hao, Xin-ping Wang, and Xiao xiao Zhang (2016). "Alpine grasslands response to climatic factors and anthropogenic activities on the Tibetan Plateau from 2000 to 2012". In: *Ecological Engineering*, 92, pp. 251–259.

Xu, Hao J., Xin P. Wang, and Tai bao Yang (2017). "Trend shifts in satellite-derived vegetation growth in Central Eurasia, 1982–2013". In: *Science of The Total Environment*, 579, pp. 1658 –1674.

Xue, Jinru and Baofeng Su (2017). "Significant Remote Sensing Vegetation Indices: A Review of Developments and Applications". In: *Journal of Sensors*, 2017, p. 1353691.

Yang, Chia-Hsiang, Sebastian Mader, Soenke Müller, Carsten Haub, Andreas Müterthies, and Andreas Hermann (2021). "Wide-area monitoring of soil moisture in peatlands using Sentinel-1 images". In: vol. 26, p. 231.

Yang, Limin, Bruce K. Wylie, Larry L. Tieszen, and Bradley C. Reed (1998). "An analysis of relationships among climate forcing and time-integrated NDVI of grasslands over the U.S. northern and central Great Plains". In: *Remote Sensing of Environment*, 65, pp. 25–37.

Yang, Shudong, Xueying Yu, and Ying Zhou (2020). "LSTM and GRU Neural Network Performance Comparison Study: Taking Yelp Review Dataset as an Example". In: pp. 98–101.

Yang, Shuxia, Qisheng Feng, Tiangang Liang, Baokang Liu, Wen juan Zhang, and Hongjie Xie (2018). "Modeling grassland above-ground biomass based on artificial neural network and remote sensing in the Three-River Headwaters Region". In: *Remote Sensing of Environment*, 204, pp. 448–455.

Yang, Wen bin, Tao Lu, Siyao Liu, J. Jian, Fusun Shi, Yan Wu, and Ning Wu (2017). "Satellite-based estimation of net primary productivity for southern China's grasslands from 1982 to 2012". In: *Climate Research*, 71, pp. 187–201.

Yang, Xiaohui, Xulin Guo, and Michael J. FitzsimmonsM.J. Fitzsimmons (2012). "Assessing light to moderate grazing effects on grassland production using satellite imagery". In: *International Journal of Remote Sensing*, 33, pp. 5087 –5104.

Yang, Xiuchun, Bin Xu, Yunxiang Jin, Zhihao Qin, Hailong Ma, Jinya Li, Fen Zhao, Shi Chen, and Xiaohua Zhu (2015). "Remote sensing monitoring of grassland vegetation growth in the Beijing-Tianjin sandstorm source project area from 2000 to 2010". In: *Ecological Indicators*, 51, pp. 244–251.

Yang, Yanlin, Jinliang Wang, Yuxiang Chen, Feng Cheng, Guangjie Liu, and Zenghong He (2019a). "Remote-Sensing Monitoring of Grassland Degradation Based on the GDI in Shangri-La, China". In: *Remote Sensing*, 11, p. 3030.

Yang, Yi, David Tilman, George Furey, and Clarence Lehman (2019b). "Soil carbon sequestration accelerated by restoration of grassland biodiversity". In: *Nature Communications*, 10.1, p. 718.

Yang, Yuanhe, Jingyun Fang, Yude Pan, and Chengjun Ji (2009). "Aboveground biomass in Tibetan grasslands". In: *Journal of Arid Environments*, 73, pp. 91–95.

Yin, Fang, Xiangzheng Deng, Qin Jin, Yongwei Yuan, and Chunhong Zhao (2014). "The impacts of climate change and human activities on grassland productivity in Qinghai Province, China". In: *Frontiers of Earth Science*, 8.1, pp. 93–103.

Yin, Gaofei, Ainong Li, Chaoyang Wu, Jiyan Wang, Qiaoyun Xie, Zhengjian Zhang, Xi Nan, Huaan Jin, Jinhu Bian, and Guangbin Lei (2018). "Seamless Upscaling of the Field-Measured Grassland Aboveground Biomass Based on Gaussian Process Regression and Gap-Filled Landsat 8 OLI Reflectance". In: *ISPRS International Journal of Geo-Information*, 7.7.

Yin, Gaohong, Gregoire Mariethoz, Ying Sun, and Matthew F. McCabe (2017). "A comparison of gap-filling approaches for Landsat-7 satellite data". In: *International Journal of Remote Sensing*, 38.23, pp. 6653–6679.

Yin, Jianpeng, Qisheng Feng, Tiangang Liang, Baoping Meng, Shuxia Yang, Jinlong Gao, Jing Ge, Mengjing Hou, Jie Liu, Wei Wang, Hui Yu, and Baokang Liu (2020). "Estimation of Grassland Height Based on the Random Forest Algorithm and Remote Sensing in the Tibetan Plateau". In: *IEEE Journal of Selected Topics in Applied Earth Observations and Remote Sensing*, 13, pp. 178–186.

Yin, Junjun, Tao Wang, Yanlei Du, Xiyun Liu, Liangjiang Zhou, and Jian Yang (2021). "SLIC Superpixel Segmentation for Polarimetric SAR Images". In: *IEEE Transactions on Geoscience and Remote Sensing*, pp. 1–17.

You, Yongfa, Siyuan Wang, Yuanxu Ma, Xiaoyue Wang, and Weihua Liu (2019). "Improved Modeling of Gross Primary Productivity of Alpine Grasslands on the Tibetan Plateau Using the Biome-BGC Model". In: *Remote Sensing*, 11, p. 1287.

Yu, Hao, Lei Wang, Zongming Wang, Chun-Ying Ren, and Bai Zhang (2019). "Using Landsat OLI and Random Forest to Assess Grassland Degradation with Aboveground Net Primary Production and Electrical Conductivity Data". In: *ISPRS Int. J. Geo Inf.*, 8, p. 511.

Yu, Rui, Andrew J. Evans, and Nick Malleson (2018). "Quantifying grazing patterns using a new growth function based on MODIS Leaf Area Index". In: *Remote Sensing of Environment*, 209, pp. 181–194.

Zalite, Karlis, Oleg Antropov, Jaan Praks, Kaupo Voormansik, and Mart Noorma (2016). "Monitoring of Agricultural Grasslands With Time Series of X-Band Repeat-Pass Interferometric SAR". In: *IEEE Journal of Selected Topics in Applied Earth Observations and Remote Sensing*, 9.8, pp. 3687–3697.

Zalite, Karlis, Kaupo Voormansik, Jaan Praks, Oleg Antropov, and Mart Noorma (2014). "Towards detecting mowing of agricultural grasslands from multi-temporal COSMO-SkyMed data". In: *2014 IEEE Geoscience and Remote Sensing Symposium*, pp. 5076–5079.

Zekoll, Viktoria, Magdalena Main-Knorn, Kevin Alonso, Jerome Louis, David Frantz, Rudolf Richter, and Bringfried Pflug (2021). "Comparison of Masking Algorithms for Sentinel-2 Imagery". In: *Remote Sensing*, 13.1.

Zeng, Linglin, Brian D. Wardlow, Daxiang Xiang, Shun Hu, and Deren Li (2020). "A review of vegetation phenological metrics extraction using time-series, multispectral satellite data". In: *Remote Sensing of Environment*, 237, p. 111511.

Zeng, Na, Xiaoli Ren, Honglin He, Li Zhang, Dan Zhao, Rong Ge, Pan Li, and Zhongen Niu (2019). "Estimating grassland aboveground biomass on the Tibetan Plateau using a random forest algorithm". In: *Ecological Indicators*.

Zhang, Binghua, Li Zhang, Dong Xie, Xiaoli Yin, Chunjing Liu, and Guang Liu (2016). "Application of Synthetic NDVI Time Series Blended from Landsat and MODIS Data for Grassland Biomass Estimation". In: *Remote Sensing*, 8.1.

Zhang, Chuanrong, Weidong Li, and David J. Travis (2007). "Gaps-fill of SLC-off Landsat ETM+ satellite image using a geostatistical approach". In: *International Journal of Remote Sensing*, 28.22, pp. 5103–5122.

Zhang, Haiyan, Jiangwen Fan, Junbang Wang, Wei Cao, and Warwick Harris (2018). "Spatial and temporal variability of grassland yield and its response to climate change and anthropogenic activities on the Tibetan Plateau from 1988 to 2013". In: *Ecological Indicators*, 95, pp. 141–151.

Zhang, Lining, Huadong Guo, Gensuo Jia, Bruce K. Wylie, Tagir Gilmanov, Daniel M. Howard, Lei Ji, Jingfeng Xiao, Jin long Li, Wenping Yuan, Tianbao Zhao, Shiping Chen, Guangsheng Zhou, and Tomomichi Kato (2014a). "Net ecosystem productivity of temperate grasslands in northern China: An upscaling study". In: *Agricultural and Forest Meteorology*, 184, pp. 71–81.

Zhang, Shengwei, Rui Zhang, Tingxiang Liu, Xin Song, and Mark A Adams (2017). "Empirical and model-based estimates of spatial and temporal variations in net primary productivity in semi-arid grasslands of Northern China". In: *PLoS ONE*, 12.

Zhang, Xiaoyang, Mark A. Friedl, Crystal B. Schaaf, Alan H. Strahler, John C.F. Hodges, Feng Gao, Bradley C. Reed, and Alfredo Huete (2003). "Monitoring vegetation phenology using MODIS". In: *Remote Sensing of Environment*, 84.3, pp. 471–475.

Zhang, Yili, Wei Qi, Cai ping Zhou, Mingjun Ding, Linshan Liu, Jungang Gao, Wanqi Bai, Zhaofeng Wang, and Du Zheng (2014b). "Spatial and temporal variability in the net primary production of alpine grassland on the Tibetan Plateau since 1982". In: *Journal of Geographical Sciences*, 24, pp. 269–287.

Zhang, Yu and Qiang Yang (2021). "A Survey on Multi-Task Learning". In: *IEEE Transactions on Knowledge and Data Engineering*, pp. 1–1.

Zhao, Fen, Bin Xu, Xiuchun Yang, Yunxiang Jin, Jinya Li, L. Xia, Shi Chen, and Hailong Ma (2014). "Remote Sensing Estimates of Grassland Aboveground Biomass Based on MODIS Net Primary Productivity (NPP): A Case Study in the Xilingol Grassland of Northern China". In: *Remote Sensing*, 6, pp. 5368–5386.

Zhao, Fen, Bin Xu, Xiuchun Yang, L. Xia, Yunxiang Jin, Jinya Li, Wenbo Zhang, Jian Guo, and Ge Shen (2019). "Modelling and analysis of net primary productivity and its response mechanism to climate factors in temperate grassland, northern China". In: *International Journal of Remote Sensing*, 40, pp. 2259 –2277.

Zhao, Wenzhi, Yang Qu, Jiage Chen, and Zhanliang Yuan (2020). "Deeply synergistic optical and SAR time series for crop dynamic monitoring". In: *Remote Sensing of Environment*, 247, p. 111952.

Zheng, Zhoutao, Wenquan Zhu, and Yang jian Zhang (2020). "Seasonally and spatially varied controls of climatic factors on net primary productivity in alpine grasslands on the Tibetan Plateau". In: *Global Ecology and Conservation*, 21.

Zhou, Jie, Li Jia, and Massimo Menenti (2015). "Reconstruction of global MODIS NDVI time series: Performance of Harmonic ANalysis of Time Series (HANTS)". In: *Remote Sensing of Environment*, 163, pp. 217 –228.

Zhou, Muqing, Zhaoguo Wu, Difan Chen, and Ya Zhou (2013). "An improved vein image segmentation algorithm based on SLIC and Niblack threshold method". In: *2013 International Conference on Optical Instruments and Technology: Optoelectronic Imaging and Processing Technology*. Ed. by Xinggang Lin and Jesse Zheng. Vol. 9045. International Society for Optics and Photonics. SPIE, pp. 89 –98.

Zhou, Wei, Han Yang, Lu Huang, Chun Chen, Xiaosong Lin, Zhongjun Hu, and Jianlong Li (2017a). "Grassland degradation remote sensing monitoring and driving factors quantitative assessment in China from 1982 to 2010". In: *Ecological Indicators*, 83, pp. 303–313.

Zhou, Wei Yuan, Jianlong Li, Shaojie Mu, Chencheng Gang, and Zheng guo Sun (2014a). "Effects of ecological restoration-induced land-use change and improved management on grassland net primary productivity in the Shiyanghe River Basin, north-west China". In: *Grass and Forage Science*, 69, pp. 596–610.

Zhou, Yu, Li Zhang, Jingfeng Xiao, Shiping Chen, Tomomichi Kato, and Guangsheng Zhou (2014b). "A Comparison of Satellite-Derived Vegetation Indices for Approximating Gross Primary Productivity of Grasslands". In: *Rangeland Ecology & Management*, 67.1, pp. 9–18.

Zhou, Yuting, K. Colton Flynn, Prasanna H. Gowda, Pradeep Wagle, Shengfang Ma, Vijaya G. Kakani, and Jean L. Steiner (2021). "The potential of active and passive remote sensing to detect frequent harvesting of alfalfa". In: *International Journal of Applied Earth Observation and Geoinformation*, 104, p. 102539.

Zhou, Yuting, Xiangming Xiao, Pradeep Wagle, Rajen Bajgain, Hayden Mahan, Jeffrey B. Basara, Jinwei Dong, Yuanwei Qin, Geli Zhang, Yiqi Luo, Prasanna H. Gowda, James P.S. Neel, Patrick J. Starks, and Jean L. Steiner (2017b). "Examining the short-term impacts of diverse management practices on plant phenology and carbon fluxes of Old World bluestems pasture". In: *Agricultural and Forest Meteorology*, 237-238, pp. 60–70.

Zhu, Xiao Xiang, Devis Tuia, Lichao Mou, Gui-Song Xia, Liangpei Zhang, Feng Xu, and Friedrich Fraundorfer (2017). "Deep Learning in Remote Sensing: A Comprehensive Review and List of Resources". In: *IEEE Geoscience and Remote Sensing Magazine*, 5.4, pp. 8–36.

Zhu, Xiaohua, Chuanrong Li, and Lingli Tang (2019). "Assessing the spatiotemporal dynamic of NPP in desert steppe and its response to climate change from 2003 to 2017: a case study in Siziwang banner". In: *Remote Sensing for Agriculture, Ecosystems, and Hydrology XXI*. Ed. by Christopher M. U. Neale and Antonino Maltese. Vol. 11149. International Society for Optics and Photonics. SPIE, pp. 449 –454.

Zhu, Xiaolin, Eileen H. Helmer, Feng Gao, Desheng Liu, Jin Chen, and Michael A. Lefsky (2016). "A flexible spatiotemporal method for fusing satellite images with different resolutions". In: *Remote Sensing of Environment*, 172, pp. 165 –177.

Zhu, Zhe, Shixiong Wang, and Curtis E. Woodcock (2015). "Improvement and expansion of the Fmask algorithm: cloud, cloud shadow, and snow detection for Landsats 4–7, 8, and Sentinel 2 images". In: *Remote Sensing of Environment*, 159, pp. 269–277.

Zongyao, Sha and Bai Yongfei (2013). "Mapping grassland vegetation cover based on Support Vector Machine and association rules". In: 2013 *Ninth International Conference on Natural Computation (ICNC)*, pp. 44–49.

Monitoring grassland dynamics by exploiting multi-modal satellite image time series.

Anatol Garioud

Abstract

The vast grassland surfaces as well as the growing recognition of the ecosystem services they provide have revealed urgent needs for their conservation and sustainable management. Despite the acknowledged importance of grassland management practices, there are currently no large-scale efforts reporting on their frequency and nature. Satellite remote sensing time series appear to be a suitable tool for efficient grassland monitoring and allow synoptic and regular analysis. The research conducted in this PhD aims to develop methods for the detection of grassland management practices from complementary optical and SAR multivariate time series. Advances in deep learning are employed to regress multivariate SAR time series and contextual knowledge towards optical NDVI. Resulting gap-free time series are used to efficiently explore methods aiming to detect vegetation status changes related to management practices on grasslands.

Résumé

Les vastes surfaces de prairies et la reconnaissance croissante des services écosystémiques qu'elles rendent impliquent d'urgents besoins pour leur conservation et leur gestion durable. En dépit de l'impact avéré des pratiques culturales sur les prairies, l'observation de la fréquence et de la nature de l'exploitation des prairies demeure restreinte. La télédétection par satellite est un outil approprié pour un suivi efficace des prairies, permettant une analyse synoptique et régulière. Cette thèse vise à développer des méthodes de détection de l'exploitation des prairies à partir de séries temporelles complémentaires multivariées optiques et radars. Les progrès permis par l'apprentissage profond sont utilisés pour régresser des séries temporelles radars multivariées et des connaissances contextuelles vers le NDVI optique. Les séries temporelles sans données manquantes qui en résultent sont utilisées pour explorer différentes méthodes permettant de détecter l'exploitation hétérogène des prairies.